Microstreaming induced in the vicinity of an acoustically excited, nonspherically oscillating microbubble

Sarah Cleve

N° d'ordre NNT: 2019LYSEC28

THÈSE de DOCTORAT DE L'UNIVERSITÉ DE LYON
opérée au sein de l'École Centrale de Lyon

École Doctorale N° 162
Mécanique Énergétique Génie Civil Acoustique

Spécialité de doctorat : Acoustique

Soutenue publiquement le 04/10/2019, par

Sarah Cleve

Microstreaming induced in the vicinity of an acoustically excited, nonspherically oscillating microbubble

Microstreaming induit au voisinage d'une bulle micrométrique excitée acoustiquement en mode de surface

---

Devant le jury composé de:

Mettin, Robert	Senior Researcher, Georg-August-Universität Göttingen	Rapporteur
Marmottant, Philippe	Directeur de Recherche CNRS, Université Grenoble Alpes	Rapporteur
Derec, Caroline	Maître de Conférences, Université Paris Diderot	Examinatrice
Spelt, Peter	Professeur des Universités, Université Claude Bernard Lyon 1	Président du jury
Blanc-Benon, Philippe	Directeur de Recherche CNRS, LMFA, École Centrale de Lyon	Directeur de thèse

Invités:

Inserra, Claude	Maître de Conférences, Université Claude Bernard Lyon 1	Co-Directeur de thèse
Mauger, Cyril	Maître de Conférences, INSA de Lyon	Co-Directeur de thèse

Acknowledgments

First of all, I want to thank my supervisors Philippe, Claude and Cyril. They have all played very different roles during my three years of PhD and together this made the whole experience more than worth it. I want to thank the LabEx CeLyA for financing my PhD and the two laboratories which I was affiliated to - the LabTAU and LMFA. At any moment I was welcome at the different places. A large thanks also to Paul for two great months at the University of Glasgow. And also a large thanks to the jury members for the time spent on reviewing my manuscript and for all the detailed little comments. Thanks to Sascha for such a beautiful theoretical model. Thanks to Matthieu, without whose preliminary work my start into experimental bubble dynamics would have been much more laborious. Thanks to Gabriel and Maxime for the common work on all aspects of bubbles. Thanks to Elliot for beautiful snapshots of pairs of bubbles. Thanks to Tom, Armando and Dai for three years for braving the elements through our hardly existing office windows. Thanks to Clément and Jonas for reading my manuscript from an outside point of view. Thanks to Andrea, Stefan, Pierre and Moira for the help in the last preparations. And thanks to Felix, Fine and Johannes for the long-distance call. In the same ways as the rest of my manuscript I keep the acknowledgments short. Concerning the allusions made here, I hope that all those who are concerned, will understand the rest of the stories without need to write every detail down. A last thanks to everyone who I might have forgotten here or whose name is not specifically mentioned.

Abstract

Microbubbles find use in several domains, one of them being medical ultrasound applications. Different characteristics of those bubbles, such as their acoustic resonance or their destructive effect during inertial cavitation, can be exploited. Another phenomenon induced around acoustically excited bubbles is microstreaming, that means a relatively slow mean flow with respect to the fast bubble oscillations. While microstreaming and its associated shear stresses are commonly agreed to play a role in the permeabilization of cell membranes, a detailed understanding of the induced flows is, however, missing. To acquire basic physical knowledge, this work focuses on the characterization of streaming induced around an air bubble in water, more precisely around a single acoustically trapped and excited, nonspherically oscillating bubble. The experimental part consists of two steps. First, the bubble dynamics has to be controlled, in particular the triggered shape mode and the orientation of the bubble. For this, the use of bubble coalescence proves to be an adequate method. In a second step, the microstreaming is recorded in parallel to bubble dynamics. This allows to correlate the obtained streaming patterns to the respective shape oscillations. The large number of obtained pattern types can be classified, in particular with respect to the mode number and bubble size. A close investigation of the bubble dynamics furthermore allows finding some important physical mechanisms which go along with such a variety of streaming patterns. In order to confirm the experimental findings, an analytical model has been developed. It is based upon time-averaged second-order fluid mechanics equations and the experimentally obtained bubble dynamics serves as input parameters. Supplementary to the microstreaming work, this manuscript contains a short section on directed jetting of contrast agent microbubbles, which might appear at high acoustic driving. The impact of these microjets on cells presents another mechanism made responsible for the permeabilization of cell membranes.

Key words: bubbles, microstreaming, cavitation, coalescence, surface modes, microstreaming model, jetting, contrast agent microbubbles

Résumé

Des bulles micrométriques sont utilisées dans divers domaines, notamment pour des applications médicales basées sur les ultrasons. Il est possible d'exploiter différentes propriétés de ces bulles, comme par exemple leur résonance acoustique ou leur effet destructeur en cavitation inertielle. Un autre mécanisme exploitable est la génération de micro-écoulements, appelés *microstreaming*, induits autour d'une bulle. Ces écoulements sont relativement lents par rapport aux oscillations rapides de la bulle. Le *microstreaming* et les contraintes de cisaillement associées jouent un rôle important dans la perméabilisation d'une membrane cellulaire, mais il manque encore une compréhension détaillée de l'écoulement induit. Afin d'améliorer la compréhension des phénomènes physiques en jeu, ce travail se concentre sur les écoulements induits autour d'une bulle d'air dans de l'eau piégée et excitée acoustiquement et oscillant en modes de surface. La partie expérimentale se décompose en deux étapes. Dans un premier temps, il est nécessaire de contrôler la dynamique de la bulle, en particulier ses modes de surface et son orientation. Ceci est réalisé par coalescence entre deux bulles. Dans un second temps, le *microstreaming* est généré et enregistré simultanément à la dynamique de bulle. De cette manière il est possible de corréler les motifs d'écoulement aux oscillations de la bulle. Le grand nombre de motifs obtenus peut être classé selon le mode dominant et la taille de la bulle. Une étude plus détaillée de la dynamique de bulle permet de déduire les paramètres importants qui mènent à une telle variété de motifs de *microstreaming*. Afin de confirmer les résultats expérimentaux, un modèle analytique a été développé. Il est basé sur les équations de la mécanique des fluides de deuxième ordre et moyennées en temps. La dynamique d'interface de la bulle obtenue expérimentalement sert de donnée d'entrée au modèle. Ce manuscrit contient en supplément une section sur la génération de microjets par l'implosion d'agents de contraste. Ces jets peuvent apparaître en cas d'excitation acoustique suffisamment élevée. L'impact de ces jets sur parois présente un autre mécanisme responsable de la perméabilisation de membranes cellulaires.

Mots-clés : bulles, microstreaming, cavitation, coalescence, modes de surface, modèle de microstreaming, jetting, agents de contraste

Contents

Introduction

If you ask a child, they will probably associate the word *bubble* with chewing gum, soap bubbles or sprinkling water. Indeed, different types of bubbles appear everywhere in our daily life. Some of them are obvious, such as in beverages and whirlpools, others are much more hidden such as bubbles in foams, in the ocean, and even in trees. Asking an engineer, he might link bubbles to cavitation, a topic that in this context is mostly associated with damage. And indeed, cavitation bubbles, that means, small vapor bubbles created due to a pressure drop below vapor pressure, have been first observed in hydraulic systems such as ship propellers and pumps due to their destructive effect. Nowadays, bubbles are also exploited in many different positive ways. Two topics that I will briefly discuss in this manuscript are microfluidics and the medical field. Some of these applications motivate us to take a closer look at single bubble dynamics and the question how this affects the surrounding liquid.

The subjects of my study are small air bubbles in water. We trap and excite these bubbles with ultrasound, which forces them to oscillate radially and, under more specific conditions, to show surface deformations, the so-called surface modes. These relatively fast oscillations induce a relatively slow mean flow, called microstreaming, in the vicinity of the bubble. Microstreaming is due to nonlinear second-order effects in the fluid mechanics equations. Interesting for practical applications is that streaming implies shear flow which itself implies shear stresses in the liquid. These effects are already exploited to manipulate for instance cells, particles and others. However, the underlying physical mechanisms are not completely understood for all existing applications, the present work hence aims to develop further understanding. More precisely, the objective of my work is to characterize the microstreaming patterns induced around acoustically excited, nonspherically oscillating microbubbles far from any boundaries.

The manuscript follows the above sketched logic. The general context and the common knowledge on bubble dynamics is set up in chapter 1, the experimental control of nonspherical bubble dynamics follows in chapter 2 and the resulting microstreaming in chapter 3. Furthermore, we have developed a theoretical model which aims to complement the experiments for more understanding and which is detailed in chapter 4.

In more detail, we will discuss the following points. At the beginning of chapter 1, in section 1.1, I will give an overview mainly over the medical context that drives my work. As we will see, bubbles seem to appear everywhere, usually linked to ultrasound treatment. Bubbles

can serve as contrast agents for medical imaging, but they also naturally appear or are injected in some therapeutic applications. In one of these applications, sonoporation, the role of microstreaming is widely accepted. The induced shear stresses are made responsible for a permeablization of the cell membrane, which can then can be exploited for drug delivery into cells. A question less well studied is related to the exact mechanisms of streaming. This is where my work comes into play: understand and characterize the streaming. Section 1.2 is hence dedicated to the topic of streaming and we will discuss where information is lacking also in view of theoretical models for comparison. We will conclude that the easiest accessible theoretical models are to be found for single bubbles without any supplementary boundaries, but that no thorough experimental investigations exist so far. This sets the frame for the following work: characterize microstreaming around free bubbles. But before we do so, we first need bubbles. Section 1.3 covers different types of bubbles and ways to create them. Note that in the main part of my manuscript, the term *bubble* implies a gas or air bubble in water. As a next step, we want to understand how a bubble reacts when exposed to ultrasound. One effect comes from the so-called Bjerknes forces, which attract our subresonant size bubbles to acoustic pressure antinodes. Another effect leads to radial oscillations, explained in section 1.4. High acoustic pressure and the choice of the correct parameters furthermore allows the excitation of surface modes, detailed in section 1.5. Once we understand this theoretical background, we can move on to experimentally controlling the bubble dynamics in chapter 2.

As a first step, in section 2.1, I will evoke the current experimental methods that are used to trigger surface modes. As we will see, none of them fulfills our two requirements, controlled orientation of the bubble and steady-state oscillations. A new solution that we found is to trigger surface modes by bubble coalescence. A short introduction will be given in section 2.2. In section 2.3 I will then introduce the experimental setup and discuss its important features. Section 2.4 is dedicated to the main results obtained for bubble coalescence. The important aspects are that it is possible to control the axis of symmetry and to obtain steady-state oscillations. With the theoretical knowledge on surface modes we thus master a rapid method to trigger nonspherical oscillations with a desired mode number. But experiments inevitably entail uncertainties and sometimes care has to be taken with their interpretation. Some of these aspects will be addressed in section 2.5. Before closing the chapter on the experimental control of bubble dynamics, I will include a short outlook on some experiments I have conducted before and during my stay at the University of Glasgow: bubble dynamics of a bubble attached to a wall. This topic is not a requirement for the rest of my manuscript, but an outlook on where the topic might go in the future. The reason is that in real life, bubbles are not always freely floating, but might also have supplementary boundary conditions. In particular for comparison to theoretical models, taking into account boundaries will be a challenge.

Chapter 2 leaves us with a tool and the necessary comprehension on bubble dynamics. Chapter 3 is then finally dedicated to microstreaming itself. The previous experimental setup is extended to visualize the streaming, see section 3.1. In sections 3.2 to 3.4 different experimental

results are presented. More precisely, section 3.2 sets the reference case for pure radial oscillations for which no streaming is observed. Section 3.3 then presents the full characterization of bubbles, including their dynamics and induced streaming patterns. As we will see, there are not one or two different streaming patterns, but a large variety of them. Obviously, the mode number plays a role in their definition, but this is not sufficient. For this reason, I proceed to classify the different patterns in section 3.4. In particular, we find on the one hand large cross-like patterns and on the other hand smaller lobe-like patterns. I will then show that the bubble size, smaller or larger than the resonant size of the respective mode, will play an important role. In section 3.5, we will see some possible assumptions to explain the underlying physics that leads to the found distinction in large cross-like and smaller lobe-like patterns. We will discuss the richness of the modal content, translational oscillations and phase differences between different modes. In particular, the latter aspect seems to be a good candidate to explain a considerable part of our observations. Chapter 3 will end with an outlook on further observations, in particular the streaming induced by a pair of closely trapped bubbles.

The manuscript closes with a theoretical model in chapter 4. The model has been derived mainly by A. Doinikov and C. Inserra, the implementation has furthermore been carried out by G. Regnault and myself. The model aims to provide an analytical/numerical tool, that allows us to predict the shape of the appearing microstreaming when the bubble dynamics is provided as input parameters. In particular, we consider the fac, that different modes might oscillate at different frequencies. In section 4.1, I summarize the main idea of the model and explain its global steps. The general solutions for the first-order solution of the time dependent velocity and for the time-averaged second-order equation follow in section 4.2. As it is not obvious to find a general analytical solution for this equation, we first solve it for specific cases such as the streaming induced by the interaction between the radial mode 0 and a shape mode m. These specific cases for which we have found solutions are gathered in section 4.3, while the general case is still in progress. In a next step, in section 4.4, we validate our model through comparison to previous models, in particular those by Longuet-Higgins [74] and Spelman and Lauga [117]. The last part, section 4.5, then compares our theoretical model to our experimental results. We can in particular reproduce numerically some of the patterns observed in experiments. Furthermore we can confirm that the phasing between different interacting modes plays a role. The theoretical model already gives valuable information and we expect that, as soon as it is completed for the general case, we will be able to cover our whole set of experimental findings.

At this point, the main body of my manuscript ends. In short, the main objective, the experimental characterization of microstreaming patterns, has been successfully fulfilled. As we will have seen, many more paths for further investigations have been opened. However, I want to draw attention to one more chapter, appendix A. During my stay at the University of Glasgow, I worked on jetting of contrast agent microbubbles. This topic has arisen from a given occasion, but as it is not directly linked to the general objective of microstreaming, I included the chapter as an appendix. Nonetheless, the study is not completely off topic. In fact, jetting of contrast

agent microbubbles can occur during medical ultrasound applications. It can have many different effects, one of them being another mechanism held responsible for sonoporation. In appendix A.1 I will briefly introduce the experimental setup used and in appendix A.2 present the main results.

As a last note of this introduction, let me give a short comment on the way of referencing bibliography. While I use standard referencing such as [1], [2], [3] for external sources, my own work where I have contributed as first author or co-author is referenced as [OP1], [OP2], [OP3] and so on. The two separate bibliographies can be found at the end of this manuscript.

Chapter 1

About bubbles

This introductory chapter aims to introduce the state of the art that is helpful to motivate and understand my work. To situate the research on bubbles, let me first draw a broad picture of cavitation and bubbles, in particular in the field of medical applications, see section 1.1. We will then concentrate on existing literature in the context of microstreaming in section 1.2. I will in particular highlight the discrepancy between advances in analytical and experimental work, which motivates the exact nature of my work. The second half of the chapter is then dedicated to phenomena which we have to understand before devoting ourselves to streaming: creation of bubbles in section 1.3, spherical bubble dynamics in section 1.4 and nonspherical bubble dynamics in section 1.5.

1.1 Context of cavitation and microbubbles

The objective of my PhD work is to understand the physical principles of bubble dynamics and particularly its effects on the surrounding liquid. Even though I do not study more practical applications of bubbles myself, I hope that my findings will eventually be useful for such purposes. The main driving force to my work is its possible use in medical applications, particularly in sonoporation, a method that I will explain more closely at the end of section 1.1.2. I will make use of section 1.1.2 to give a slightly larger overview on where bubbles and cavitation are used or exploited in the medical context. The section is not meant to be exhaustive but rather to give insight glimpses into the large picture that motivates my work. It furthermore allows me to set the context for the supplementary project on bubble jetting conducted during my stay at Glasgow University with P. Prentice, as detailed in appendix A.

Before talking about the medical field, let me very briefly recall the historical context of cavitation including its definition in section 1.1.1. Furthermore, in the last part of the current section, see section 1.1.3, I will bring up a second field where microbubbles come into practice: the field of microfluidics and micromixing.

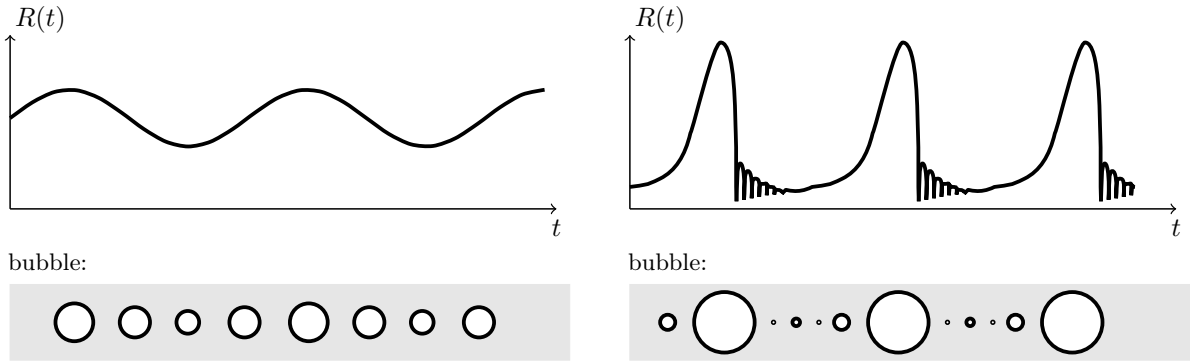

Figure 1.1: Schematic presentation of the bubble radius R with respect to time t during stable cavitation (*left*) and sustained inertial cavitation (*right*). During inertial cavitation the bubble implodes with possible creation of shock waves, the fast collapse is usually followed by a certain number of small afterbounces. Note that the bubble might also fragment instead of regaining spherical shape as sketched here.

1.1.1 Cavitation

In the context of engineering, cavitation is mainly known for its damaging effect. It occurs for instance around ship propellers or in hydraulic facilities. So, historically cavitation was essentially studied in the context of marine technology. Today, cavitation and more broadly bubbles are the focus of a much larger variety of research activity. They find application in the medical field, in microfluidics, ultrasonic cleaning and sonochemistry [65]. Besides of that, bubbles also play a role in foams, as well as in beverages and nature [3].

Apfel [3] defines cavitation as stimulated bubble activity. When pressure drops below the vapor pressure (and surface tension is overcome) vapor bubbles are formed. In the case of acoustic cavitation the low pressure is obtained by the minimum pressure of an acoustic wave. In this context, the literature currently distinguishes between two kinds of cavitation, stable and inertial cavitation as illustrated in figure 1.1. During stable cavitation, a bubble can be maintained in stable oscillation around a mean radius for a very long time. During inertial cavitation, the bubble collapses and might entail shock waves and hence damage to nearby structures.

Strictly speaking, the term *cavitation bubble* only applies to bubbles which are created due to a pressure drop. Cavitation then occurs preferentially at nuclei such as tiny gas bubbles, gas in crevices and certain solid particles. However, bubbles can be created in many different ways so that they do not always deserve the name *cavitation bubble*. I will explain the exact terminology used in this manuscript at the end of the current section, more precisely in section 1.1.4, once we have gained insight into the general context.

1.1.2 Application of cavitation and microbubbles in medical applications

Some medical therapies take advantage of the mechanical impact of inertial cavitation, others are based on the less destructive effects of stable cavitation bubbles. Cavitation might be a side

product of the ultrasound wave, but it is also possible to inject stabilized microbubbles into the human body. As a further distinction, microbubbles can be used for diagnostics but also for therapeutic purposes. A summary of different types of treatments can be found for example in a review by Coussios and Roy [20].

One important therapeutic field is cancer research and several of the techniques that I will mention in the following find their application in this field. But why are there so many of them? In fact, even though cancer tumors are all characterized by some specific attributes, a large variety of types of cancer exists [50, 51]. Consequently, the very different forms of cancer require different types of therapy. The main axes of therapy are surgery, chemotherapy, radiotherapy or ultrasound therapy and more recently immunotherapy. To enhance the likelihood of success, several types are oftentimes applied together, for instance surgery plus chemotherapy [24]. In this context, advantages of ultrasound treatment are that it is noninvasive and has no chemical side effects. Interesting for the present manuscript is that in many cases, cavitation and microbubbles have been found to enhance the effectiveness of ultrasound treatment.

Cavitation bubbles and shelled microbubbles

Let us first take a look at the different types of bubbles used in the medical context. Gas or vapor bubbles can be created directly inside the body by classical high intensity focused ultrasound (HIFU) or they can be injected. These unstabilized bubbles are convenient for use with inertial cavitation, however, it is difficult to maintain them stable for a long time.

Therefore, prefabricated bubbles with a shell have been developed. The shell stabilizes the bubble as it keeps the gas inside the bubble and reduces the surface tension [41]. A common shell material is based on lipids, other materials include proteins and polymers. An overview of further materials is given by Ferrara, Pollard and Borden [41], and a list of commercially available bubbles by Lindner [71]. When designing shelled microbubbles, additional features might be added. If bubbles are desired in a certain part of the body, they can be equipped with ligands designed to connect to the specific cell or tissue type. There are different classes of ligands, for instance antibodies, peptides and vitamins [41]. If enhanced drug delivery is desired, different techniques can be used. A payload such as drugs, genes or DNA can be placed inside bubbles to be transported to a desired target [71]. Alternatively, drugs can be placed in liposomes (small lipid vesicles) in the bubble shell. Yet another possibility is the co-injection of bubbles and medication.

Ultrasound imaging and guidance

Bubbles can be used to optimize ultrasound imaging or to make it possible. One clinical application is flow assessment and enhanced visibility, for instance in echocardiography which is made possible by the presence of bubbles in the blood. The technique takes advantage of the fact that the bubbles have a much higher scattering efficiency than the blood itself [71].

Bubbles as contrast agents can be used for simple ultrasound detection when the organ itself is not an acoustic reflector. In this case, targeted bubbles, which will migrate to the targeted organ, are used. Some examples can be found, for instance, in the reviews by Ferrara, Pollard and Borden [41], Qin, Caskey and Ferrara [103] and Lindner [71]. As a last example in this paragraph, there are bubbles used for time-reversal focusing. When clinicians want to focus ultrasound behind a skull, for example, the heterogeneities of the bone structure induce large uncertainty of the actual acoustic field. By introducing a cavitation bubble, its acoustic signal can be registered, time-reversed and then used for correct focusing. Pernot et al. [92] validate this method for acoustically induced cavitation bubbles, Couture et al. [21] for targeted microbubbles.

Ultrasound therapy: destruction of blood clots, stones and tissue

Some ultrasound therapies are based on the deliberate creation of cavitation and some are largely improved by the presence of bubbles. The italic words in the following paragraphs indicate the Greek origins upon which the names of the ultrasound applications are based.

Thrombolysis (*thrómbos* = lump / blood clot, *lúsis* = loosen / release) is the disintegration of a blood clot of a stroke patient. It has been shown that the effect of tissue plasminogen activators can be enhanced by the parallel application of ultrasound, a method then called sonothrombolysis (e.g., Alexandrov et al. [2]). Some authors find that sonothrombolysis can be accelerated even more by the use of microbubbles in the clot region (e.g., Molina et al. [81]).

Lithotripsy (*lithos* = stone, *trípsis* = rubbing / friction) is a treatment where shock waves are sent onto targets such as kidney stones or bladder stones in order to destroy them. Coleman et al. [18] were the first to show experimentally that cavitation bubbles may be produced close to the object. In fact the presence of bubbles largely enhances the effect of the shock wave due to jet formation and destruction of the surface. More recently, studies show that it moreover the growth and collapse of bubble clusters that cause the largest damage [93].

Histotripsy (*histos* = tissue, *trípsis* = rubbing / friction) is a high intensity focused ultrasound (HIFU) application. Unlike most HIFU applications, it is based not on thermal ablation but on the purely mechanical mechanisms of cavitation. Khokhlova et al. [59] give an overview of different applications of histotripsy, but to summarize briefly, two different types exist. Cavitation cloud histotripsy uses high intensity, short (microsecond) pulses which create cavitation clouds. Boiling histotripsy uses longer (millisecond) pulses that create a vapor cavity due to shock induced heating. Both types work due to the interaction between the bubbles and a shock front. This leads to disintegration of tissue. Histotripsy can also be operated as microtripsy with a single bubble, allowing a very localized treatment.

Ultrasound therapy: sonoporation

The need to deliver for instance drugs or genes into cells gave rise to studies on sonoporation in the late 1990s. Sonoporation is the creation of pores in the cell membrane. In the ideal case

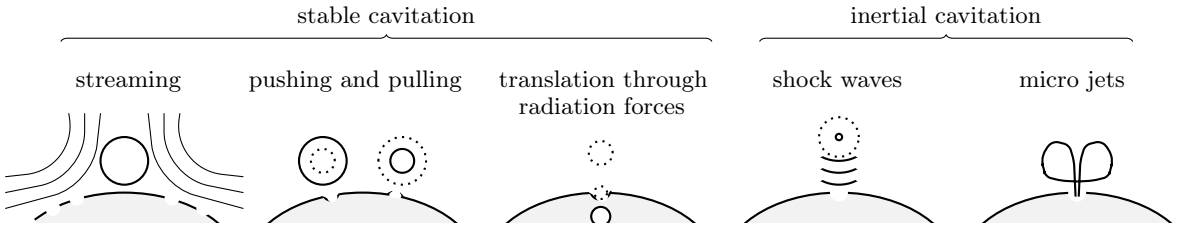

Figure 1.2: Schematic representation of different mechanical effects leading to sonoporation. The dotted bubbles are meant to represent the bubble position or size occupied by the bubble just a moment ago. [Inspired by similar figures in [26, 69].]

sonoporation is reparable, which means that the pores will close again. Studies have been conducted with very different experimental parameters leading to a variety of mechanical, chemical and biological effects. Furthermore, some effects are well validated while others still seem to be rather hypothetical. A recent review summarizing different mechanisms was written by Lentacker et al. [69]. For the present work, we are only interested in the mechanical effects, which can be classified in resulting from stable cavitation, inertial cavitation or ultrasound alone. The effects including bubbles are sketched in figure 1.2. For bubbles in stable cavitation, Van Wamel et al. [125] have observed bubbles pushing and pulling on the cell membrane which may eventually lead to rupture. Lentacker et al. [69] also suggest that bubbles might be transported into cells by radiation forces, the exact effects, however, do not seem to be very clear as the cited studies mainly discuss inertial cavitation [133] or time scales not directly related to the ultrasound bursts [26]. A widely discussed phenomenon, which is commonly agreed to have at least some influence on sonoporation, is microstreaming and associated shear stresses induced by an oscillating bubble. First successful experiments have been conducted by Wu, Ross and Chiu [129] with streaming around a Mason horn tip and by Marmottant and Hilgenfeldt [77] with microbubbles. In general, pores in the cell membrane caused by stable cavitation are typically tens to hundreds of nanometer in size and the pores close again within a few miliseconds to seconds [69]. During inertial cavitation, shock waves of imploding microbubbles might interact with the cell membrane. Most studies concentrate, however, on the presence of microjets which perforate the membrane [127, 99, 89] or the shear flows induced during asymmetrical bubble collapse [91]. In general, pores created by inertial cavitation are larger and they close more slowly than pores created by stable cavitation, the order of magnitude ranges around hundreds of nanometers to millimeter sized pores and a closing within seconds.

Similar effects as the ones for sonoporation on cells can lead to the permeabilization of blood vessels. A very specific case is the attempt to open the blood-brain barrier (BBB) starting around the year 2000 [82, 54]. The blood-brain barrier is a barrier which lets only very few particles pass from the blood into the brain and is naturally meant to keep harmful things out. However, it has to be passed if treatment inside the brain becomes necessary. Hence, the BBB opening has become an important field of study.

The fact that microstreaming is commonly agreed to play a role in sonoporation and BBB opening motivates my PhD work. Jetting of bubbles can be seen as another possible source of sonoporation. Even though the mechanisms are not the same, the broad picture for my excursion on jetting (appendix A) stays the same. Let me stress at this point, that not all effects from bubbles are positive. For instance, too violent disruption during sonoporation may lead to non-reparable effects and is hence to be avoided. The implementation in the medical field is left to others, but as not all mechanisms are clearly understood at present, I hope that our rather physics-oriented studies will help to advance the open questions in the more applied fields.

1.1.3 Microfluidics and micromixing

Let me briefly bring up another topic in which bubbles and their influence on the surrounding liquid can be exploited. Microfluidics is about liquid flows with millimeter to micrometer dimensions. At these scales, flows are usually laminar and the diffusive nature of turbulence cannot be exploited. However, it is possible to profit from the fluid motion induced around an acoustically excited bubble. Successful examples have been published by Liu et al. [73] and later Collis et al. [19] who experimentally mixed a liquid by using a grid of oscillating bubbles. Each acoustically excited bubble induces fluid motion around its surface. Another advantage of bubbles in these applications is that no movable mechanic device has to be used and bubble activation can simply be switched on and off by ultrasound exposure.

But bubbles cannot only induce a random flow for mixing, the induced flow can also be used to transport or sort small particles, cells or other. For example, Wang, Jalikop and Hilgenfeldt [126] demonstrate a small device containing an acoustically excited bubble that allows to sort small particles according to their size. Furthermore, grids of bubbles can be used to guide solid particles and vesicles without the need of microchannels [78], cells and cell-structures can be transported and rotated [1] and occurring shear stresses inside the flow can be sufficiently high to lead to sonoporation [77]. As a last example to mention here, attempts have been made to create self-propelled microswimmers [7] which are based upon the forces created through microstreaming.

1.1.4 Annotation on the terms bubble, microbubble and free bubble

Let me recall that, despite the large variety of bubbles, the main body of this manuscript only deals with air/gas bubbles in water with approximate radii of 20 µm to 100 µm. The terms *bubble* and *microbubble* will be used synonymously and will always refer to this kind of bubble. The only exception concerns appendix A which deals with contrast agent microbubbles.

Furthermore, I will use the expression *free bubble* in opposition to a bubble attached to a wall and hence not influenced by any supplementary boundary conditions. Note that in the context of contrast agent microbubbles for medical applications the expression *free bubble* is sometimes used differently by denoting a bubble without a stabilizing shell.

1.2 Overview on microstreaming

Microstreaming is a slow mean flow induced by a fast oscillating body. Unlike acoustic streaming caused by the attenuation of an acoustic wave in the fluid [104, 111, 35, 70, 131], microstreaming is driven by streaming inside the oscillatory boundary layer around the bubble, the so-called Stokes layer. Nonlinear second-order effects are responsible for extending the streaming patterns much further than the Stokes layer. In this way, outer streaming appears further from a bubble where at leading order, the flow is commonly considered irrotational [25].

As mentioned in section 1.1.1, the context of medical applications such as sonoporation drives our interest to understand microstreaming induced by bubbles which are oscillating due to ultrasound excitation. In most existing studies bubbles are very close to a surface or attached to it. Some authors even conclude that bubbles have to touch the cell membrane to induce successful sonoporation [69]. It is true that we might expect stronger streaming velocities close to a bubble, but their assumption is not based on experimental evidence. In the present work, we rather choose to study streaming around free bubbles, mainly due to the fact that analytical models are easier to obtain and hence that experiments can be validated. But let me explain the whole situation in detail. To be complete, we must include not only the streaming itself but also the study of the bubble dynamics. This means that in order to be able to characterize a streaming pattern or streaming velocities, it is more than helpful to know its origin. Hence, we have to understand and control the dynamics of a bubble which might oscillate radially or with shape modes. A schematic representation of the issues involved is given in figure 1.3. In the following, I will discuss these points in view of existing experimental and theoretical studies.

Bubble dynamics

As knowledge of bubble dynamics is necessary to correctly study microstreaming, this topic accounts for an important part of the present manuscript. Key points of spherical and nonspherical bubble dynamics are briefly resumed in sections 1.4 and 1.5. Furthermore, chapter 2 aims to provide controllable free bubble dynamics for our microstreaming experiments. For now, it is important to state that bubble dynamics of free bubbles is theoretically well covered and that also a fair amount of experimental studies exists. Consequently, free bubbles are manageable in terms of effort to control and to implement in new experiments. Experimental studies on bubbles attached to a wall started before those on free bubbles, notably because they are much easier to handle. However, comparably little interest has been shown to the exact surface dynamics. This might also be due to the fact that these bubbles are difficult to treat from a theoretical point of view. In fact, for attached bubbles, additional boundary conditions have to be taken into account and the contact line between the bubble and the wall is not necessarily easy to define [115].

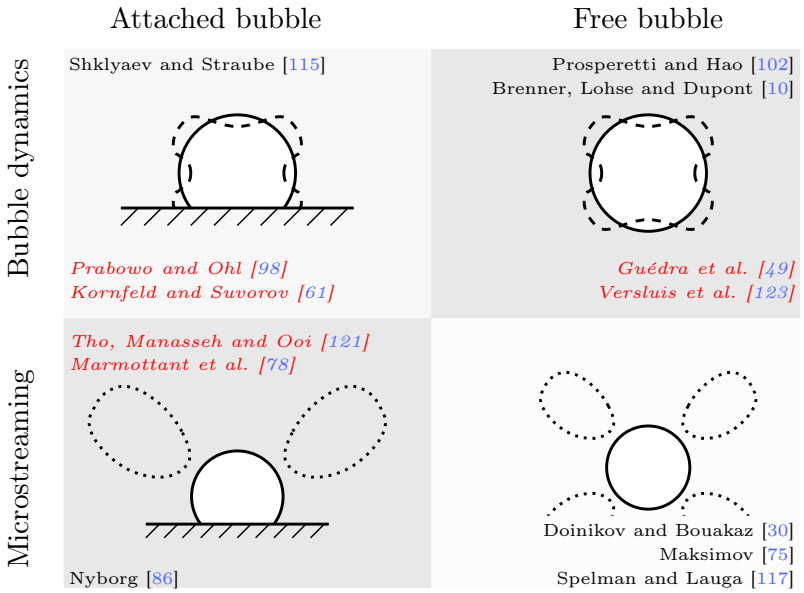

Figure 1.3: Schematic representation of the different aspects involved in the study of microstreaming. For understanding microstreaming, first the bubble dynamics has to be controlled. Furthermore, bubbles attached to a wall are usually easier to tame experimentally but more difficult to describe in theoretical models. In the figure, some chosen references for experimental (red italics in the center of the figure) and theoretical work (black plain text at the upper and lower border) are added.

Experimental studies on microstreaming

Microstreaming has first been observed in 1954 by Kolb and Nyborg [60] by placing a bubble on a vibrating tip. Slightly later Elder [36] reported on experimental microstreaming observed from the side view around a bubble placed on a boundary and excited by an acoustic wave. The author sketched four different types of streaming patterns and stated that the appearance depends in particular on the bubble surface velocity induced by the acoustic amplitude and on the fluid viscosity. The author did not expect to find more than one characteristic regime, but he could fit at least one of them to current analytical models. Another systematic study of streaming patterns of bubbles attached to a substrate has been effected much later by Tho, Manasseh and Ooi [121]. These authors also found a large number of streaming patterns, all presented in camera top view. More specifically, the authors studied cases of varying translational and/or oscillating motion. Furthermore, they also showed three examples of surface modes but their observations did not reveal any particular correlation between the streaming patterns and the mode number. As already stated by Tho, Manasseh and Ooi [121], no other fundamental studies on streaming patterns exist. Other studies on microstreaming around bubbles focus on one of its applications either in the field of micromixing or medicine.

Microstreaming around free bubbles has only been visualized by very few studies about twenty years ago. Gormley and Wu [46] observed microstreaming around acoustically trapped contrast

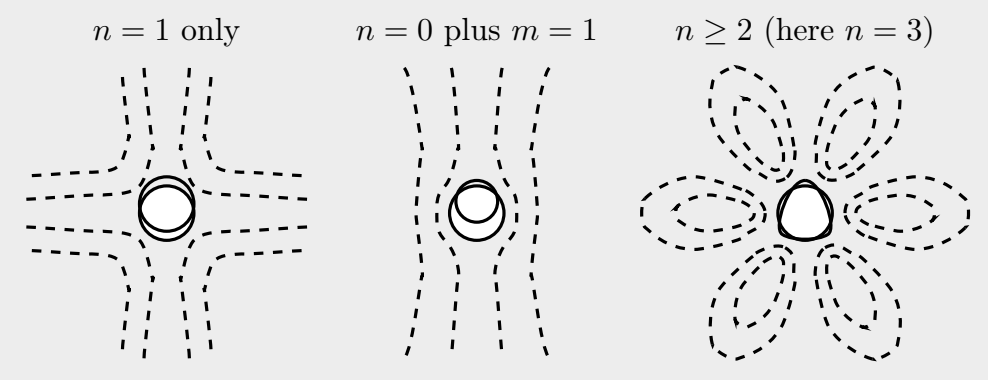

Figure 1.4: Schematic presentation of different streaming patterns obtained with different theoretical models: *left* – purely translating bubble [74, 117, 128]; *center* – bubble both translating and oscillating radially [74, 128]; *right* – bubble oscillating with surface modes, here a mode 3, [75, 30, 117].

agent microbubbles. They observed streaming for what they say to be radial oscillation only and radial plus translational motion. Verraes et al. [122] put into evidence streaming around single sonoluminescent bubbles by observing a point of dye being dispatched. The authors conclude that their bubbles are oscillating spherically and translationally and find good comparison with a theoretical model established by one of the authors [74].

Theoretical studies on microstreaming

Early theoretical work on microstreaming took place in the general framework of fluid-solid interfaces. In this context, Nyborg [86] discussed two cases which are related to bubbles. Firstly, he studied the case of a point source such as a gas bubble close to a solid boundary. This model has been confirmed by one of the experiments conducted by Elder [36]. Secondly, he considered the case of streaming around a solid sphere by placing nodes and antinodes on its surface. Other authors such as Riley [107] and Lee and Wang [66] refined models for solid spheres, but further aspects need to be taken into account for the specific case of gas bubbles. Davidson and Riley [25] were the first to consider bubbles with a fluid-gas interface. Their approach is based on fluid dynamics equations and the matching between an inner solution inside the boundary layer and the outer solution outside the boundary layer. They stated that, for small viscosity, streaming around a bubble has the opposite sign as around a solid sphere. Their model treats a purely translational bubble and the resulting streaming pattern has a cross-like structure, see figure 1.4 on the left. Longuet-Higgins [74] later refined this mathematical formulation by incorporating the radial oscillations of the bubble. He confirmed the results of Davidson and Riley [25] and further derived a solution for combined radial-translational oscillations which corresponds to a flow in one direction along the bubble, see figure 1.4 in the center. More recently, surface modes have been considered by Maksimov [75] and by Spelman and Lauga [117] using similar approaches. For a surface mode n, streaming patterns showing rotational symmetry with a number of $2n$

lobes are obtained, see figure 1.4 on the right. Another approach to describe streaming is based on acoustic formulations and has been developed first by Wu and Du [128] for pure translation (streaming pattern with a cross-like structure) and pure radial oscillation (pattern corresponding to a flow around the bubble in one direction). Later Doinikov and Bouakaz [30] extended this approach by taking into account viscosity not only in the boundary layer but in the whole liquid. Furthermore, they included surface modes in their model which result in equations predicting that $2n$ lobes around a surface mode n should appear. Bertin et al. [7] compare experimentally obtained patterns around a microswimmer (hollow solid sphere containing a bubble and an opening on one side) with a model derived from the previously cited models. However, they do not give any details on how to obtain these results.

To the best of my knowledge, purely theoretical works for a bubble placed on a solid, stationary boundary do not exist. Doinikov and Bouakaz [32] study the effect of a distant rigid surface on the streaming around a translating and radially oscillating bubble by means of introducing a virtual image bubble on the other side of the wall. The image method has also been applied by Marmottant and Hilgenfeldt [77] and Marmottant et al. [78] when searching for a theoretical comparison to their experimental results. Their results are based upon the model by Longuet-Higgins [74] and likewise take into account radial and translational oscillations.

Conclusions

Let us take one more look at figure 1.3 taking into account the above review on theoretical and experimental studies. Bubbles attached to a wall have been studied very little, both experimentally and theoretically. This is probably mostly due to the difficulty in taking into account the boundary conditions in theoretical models. The same applies for theoretical models of streaming around such bubbles. However, the modeling with the image method by Marmottant and Hilgenfeldt [77] based on Longuet-Higgins [74] seems to be adequate for radial plus translational oscillations. More complex characteristics such as shape modes are, however, not covered in this model.

On the other hand, oscillatory dynamics of free bubbles have been very thoroughly studied theoretically and experimental observations are rather complete. For the streaming induced by such bubbles a couple of theoretical models exist, a thorough validation of those is however lacking as no such experimental studies exist.

For this reason, the aim of this work is a fundamental study on experimental streaming patterns around a free bubble. As we will see, streaming only occurs around bubbles oscillating with shape modes, as we cannot trigger pure translational motion. The work is complemented by a new theoretical model that takes into account all relevant experimental aspects in order to provide a real means of comparison. But let us first cover the whole topic step by step. First we need to obtain bubbles, see section 1.3, and then understand the spherical bubble dynamics, to be found in section 1.4, nonspherical oscillations, detailed in section 1.5 and a means to control those, see chapter 2.

1.3 Creation of microbubbles

To study microbubbles we first need to obtain them. For this reason, the present section is meant to give an overview on different techniques currently applied in bubble research and some of their advantages and disadvantages. I will furthermore comment on which methods I used in the different experiments and why. As defined by Lauterborn and Kurz [65], a bubble is *a volume of gas and vapour (and at times plasma) surrounded by a liquid.* Depending on its creation and surrounding it may have different properties.

Syringe

A syringe with a very fine needle can be used to inject gas bubbles into water. A bubble will form at the needle tip and detach once the force of buoyancy is larger than the force that attaches the bubble to the needle. We use this method in a small supplementary study on streaming around several bubbles, see section 3.6.3. We dispose of a syringe-pump-system which allows for a large set of parameters to control bubble size and repetition rate. However, we are not able to create very small bubbles due to constraints from the needle (or in our case more precisely the capillary) diameter, and with our particular system it is much easier to create bubble filaments instead of single bubbles. Furthermore the capillary including its support has to be inserted inside the water tank, possibly influencing the acoustic field.

Electrolysis

It is possible to do an electrolysis of water by placing two electrodes inside the liquid and applying a DC current. As the current requires free electrons to move through the water, chemical reactions take place at either electrode. At the anode, an oxidation

$$2H_2O(l) \longrightarrow O_2(g) + 4H^+(aq) + 4e^-$$

and at the cathode, a reduction

$$4H^+(aq) + 4e^- \longrightarrow 2H_2(g)$$

takes place. The electrons e^- drive this process which on one side transforms liquid (l) water molecules H_2O into gaseous (g) oxygen O_2 and on the other side creates gaseous (g) hydrogen molecules H_2. The ions H^+ are part of the water (aq), they are necessary for the conductivity of the liquid but do not interact in the final equation which is

$$2H_2O(l) \longrightarrow 2H_2(g) + O_2(g).$$

While a voltage of 1.23 V is theoretically sufficient to split water into hydrogen and oxygen, a somewhat higher voltage might be necessary in practice depending on the metal conductor used for the electrodes.

In one part of my work, I used electrolysis to create bubbles attached to a wall, see section 2.6. I exploited the fact that gas is formed at the electrodes and forms a bubble which can then be attached to another support. Its advantage is that it requires only a DC current generator and some fine wire to work and that it is fairly easy to place bubbles on a solid surface. Of course, this method requires access to the bubble location. We found it not adequate for creating free bubbles as they tend to stick to the electrodes (even very fine wires) until they reached a too large size.

Laser pulses

Short laser pulses of a well focused laser can be used to generate bubbles. As was stated by Ohl et al. [90], the laser pulse causes heating of impurities and/or dielectric breakdown with avalanche ionization at the focal spot which leads to the creation of plasma. The plasma then expands to form a cavity. As explained by Obreschkow et al. [87], the transformation from liquid into plasma leads to very high pressures. Consequently the hot plasma expands explosively reaching bubble radii around a 100-times larger than the initial plasma. The plasma quickly cools down due to the great expansion and due to heat transfer so that it deionizes and recondensates. The bubble hence becomes nearly identical to a bubble created due to "real" cavitation. Small differences due to non-condensible gases created through the laser pulse have been measured by Sato et al. [110]. For further reading, some more references can be found in the paper by Obreschkow et al. [87], a detailed energy balance of the optical breakdown has been conducted by Vogel et al. [124] and the competing or complementing mechanism of thermal breakdown by Byun and Kwak [11].

I use this method for the most part of my work. Once the laser is well adjusted, it allows to always create the bubble at the same spot without needing access to the water tank. Other authors [90] report that the bubble size is easily reproducible. We cannot confirm this statement for our current experiments. However, this might simply be due to the fact that the bubble is generated some millimeters away from the final position, where the bubble is trapped and where we do our recordings. During the relatively long path, the bubble has plenty of time to change size due to diffusion or rectified diffusion. Compared to the acoustic time scale, a long time has passed before we can actually see the bubble.

Spark generation

Spark generation between two thin wires also works with a dielectric breakdown and hence creation of plasma. Its advantage is that bubbles can be created at very well located places and that the bubble size can be regulated with the electric discharge. Furthermore, it is fairly easy to place two systems of wires close to another and control distance, size and phasing of two bubbles. This method has been notably used in experiments where the interaction of collapsing bubbles has been studied, e.g. by Fong et al. [42]. The disadvantages that make the method not convenient four our work are that the access to the tank is necessary and that the bubbles would

probably stick to the wires if we tried to keep them alive for a longer time inside an acoustic field.

Acoustics

Acoustically induced bubbles are the only type of bubbles that correctly deserve the name cavitation bubbles. When applying a sufficiently strong acoustic pressure, the peak negative pressure leads to a pressure lower than vapor pressure. Consequently, a gas bubble will form. An advantage is that they can be created with a transducer and do not require access to the area of interest. The two main disadvantages for our purpose are that a sufficiently strong acoustic field is necessary and that multiple cavitation bubbles are likely to be created due to several pressure antinodes. Furthermore, the bubble size is difficult to control. Even though we use acoustics to excite, expand and trap bubbles, we do not create them by acoustics in the experiments reported here.

Prefabricated bubbles

Prefabricated bubbles have already been discussed in section 1.1.2. Their primary use is in the medical context. A large advantage is that they can be stored a long time and just used upon demand. Furthermore, it is possible to let them travel a long way, for example in the body, before they are activated at a location of interest. Activation oftentimes means exposure to ultrasound and hence stable or inertial cavitation. Those prefabricated bubbles are different insofar that they have a rigid shell which alters their response to ultrasound exposure. During my stay at the University of Glasgow we used such prefabricated bubbles and exposed them to strong ultrasound waves in order to study their jetting behavior, see appendix A.

1.4 Spherical bubble dynamics and positional stability

In order to understand microstreaming induced by acoustically excited bubble dynamics, we first have to understand the bubble dynamics itself. A bubble subject to an ultrasound field will experience different effects. The most important aspects are introduced in the following. The present section 1.4 is dedicated to spherical bubble oscillations induced by an acoustic field. In this context we will also discuss the so-called Bjerknes forces which act upon a bubble and influence its position in a standing acoustic field. Furthermore, basic notions of stability will be introduced. One type of instability is spherical instability expressed by surface modes which might be excited by sufficiently strong pressure amplitudes. As this is a key aspect upon which the remainder of this manuscript is built, section 1.5 is entirely dedicated to nonspherical bubble dynamics.

Note that for the main body of this manuscript we are only interested in stably oscillating cavitation bubbles. Consequently, I do not consider the case of an imploding bubble in the present chapter.

1.4.1 Spherical bubble dynamics

An acoustic field acts as a periodic driving force upon a bubble. Intuitively the volume of a compressible bubble will decrease when the acoustic pressure increases and *vice versa*. Reality is more complex as parameters such as viscosity, surface tension and sound radiation might have a considerable influence depending on the exact set of physical quantities. Consequently, a certain number of models has been developed for use in different contexts. One well-known model is the Rayleigh-Plesset model. It was developed by Plesset [94] who extended an approach formerly developed by Rayleigh [105] in order to take into account periodic acoustic driving.

Rayleigh-Plesset model

For the derivation, Plesset [94] assumes spherical symmetry and liquid incompressibility and thus a velocity potential $\Phi = R^2\dot{R}/r$, where r is the radial coordinate, R is the time-dependent bubble radius and the overdot means differentiation with respect to time t. A very detailed derivation of this velocity potential can for instance be found in a report by Leighton [67]. Applying the Bernoulli integral of motion and assuming spherical symmetry gives

$$-\frac{\partial\Phi}{\partial t}+\frac{1}{2}\left(\nabla\Phi\right)^2+\frac{p(r)}{\rho_0}=\frac{P(t)}{\rho_0}\ , \tag{1.1}$$

where ρ_0 is the liquid density, $p(r)$ the static pressure at the position r from the center of the bubble and $P(t)$ the static pressure far from the bubble. Applying equation (1.1) at the bubble surface $r = R$ gives

$$\rho_0 R\ddot{R}+\frac{3}{2}\rho_0\dot{R}^2=p(R)-P(t)\ . \tag{1.2}$$

The special case $p(R) - P(t) = \text{const}$ corresponds to Rayleigh's original model. In more recent work the pressure on the right hand side of equation (1.2) is usually detailed further [68] so that the final equation reads

$$\underbrace{\rho_0 R\ddot{R}+\frac{3}{2}\rho_0\dot{R}^2}_{\text{inertial terms}}=\underbrace{\left(p_0-p_v+\frac{2\sigma}{R_0}\right)\left(\frac{R_0}{R}\right)^{3\gamma}+p_v}_{\text{total internal pressure}}-\underbrace{\frac{2\sigma}{R}-4\nu\rho_0\frac{\dot{R}}{R}-p_0-p(t)}_{\text{total external pressure}}\ . \tag{1.3}$$

This equation was suggested to be called RPNNP-model [64], according to its contributors Rayleigh [105], Plesset [94], Noltingk and Neppiras [84, 83], and Poritsky [96]. In equation (1.3), p_v is the vapor pressure (the pressure at which water vaporizes), σ the surface tension between water and the gas phase, ν is the kinematic viscosity of the water ($\nu = \eta/\rho_0$ with the dynamic viscosity η), γ is the polytropic index of the gas phase and $p(t)$ is the acoustic pressure. For a better readability in the above and in following equations, I omit all time-dependencies but the ones that are useful for highlighting specific aspects, here for instance to underline the driving pressure $p(t)$. Note that in particular $\Phi(r, t)$ and $R(t)$ are functions of time. Throughout the

whole manuscript, I consider harmonic driving pressure only, so that for instance

$$p(t) = p_a \sin(\omega t) \ , \tag{1.4}$$

where p_a is the pressure amplitude and ω the angular driving frequency.

Other models than the Rayleigh-Plesset model exist. A very extensive list of models is given by Qin, Caskey and Ferrara [103], a good introduction can be found in Lauterborn and Kurz [65]. These authors recall the Rayleigh-Plesset, Gilmore and Keller-Miksis models and state that those three basic models are usually sufficiently precise for most experiments with spherical bubbles. The Gilmore and Keller-Miksis model are similar to the Rayleigh-Plesset model, with some additional parameters in the differential equation to consider, for instance, sound radiation by the bubble. A short implementation has shown that the Keller-Miksis model [58] gives quasi-identical results with the Rayleigh-Plesset model for the bubble sizes and acoustic pressures used in my work.

Linearization of the Rayleigh-Plesset model

Equation (1.3) is a non-linear differential equation which can only be solved numerically. Its linearization for small radial oscillations however leads to a new differential equation which has an analytical solution. The derivation can be made in a few relatively simple steps. First, the decomposition into a mean and fluctuating part $R(t) = R_0 + R'(t)$ has to be applied to equation (1.3). Using a Taylor series $1/(1+x)^b \approx 1 - bx$ and then only considering terms up to first order in the newly obtained differential equation, we find

$$\ddot{R}' + \underbrace{\frac{4\nu}{R_0^2}}_{\alpha} \dot{R}' + \underbrace{\left(\frac{1}{\rho_0} \left(p_0 - \frac{2\sigma}{\rho_0 R_0} \right) 3\gamma - \frac{2\sigma}{\rho_0 R_0} \right) \frac{1}{R_0^2}}_{\omega_0^2} R' = -\frac{p(t)}{\rho_0 R_0} \ . \tag{1.5}$$

Equation (1.5) is the differential equation of a simple harmonic oscillator with the eigenfrequency ω_0 to which an analytical solution is known. For the present purpose the factor α, which contains the damping of the system, is very small compared to ω_0^2 and can then be neglected. Moreover, as we are not interested in the transient solution, we only need the steady-state solution

$$R'(t) = -\frac{p(t)}{\rho_0 R_0 \left(\omega_0^2 - \omega^2\right)} \ . \tag{1.6}$$

We shall keep in mind that equation (1.6) is only valid for harmonic driving such as given in equation (1.4). From the $(\omega_0^2 - \omega^2)$ term in equation (1.6) we see, that the bubble radius is oscillating in phase opposition to the driving pressure for bubbles smaller than resonant size ($\omega_0 \gg \omega$) and in phase for bubbles larger than resonant size ($\omega_0 \ll \omega$). If we wanted to consider bubbles close to resonant size, a supplementary phase shift would have remain in the above linearization.

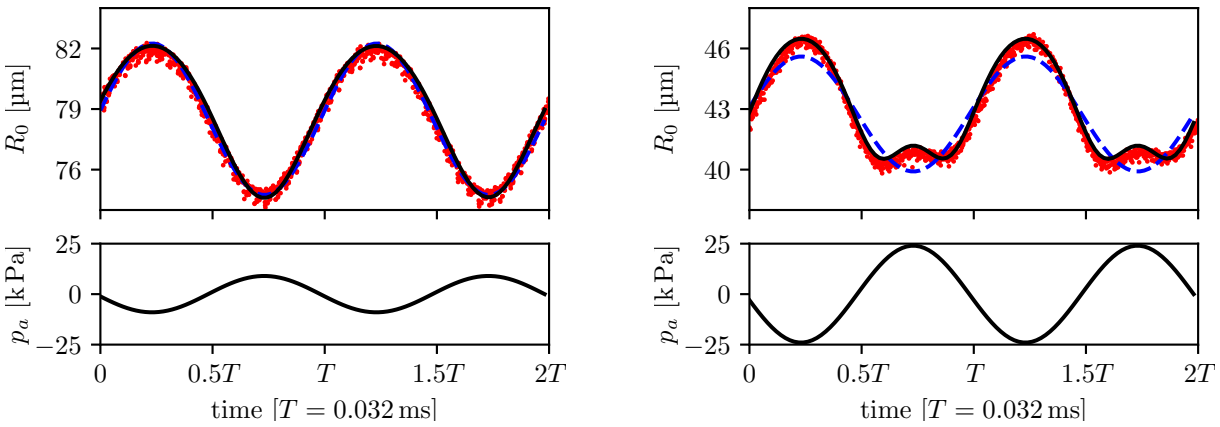

Figure 1.5: Two examples of radial oscillations with the acoustic driving frequency $f_{\mathrm{ac}} = 31.25\,\mathrm{kHz}$; *left:* bubble with $R_0 = 78.5\,\mu\mathrm{m}$ and $p_a = 9\,\mathrm{kPa}$; *right:* bubble with $R_0 = 42.8\,\mu\mathrm{m}$ and $p_a = 24\,\mathrm{kPa}$ where nonlinearities become obvious. *Top:* bubble radius with respect to time, where T is the acoustic period; black continuous line – solution of the Rayleigh-Plesset differential equation; blue dashed line – linearized solution of the Rayleigh-Plesset equation; red dots – 1000 experimental points reported/backfolded on the shown interval. Note that the scale on the left and right plot are different to show the full dynamics. *Bottom:* Pressure signal used for the numerical simulation.

We can find one further useful relation when taking a look at the eigenfrequency $\omega_0 = 2\pi f_0$ in equation (1.6). When neglecting surface tension, we find

$$\omega_0^2 = \frac{3\gamma p_0}{\rho_0 R_0^2} \quad \Rightarrow \quad f_0 R_0 \approx 3.26\,\mathrm{m\,s^{-1}}\ , \tag{1.7}$$

with $\gamma = 1.4$ for adiabatic air, $p_0 = 10^5\,\mathrm{Pa}$ and $\rho_0 = 1000\,\mathrm{kg\,m^{-3}}$. The relation in equation (1.7) has been first shown by Minnaert [80] and f_0 in this relation is accordingly called Minneart frequency.

Two examples

We now have two formulations to describe spherical bubble oscillations, the Rayleigh-Plesset differential equation (1.2) and its linearized solution in equation (1.6). Let us compare them for two examples in figure 1.5. Note that both the acoustic pressure and the bubble radius are different for the two simulations. Besides the solution of the differential equation (black continuous line) and the linearized solution (blue dashed line), experimental results (red dots) are shown. For the example shown on the left, both numerical solutions fit well with the experimental results, whereas for the example shown on the right, the nonlinearities can only be simulated by equation (1.2).

Let us note one useful fact in this context. Fitting a numerical solution to the experimental data allows us to find information previously unknown, namely the driving pressure p_a and the radius at rest R_0. In practice, the radius at rest is always very close to the mean radius, even for

cases such as presented on the right of figure 1.5. Here a difference of less then 1% is obtained between the mean radius and a best fit for the radius at rest, so that the two can be used quasi synonymously.

1.4.2 Bubble position and Bjerknes forces

Now that we know how a bubble will oscillate due to acoustic excitation, we can take a look at the forces that trap a bubble inside an acoustic field, the so-called primary Bjerknes forces. If two bubbles oscillate close to each other, the attracting or repelling forces are called secondary Bjerknes forces. The names give credit to the work of Vilhelm Bjerknes and his son (see for example [8]), who studied the forces on and between oscillating bodies in a synchronously oscillating current. Later, Blake [9] expands and applies Bjerknes' theory for the specific case of bubbles in an acoustic field to explain observations of bubbles trapped at both pressure nodes and antinodes. Around the same time, Bjerknes forces between two bubbles have been mentioned by Kornfeld and Suvorov [61].

Crum [22] retakes Bjerknes' original text (according to [106] an approach only valid for weak oscillations) and translates this into mathematical expression. He resumes that, similar to Archimedes law which leads to a buoyancy force proportional to the mass of the water volume to be displaced, Bjerknes' model is based upon kinematic buoyancy. The fluid particles oscillate due to acoustic driving at a particle velocity $u(t) = \hat{u}\sin(\omega t)$, where $\hat{u}$ is the amplitude of the particle velocity oscillation. The resulting force equals the displaced mass (proportional to the bubble volume V) times the acceleration of the fluid particles,

$$F(t) = \dot{u}(t)\rho_0 V(t) \ . \tag{1.8}$$

(Here, $\dot{u}$ and in the following ∇p_a are assumed to be the values which could be measured at the bubble center without the presence of the bubble.) As mentioned before, viscosity can be neglected and consequently we can use the linearized Euler equation

$$\rho_0 \dot{u}(t) = -\nabla p_a(t) \tag{1.9}$$

to replace the particle velocity by the acoustic pressure gradient and obtain upon time-averaging

$$F_B = -\langle V(t)\nabla p_a(\boldsymbol{r}, t)\rangle \ , \tag{1.10}$$

where $\boldsymbol{r}$ is the bubble position and $\langle\cdot\rangle$ denotes the time average, or more precisely, in the present periodic case, the time average over one acoustic period. Equation (1.10) can be interpreted in a very visual way: the pressure gradient means different pressures on either side of bubble which obviously leads to a force in the opposite direction of the gradient. Of course, the pressure gradient and fluid particle acceleration have to be close enough to constant throughout the whole bubble volume for the above simplifications to be valid. Equation (1.10) is the definition usually

given when discussing Bjerknes forces. From this equation we can derive both primary and secondary Bjerknes forces, the only difference lies in the origin of the pressure gradient.

Primary Bjerknes forces

Primary Bjerknes forces describe the forces that are induced on a bubble by an acoustic field. Following Eller [37], we can assume a plane standing wave with cylindrical symmetry (r, θ, z). The only non-zero component of the pressure gradient is the one in the z-direction so that

$$p_a(z,t) = \hat{p}_a \sin\left(\frac{2\pi z}{\lambda_z}\right)\sin(\omega t) \quad \Rightarrow \quad \nabla p_a(z,t) = \frac{2\pi}{\lambda_z}\hat{p}_a \cos\left(\frac{2\pi z}{\lambda_z}\right)\sin(\omega t)\ , \tag{1.11}$$

where $\hat{p}_a$ is the pressure amplitude at a pressure maximum and $\lambda_z = 2\pi/k = 2\pi c/\omega$ is the wavelength in z-direction, with $k = \omega/c$ the wave number, c the speed of sound propagation, and $\omega = 2\pi f$ the driving angular frequency. We can apply the pressure from equation (1.11) to the linearized radial amplitude in equation (1.6) and obtain an expression for the bubble radius

$$R(z,t) = R_0 - \frac{p(z,t)}{\rho_0 R_0\left(\omega_0^2 - \omega^2\right)} = R_0\left(1 - \frac{a_0(z)}{R_0}\sin(\omega t)\right)$$
$$\text{with} \quad a_0(z) = \frac{\hat{p}_a \sin\left(\frac{2\pi z}{\lambda_z}\right)}{\rho_0 R_0\left(\omega_0^2 - \omega^2\right)}\ . \tag{1.12}$$

In the case of small oscillations $a_0 \ll R_0$, we can simplify the expression of the bubble volume to

$$V(z,t) \approx \frac{4\pi}{3}R_0^3\left(1 - 3\frac{a_0(z)}{R_0}\sin(\omega t)\right). \tag{1.13}$$

Applying both equation (1.13) and (1.11) to the expression of the resulting force in equation (1.10), we obtain

$$F_{B_1}(z) = \frac{2\pi^2 \hat{p}_a^2 R_0^3}{3\gamma\lambda_z p_0\left(1 - \frac{\omega^2}{\omega_0^2}\right)}\sin\left(\frac{4\pi z}{\lambda_z}\right)\ . \tag{1.14}$$

Equation (1.14) is hence an expression for the primary Bjerknes force in a standing wave field. It differs from Eller [37] only by a factor γ as it seems more reasonable for fast acoustic oscillations to consider an adiabatic resonance frequency such as the Minneart frequency from equation (1.7) than an isothermal one. A close look at equation (1.14) reveals that the net force is zero at the pressure nodes and antinodes, which correspond to multiples of $z = \lambda_z/4$. For bubbles smaller than resonant size or in other words for bubbles driven below their resonance frequency $\omega < \omega_0$, the force is always directed towards a pressure antinode, whereas for bubbles driven above the resonance frequency $\omega > \omega_0$ the force is always directed towards a pressure node. A schematic representation for the case $\omega < \omega_0$ is shown in figure 1.6, a complete mathematical and graphical demonstration can be found in Leighton, Walton and Pickworth [68].

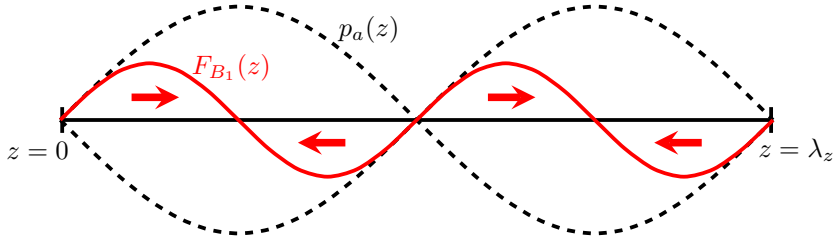

Figure 1.6: Schematic representation of primary Bjerknes forces in an acoustic standing wave λ_z for a bubble smaller than resonant size: the Bjerknes forces are always directed towards the pressure antinodes.

Bubble position when taking into account buoyancy

As only bubbles smaller than resonant size are relevant for this work, the following derivation of the bubble position is reduced to the case $\omega < \omega_0$ for simplification. A stable position in the acoustic field means that the two major forces, the primary Bjerknes force and the force of buoyancy $F_{\text{buoyancy}} = 4\pi R_0^3 \rho_0 g/3$ are in equilibrium. Consequently, the bubble will always end up closely above a pressure antinode with the Bjerknes force pointing downwards and the force of buoyancy pointing upwards. Setting the two forces equal and solving for the position Δz (where $\Delta z = z - z_{\text{antinode}}$ is the distance with respect to the antinode) gives

$$\Delta z = \frac{\lambda_z}{4\pi} \arcsin\left(\frac{2\rho_0 g \gamma \lambda_z p_0 \left(1 - \frac{\omega^2}{\omega_0^2}\right)}{\pi \hat{p}_a^2}\right) \quad . \tag{1.15}$$

To get an idea of the order of magnitude of the Bjerknes forces, let us take the spherically oscillating bubble from figure 1.5 on the left. With $R_0 = 78.5\,\mu\text{m}$, $p_a = 9\,\text{kPa}$, $\omega = 2\pi f_{\text{ac}}$, $f_{\text{ac}} = 31.25\,\text{kHz}$, $\rho = 1000\,\text{kg}\,\text{m}^{-3}$, $g = 9.81\,\text{m}\,\text{s}^{-2}$, $\gamma = 1.4$, and $p_0 = 10^5\,\text{Pa}$ we obtain $f_0 = 41.6\,\text{kHz}$ and $\lambda_z = 47.9\,\text{mm}$. Consequently, the stable position of the bubble will be at $\Delta z = 0.86\,\text{mm}$ above a pressure antinode. At this coordinate, both forces have the magnitude $2 \times 10^{-8}\,\text{N}$. The maximum Bjerknes force would occur at $\lambda_z/8$, at $3\lambda_z/8$ and so on (see figure 1.6) and is about five times larger than the one at the above calculated stable position. In our example, the distance from the antinode is approximately five times the bubble size. Note, that in practice we are only able to derive from the $R(t)$ observations the pressure at the bubble position and not the maximum pressure at an antinode.

Secondary Bjerknes forces

Secondary Bjerknes forces describe the forces between two oscillating bubbles. More precisely, they consider the effect of the acoustic radiation of the first bubble on the second one and *vice versa*. Let us look for the Bjerknes force on the second bubble, requiring hence knowledge of the sound field of the first bubble at the position of the second bubble. The pressure radiated by a

spherical bubble in an incompressible liquid is [100]

$$p_{\mathrm{a1}} = \frac{\rho}{d}\left(R_1^2\ddot{R}_1 + 2\dot{R}_1^2 R_1\right) - \frac{1}{2}\rho\dot{R}^2\left(\frac{R}{d}\right)^4 \quad , \tag{1.16}$$

where d is the distance from the bubble center. In our case d will of course be the distance between the two bubbles. For small amplitudes, the second term in equation (1.16) can be neglected [100, 4] so that

$$p_{\mathrm{a1}} = \frac{\rho}{d}\left(R_1^2\ddot{R}_1 + 2\dot{R}_1^2 R_1\right) = \frac{\rho_0\ddot{V}_1}{4\pi d} \quad . \tag{1.17}$$

The pressure gradient is hence

$$-\nabla p_{a1} = \frac{\rho_0\ddot{V}_1}{4\pi d^2}. \tag{1.18}$$

Applying this to equation (1.10) gives

$$F_{B2} = -\left\langle V_2\frac{\rho_0\ddot{V}_1}{4\pi d^2}\right\rangle = -\frac{2\pi\rho_0\omega^2 R_{01}^2 R_{02}^2 a_{01}a_{02}}{d^2}\cos(\Delta\varphi) \quad , \tag{1.19}$$

where the phase difference between the oscillation of the two bubbles $\Delta\varphi$ has been introduced. Note that in this context a_{01} and a_{02} are real numbers. Alternatively, the amplitudes including their phasing can be expressed by complex numbers. In practice, two special cases for $\Delta\varphi$ are important. Two bubbles oscillating in phase opposition, i.e. $\Delta\varphi \approx \pi$, lead to $F_{B2} > 0$ and hence to repulsion. This can be the case if one bubble is larger and one smaller than the resonant size. For our work we are only interested in bubbles smaller than the resonant size and hence oscillating in phase, i.e. $\Delta\varphi \approx 0$, leading to $F_{B2} < 0$ and hence to attraction.

Note that another common expression for secondary Bjerknes forces can be obtained from equation (1.19) by integration by parts [100]

$$F_{B2} = -\left\langle V_2\frac{\rho_0\ddot{V}_1}{4\pi d^2}\right\rangle = \frac{\rho_0}{4\pi d^2}\langle\dot{V}_2\dot{V}_1\rangle \quad . \tag{1.20}$$

If we retake our example from above, a bubble of 78.5 µm at an acoustic pressure of 9 kPa, we obtain a theoretical oscillation amplitude of 3.9 µm from equation (1.6). This corresponds well to the experimental observation in figure 1.5. For a first order of magnitude we can assume that two such bubbles exist and calculate the distance at which the secondary Bjerknes forces have the same order of magnitude as the primary Bjerknes forces. The resultant distance is of the order of $30R_0$, obviously a very large value. In reality, the second bubble is further away from a pressure maximum and thus exposed to a much weaker sound field. Consequently, the influence of the secondary Bjerknes forces becomes less strong.

Experimentally, secondary Bjerknes forces have been first studied by Crum [22] by a system which equals out primary Bjerknes forces. A more recent work by Lanoy et al. [63] shows that secondary Bjerknes forces, when they dominate over primary Bjerknes forces, could be used for microfluidic applications. In fact, in a system with two or more bubbles in an acoustic field,

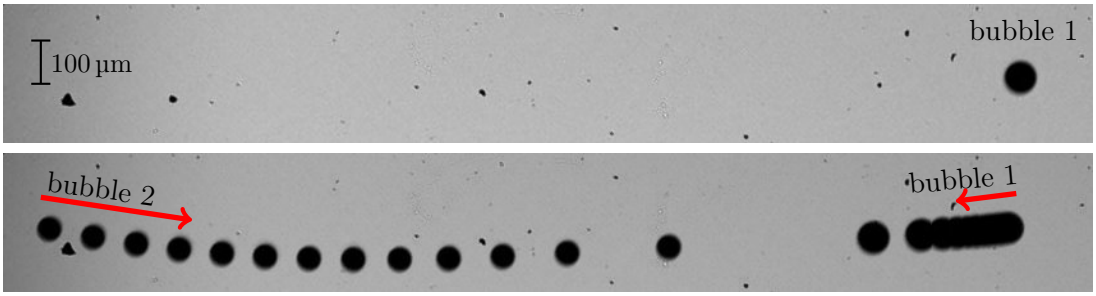

Figure 1.7: Example of two bubbles moving towards one another due to primary and secondary Bjerknes forces. The first bubble is initially trapped close to a pressure antinode of the acoustic field (*above*). Once the second bubble comes close enough to the first one, the two will also be attracted towards each other due to secondary Bjerknes forces leading to the superposed snapshot series (*below*).

there will always be the two kinds of forces. One snapshot of free two bubbles being attracted towards one another is shown in figure 1.7. The first bubble is trapped by primary Bjerknes forces, its position is slightly altered due to secondary Bjerknes forces. The second bubble is attracted towards the first bubble by secondary Bjerknes forces and at the same time towards the pressure antinode by primary Bjerknes forces.

1.4.3 Some aspects of stability

Spherical bubble oscillations are excited as soon as the bubble is placed in an acoustic field. When choosing the correct set of parameters, in particular for the bubble size, driving frequency, acoustic pressure, bubble position and saturation of the liquid, the bubble will keep stable for a very long time. If this is not the case, instabilities might appear. According to Lauterborn and Kurz [65], there are three main aspects of stability: positional, spherical and diffusional. For the here discussed air or gas bubbles in water we can safely neglect any chemical aspects.

Diffusional stability

The bubble radius at rest R_0 is influenced by the number of gas molecules in the bubble volume. Their number might change due to diffusion, that means due to gas molecules dissolving from the bubble into the surrounding liquid (because of overpressure caused by surface tension). However, there is also the inverse effect called rectified diffusion when gas molecules from the surrounding liquid join the bubble volume. During bubble oscillations the two effects occur and we can call it diffusionally stable if the two equal each other out. In the scope of this work, we occasionally observe changes of the bubble size due to diffusion or rectified diffusion over timescales of the order of minutes depending probably on the slightly variable gas content in our water. I consider this slow enough to neglect diffusional effects during the otherwise millisecond to second observation lengths. I will hence not go into further detail at this point, but content myself to note that important parameters for diffusional stability are the acoustic pressure and

driving frequency as well as the saturation of gas in the liquid. More information can be found for instance in papers published by Eller and Flynn [39], who were among the first to derive a model which takes into account the actual bubble oscillations and find a pressure threshold at which the bubbles are diffusionally stable, Gould [47], who considered the importance of taking into account streaming but without proposing any concrete method to do so, Crum [23], who summarized the first years on the subject, Fyrillas and Szeri [44], who introduced a new solution to solve the problem of mass transport across the moving bubble interface, and recently Zhang and Li [132], who improved the early models notably for regions well above resonance.

Positional stability

The positional stability of oscillating bubbles in an ultrasound field is studied relatively little. In this context, two different mechanisms are addressed in literature. The first concerns a stable position in terms of the Bjerknes forces that have been discussed in section 1.4.2. Theoretical models suggest that there are bubbles that have no stable position which in consequence makes them travel continuously between the pressure node and antinode due to a hysteresis effect in the main resonance [79] or that bubbles move around the pressure node because Bjerknes forces change sign in very high pressure fields due to nonlinear effects [28].

The second mechanism discussed in literature is the so-called erratic dancing motion. Experiments to find the threshold for one given frequency have been conducted by Eller and Crum [38]. These authors as well as later theoretical studies suggest that the erratic dancing is induced by surface modes due to nonlinear coupling. Benjamin and Ellis [6] showed theoretically that two adjacent modes which have not the same temporal phase induce self-propulsion of a bubble. As an important assumption, these authors consider that each mode might have a different orientation which leads to different directions of propulsion at every moment in time. The resulting movement then corresponds to erratic dancing with seemingly arbitrary changes of direction. Other models referring to the dancing motion, e.g. [40, 29], consider one common orientation for all modes. In this case, the dancing motion will only take place along one direction, the common axis of symmetry. We will recognize this kind of motion as the translational motion in the model of mode coupling introduced in section 1.5.3.

As Reddy and Szeri [106] have shown, it is also possible to include Bjerknes forces in the equation of translational motion. This aspect is, however, in particular important for collapsing bubbles as considered in their study.

Spherical stability

For the present work the most relevant part of instabilities concerns deviations from spherical stability. As relevant aspects are numerous, the complete section 1.5 is dedicated to this topic. It is important to note that while we try to avoid all other types of instabilities, our actual goal is to obtain and control nonspherical bubble dynamics.

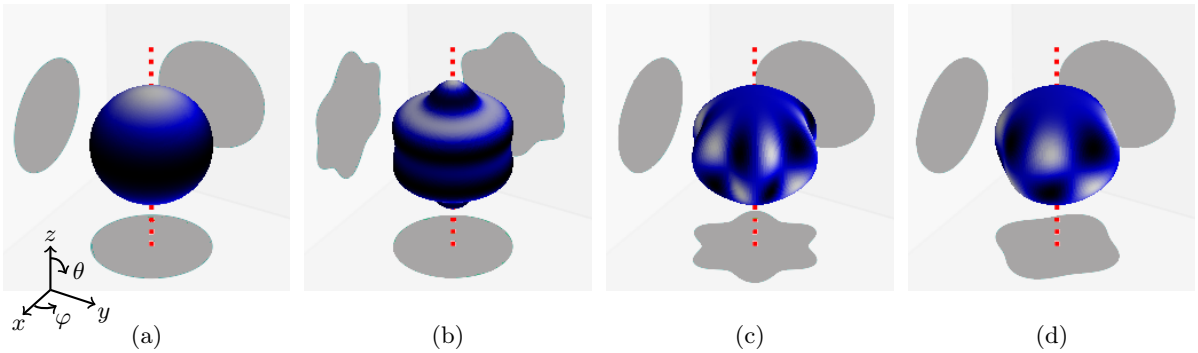

Figure 1.8: Simulations of bubble shapes and their respective projections in the x-y, x-z and y-z planes, the coordinate system is indicated on the lower left of subfigure (a). The axis of symmetry is plotted by the red dashed line. (a) Spherical bubble; (b) zonal harmonic $n = 6$ and $m = 0$ which will be called mode n in the remainder of the manuscript; (c) sectorial harmonic $n = m = 6$; (d) tesseral harmonic $n = 6$ and $m = 4$.

1.5 Nonspherical bubble dynamics

The loss of spherical stability usually goes along with the excitation of surface or shape modes, two terms that I will use synonymously throughout this manuscript. First, let us discuss in section 1.5.1 what kind of surface modes appear and how they look like. We will then address the question of stability or, in other words, which mode is excited under which conditions. A set of equations can be set up and solved. Its simplified versions lead to an analytical solution for pressure thresholds and the complete solution to more detailed stability-maps depending essentially on the bubble size, driving frequency and acoustic pressure, see section 1.5.2. These models consider parametric excitation and lead to either stable, damped solutions or unstable, exponentially growing ones. To model finite amplitudes, viscous losses and more importantly nonlinear coupling have to be taken into account. One model, which we use for comparison to our experimental work, is introduced in section 1.5.3. It is important to note that this nonlinear model allows in particular for the simulation of time-dependent bubble dynamics.

1.5.1 Nonspherical modes

Before discussing the conditions under which we may obtain nonspherical oscillations, let us talk about the shape modes that we expect to see. An overview is depicted in figure 1.8. The case of a spherical bubble, see figure 1.8 (a), has already been discussed in section 1.4. The bubble changes its size but it will always stay spherical, and whichever projection we choose we will always obtain the same image. The general solution for surface deformations is given by a set of spherical harmonics functions

$$Y_n^m(\theta, \phi) = N_n^m P_n^m(\cos\theta)\, \mathrm{e}^{\mathrm{i}m\varphi} \quad . \tag{1.21}$$

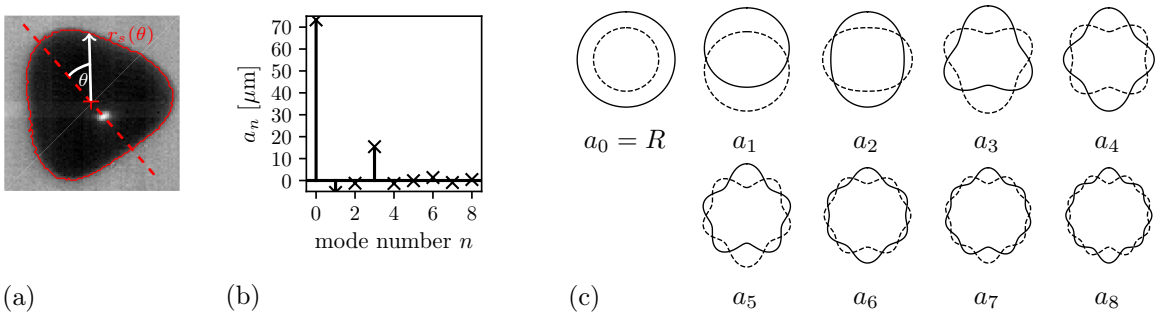

(a) (b) (c)

Figure 1.9: Decomposition into Legendre polynomials: (a) snapshot of a bubble with its contour $r_s(\theta)$ and (b) the corresponding modal decomposition. A predominance of the mode 3 can be observed. Note that the component a_0 includes the radius at rest. (c) Schematic representations of different bubble shape modes: radial mode $a_0 = R$, translation a_1 and surface modes a_n for $n = 2, \ldots, 8$. The shapes are defined by the respective Legendre polynomial P_n added to the rest radius R_0, the two extreme deformations of the bubble are shown.

Here, we are not interested in the scaling factor N_n^m, but rather focus on the θ- and φ-dependence. The solutions in the θ-direction are associated Legendre polynomials $P_n^m(\cos\theta)$ defined for $m \leq n$ and in the φ-direction the exponential can as well be understood by cos/sin-functions. An example of a sphere deformed by such a function is shown in figure 1.8 (d) for $n = 6$ and $m = 4$, the name for such a case $n \neq m$ is tesseral harmonics. Figure 1.8 (b) shows an example for $n = 6$ deformation only ($m = 0$), called zonal harmonics, and figure 1.8 (c) the case $n = m = 6$ which is called sectoral harmonics. In practice, with no driving force to deviate from axis symmetry, we usually observe $m = 0$ for the shape of free bubbles, so that the spherical harmonics simplify to zonal spherical harmonics. Consequently, for a given mode, the bubble shape is completely defined by the Legendre polynomial $P_n(\cos\theta)$. For the remainder of the manuscript, the *mode* n implies hence these zonal spherical harmonics.

Decomposition into Legendre Polynomials

In the previous paragraph, I stated that our bubbles normally have a form defined by Legendre polynomials as shown in figure 1.8 (b). This figure is, however, strongly simplified insofar that it assumes that only one single mode is present. In reality, the deformation can be composed of a superposition of several surface modes, so that the shape becomes

$$r_s(\theta, t) = \sum_{n=0}^{\infty} a_n(t) P_n(\cos\theta) \ , \tag{1.22}$$

where $a_n(t)$ is the time dependent modal amplitude. Such an example is given in figure 1.9. The contour $r_s(\theta)$ can be decomposed into a sum of Legendre polynomials. In the shown example, a mode 3 is predominant. As a supplementary illustration, the theoretically expected shapes for single modes up the eighth mode are presented in figure 1.9 (c). For each mode, the two extreme deformations that the bubble will experience during one cycle are sketched.

1.5.2 Pressure thresholds

Surface modes have been observed experimentally as early as 1944 by Kornfeld and Suvorov [61] for a bubble placed on a surface. The authors observed a linearly growing surface mode number with respect to the bubble size while keeping the driving frequency and pressure constant. A first theoretical model for a free bubble has been developed by Plesset [95] and Hsieh and Plesset [52] taking into account earlier publications by Lamb [62]. The model consists of a set of differential equations, more specifically the Rayleigh-Plesset equation for the radial oscillations and one supplementary differential equation for each surface mode a_n. It allows to calculate whether instabilities occur for a given set of parameters. Consequently, it also allows to deduce a pressure threshold between stable and unstable regions. Their model was later improved by Eller and Crum [38] who furthermore succeeded a comparison with their experimental results. At around the same time, Strube [119] also studies theoretical surface modes. However, all these models take into account viscosity *a posteriori* by assuming a certain exponential decay. The first to implement viscosity directly is Prosperetti [101] whose approach is later retaken by Francescutto and Nabergoj [43]. Their modeling, which also confirms experimental results by Hullin [53], provides the set of differential equations

$$R\ddot{R} + \frac{3}{2}\dot{R}^2 + \frac{1}{\rho}\left(-\left(p_\infty - p_v + \frac{2\sigma}{R_0}\right)\left(\frac{R_0}{R}\right)^{3\gamma} - p_v + \frac{2\sigma}{R} + 4\mu\frac{\dot{R}}{R} + p(t) + p_0\right) = 0 \tag{1.23a}$$

$$\ddot{a}_n + B_n\dot{a}_n - A_n a_n = 0 \tag{1.23b}$$

$$\text{with} \quad B_n = \left(3\frac{\dot{R}}{R} + \frac{2(n+2)(2n+1)\mu}{\rho R^2}\right) , \tag{1.23c}$$

$$\text{and} \quad A_n = \left((n-1)\frac{\ddot{R}}{R} - \frac{(n-1)(n+1)(n+2)\sigma}{\rho R^3} - \frac{2(n-1)(n+2)\mu\dot{R}}{\rho R^3}\right) , \tag{1.23d}$$

where equation (1.23a) is obviously a form of the Rayleigh-Plesset equation (1.3) and the equations (1.23b) describe the time dependent mode shape amplitudes $a_n(t)$. According to the coefficients B_n and A_n given in equations (1.23c) and (1.23d), the shape mode dynamics depends on the radial oscillations $R(t)$ and its time derivatives. With some mathematical tricks and linearization, it is possible to obtain a linear differential equation with periodic coefficients which is known as Mathieu's equation. Limiting their analysis to first parametric resonances (corresponding to a solution oscillating at half the driving frequency), Francescutto and Nabergoj [43] find an amplitude threshold that we can transform into the pressure threshold

$$p_{\mathrm{n,thresh}} = \rho_0 R_0(\omega_0^2 - \omega^2)\sqrt{\frac{(a-1)^2 + 4b}{\left(-\frac{3}{2}a + 2b + 2\left(n+\frac{1}{2}\right)\right)^2 + c^2}} , \tag{1.24}$$

$$\text{with} \quad a = \frac{4(n-1)(n+1)(n+2)\sigma}{\rho\omega^2 R_0^3}, \quad b = \left(\frac{2(n+2)(2n+1)\mu}{\rho\omega R_0^2}\right)^2, \quad c = \frac{6(n+2)\mu}{\rho\omega R_0^2} .$$

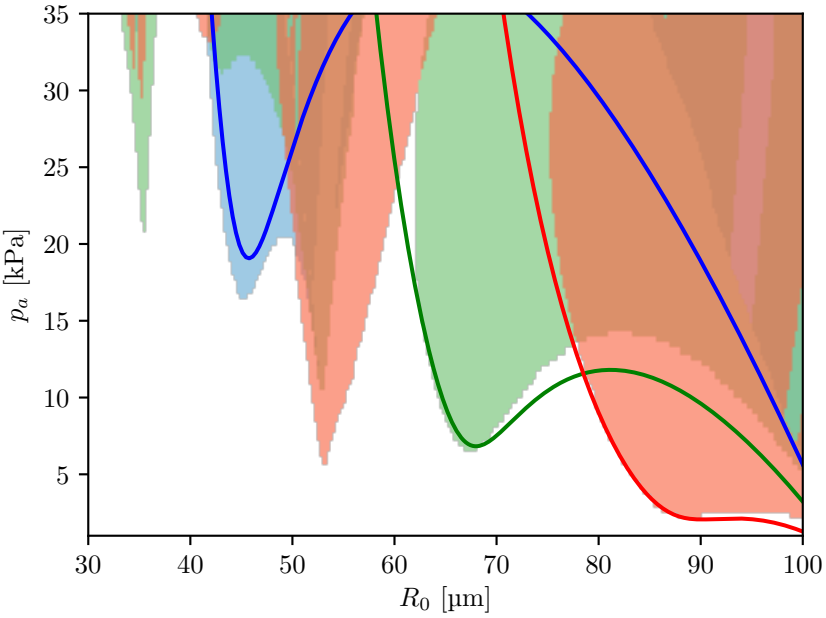

Figure 1.10: Pressure-radius map for $f_{\mathrm{ac}} = 31.25\,\mathrm{kHz}$: Solid lines correspond to the stability thresholds calculated with the model by Francescutto and Nabergoj [43], equation (1.24), background colors have been evaluated with the stability analysis by Brenner, Lohse and Dupont [10]. The same color code is used for background colors and solid lines: blue – mode 2; green – mode 3; red – mode 4.

The pressure threshold depends on the mode number n, the bubble radius, and the driving frequency. If we assume a fixed driving frequency, we find that for every mode number the threshold is a function of the bubble radius. Such examples are presented in figure 1.10 by the solid lines for $f_{\mathrm{ac}} = 31.25\,\mathrm{kHz}$ and the modes $n = 2$, 3, and 4. Brenner, Lohse and Dupont [10] develop this theory further. Instead of searching for analytical, simplified solutions for the pressure threshold, these authors solve the system of differential equations (similar to equation (1.23)) directly. Equation (1.23b) with periodic A_n and B_n is called Hill's equation. Its linearized form and solution is the previously discussed Mathieu's equation. The direct solution can be obtained via the system

$$\begin{pmatrix} a_n(T) \\ \dot{a}_n(T) \end{pmatrix} = F_n(T) \begin{pmatrix} a_n(0) \\ \dot{a}_n(0) \end{pmatrix} \quad , \tag{1.25}$$

where $T = 2\pi/\omega$ is one acoustic period. $F_n(T)$ is the so called Floquet matrix which can be calculated numerically and its eigenvalues give information on the stability. The result of such an analysis is presented in figure 1.10 by the background colors for modes $n = 2$, 3, and 4 and $f_{\mathrm{ac}} = 31.25\,\mathrm{kHz}$. We can observe regions of first parametric resonance (oscillating at $\omega/2$) which correspond well to those previously calculated from equation (1.24). In addition, there are also regions of higher parametric resonance (oscillating at ω), notably a mode 4 unstable at its second

parametric resonance situated between 50 µm and 60 µm.

In conclusion, we have a system of differential equations which allows to predict parametric instability. We can either solve the system directly for any set of parameters or linearize it to obtain analytical pressure thresholds. But why parametric stability? This question is addressed by Brenner, Lohse and Dupont [10]. These authors explain that parametric instabilities are accumulated perturbations from sphericity over many oscillations and are comparatively easy to stabilize. There is another type of spherical instabilities called Rayleigh-Taylor instabilities which occur when gas is strongly accelerated into a liquid. This effect is very fast and the bubble has, in general, no time to stabilize. For the bubbles of interest in the present study, the threshold for parametric instabilities is reached well before the threshold for Rayleigh-Taylor instabilities. For highly viscous liquids however, the situation reverses.

1.5.3 Nonlinear coupling and temporal nonspherical bubble dynamics

The previous paragraph discusses the question whether a parametric surface mode will occur or not. The answer is, however, reduced to *yes* or *no* as the presented models implicate either exponential growth or exponential decay. Consequently, they are not sufficient to predict a real temporal evolution with a finite modal amplitude. Coupling terms between the different modes have to be taken into account in order to predict finite amplitudes of temporal bubble dynamics. A first adequate model has been derived by Feng and Leal [40] with the aim to explain erratic dancing motion. These authors confirm earlier work by studying the interaction of two neighboring modes that leads to translational motion (a second-order effect), but they also discover a direct coupling between shape modes and translation. Doinikov [29] follows a similar approach taking into account all surface modes and not limited to first parametric resonance. The author furthermore gives explicit equations up to the fourth mode. Besides confirming previous results, he finds that odd modes (including the translational mode) have the ability to excite all other modes (including the translational and radial mode) even if they have been nil, while even modes can only excite other even modes (including the radial mode). Shaw [114] extends this model for third order terms and calculates results for higher modes. In our work [OP1], we use a Shaw's model reduced to second order and adding viscosity to the first order terms as specified in [10, 112] so that

$$
\begin{aligned}
0 =& \ddot{R}R + \frac{3}{2}\dot{R}^2 + \frac{2\sigma}{\rho R} - \frac{1}{\rho}\left(p_b - p\right) + 4\nu\frac{\dot{R}}{R} \\
&+ \sum_{n=2}^{\infty} \frac{1}{(2n+1)(n+1)} \left[\left(n + \frac{3}{2}\right)\dot{a}_n^2 + (n+3)a_n\ddot{a}_n - (n-3)\left(\frac{\ddot{R}a_n^2}{R} + \frac{\dot{R}^2 a_n^2}{2R^2} + \frac{2\dot{R}a_n\dot{a}_n}{R}\right)\right] \\
&- \left[\frac{p_b}{\rho}(1-3\gamma)\left(\frac{R_0}{R}\right)^{3\gamma} - \frac{p}{\rho}\right] \sum_{n=2}^{\infty} \frac{a_n^2}{(2n+1)R^2} - \frac{a_1^2}{4} \ , \qquad (1.26a) \\
0 =& R\dot{a}_1 + 3\dot{R}a_1 + 18\nu\frac{a_1}{R^2} - \dot{a}_1\frac{9}{5}a_2 - a_1\left(\frac{9}{5}\dot{a}_2 + \frac{18}{5}\frac{\dot{R}}{R}a_2\right)
\end{aligned}
$$

$$+\sum_{n=2}^{\infty}\frac{9}{(2n+1)(2n+3)}\left[\frac{2\dot{R}}{R}(\dot{a}_{n+1}a_n-2n\dot{a}_n a_{n+1})-2na_n a_{n+1}\left(\frac{\dot{R}^2}{R^2}+\frac{\ddot{R}}{R}\right)\right.$$
$$\left.+(n+1)\ddot{a}_{n+1}a_n+\dot{a}_{n+1}\dot{a}_n-n\ddot{a}_n a_{n+1}\right], \tag{1.26b}$$

$$\begin{aligned}0=&R\ddot{a}_n+3\dot{R}\dot{a}_n+(n-1)\left[-\ddot{R}+(n+1)(n+2)\frac{\sigma}{\rho R^2}\right]a_n\\&+\left[(n+2)(2n+1)-2n(n+2)^2\frac{\delta}{R}\right]\frac{2\nu}{R}\dot{a}_n+\left[(n-1)(n+2)+2n(n+2)(n-1)\frac{\delta}{R}\right]\frac{2\nu\dot{R}}{R^2}a_n\\&+\frac{9}{4}\delta_{2n}a_1^2-\frac{3n(n+1)}{2(2n+3)}\dot{a}_1a_{n+1}-\frac{3(n+1)(2n+1)}{2(2n+3)}a_1\dot{a}_{n+1}\\&+(1-\delta_{2n})\left[\frac{3n(n+1)}{2(2n-1)}\dot{a}_1a_{n-1}+\frac{3(n+1)\dot{R}}{R}a_1a_{n-1}+\frac{3}{2}(n+1)a_1\dot{a}_{n-1}\right]\\&+\sum_{i=2}^{\infty}\sum_{j=2}^{\infty}\frac{(2n+1)(n+1)}{4}\left[\frac{\ddot{R}}{R}a_ia_jG_{d_{ijn}}+\frac{\dot{R}^2}{R^2}a_ia_jM_{a_{nij}}+\frac{\dot{R}}{R}\dot{a}_ja_iM_{b_{nij}}+a_i\ddot{a}_jM_{c_{nij}}\right.\\&\left.+\dot{a}_i\dot{a}_jM_{d_{nij}}\right]\\&-\sum_{i=2}^{\infty}\sum_{j=2}^{\infty}a_ia_jI_{a_{nij}}\frac{(2n+1)(n+1)}{2R^2}\frac{p_b-p}{\rho}\ .\end{aligned} \tag{1.26c}$$

Equation (1.26a) rules radial oscillations. The first line corresponds to a standard Rayleigh-Plesset equation, where the vapor pressure p_v has been neglected (as compared to equation (1.3)). We use the abbreviation $p = p_0 + p(t)$, and $p_b = (p_0 + 2\sigma/R_0)\,(R_0/R)^{3\gamma}$ is the pressure of the bubble at its rest radius R_0 and atmospheric pressure p_0. Equation (1.26b) describes the translational motion a_1 and with equation (1.26c) we can calculate any shape mode a_n. $\delta = \sqrt{\nu/\omega}$ is the thickness of the boundary layer, not to be confused with the Kronecker delta δ_{ij}. The terms $G_{d_{ijn}}$, $M_{a_{nij}}$, $M_{b_{nij}}$, $M_{c_{nij}}$, $M_{d_{nij}}$ and $I_{a_{nij}}$ are defined in the appendix of [114], but they are also added in appendix C.1 for completeness of this manuscript.

Comparison of different numerical solutions and evidence of mode coupling

Figure 1.11 shows the comparison between three numerical solutions of analytical models. As the bubble radius and acoustic pressure are set to 70 µm and 10 kPa respectively, we expect to obtain a parametrically excited mode 3 because the pressure exceeds the pressure threshold $p_{3,\text{thresh}} \approx 8$ kPa. This is indeed the case for all three simulations. The plot on the left shows an uncoupled model. It is well visible that modes 2 and 4 decay and that mode 3 starts to increase very rapidly once it is triggered. Note in particular, that the scale becomes 10^8 µm in the plot, hence a physically unrealistic value. The plot in the center shows the result of the above coupled model from equation (1.26). Here, the mode 3 is amplified until it reaches a steady-state value. Meanwhile, the initial modal amplitudes of modes 2 and 4 have decreased but in particular

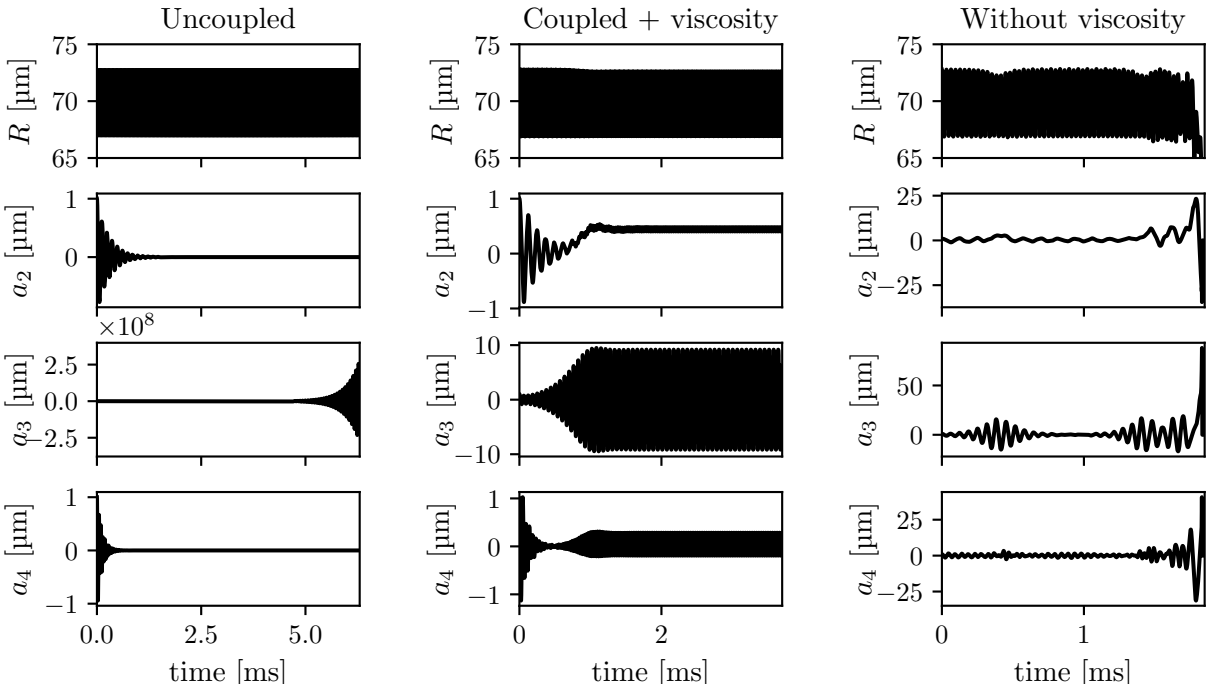

Figure 1.11: Comparison between different analytical models. All have been supplied with the same initial conditions: acoustic pressure $p_a = 10\,\mathrm{kPa}$, radius at rest $R_0 = 70\,\mu\mathrm{m}$, initial deformation for the shape modes $a_n = 1\,\mu\mathrm{m}$ for $n = 2, 3, \ldots, 10$. The calculation is done up to $n = 10$, but only the radial mode R and the shape modes 2, 3 and 4 are presented. The not presented translational mode and higher surface modes are small compared to the here shown modal amplitudes. Note the different time scales for the three plots and the different amplitudes for the subplots. *Left:* Uncoupled model, modes 2 and 4 are damped while mode 3 grows exponentially (order of magnitude of the amplitude becomes $10^8\,\mu\mathrm{m}$!); *center:* coupled model where first the modes 2 and 4 decrease whereas the mode 3 increases, once the mode 3 is large enough, mode coupling can be observed through the re-appearance of the mode 4 and the finite modal amplitude of the mode 3; *right:* the model with mode coupling but without viscosity is unstable for this particular case.

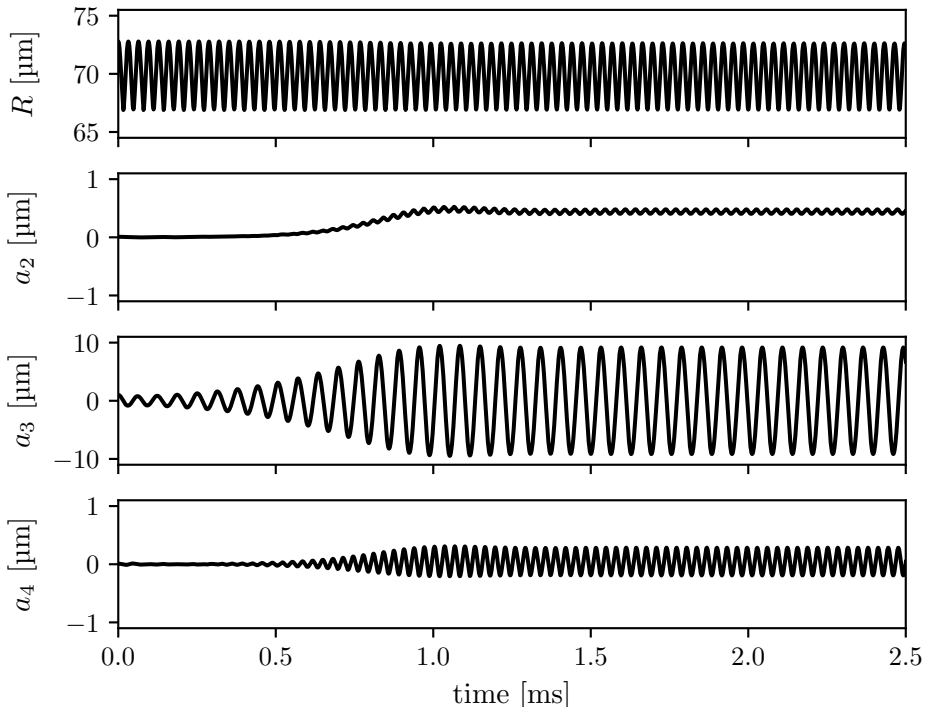

Figure 1.12: Simulation of the coupled model including viscosity, initial conditions are $p_a = 10\,\text{kPa}$, $R_0 = 70\,\mu\text{m}$, and $a_3 = 1\,\mu\text{m}$, all other modes are set to zero. Mode 3 is excited parametrically (oscillating at half the driving frequency) which then excites modes 2 and 4 through nonlinear coupling (oscillating at the driving frequency). Note the different length scales for the modal amplitudes.

the mode 4 is then re-amplified due to mode coupling. The effect of mode coupling has been discussed in more detail by Guédra et al. [49] through comparison of experimental results and numerical implementation of such a coupled model. By the way, mode 3 is an odd mode which can excite any other mode. An even mode such as mode 4 would only be able to excite other even modes through nonlinear coupling. The same simulation but without viscosity is shown in the plot on the right of figure 1.11. In this particular case, the simulation becomes unstable after about 1.8 ms. Even though the model with viscosity can become unstable as well upon choice of certain parameters, it is interesting to observe the expected fact that viscosity plays a stabilizing effect.

Figure 1.11 is appropriate to show the overall evolution of the modal amplitude, but it lacks visibility into the detailed oscillations. A single enlarged plot of the coupled model including viscosity is therefore given in figure 1.12. As opposed to the initial conditions of the first simulation, only $a_3 = 1\,\mu\text{m}$ while all other modal amplitudes are set to zero. This once more underlines the presence of mode coupling. Note, however, the different scales: the y-interval for the radial mode and mode 3 is ten times larger than for modes 2 and 4. One last fact to highlight is the frequency of the oscillations. The modal amplitude 3 oscillates at half the driving frequency due to first parametric excitation while all other modes oscillate at the driving frequency.

1.5.4 How to work with all these models

In the present section 1.5, I introduced a certain number of notions and models for nonspherical bubble dynamics. Let us shortly resume the important points to understand how we can use these notions for the later experimental work. In section 1.5.1 we discussed the possible shape of bubbles and it is important to retain that we can simplify our cases to zonal harmonics or, in other words, to a decomposition in Legendre polynomials. For the practical use, we then follow two steps:

1. Our objective is to obtain a bubble oscillating on a desired surface mode, let us say a mode 3. With the aid of pressure thresholds (restricted to first parametric resonances) or the more precise but also more time-consuming pressure-radius maps, see figure 1.10 and section 1.5.2 for both, we can deduce parameters f_{ac}, R_0 and p_{a} for which the desired mode will be triggered. Note that at this point we will only know, which mode will be triggered parametrically, but we know neither at which frequency it will oscillate nor which other modes might be induced by mode coupling.

2. Once we know these parameters we can use them in a numerical model such as Shaw's model from equation (1.26) in section 1.5.3. The numerical output provides the temporal evolution of all modal amplitudes and allows us also to conclude on frequencies and mode coupling.

The complete control of the numerical aspects gives us a good comparison for our experimental results. So let us close the theoretical chapter at this point and go on to the experimental part.

Chapter 2

Control of nonspherical bubble dynamics

We need to control the bubble dynamics for the later study of microstreaming flow around the bubble. As existing theory has already been introduced in sections 1.4 and 1.5, the present chapter is dedicated to the question of how to implement this in practice. There are two important features to keep in mind: (1) we want to obtain steady-state surface oscillations and (2) we want to be able to characterize them in the 2D plane of our camera. As we will discuss in section 2.1, none of the commonly used methods achieve both requirements. Therefore, a new idea has to be found. One answer to this is bubble coalescence. Bubble coalescence is the encounter and merging of two bubbles and has been mostly studied in other contexts, see section 2.2. Here we exploit and optimize this method to obtain the desired surface modes with controlled orientation. The experimental setup and procedure are introduced in section 2.3, the main results and some further observations follow in section 2.4.

As we will see, the experimental results are very satisfying. However, there are some questions which regularly re-emerge during post-processing. To which extent is the extracted bubble dynamics influenced by the fact that we only have of a 2D projection? How does a badly oriented bubble influence the modal content? And are all modal contents physically present or do some of them just appear virtually due to the experimental and post-processing procedure? I will give some insight into this discussion in section 2.5.

Lastly, in section 2.6 I include a short outlook on a supplementary study on the dynamics of a bubble attached to a wall. Even though this topic is not directly necessary for the rest of my work, it plays an important role for the general context. In real applications, there are not only single free bubbles, but oftentimes they might be in contact with other objects.

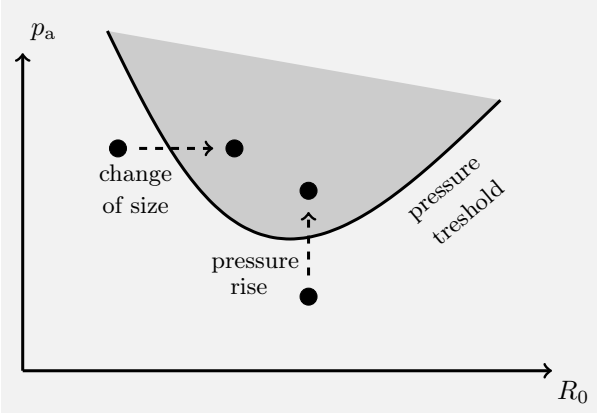

Figure 2.1: Sketch of one shape unstable zone in a pressure-radius map and of different ways to trigger the expected surface mode. The region can be reached either by raising the acoustic pressure amplitude or by a change of bubble size (for instance through diffusion or rectified diffusion, and as we will see in section 2.2 through bubble coalescence).

2.1 Existing experimental methods to trigger surface modes

Theoretically, in order to obtain surface modes, we just have to set the correct acoustic pressure and bubble size. But how can this be done in practice? In the following, I introduce some possible methods, a sketch of different procedures is added in figure 2.1.

Rising the acoustic pressure

It is possible to take a bubble at a relatively low pressure and then slowly rise the pressure until it is above the pressure threshold. For instance a bubble with $R \approx 70\,\mu m$ should exhibit mode 3 oscillations beyond a pressure threshold of roughly 10 kPa, see figure 1.10. We have indeed conducted such experiments, but found them inconvenient as they oftentimes demand a very fine tuning of the pressure amplitude and hence a good deal of patience. If the pressure is increased too quickly, positional instabilities take over and the bubble is no longer controllable. Also, even when a slow rise with a stable bubble succeeds, we have no influence on the orientation of the shape modes. However, in order to correctly visualize the 3D bubble in the 2D camera plane it is essential to control the axis of symmetry so that it is in the camera plane. I will include examples of a non-controlled symmetry axis later in section 2.5.2 when addressing the errors that are induced in such cases.

Short ultrasound burst

A possible method to visualize bubble dynamics is to expose a bubble to a short ultrasound burst. This method was for example applied by Versluis et al. [123] who were able to make a detailed study including modal decompositions and validation of theoretically expected parametrically excited modes. It is convenient that the axis of symmetry is normally defined by the direction

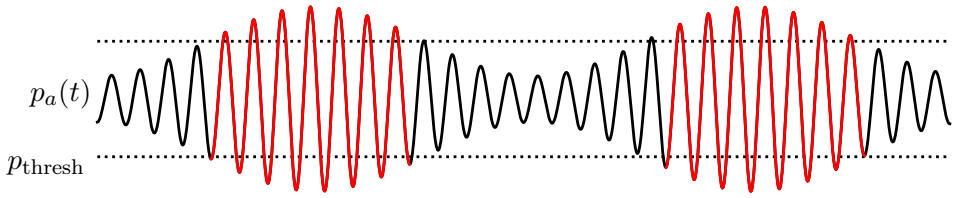

Figure 2.2: Schematic representation of a modulated pressure amplitude. Surface oscillations can be triggered when the amplitude rises above the pressure threshold, here plotted in red.

of the traveling ultrasound wave. Another advantage is that even if there are modal amplitudes that grow very fast (theoretically exponentially), the maximum amplitude is limited due to the shortness of the ultrasound burst. However, short ultrasound bursts are by definition a transient phenomenon and the method is hence not usable for our purpose of steady-state oscillations.

Modulated pressure amplitude

Another way to limit surface mode amplitudes was employed for instance by Guédra et al. [49]. The acoustic signal of frequency f_{ac} is modulated with a second much lower frequency f_{m}. The ratio employed in their study was 400 with $f_{\text{ac}} = 31.25\,\text{kHz}$ and $f_{\text{m}} = 78.125\,\text{Hz}$. The pressure amplitude can be expressed as

$$p_a(t) = \hat{p}_a \cos(2\pi f_{\text{ac}} t)(1 - \eta \cos(2\pi f_{\text{m}} t)) \ , \tag{2.1}$$

where η is the modulation amplitude. An example of such a pressure signal is sketched in figure 2.2. Here, the amplitude rises periodically above the pressure threshold and allows a surface mode to be triggered. Consequently, there is a periodic on- and offset of the surface modes. This method has the convenience to allow a large number of recordings under the same conditions. However, as we only rely on parametric excitation, there is no preference direction of the acoustic field and consequently no control of the bubble orientation. Furthermore, per definition no steady-state regime is reached.

Diffusion or rectified diffusion

In principle, we could also wait for the bubble to change size due to diffusion or rectified diffusion. However, as the bubble size is rather stable in our experiments, we have never tried to exploit this method. Furthermore, we do not have any influence on the axis of symmetry of the triggered surface modes.

Other methods

According to theoretical predictions by Shaw and Spelt [113], surface modes could also be triggered by an electric field, a method which might succeed in defining the axis of symmetry.

However, according to the authors, only even modes can be triggered without an initial deformation. For this reason and also in view of possible difficulties in the practical implementation, this method has not been taken into closer consideration.

In conclusion, none of the above experimental techniques are suitable for the experiments of microstreaming, because they fail either in controllability of the bubble orientation or in the possibility of reaching a steady-state regime. For this reason, we need another method which allows us to fulfill both requirements. As a first milestone for my PhD work I therefore investigated bubble coalescence as a means to control the bubble dynamics. I will give a short overview of what bubble coalescence is and introduce the general idea in the context of my work in the following section 2.2 before moving on to the actual experimental setup and the corresponding results.

2.2 An overview on bubble coalescence

Bubble coalescence in literature

Bubble coalescence is the meeting and merging of two (or more) bubbles to form one new single bubble. Depending on literature, bubble coalescence contains either the time from approach to a final bubble or only the mechanisms implied just before and after liquid film rupture. Consequently, the process can be divided into three (e.g. [13]) to six steps (e.g. [97]). Following the three-step division, the following stages can be named.

- Formation of a thin liquid film at quasi equilibrium film thickness controlled by hydrodynamics.
- Thinning of the film due to drainage. The main influences are gravity and suction due to capillary forces. Viscosity can also play a small role. When films become very thin, van der Waals attraction starts to play an important role by increasing the film draining, while electrostatic forces decrease it. The film becomes either metastable or gets thinner until reaching a critical thickness.
- Rupture at a critical thickness of $< 10\,\mathrm{nm}$ according to Chaudhari and Hofmann [13].

When searching for existing work on bubble coalescence, it is striking that most of them report on hydrodynamic coalescence, that means without the presence of ultrasound. In this context, parameters such as the bubble approach [109], film drainage [13], and bouncing behavior [34] are of interest. One paper written by Stover, Tobias and Denn [118] is interesting in the context of the present manuscript. It concerns the observation of surface dynamics, more specifically the fact that coalescence is followed by oscillations of an elliptical shape, in other words a mode 2. Of course, as there is no sound field applied, the oscillations decay and, as gravity can be neglected for very small bubbles, this result in a purely spherical bubble.

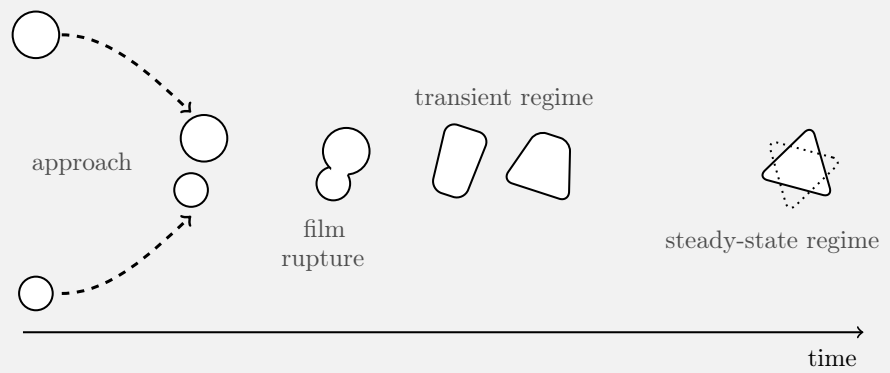

Figure 2.3: Schematic sketch of bubble coalescence.

Recently, bubble coalescence was investigated by applying an ultrasound field so that the main force ruling the approach and collision of the bubbles became the primary and secondary Bjerknes forces [56]. The main findings were an increase in the coalescence time for free micrometric bubbles [57], which led to the modification of the film drainage theory [97]. These studies were all carried out in a relatively low amplitude ultrasound field, and consequently, the coalesced bubble returned to purely spherical oscillations.

The idea of applying bubble coalescence for triggering surface modes

As reported above, bubble coalescence has been mainly studied in terms of the parameters that influence the merging of the bubble before film rupture. The fact that this evidently leads to one single, initially deformed bubble has never been exploited any further. Also, all previous studies have been conducted without acoustic pressure or at relatively low pressures, so that the bubble was expected to return to spherical shape.

We propose a new setting for bubble coalescence in relatively high pressure fields. Let me recall that from theory (section 1.5.2) we expect to obtain surface modes if we choose the correct set of parameters, in particular bubble size and acoustic pressure (for a fixed driving frequency). So, if a newly coalesced bubble fulfills these conditions, we expect surface modes to appear. While all above explained methods for triggering of surface modes rely on parametric excitation of surface modes starting with a spherical bubble, in the case of bubble coalescence the bubble is already deformed. In fact, at the moment of film rupture, there is one single deformed bubble whose shape can be decomposed over a large number of surface modes. Following this moment, bubble dynamics is ruled by a transient regime during which the naturally (parametrically) excited mode(s) will grow while all others will be damped. As in the simulations of section 1.5.3, figures 1.11 and 1.12, we expect a steady-state regime with constant modal amplitudes to establish. A sketch of coalescence in our experiments is given in figure 2.3. For the observation of microstreaming we are in particular interested in the steady-state regime. The present chapter is dedicated to understanding the bubble dynamics obtained through bubble coalescence but also to spherical and non-spherical bubble dynamics in general.

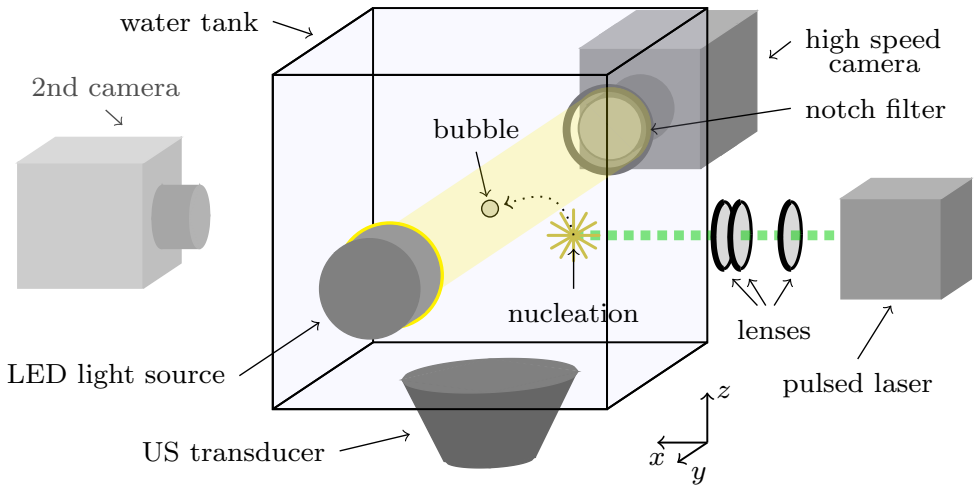

Figure 2.4: Experimental setup for the observation of temporal bubble dynamics. The second camera is only used in a small part of the experiments discussed in section 2.5, the corresponding light source is left out in the figure for sake of readability.

2.3 Experimental setup to observe bubble dynamics

2.3.1 Experimental setup

A schematic drawing of the experimental setup used for the bubble coalescence experiments is given in figure 2.4. All our experiments are conducted in an 8-cm-edge cubic water tank filled with nondegassed water. We do not control the saturation of gas inside the tank, but it corresponds to standard values, the saturation of oxygen is approximately $8.2\,\mathrm{mg\,L^{-1}}$ depending slightly on temperature. The water tank is placed on a movable device which allows to adjust its position in the three directions x, y, and z (defined in figure 2.4) to adjust its position for visualization with the camera.

Nucleation and trapping of bubbles

Single bubbles are nucleated by short laser pulses ($\lambda = 532\,\mathrm{nm}$, second harmonic of a Nd:YAG pulsed laser, New Wave Solo III, 6 ns pulse duration). The laser beam is focused by a set of three lenses: it is enlarged by a first spherical concave lens ($f = -25\,\mathrm{mm}$), then collimated by a second spherical convex lens ($f = 125\,\mathrm{mm}$) and finally focused by an aspherical lens ($f = 40\,\mathrm{mm}$) to minimize optical aberrations. The size of the nucleated bubble depends strongly on how well focused the laser beam is. Furthermore, the size can be slightly influenced by tuning the energy of the laser. To give an order of magnitude, the energy per laser pulse is a few mJ. We nucleate bubbles with radii ranging between 20 µm and 40 µm, higher energy laser pulses would usually lead to several bubble fragments and are not sufficiently controllable. Larger bubbles can be obtained by coalescence of two smaller bubbles. For example, a bubble of radius 70 µm can typically be obtained from coalescing five to ten individual bubbles.

An ultrasonic plane transducer (SinapTec®, diameter of the active area 35 mm) is attached to the bottom of the tank. Gel is used to provide impedance matching and no air between the transducer and tank. The voltage amplitude of the transducer is varied between 1 V and 10 V, no gain amplifier is used. All experiments are conducted at a driving frequency set to 31.25 kHz, which corresponds to a resonant radius $R_{\text{res}} \approx 104\,\mu\text{m}$ according to Minnaert's theory, see equation (1.7). The bubbles considered in this study have radii smaller than 90 µm and hence are all smaller than resonant size. Consequently, they are naturally driven towards pressure antinodes due to primary Bjerknes forces.

Visualization

Experiments are captured with a CMOS camera (Vision Research® V12.1) equipped with a 12× objective lens (Navitar® equipped with an additional 1.5× lense). For the different experiments described in the present chapter, the frame rate varies between 67 kHz and 180 kHz, the frame size between 256 × 256 pixels and 128 × 128 pixels. Naturally, the higher the frame rate the more limited the frame size and *vice versa*. The pixel size for most measurement series was $3.5\,\mu\text{m}\,\text{pixel}^{-1}$, some additional recordings have been done for a pixel size of $7.5\,\mu\text{m}\,\text{pixel}^{-1}$. The depth of field of the camera objective and lenses is about 200 µm. Backlight illumination is assured by a continuous light-emitting diode (LED) of 3 W. The pixel size was evaluated before the measurement series with a test pattern which had 80 µm to 160 µm thick stripes.

For the specific series of measurements discussed in section 2.5, we use a second camera of the same type and triggered synchronously with the first one. The second camera was not available for the other experiments, for this reason it is indicated in lighter gray in figure 2.4.

2.3.2 Experimental procedure

One bubble is nucleated at a few millimeters distance from a pressure antinode of the acoustic field. Due to primary Bjerknes forces the bubble will be driven towards the pressure antinode and trapped slightly above it. Then, a second bubble is nucleated. Its trajectory is influenced by primary Bjerknes forces but also by secondary Bjerknes forces induced by the first bubble, see once more the example in figure 1.7. The coalescence is recorded, covering the approach of the two bubbles, their impact, and the coalesced bubble. If desired, a trapped bubble can be grown by multiple coalescences.

The time that passes between the nucleation of a new bubble and its coalescence with an already trapped bubble is of the order of a second. One experiment includes the creation of a first bubble, its growth by multiple coalescences to a desired approximate size and a last coalescence, which triggers the surface modes and which is recorded. Once the overall parameters well understood it is possible to repeat experiments every few minutes. One of the key issues is to predict the actual spot of coalescence so that it takes place inside the relatively small field of view of our camera.

2.3.3 Postprocessing

Surface mode analysis

During the postprocessing the bubble shape is analyzed for each snapshot. Image processing is applied to extract the centroid and the bubble contour. As shown in section 1.5.1 and more specifically in equation (1.22), the contour can be described as a sum of Legendre polynomials

$$r_s(\theta, t) = \sum_{n=0}^{\infty} a_n(t) P_n(\cos\theta) \ . \tag{2.2}$$

The modal amplitudes a_n can be obtained by projection of the shape on the respective Legendre polynomial [49] so that

$$a_n(t) = \frac{2n+1}{2} \int_{-1}^{1} r_s(\mu, t) P_n(\mu) \mathrm{d}\mu \quad \text{with} \quad \mu = \cos\theta \ . \tag{2.3}$$

An example has been shown in figure 1.9. One important point before doing the modal analysis is the definition of the axis of symmetry. The choice of the axis imposes a reference for the angle θ for which the Legendre decomposition is valid. If we have no supplementary information on its orientation, a search for direction along which the maximum deformation occurs is a good hypothesis. Usually, a badly chosen axis gives incoherent information over time. I will explain how to find the axis of symmetry in the case of bubble coalescence in section 2.4.2. Furthermore, some aspects will be recalled in section 2.5, where I will discuss potential errors on the modal amplitudes induced through the experimental method.

Uncertainties on the radius are mainly due to the pixel size and the image processing parameters, and we estimate them to be approximately $\pm 3\,\mu\mathrm{m}$. For experiments where two spherical bubbles coalesce into a single spherical one we have approximate conservation of volume, as $V_1 + V_2 \approx V_{coal}$.

Acoustic field characterization.

In section 1.4 we have discussed the dynamics of spherical bubble oscillations and in particular the Rayleigh-Plesset model. It gives a relation between the bubble size and the forcing acoustic pressure. Two examples have been shown in figure 1.5. As we are able to measure the bubble radius, we can deduce the acoustic pressure by fitting a numerical model to the experimental data. Doing this for a large number of spherically oscillating bubbles, we obtained a linear relation between the applied voltage and the acoustic pressure varying between 5 kPa and 35 kPa. Such a pressure-voltage relation is shown in figure 2.5. Two example fits of the bubble size are added, each of them leading to one single point of the pressure-voltage relation. Note that the different points have been obtained for random bubble sizes ranging between 30 µm and 70 µm. Due to the way we obtain the pressure, it is difficult to estimate the uncertainty, but a ± 5 kPa deviation is observed on the plot. Furthermore, we observed differences depending on the measurement series,

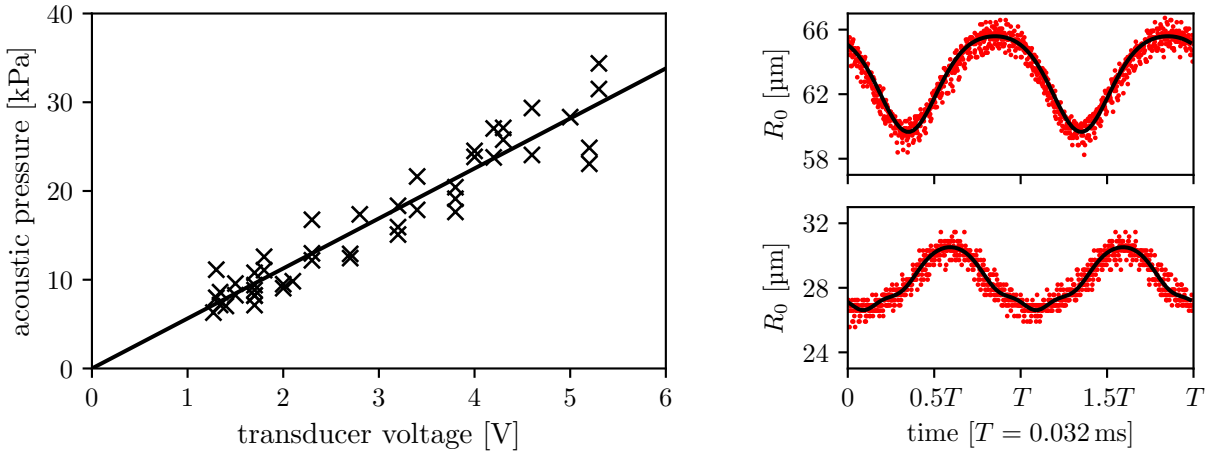

Figure 2.5: *Left:* a linear pressure-voltage relation is obtained when combining the information from a large number of spherical bubbles. Each point is obtained from the experimentally controlled transducer voltage and a pressure deduced from a Rayleigh-Plesset fit. *Right:* Two examples of a Rayleigh-Plesset model (black line) fitted to experimental data (red dots), each leading to one point on the left plot. For the *upper right* graph the transducer voltage was set to 2.7 V which leads to an acoustic pressure of 12.9 kPa according to the model. For the *lower right* graph the transducer voltage was set to 4.3 V which here leads to an acoustic pressure of 25.8 kPa. To obtain the fits, I conducted a first approximate simulation which was then optimized by letting a Matlab function fit the model parameters (pressure, mean radius and phase) over 30 iterations.

probably due to slightly changed experimental conditions such as temperature and thickness of the matching gel layer.

The measurement gives us information on the acoustic field at the bubble position. During experiments, the bubble was always trapped close to the same pressure antinode along the z-axis at approximately 3/4 the height of the water tank. Furthermore we observed that with a differently adjusted laser, bubbles could be trapped towards the corners of the tank. These observations are confirmed by a simulation with Comsol Multiphysics®. In the model, a resonance is obtained for 31.7 kHz corresponding to our experimental frequency of 31.25 kHz when taking into account some small variations between physical and theoretical parameters. The corresponding pressure field is displayed in figure 2.6. The global field can be best understood with the iso-pressure lines above, while the two planes show the situation around the pressure maximum. Experimentally, the dark red pressure maximum corresponds to the position where our bubbles are usually trapped. At first, it might seem surprising that the walls of the tank correspond to pressure minima and not to the usual rigid boundary pressure maxima. In fact, the thin acrylic glass walls (2 mm) and its characteristics similar to water (speed of sound 2700 m s^{-1} and density 1200 kg m^{-3}) lead to an approximate free surface condition with the surrounding air and hence to pressure minima.

Now that we have discussed the experimental procedure, post-processing and that we understand the acoustic field, let us move on to the experimental results.

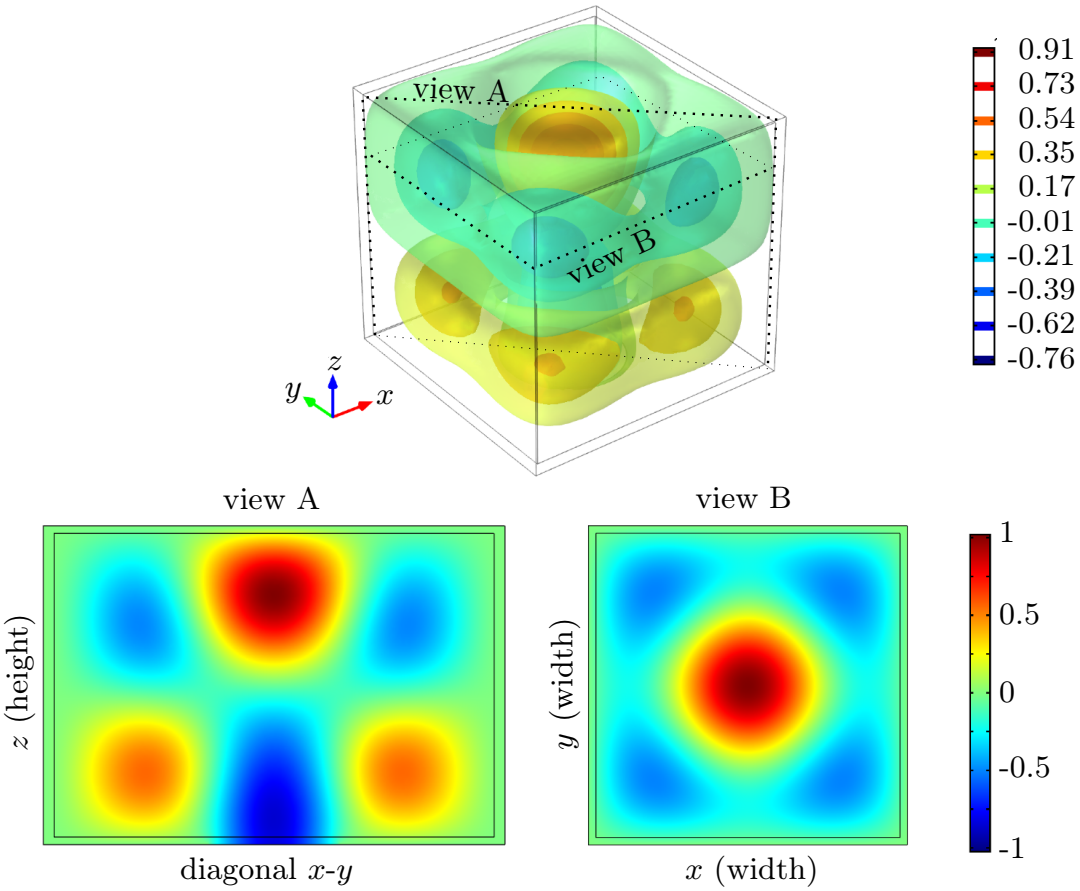

Figure 2.6: Simulation of the instantaneous acoustic pressure inside the cubic tank with inner dimensions of 8 cm. *Top:* iso-pressure in a 3D view, *bottom:* pressure distribution in the two planes through the pressure maximum (view B at a height of $z \approx 6.4$ cm). Note that all pressures are normalized by the maximum pressure and that both high positive and high negative pressure values of the instantaneous field correspond to pressure maxima.

2.4 Bubble coalescence for triggering surface modes

The present section covers the main results of the coalescence experiments which are also published in [OP1]. In the following, in section 2.4.1, we will first look at the steady-state regime and discuss which surface modes can be triggered in our experimental setup. Next, we will consider the temporal bubble dynamics in more detail for both transient and steady-state regime. A first important observation consists in the definition of the axis of symmetry, see section 2.4.2. Furthermore, the temporal evolution of the different modal components gives very helpful information for controlling and understanding bubble dynamics, see section 2.4.3. At last, I will briefly discuss the case of failed bubble coalescence [OP4], which was not part of the initial study, but whose observations are interesting nonetheless.

2.4.1 Steady-state surface modes triggered by bubble coalescence

It is fairly easy to judge by just looking at the recordings of bubble coalescence which mode persists in the steady-state regime, without the need of detailed surface mode analysis. In figure 2.7, the ensemble of our experiments is presented in a pressure-radius diagram. It is obvious that experimental results (represented by the markers) correspond very well to the theoretically expected surface modes (background colors). As long as the acoustic pressure is

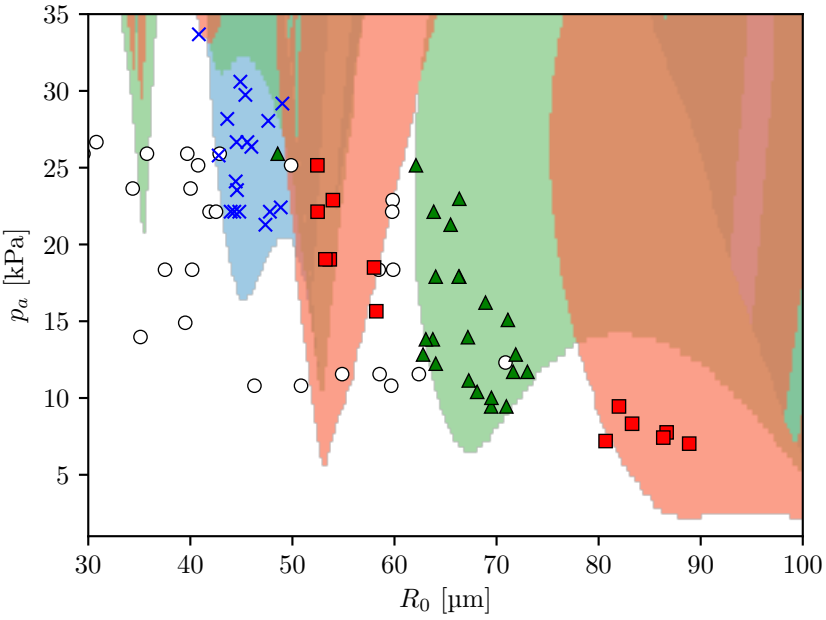

Figure 2.7: Pressure-radius diagram showing the different modes of the coalesced bubbles in the steady-state regime for $f_{ac} = 31.25\,\mathrm{kHz}$. ○, spherical mode; ×, mode 2; △, mode 3; □, mode 4. The background colors correspond to the analytical solutions: white, spherical mode; blue, mode 2; green, mode 3; red, mode 4.

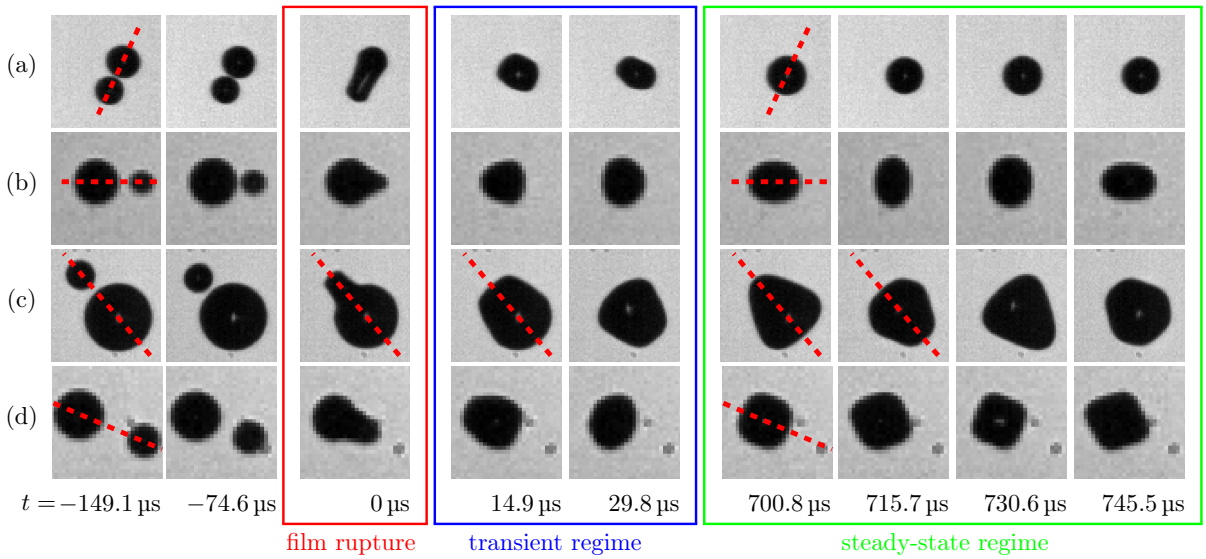

Figure 2.8: Snapshots of two coalescing bubbles which result in a single bubble with different modes: (a) spherical mode; (b) mode 2; (c) mode 3; and (d) mode 4. The reference time of 0 µs corresponds to the first image after the film rupture, indicated by the red box. The frames presented here have a height and width of 220 µm. The bubble sizes are summarized in table 2.1.

below the pressure threshold, the initially deformed bubble will soon oscillate in a purely spherical way. Surface modes appear when the respective pressure threshold is exceeded. We were able to see modes 2, 3 and 4 of first parametric resonance and modes 4 of second parametric resonance. In the following, we will only analyze the modes 2, 3 and the second parametric resonance of the mode 4 (at $R_0 \approx 55\,\mu m$). The first parametric resonance of the mode 4 is difficult to obtain due to issues of translational stability.

With the knowledge of this pressure map we can now deliberately trigger a desired surface mode. We just have to trap a bubble slightly smaller than the desired size, regulate the acoustic pressure to the desired value and then nucleate a last small bubble to trigger surface modes by coalescence. The largest inconvenience is that in this way, the bubble size can only be chosen approximately, the actual size depends on the slightly variable size of the nucleated bubble. Furthermore, we do not measure the bubble size in real time and only estimate it approximately. The triggering of the surface modes depends for a good part on experience, but this is sufficient for our purposes.

2.4.2 Axis of symmetry defined by bubble coalescence

Examples of bubble coalescence leading to different modes are shown in figure 2.8, the corresponding sizes and pressures are summarized in table 2.1. For each series, the first two snapshots are taken during the approach. The third snapshot, the one with the red frame, corresponds to the first image after film rupture and we consider it as our new initially deformed bubble. We define this moment as $t = 0\,\mu s$, which will also serve as reference for later numerical simulations.

Table 2.1: Bubble size, acoustic pressure, and pressure thresholds of mode n for the cases of bubble coalescence presented in Fig. 2.8 (a)-(d).

	$R_{0,1}$ [µm]	$R_{0,2}$ [µm]	$R_{0,\mathrm{coal}}$ [µm]	p_a [kPa]	n	p_{th}^n [kPa]
(a)	25.3	30.3	39.5	14.8	–	––
(b)	40.3	19.8	44.9	30.6	2	16.4
(c)	62.9	26.2	68.1	10.4	3	6.6
(d)	49.2	32.6	53.6	24.1	4	6.5

The two following snapshots, the ones with the blue frame, show the bubble during the transient regime and the last four snapshots, green frame, are consecutive snapshots taken during the steady-state regime.

The red dashed lines in figure 2.8 indicate the axis along which the two bubbles approach each other just before the impact and the axis of symmetry of the bubble oscillations. It can be seen that the axis stays the same over the whole period shown in the snapshot and even beyond during several seconds of recording. Therefrom we can conclude that the axis of symmetry is defined by the direction of impact between the two bubbles. This finding is coherent with the consideration that the preferential direction, which is otherwise missing in our experimental setup, is given by the impact.

All examples presented in this section contain bubbles that stay in the camera plane all along their trajectories and coalescence. Consequently, the axis of symmetry is in the camera plane as well.

2.4.3 Temporal bubble dynamics

With the knowledge of the axis of symmetry, we can proceed to do the modal decomposition for the complete recordings. In this way, we do not only evaluate the predominant mode by a sharp look but obtain real quantitative data. Let us retake the four examples from the snapshot series shown in figure 2.8. The respective temporal modal decompositions are presented in figures 2.9 to 2.12 by the black lines in parts (a) and the black points in parts (b). For the sake of readibility, I limit the figure to the first four shape modes, as higher modal amplitudes were negligible in comparison to the predominant nonspherical contribution. Every acquisition covers at least 15 ms of signal (corresponding to ∼500 acoustic periods) from the first image following the film rupture ($t = 0\,\mu\mathrm{s}$) to the established steady-state regime. Figure 2.9 (a) to figure 2.12 (a) present only the first 1.5 ms after film rupture. Note that a frame rate of 67.065 kHz and a driving frequency of 31.25 kHz correspond to a sampling of 2.15 frames per acoustic period. The seemingly periodic effect that is visible on the spherical oscillations $R(t)$ in parts (a) of the figures is due to this low sampling and does not have any physical meaning. Figure 2.9 (b) to figure 2.12 (b) present plots where experimental data during the steady-state regime, typically between 10 ms to 15 ms, is reported on two acoustic periods. These plots also allow a direct interpretation of the frequencies

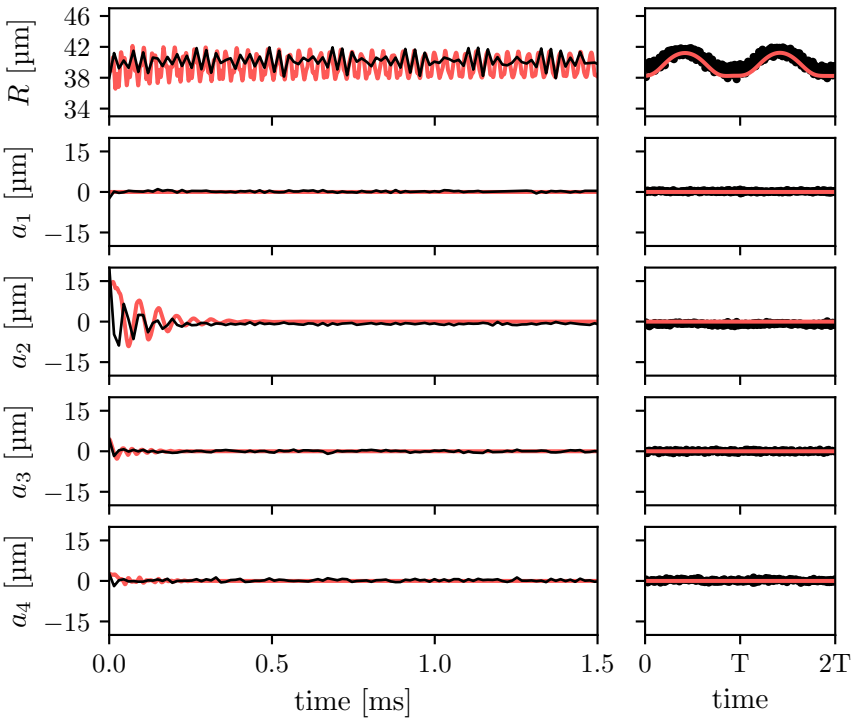

(a) first oscillations (b) steady-state

Figure 2.9: Temporal evolution of the radius $R(t)$ and the surface mode coefficients $a_1(t)$ to $a_4(t)$ extracted from the modal decomposition. For this bubble (for parameters, see table 2.1(a)) only spherical oscillations remain in the steady-state regime, once the surface modes have decayed. Red line, simulation; black line/ points, experimental data. (a) The first 1.5 ms of the experiment, starting at the moment of film rupture $t = 0$ ms. (b) During the steady-state regime (in the range 10 ms to 15 ms), with 200 experimental points reported on two acoustic periods $2T = 2/f_{\mathrm{ac}} = 0.064$ ms.

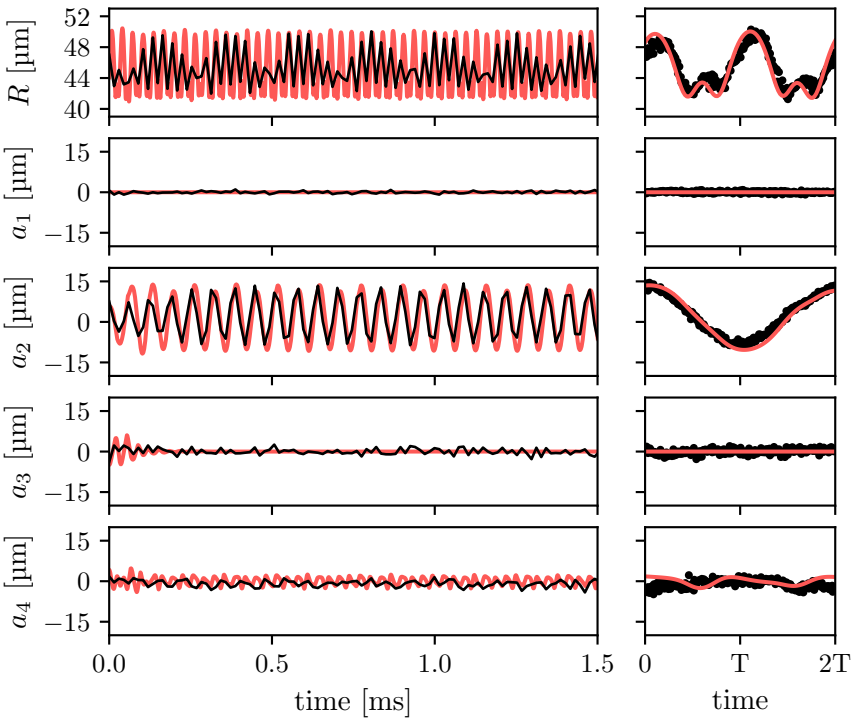

(a) first oscillations (b) steady-state

Figure 2.10: As for figure 2.9. This bubble (for parameters, see table 2.1(b)) shows dominant mode 2 oscillations in the steady-state regime, oscillating at half the driving frequency due to the first parametric resonance.

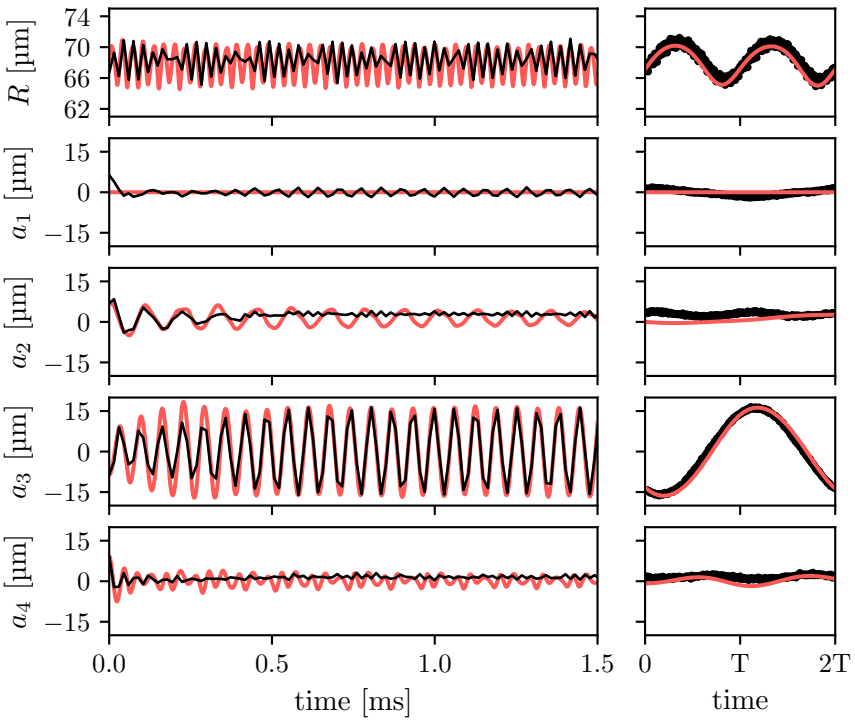

(a) first oscillations (b) steady-state

Figure 2.11: As for figure 2.9. This bubble (for parameters, see table 2.1(c)) shows dominant mode 3 oscillations in the steady-state regime, oscillating at half the driving frequency due to the first parametric resonance.

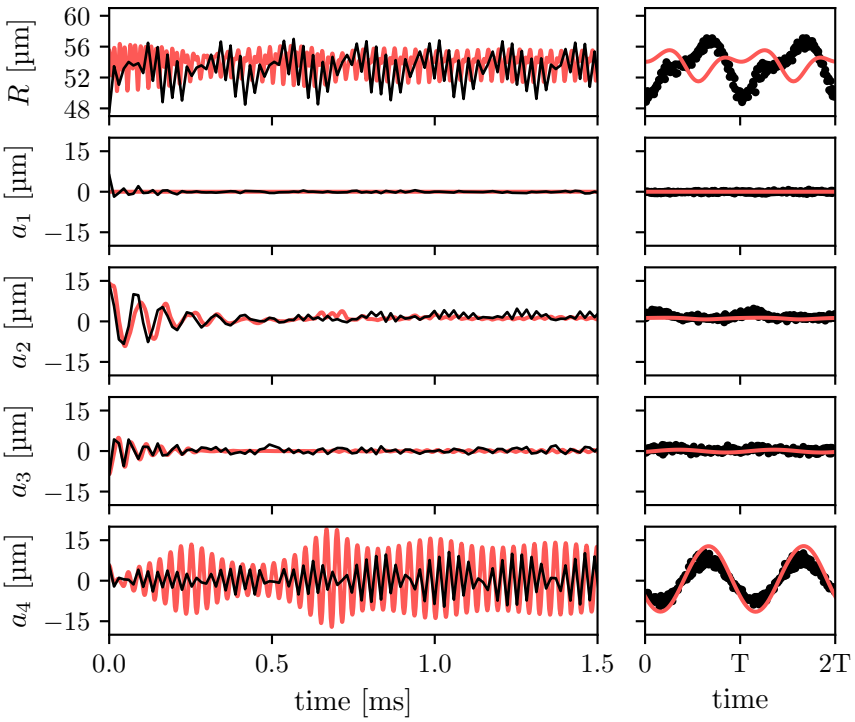

(a) first oscillations (b) steady-state

Figure 2.12: As for figure 2.9. This bubble (for parameters, see table 2.1(d)) shows dominant mode 4 oscillations in the steady-state regime, oscillating at the driving frequency due to the second parametric resonance. The phase difference between the experimental and numerical results of the radial mode $R(t)$ might be due to the fact that we are on either side of the resonance frequency of the second parametric resonance. A validation of this hypothesis was however not possible due to stability problems of the numerical model in this region. The limited stability also leads to the abnormal evolution of a_4 during the first millisecond of simulation. In fact, in order to obtain a stable simulation, it was done with a pressure of 8.0 kPa instead of the experimental 24.1 kPa. The numerical model clearly reaches its limits in the region around 52 µm, which also corresponds to half the resonant size of the radial mode.

at which the different modal amplitudes oscillate. It becomes obvious that the parametrically excited mode 2 (figure 2.10) and mode 3 (figure 2.11) are first parametric resonances and oscillate at half the driving frequency, whereas the parametrically excited mode 4 (figure 2.12) is a second parametric resonance which oscillates at the driving frequency. It is important to note that all modes reach a finite and constant modal amplitude which is important in view of the experiments of microstreaming. Modes that are not parametrically excited decay rapidly and in the here presented cases we do not observe any strong mode coupling. Furthermore, the radial mode is of course excited in all cases.

The red lines in figures 2.9 to 2.12 correspond to a numerical simulation done with Shaw's model (see section 1.5.3). For the simulation, the following initial conditions are used. A preliminary simulation of the spherical mode alone, using the experimentally obtained mean radius as approximation of the radius at rest R_0 and the acoustic pressure p_a, provides physically reasonable initial conditions for $R(t = 0\,\mu\text{s})$ and its derivative $\dot{R}(t = 0\,\mu\text{s})$. $a_1(t = 0\,\mu\text{s})$ is always assumed to be zero, and $a_2(t = 0\,\mu\text{s})$, $a_3(t = 0\,\mu\text{s})$, and $a_4(t = 0\,\mu\text{s})$ are taken from the experimental decomposition at the moment of film rupture. The shape modes are accounted for up to the fourth mode ($n = 4$) in the simulations. Fairly good agreement between experiments and theory can be observed in figures 2.9 to 2.12 including transient regimes with damped oscillations and steady-state regimes with finite-amplitude shape oscillations. Let me stress in particular that the modal amplitudes are the real physical amplitudes without need to normalize for good agreement. Furthermore the characteristic times are of the same order of magnitude. Consequently, this is a verification of the theoretical model including its real amplitudes by my experimental results. For future work, this allows to go one step further, so that we will be able to confidently use the model in order to predict nonspherical deformation amplitudes without need of an experiment for each single case.

A discordance between the experimental results and the numerical model can however be noticed for the parametrically excited mode 4 in figure 2.12. A probable explanation is that in addition to lying in the second parametric resonance area of the fourth shape mode, the bubble also comes closer to the second harmonic resonance of the spherical mode $R_{\text{res}}/2 \approx 52\,\mu\text{m}$. The considered radii and driving pressures lead us to infer that stronger nonlinearities in the bubble dynamics probably make the asymptotic character of the model reach its limits here. To obtain a stable numerical solution in this particular case, I had to adjust the acoustic pressure of the model to 8.0 kPa, instead of the experimentally obtained 24.1 kPa.

2.4.4 Inhibited coalescence

Before concluding the section about bubble coalescence it is worth evoking one other observation made during coalescence experiments, even though we have not exploited this for our further studies. As briefly reported in [OP4], not every encounter of two bubbles during our experiments leads to actual coalescence. In fact, in some cases bubbles would rebound repetitively, mostly at least a few hundred acoustic cycles up to tens of seconds. Three examples are shown in

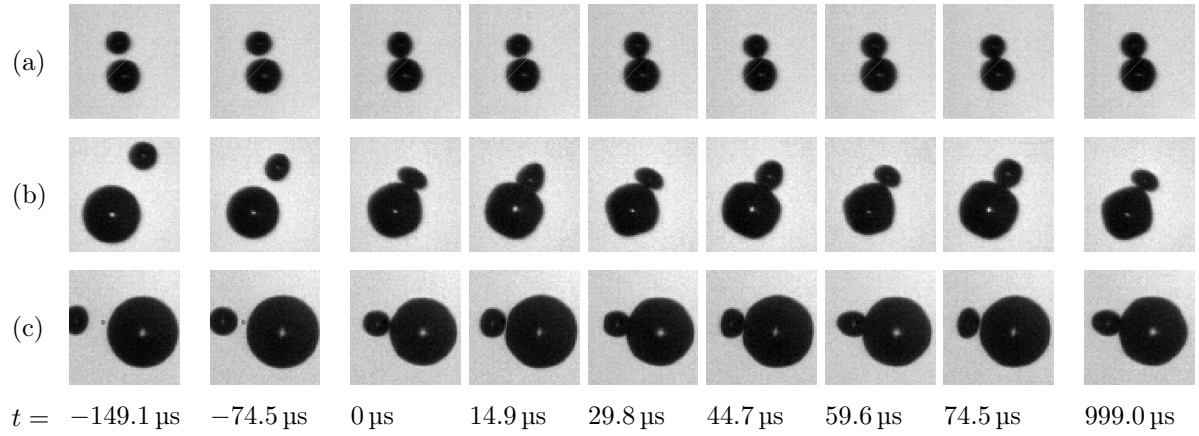

Figure 2.13: Three examples of inhibited bubbles coalescence. As before, the driving frequency is set to 31.25 kHz and the recordings are done at 67.065 kHz. All frames have a size of 260 µm × 260 µm. The acoustic pressure is respectively (a) 20 kPa, (b) 30 kPa and (c) 12 kPa.

figure 2.13. For each series, two snapshots during the approach are shown. Unlike for "real" coalescence, it is not possible to define the moment $t = 0\,\mu s$ as the moment of film rupture as there is none. Alternatively, I chose the first moment where the two bubbles touch. Each series then shows the first six consecutive snapshots starting with $t = 0\,\mu s$. The last snapshot is taken after about 1 ms to illustrate that the oscillations are stable much longer than just a few acoustic periods. In fact, they stay stable for even a much longer time, but for the cases (b) and (c) translational motion will eventually make them leave the chosen frame. Here, the translational motion is at least partly due to the more important inertia of the larger bubble compared to the smaller bubble. Another possible reason for translation of a pair of bubbles is self-propulsion [27].

It is also interesting to note that the example in figure 2.13 (a) shows purely spherical bubbles while in figure 2.13 (b) and (c) the bubbles show surface modes. The small newly nucleated bubbles have a size of $R_0 \approx 27\,\mu m$, the larger ones are (a) 37 µm, (b) 56 µm and (c) 79 µm large. Taking a look at the pressure-radius map makes it obvious that for case (a) at a relatively low pressure, both bubbles are below any pressure threshold. For the case (b), the observed mode 4 for the large bubble can be explained by the second parametric resonance. The mode 6 in case (c) can be explained when expanding a radius pressure map up to sixth mode: in fact, at the intersection between the first parametric modes 3 and 4 around 80 µm and above approximately 12 kPa the sixth mode is expected. At some point, the interaction between the two bubbles plays a role as well, in particular in cases (b) and (c). The mode 4 of the large bubble in figure 2.13 is for instance clearly deformed towards the small bubble and the small bubble itself is largely deformed in a kind of mode 2, which is not expected theoretically for a single bubble.

Possible reasons for the rebound

So far, I have only talked about the behavior of the pair of bubbles, but I have omitted the initial question. Why do the bubbles rebound and why do they not coalesce as the other ones do?

It has been discussed by other authors that coalescence can be inhibited if the approach velocity is too large. As has been explained for instance by Duineveld [33], intuitively the inertia of the two approaching bubbles becomes larger with a rising approach velocity. However, at the same time the pressure in the liquid film between the two bubbles becomes even larger and counteracts the motion. If the bubbles are stopped before film rupture, they will rebound rather then coalesce. To quantify this for hydrodynamic coalescence without sound, Chesters and Hofman [16] proposed the Weber number

$$\mathrm{We} = \frac{\rho_0 u^2 R_{\mathrm{eq}}}{\sigma} \ , \tag{2.4}$$

where u is the approach velocity, R_{eq} is the equivalent radius (for bubbles that are not exactly spherical), ρ_0 is the liquid density and σ the surface tension. Duineveld [33] finds experimentally a critical Weber number of about 0.18 separating coalescence from rebound for millimeter sized bubbles. When a sound field is applied to the bubbles, the situation changes because now the relative velocity between the bubble walls has to be considered. Different aspects of bouncing bubbles in an acoustic field have been studied by Duineveld [34], Postema et al. [97] and Jiao et al. [56, 57].

Concerning our experimental setup, it is difficult to correctly characterize the relative velocities between the two approaching bubbles. The spatial resolution but more importantly the temporal resolution is too low to obtain precise enough information on the velocity. By the way, as expected the Weber number calculated based on the bubble centers does not allow any conclusions. Therefore, we can unfortunately only report the appearance of bouncing but not validate its origin.

A second, less sophisticated hypothesis on the reason for bubble bouncing is the presence of dust or dirt particles on the bubble surface. Experimentally, bouncing has been observed much more frequently at some moments when the water had become “dirty” (e.g. through an open lid during experimental adjustments) and would usually stop when the tank was cleaned and the water changed. This is a personal opinion and we do not have any validating material. However, it does not seem unlikely, that a dust particle may act at the same time as a distance keeper and as a connecting link between the two bubbles.

2.5 Possible errors induced by the bubble orientation and post-processing

Naturally, our experimental procedure and post-processing may induce errors in the analysis of the bubble dynamics. Knowing and discussing such errors allows to avoid misleading interpret-

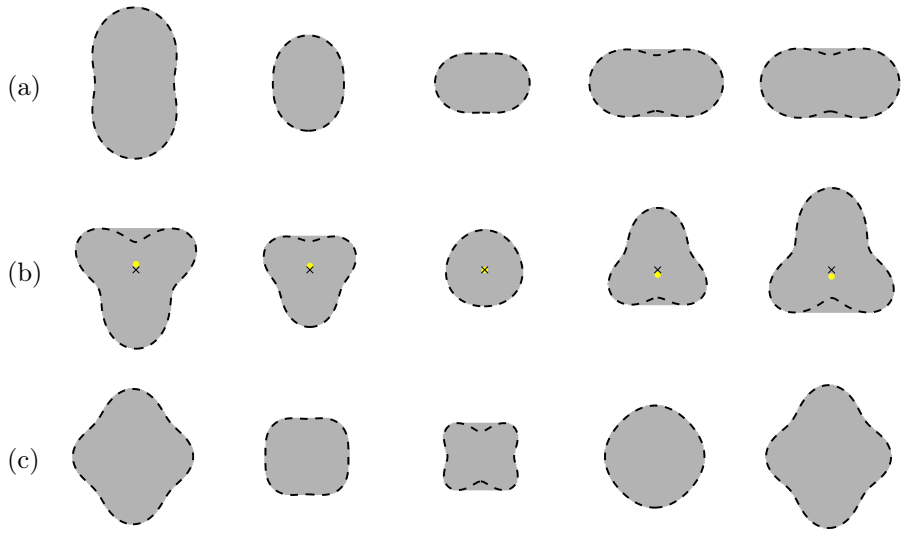

Figure 2.14: Comparison between the theoretical bubble shape (black dashed line) and the actual projection of a bubble (gray background) composed of a radial mode $R(t)$ and Legendre polynomials for (a) a mode 2, (b) a mode 3 and (c) a mode 4. As in the experiments, modes 2 and 3 are oscillating at half the driving frequency, while the radial mode and mode 4 are oscillating at the driving frequency. For the mode 3, the black $\times$ indicates the center of the displayed surface, the yellow $\circ$ the center of the corresponding volume.

ations. Even though I will not go into quantitative details, I want to discuss some aspects, in particular linked to the orientation of the bubble and the effects which occur during the projection of the 3D bubble on the 2D camera plane.

2.5.1 Numerical simulations

Projection of a 3D bubble in a 2D plane

Let us first take a look at a perfectly oriented bubble that is projected in a 2D plane. Three examples are given in figure 2.14. Even though the differences are rather small, it is obvious that the shape of the theoretical bubble contour (black dashed lines) and the projection (gray background) is not the same. Differences occur for instance for the last images in row (a), nearly any image in row (b) and the center image in row (c). Consequently, an error might occur in the post-processing when the decomposition in Legendre Polynomials (corresponding to the theoretical cut, see dashed black lines in figure 2.14) is applied on the projected shape (gray background). The result over two acoustic periods for the bubble in row (b) which is artificially oscillating on a mode 3 superposed with radial oscillations is shown in figure 2.15. As could be expected from the snapshots no big difference can be seen between the perfect shape (black continuous line) and the projection (red dashed line). Note also, that I purposely chose a rather large modal amplitude to make the effect visible, for smaller modal amplitudes the differences becomes obviously even smaller.

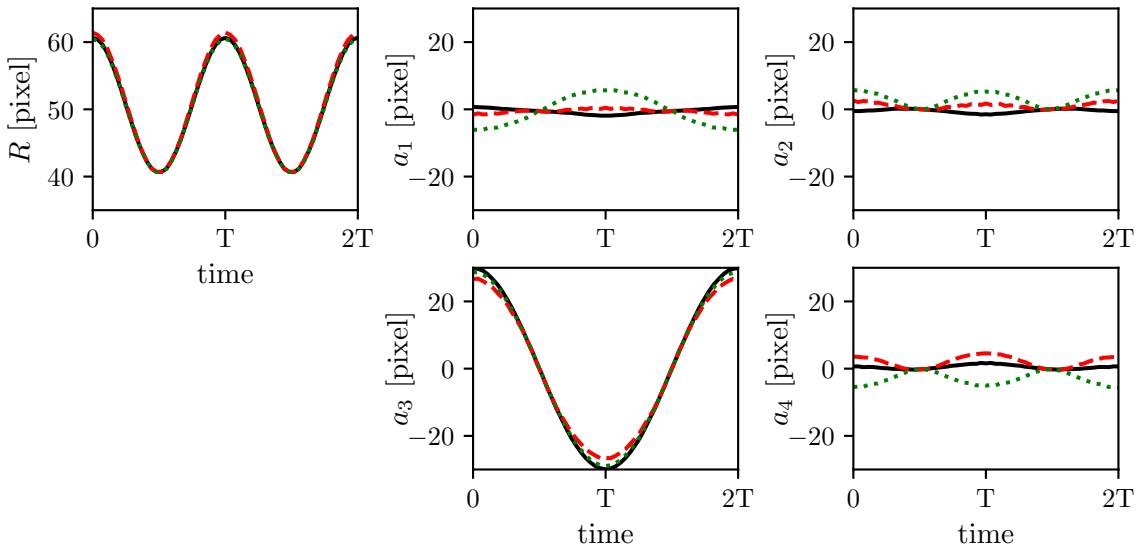

Figure 2.15: Modal decomposition of the bubble from figure 2.14 (b). The first four modal amplitudes are presented over two periods of oscillation T of the radial mode. Black continuous line, evaluation of the theoretical bubble shape; red dashed line, evaluation of the theoretical projection; green dotted line, evaluation of the projection when assuming the volume center as center of the projected shape.

For uneven modes such as the here presented mode 3, there is one further aspect to take into account. Due to its asymmetry, the center of the projected 2D area is not equal to the center of the corresponding 3D volume. The respective points are indicated in figure 2.14. The black cross corresponds to the center of the 2D projection, which by the way is basically the same as the center of the 2D Legendre polynomial. The yellow dot corresponds to the center of the 3D bubble volume. Conducting a modal decomposition while taking the volume center as origin leads to the green dotted lines in figure 2.15. We can see that this leads to the occurrence of a mode 1. Note that here, I defined a fixed center of the 2D projection. If in reality the volume center is fixed, the inverse effect appears when we do a 2D projection.

Wrong bubble orientation

In the previous section of the present chapter, I already stressed the fact that the bubble has to be correctly oriented. So let us see what happens theoretically if we post process a badly oriented bubble. In figure 2.16, the bubble is turned 20° into the paper sheet. We can observe that the corresponding modal decomposition underestimates the modal amplitude a_3 while a modal amplitude a_1 appears.

In conclusion, there are several factors that might induce error on the modal decomposition of the bubble shape. The largest influence can be observed for a mode 3. The combination of differences between projection and bubble center plus a slightly deviated axis of symmetry lead to a seeming appearance of a mode 1. For the coalescence experiments in section 2.4, I used a

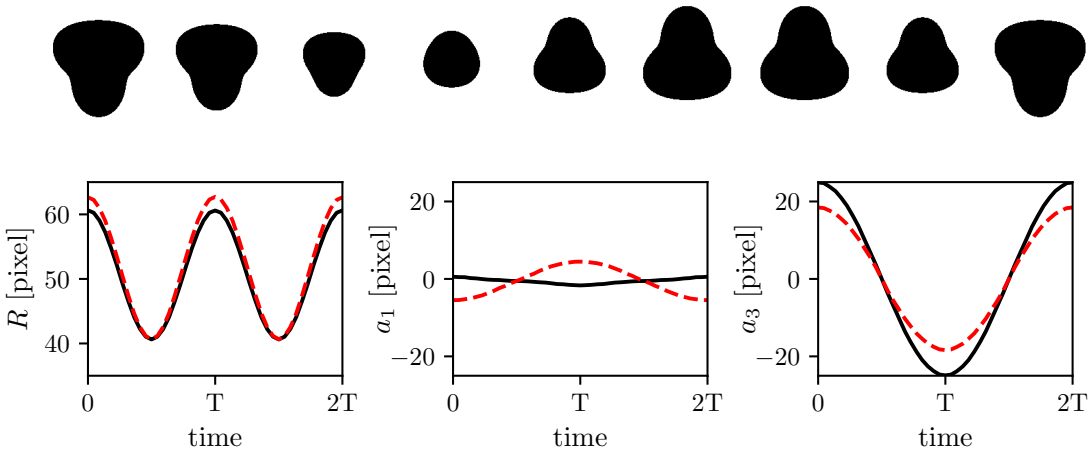

Figure 2.16: Simulation of a bubble oscillating on a mode 3 over tow acoustic periods T, the axis of symmetry is turned 20° into the paper sheet. *Above:* snapshot series of the numerically created projection; *below:* red dashed line, temporal modal decomposition of the here presented bubble; black continuous line, temporal modal decomposition of a correctly oriented bubble.

filtered bubble center and succeeded in extinguishing the mode 1. In terms of figure 2.15 this corresponds to the black continuous line.

2.5.2 Experimental observation with two cameras

In order to demonstrate the importance of the correct bubble orientation we have conducted measurement series with two cameras at the very beginning of my PhD work. The main contribution to the corresponding publication [OP8] has been done by Matthieu Guédra. Here, I want to draw attention to two important conclusions for the present manuscript. The first concerns the arbitrary orientation of the surface modes already mentioned in section 2.1 and stresses the reason for using bubble coalescence. The second and more important point in view of this section concerns the errors induced by a wrong orientation with respect to the observing camera.

The setup of the experiments is the same as in section 2.3, now using the two cameras. One single bubble was excited by a modulated pressure amplitude, see section 2.1. Consequently, surface modes were periodically excited.

Concerning the onset of surface modes and more specifically the corresponding axis of symmetry, we have observed that each time that surface modes are triggered with this method, the axis of symmetry has an arbitrary orientation. This is due to the lack of a supplementary condition which would lead to a preferential direction. As opposed to a traveling acoustic wave (e.g. [123]), the standing acoustic field does not have a preferential direction. Furthermore, our bubbles are too small to be affected by gravity [OP8]. And lastly, as we work with a free bubble, no close boundary could induce a supplementary condition. As a consequence and as already reported in section 2.1, the triggering of surface modes by exceeding the pressure threshold is not appropriate for the later study of microstreaming where we need to control the orientation of the bubble.

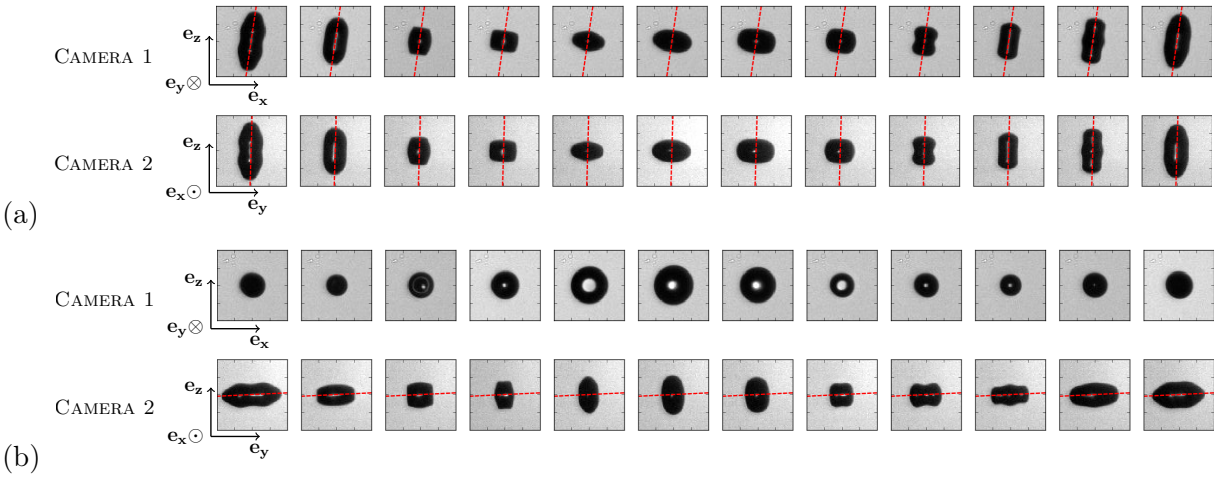

Figure 2.17: Two examples of bubbles recorded with two cameras; (a) the axis of symmetry equals the z-axis, the two cameras record the same information; (b) the axis of symmetry equals the y-axis, the camera 2 records the correct shape mode dynamics, while camera 1 records the oscillations of a seemingly spherical bubble.

Concerning the orientation with respect to the camera plane, I add two examples of our recordings, each time with two cameras filming at the same time, shown in figure 2.17. In both cases, a single bubble is oscillating with a predominant mode 2 showing a very large modal amplitude. In the first example, figure 2.17 (a), the axis of symmetry equals the z-axis which lies in the camera plane of both cameras, x-z for camera 1 and y-z for camera 2. Both cameras record essentially the same information, evidence of the earlier stated axial symmetry of the shape modes. Therefore, both recordings can be post processed to give a correct modal decomposition. In the second example, figure 2.17 (b), the axis of symmetry equals the y-axis. As a consequence, it lies only in the camera plane of camera 2, which again leads to a correct modal decomposition. The axis of symmetry is however perpendicular to the camera plane of camera 1. The resulting projection leads to a seemingly spherical bubble and the modal decomposition would evidently give a wrong result. These two examples put forward the importance for the axis of symmetry to lie in the plane of the camera, as other orientations will give faulty results. The examples here are extreme ones, more detailed information can be found in Guédra et al. [OP8].

2.6 Dynamics of a bubble attached to a wall

During my work, we were mainly interested in free bubbles far from any boundary because comparison to theory is much easier. In fact, as soon as a boundary is introduced, the mathematical description has to take into account the supplementary boundary condition at the contacting interface. Consequently, only few theoretical (e.g. [76]) and experimental attempts (e.g. [130]) to describe dynamics of bubbles attached to a wall can be found in literature. However, in real applications, bubbles will often stick to a solid boundary.

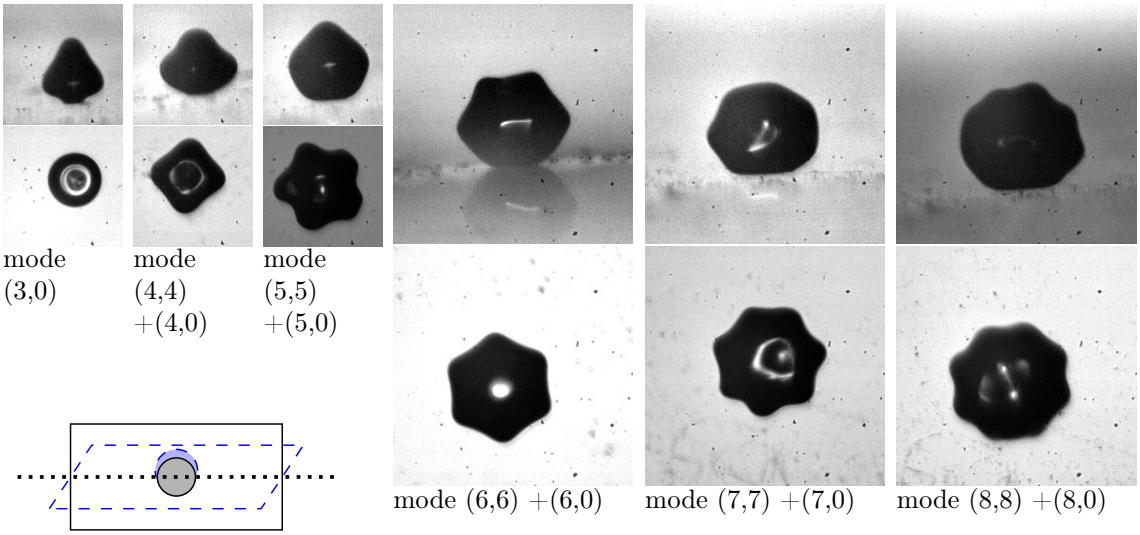

Figure 2.18: Six examples of bubbles attached to a wall and schematic presentation of the rotatable device allowing a side view *(top row of the snapshots)* and a top view *(bottom row)* on the bubble oscillations.

2.6.1 Preliminary theoretical considerations

In section 1.5.1 I have briefly introduced the possible shapes of nonspherical bubble oscillations. As explained, they are in general expressed by the spherical harmonics Y_{nm} and in the rest of this manuscript the simplification to zonal harmonics with $m = 0$ is assumed. In section 1.5.2 I have then introduced the pressure thresholds, which have to be exceeded in order to trigger surface modes. In fact, those thresholds depend only on the mode number n and are independent from m [101, 10]. For a free bubble, only the zonal harmonics are generally observed, but for bubbles attached to a wall this simplification is not the case and we expect to trigger other modes Y_{nm} for different m at the same threshold. The leading question is now which modes exactly occur in this case.

2.6.2 First experimental observations

I have conducted a measurement series consisting of two steps. The first step was a preliminary measurement series in Lyon, the second a more detailed one in Glasgow.

For the preliminary study I used a setup similar to the one in section 2.3 at 31.25 kHz driving frequency, but with the tank kept open. Instead of trapping laser induced bubbles inside the acoustic field, I now created bubbles via electrolysis and attached them to a thin microscope slide. The slide was mounted on a rotatable device, so that either side view or top view recordings could be done with a fixed camera. A schematic presentation of the rotation and six pairs of snapshots are shown in figure 2.18. A first view of the recordings shows that not only the zonal harmonics (Legendre polynomial from the side and spherical shape from above) but also sectoral modes (slightly flattened lens shape from the side and m lobes from above) appear. The

sectorial harmonics $n = m$ and the spherical harmonics $m = 0$ seem to dominate. But obviously some uncertainty remains due to the facts that the microscope slide with the attached bubble is rotated, that no very exact positioning can be guaranteed with this test-setup and that the snapshots are not taken at the same time.

The second, more detailed experimental series conducted in Glasgow aimed to overcome these difficulties and uncertainties. I used a very similar setup to the one for jetting, introduced in detail in appendix A.1. However, as opposed to the jetting experiments I did not use a capillary but rather a microscope slide. The experiments now could be filmed with two cameras in parallel. The different driving frequency of 200 kHz (as opposed to the 31.25 kHz driving in the preliminary experiments) lead to higher observed modes for similar size bubbles. The first purely qualitative observations seem to confirm the findings from the preliminary test, where the modes $(n, 0)$ and (n, n) tend to dominate. A thorough evaluation of the results is however not yet done due to time constraints.

2.7 Conclusions on nonspherical bubble dynamics

The aim of the present chapter was to understand how we can control nonspherical bubble oscillations in practice. Even though I have taken advantage of the general topic to address some wider aspects, the main objective of the chapter was to have a functional method for use in the microstreaming work. The most important conclusion is that bubble coalescence is suitable for our purpose. From theory, we can predict the bubble size and acoustic pressure at which a desired surface mode, let us say a mode 3, will appear. With bubble coalescence we can then create a bubble of the correct size. By furthermore controlling the direction of approach between the two bubbles, the axis of symmetry is defined. A convenient feature of this method is that the bubbles mostly oscillate in a steady-state regime. The mode 3 that we created will thus rest stable over a very long time, at least of the order of some seconds.

A second important result is the very satisfying comparison between the experimental results and the numerical implementation of Shaw's analytical model. A remarkable result is that both the transient time scales and the occurring modal amplitudes are in very good agreement and do not need to be normalized to fit. Reciprocally, this might allow in the future to predict surface modes by just providing bubble size and acoustic pressure without needing the experimental validation every time. Such an analytical approach has recently been done by Guédra and Inserra [48]. However as we have seen in figure 2.12, some care has to be taken in particular for bubbles close to resonances.

When discussing microstreaming in the following chapter, the respective bubble dynamics will play a role as well. The question will be, which surface modes induce which type of streaming. When answering these questions, we shall keep in mind that some errors or inaccuracies might occur during modal decomposition. I have mentioned some aspects in section 2.5. In particular the occurrence of a modal component mode 1 has to be questioned in the following.

I have discussed some other aspects in this chapter. Some of them, such as the inhibited coalescence or bubbles attached to a wall are out of scope for the present manuscript. They are however interesting aspects for future work. In particular the topic of bubbles attached to a wall deserves more attention. My experimental results obtained both in Lyon and in Glasgow should already bring some conclusions. Besides, M. Fauconnier, a PhD student supervised by C. Inserra, has initiated further work on this subject.

Chapter 3

Experimental microstreaming patterns

Now that we have achieved complete control over the bubble dynamics, we can dedicate ourselves to the question of microstreaming. The present chapter contains all experimental results, which are also reported in [OP2] for the most part. After an introduction of the experimental setup in section 3.1, I will briefly talk about the fact that no streaming occurs for purely spherical oscillations, see section 3.2. The essential part of the experimental observations is then reported in sections 3.3 and 3.4. Section 3.3 contains some complete characterizations of the microstreaming compared to the bubble dynamics, section 3.4 then classifies the complete variety of microstreaming patterns observed. The following section 3.5 includes our first interpretations based on the experimental observations, further conclusions will be drawn later in chapter 4 through comparison with the theoretical model. Lastly, in section 3.6, I include some supplementary interesting observations made during the experiments, among others a first try to observe streaming around a pair of bubbles.

3.1 Experimental setup to observe microstreaming

3.1.1 Experimental setup

A schematic drawing of the experimental setup for the visualization of microstreaming is given in figure 3.1. It is essentially based on the setup for coalescence, see figure 2.4, only adding a laser sheet and tracer particles for the flow visualization. We use a continuous wave laser source ($\lambda = 532\,\mathrm{nm}$, DPSS, CNI MLL-FN, 400 mW), and a laser sheet is then obtained by a cylindrical plano-concave lens ($f = 250\,\mathrm{mm}$). A cylindrical plano-convex lens ($f = -25.4\,\mathrm{mm}$) inserted just behind the first lens and oriented on the orthogonal axis is used to reduce the thickness of the laser sheet and obtain a beam waist estimated to about 250 µm.

Red fluorescent polymer microspheres (diameter 0.71 µm, Duke Scientific) are used to visualize the flow around the oscillating bubbles. The condition for inertial behavior of the particles

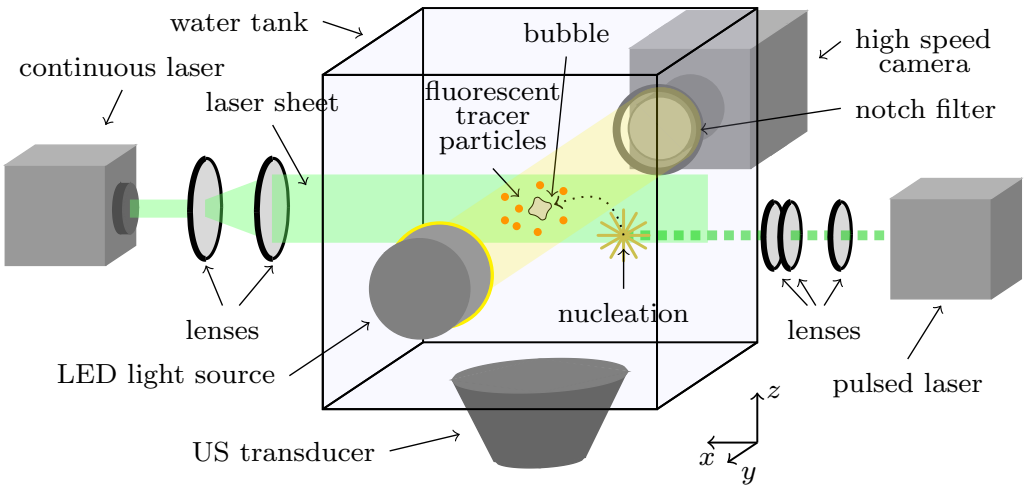

Figure 3.1: Experimental setup for the observation of microstreaming.

is fulfilled as the Stokes number St is much smaller than 1:

$$\mathrm{St} = \frac{\rho_p d_p v_{\max}}{18\mu} \approx 0.04 \ll 1 \tag{3.1}$$

with $\mu \approx 1\,\mathrm{mPa\,s}$ the liquid dynamic viscosity, $\rho_p \approx 10^3\,\mathrm{kg\,m^{-3}}$ the density of the particles, $d_p \approx 0.71\,\mu\mathrm{m}$ the diameter of the particles, and $v_{\max} \approx 2\,\mathrm{mm\,s^{-1}}$ the approximate maximum streaming velocity. In addition, the particles are small enough not to be influenced by the acoustic radiation force, since they are ten times smaller than the critical size estimated with

$$d_{p,\mathrm{crit}} = \sqrt{\frac{2\nu}{f_{\mathrm{ac}}}}\ , \tag{3.2}$$

with $\nu = \eta/\rho$ the kinematic viscosity. This estimation is based on the fact that the acoustic force on the particle has to be negligible with respect to the drag force. More detailed expressions of those considerations can be found for instance in Ahmed et al. [1] and Ben Haj Slama et al. [5].

When the fluorescent tracer particles are exposed to the laser light, they will emit light at a higher wavelength. By equipping the camera with a band reject filter (notch $532 \pm 12\,\mathrm{nm}$) corresponding to the laser wavelength, we will block out the direct laser light and only see the light emission by the tracer particles. The LED light source, which is necessary for the visualization of the bubble dynamics, is switched off during the recording of microstreaming. For the flow visualization, we use a frame size of 1024×768 pixels and frame rates typically ranging between 400 Hz and 600 Hz. The position of the continuous wave laser source including its lenses can be adjusted by a millimeter screw in order to precisely align the laser sheet with the bubble.

3.1.2 Experimental procedure

The experimental procedure that is conducted to obtain one streaming pattern with the associated temporal bubble dynamics includes three operating states:

1. the triggering of surface oscillations,
2. the visualization of the bubble dynamics and
3. the visualization of the microstreaming.

During experiments we switch rapidly between the different operating states, in particular between the two types of visualization. The experimental procedure for the triggering of surface oscillations is the method of bubble coalescence described in chapter 2, with in particular its experimental setup and procedure explained in section 2.3. Here as well, we nucleate a first bubble and trap it near the pressure antinode. By multiple coalescences we grow the bubble slightly below a critical size. If necessary, the position of the tank and of the focusing plane of the camera are adjusted. One further bubble is nucleated, which will trigger the surface oscillations. Once a steady-state regime is reached, we capture several sequences in the two operating states, visualization of the bubble dynamics and visualization of the microstreaming. Care is taken to rapidly switch between the operating states. A typical sequence is *dynamics (a) - streaming (ab) - dynamics (b) - streaming (bc) - dynamics (c)*. If the bubble dynamics is the same on recordings (a), (b) and (c), we can safely associate it with the obtained streaming pattern (ab) and (bc). A schematic presentation of the experimental procedure once surface modes are triggered is shown in figure 3.2.

3.1.3 Post-processing

The visualization and post-processing of the bubble dynamics have already been explained in section 2.3. Additionally, two types of post-processing for the microstreaming are conducted in the scope of this work, streak imaging and particle image velocimetry (PIV). Note that all images in this chapter are turned by 90° for a more convenient image format – we will see vertical shadows on many streaming patterns that are in reality horizontal ones. This has however no impact on the interpretation of the results.

Streak imaging

The purpose of the streak imaging is to visualize the streaming patterns qualitatively. All snapshots of one recording are superposed and for each pixel the maximum value is kept. In this way, the trajectories of the tracer particles become visible. As the flow is steady, trajectories, streaklines and streamlines coincide. The number of images superposed and the associated time will be specified in the respective examples.

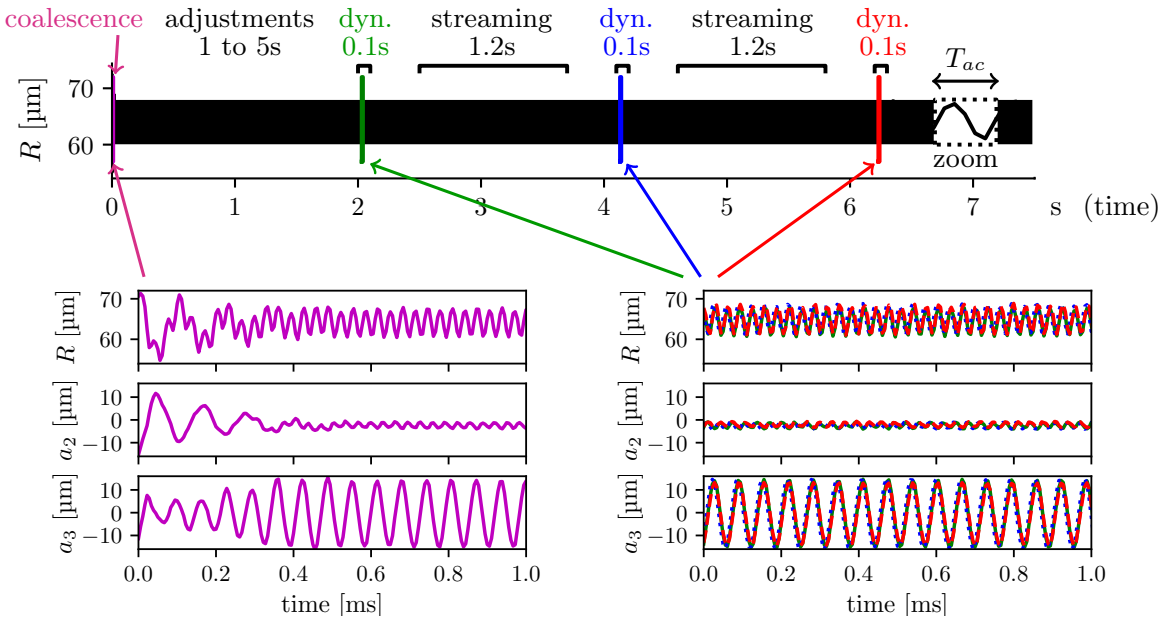

Figure 3.2: Schematic representations of the experimental procedure. As can be seen on the left zoom, the initial bubble shape caused by coalescence will lead to steady-state oscillations once the different modal components have decayed (here mode 2) or grown (here mode 3). After adjustments on the positions of camera and laser sheet, the measurement series begins, varying recordings of bubble dynamics (abbreviated by dyn. in the figure) and streaming.

Particle image velocimetry (PIV)

PIV is used to obtain quantitative information on the streaming velocities. The software DaVis® is used to extract a velocity vector field. Care has to be taken with the interpretation of the velocity data obtained for very small structures due to a limited number of tracer particles in these areas. Nevertheless, we choose to show PIV results in section 3.3 to give a rough indication of the occurring streaming velocities. The reader should keep in mind that the main aim of this work is not the discussion of streaming velocities but the overall characterization of different types of streaming patterns.

The most important aspects and parameters for the PIV post-processing are the following. In a first step, I define the region of interest, which means that I mask the bubble and the camera objective (see the black ring visible for instance in figure 3.3). Also, for more convenience, the bubble center is defined as the position $(0, 0)$. The velocity at every point in the image is obtained by correlating two snapshots and deducing the particle displacement in a known time span. For this, the field of view is divided into a certain number of interrogation windows. I use a round interrogation window with 50 % overlap. A first passage with 24 pixels window size and a second refined passage with 8 to 12 pixels window size allow the program to find one velocity vector for each interrogation window. Usually the therewith obtained vector field contains mostly correct estimations of the velocity, but oftentimes also some erroneous vectors. It is helpful to eliminate

these vectors, so that they do falsify the final result. This can be done with a supplementary post-processing step taking into account parameters such as *allowable vector range*, *maximum peak ratio* and *minimum number of vectors in a group* to give most reasonable results for every specific case. As our recordings have a rather low resolution, my aim is to only discard obviously wrong information while keeping as much useful data as possible. The above explained procedure is run for every time step, in other words for every pair of two consecutive snapshots. For a final result, I normally average the results obtained for 100 single correlations. Averaging over more images is possible, but flattens out the velocity field a little bit more. In fact, the PIV results are very sensitive to tiny variations in the bubble dynamics or position, which is not the case for the streak images.

With PIV, it is possible to obtain an Eulerian velocity field, because we consider specific interrogation windows. It would also possible to apply particle tracking velocimetry (PTV) and hence to obtain a Lagrangian velocity field by following the motion of single particles. As we will see during the discussion of the theoretical model in chapter 4, the difference between the two results are in practice rather small. The choice for PIV instead of PTV is mostly due to the relative large number of particles, which seemed easier to post-process with PIV.

3.2 No streaming without surface oscillations

Before talking about streaming around bubbles with surface modes, let me resume some observations which are useful as references. Here, it is important to correctly define what streaming is: a relatively slow mean flow induced by fast bubble oscillations (or by the here rather negligible attenuation of an acoustic wave). Fluid motion induced by other means is no microstreaming. For the following observations we start with measurements in a water filled tank, we add in a first step an ultrasound field and then a spherically oscillating bubble. The following observations result from these experiments [OP3].

1. In an empty water tank, we would expect to have no fluid motion. This is true in the ideal case. In reality however, there was often a slight parasite flow clearly visible, even though smaller than the actual microstreaming. The most probable source for this parasite flow are thermal effects, in particular due to heating by the laser sheet.

2. Upon turning on the ultrasound no supplementary effect is observed. We could expect to obtain acoustic streaming due to the attenuation of the sound wave in the water. However, for the present setup acoustic streaming is much less important than microstreaming and probably negligible compared to the parasite flow.

3. When adding a purely spherically oscillating bubble, there is still no streaming visible. Two examples, without and with parasite flow are shown in figure 3.3. We will see in chapter 4 that theory confirms that no streaming should be induced by pure spherical oscillations.

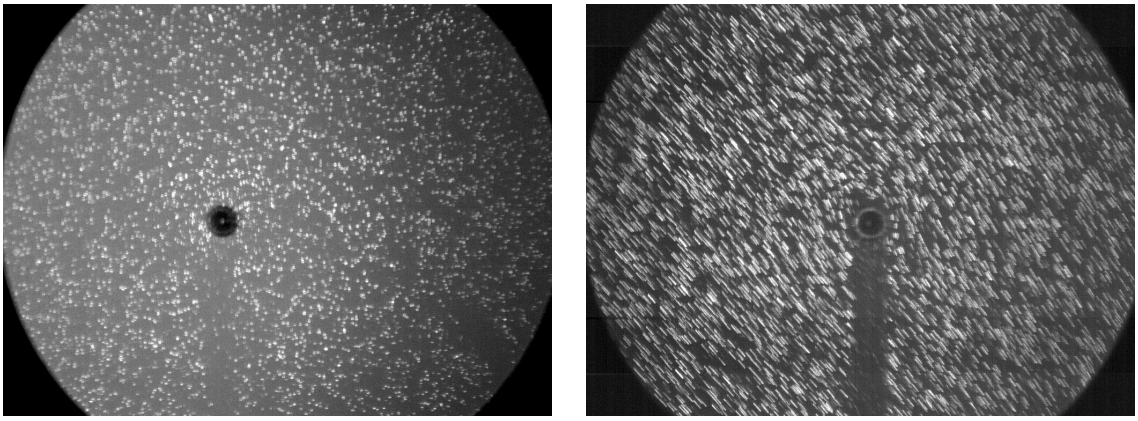

Figure 3.3: Fluorescent tracer particles around two bubbles oscillating in a purely spherical mode. Both images correspond to a superposition of 100 snapshots covering 0.25 s. *Left*: No motion of the tracer particles can be observed. *Right*: A parasite mean flow can be observed in the whole image. However, this flow is not linked to the bubble motion.

In conclusion, we do not observe any streaming induced by the ultrasound field or by a spherically oscillating bubble. It is also important to keep in mind that a parasite flow, probably due to thermal effects, might occur. This might explain why we sometimes observe streaming patterns deformed from perfect symmetry.

3.3 Joint observation of bubble dynamics and microstreaming

3.3.1 Overview

We conducted experiments for about a hundred bubbles. Each of them is oscillating predominantly either on a mode 2, mode 3 or mode 4. In figure 3.4 they are reported in a pressure-radius map. As in the map in figure 1.10 in section 1.5.2, the background indicates the theoretically unstable areas according to the model by Brenner, Lohse and Dupont [10]. The experimental results are indicated by the markers. Let me recall that the mode 2 and mode 3 presented on the map correspond to the first parametric resonance and the parametrically excited shape mode oscillates at half the driving frequency $f_{\mathrm{ac}}/2$. The here presented mode 4 corresponds to the second parametric resonance so that the parametrically excited shape mode oscillates at the driving frequency f_{ac}. We did not obtain any measurement points for the first parametric resonance of the mode 4 (obtained for bubble radii larger than 80 µm) as it was not possible to keep such a bubble stable for a sufficiently long time. A possible reason is that the first parametric resonance of the mode 4 is close to the resonance size $R_{\mathrm{res}} = 104\,\mu\mathrm{m}$. Another reason might be, that the pressure threshold is very low in this region and that the bubbles are consequently trapped at a low pressure. Slight instabilities of the bubble translation can therefore quickly lead to uncontrolled translational motion.

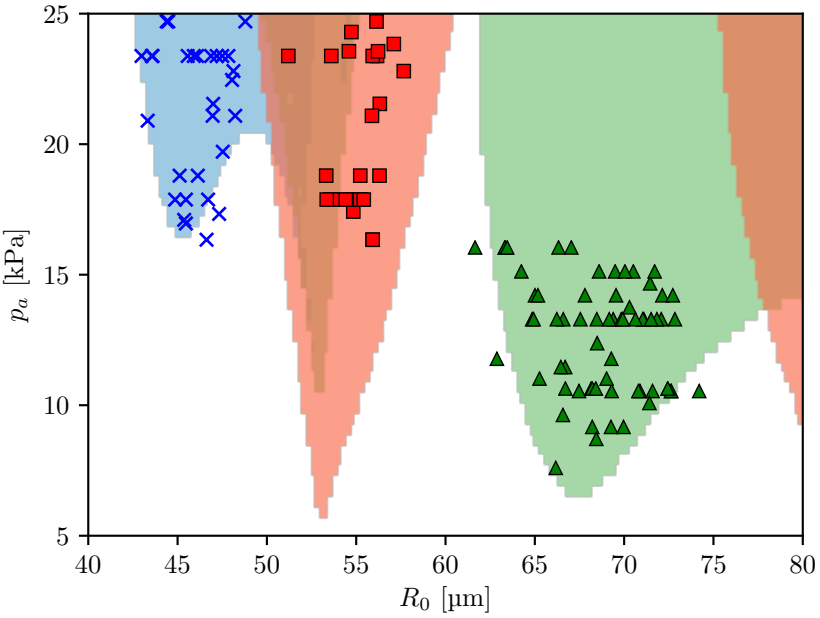

Figure 3.4: Pressure-radius map presenting experimental results classified according to the predominant mode of deformation (× – mode 2, △ – mode 3, □ – mode 4.) superimposed on numerically computed unstable areas (background colours: blue – mode 2, green – mode 3, red – mode 4).

3.3.2 Complete characterization for specific examples

As explained in the experimental procedure in section 3.1.2, we alternate measurements of microstreaming and bubble dynamics. If they are stable, we can associate the streaming pattern to the corresponding bubble dynamics. Three such examples are presented in figures 3.5 to 3.7 for a mode 2, 3 and 4 respectively. Each example contains a complete overview on the characterization of a bubble, including its dynamics (parts a, b and c) and streaming (parts d, e and f).

Figure parts (a) present a series of consecutive snapshots over two acoustic periods of the respective bubble. The modal decomposition over one millisecond is presented in parts (b). Let me recall that we restrict our analysis to the steady-state regime and that initial transient effects due to the coalescence process are no longer present. In parts (b) only 1 ms of signal out of 100 ms original recording length is shown. Furthermore, we only present the decomposition of the first eight surface modes which is sufficient to analyze surface oscillations possibly generated through nonlinear coupling. Similar information on the modal amplitude is presented in parts (c) where 500 measurement points covering 2.7 ms of signal are reported over two acoustic periods. Figure parts (d) are streak images where 700 snapshots covering 1.2 s are superposed to visualize the trajectories of the tracer particles. Parts (e) present the velocity distribution resulting from PIV. The average over 100 PIV-steps has been evaluated. Parts (f) show the absolute velocity in dependence of the radial coordinate r along the red line that is indicated in parts (e) and that

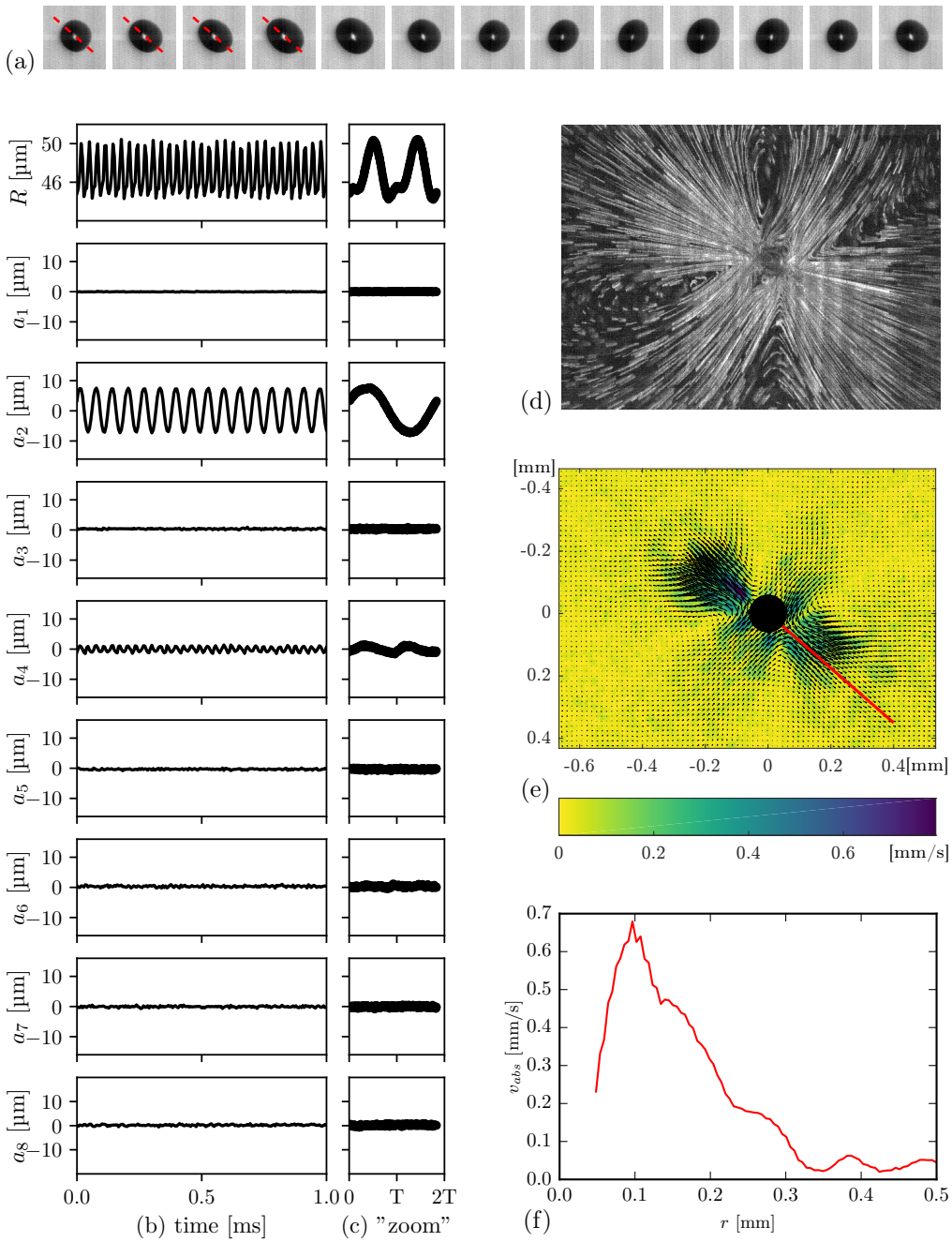

Figure 3.5: Characterisation of a bubble ($R_0 = 46.9\,\mu m$, $p_a = 20.6\,kPa$) oscillating predominantly on a surface mode 2 and its resulting streaming pattern: (a) consecutive snapshots over two acoustic periods $2T = 0.064\,ms$ recorded at 180 kHz (the axis of symmetry is indicated in the first screenshots, the image size is $180\,\mu m \times 180\,\mu m$); (b) modal decomposition of the bubble shape and (c) "zoom" on two acoustic periods (500 measurement points reported on $2T = 0.064\,ms$); (d) streak photography of the streaming pattern (700 images corresponding to 1.2 ms of signal, images size $1200\,\mu m \times 900\,\mu m$); (e) PIV of the streaming flow and (f) velocity profiles along the line indicated in (e).

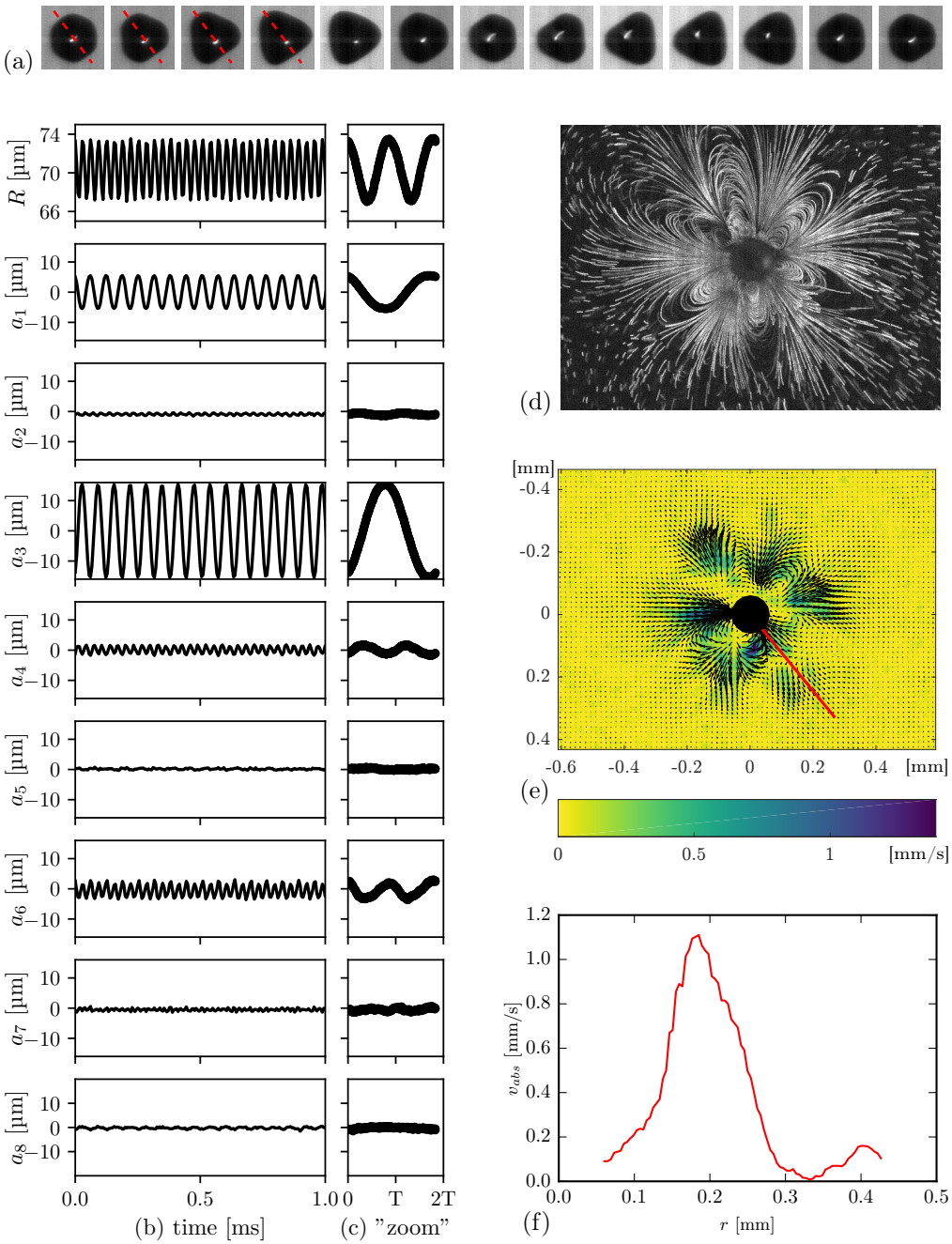

Figure 3.6: Characterisation of a bubble ($R_0 = 70.5\,\mu m$, $p_a = 12.8\,kPa$) oscillating predominantly on a surface mode 3 and its resulting streaming pattern: (a) consecutive snapshots over two acoustic periods $2T = 0.064\,ms$ recorded at 180 kHz (the axis of symmetry is indicated in the first screenshots, the image size is $180\,\mu m \times 180\,\mu m$); (b) modal decomposition of the bubble shape and (c) "zoom" on two acoustic periods (500 measurement points reported on $2T = 0.064\,ms$); (d) streak photography of the streaming pattern (700 images corresponding to 1.2 ms of signal, images size $1200\,\mu m \times 900\,\mu m$); (e) PIV of the streaming flow and (f) velocity profiles along the line indicated in (e).

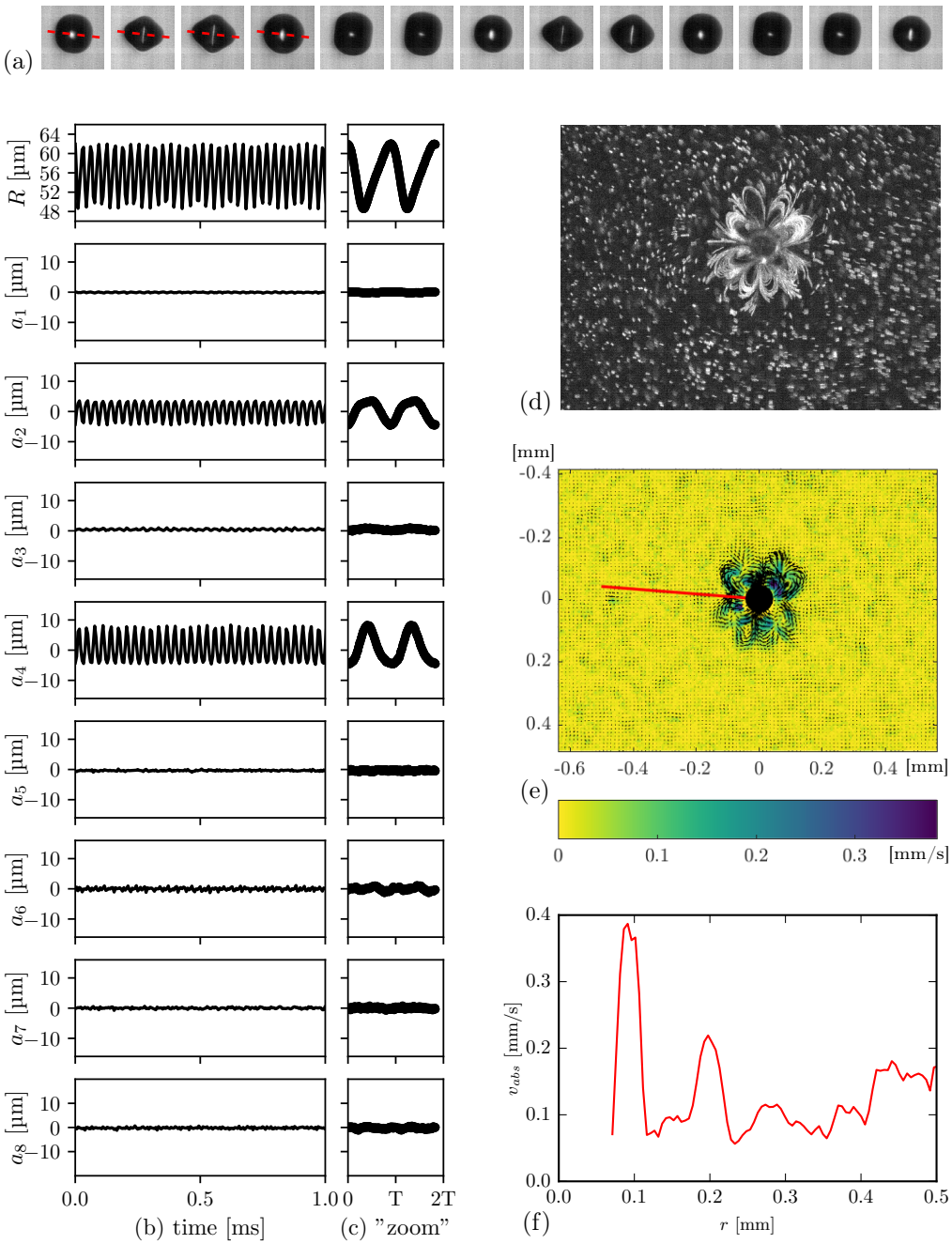

Figure 3.7: Characterisation of a bubble ($R_0 = 55.7\,\mu m$, $p_a = 23.6\,kPa$) oscillating predominantly on a surface mode 4 and its resulting streaming pattern: (a) consecutive snapshots over two acoustic periods $2T = 0.064\,ms$ recorded at 180 kHz (the axis of symmetry is indicated in the first screenshots, the image size is $180\,\mu m \times 180\,\mu m$); (b) modal decomposition of the bubble shape and (c) "zoom" on two acoustic periods (500 measurement points reported on $2T = 0.064\,ms$); (d) streak photography of the streaming pattern (700 images corresponding to 1.2 ms of signal, images size $1200\,\mu m \times 900\,\mu m$); (e) PIV of the streaming flow and (f) velocity profiles along the line indicated in (e).

is coinciding with the axis of symmetry.

Figure 3.5 presents experimental results obtained for a bubble of mean radius $R_0 = 46.9\,\mu\text{m}$ and pressure $p_a = 20.6\,\text{kPa}$, which is oscillating predominantly on a mode 2. The bubble dynamics shows the appearance of a radial component R, a large modal amplitude a_2 and a small modal amplitude a_4. The parametric excitation of the mode 2 is naturally expected as the applied acoustic pressure is higher than the pressure threshold $p_{2,\text{thresh}} = 17.5\,\text{kPa}$. The acoustic pressure is however below the pressure threshold of the mode 4 ($p_{4,\text{thresh}} = 44.1\,\text{kPa}$), so that the appearance of the mode 4 is evidence of nonlinear coupling. The streaming pattern in figure 3.5 (d) is a large cross-like structure with two pairs of small recirculation zones close to the bubble. The measured maximum absolute velocity is about $0.6\,\text{mm}\,\text{s}^{-1}$ on the axis of symmetry where the flow is flowing away from the bubble.

Figure 3.6 presents experimental results obtained for a bubble of mean radius $R_0 = 70.5\,\mu\text{m}$ and pressure $p_a = 12.8\,\text{kPa}$, which is oscillating predominantly on a mode 3. A large radial amplitude R and a large modal amplitude a_3 can be observed. As we have discussed earlier in section 2.5, the apparently large translational mode a_1 has to be considered with care. Furthermore, a modal amplitude a_6 is clearly visible, and small components of the modes a_2 and a_4 can be observed. The mode 3 is driven by parametric excitation ($p_{3,\text{thresh}} = 9.0\,\text{kPa}$), whereas the other modes appear due to nonlinear coupling (for instance $p_{6,\text{thresh}} = 39.5\,\text{kPa}$). The streaming pattern in figure 3.6 (d) consists of six lobes. Maximum velocities are about $1\,\text{mm}\,\text{s}^{-1}$.

Figure 3.7 presents experimental results obtained for a bubble of mean radius $R_0 = 55.7\,\mu\text{m}$ and pressure $p_a = 23.6\,\text{kPa}$, which is oscillating predominantly on a mode 4. The bubble dynamics shows a radial amplitude R, a modal amplitude a_4 and a slightly lower modal amplitude a_2. The mode 4 is naturally excited ($p_{4,\text{thresh}} = 11.0\,\text{kPa}$) whereas the acoustic pressure is below the threshold for the mode 2 ($p_{2,\text{thresh}} = 29.1\,\text{kPa}$). The streaming pattern shows eight small lobes of the size of the bubble diameter. The PIV analysis results in maximum velocities of about $0.4\,\text{mm}\,\text{s}^{-1}$.

The examples shown in figures 3.5 to 3.7 are rather complete characterizations of the bubbles containing all important information that we are able to extract from our recordings. They are representative for several findings. However, we have observed that the mode number is not the only parameter defining the shape of the streaming pattern. For this reason an extended comparison will follow in section 3.4.

3.4 Classification of observed streaming patterns

3.4.1 Extended characterization for the different modes

The streaming patterns shown in section 3.3 present one possible structure obtained for bubbles oscillating predominantly on a mode 2, 3 and 4 respectively. These are however not the unique possibilities and other streaming patterns can be observed. Therefore, this section contains an extensive set of observed streaming patterns in figures 3.8 to 3.10. Figure 3.8 contains two

different streaming patterns (a) and (b) for a bubble oscillating on a mode 2, figure 3.9 (a) to (d) shows four cases for a mode 3, and figure 3.10 (a) to (b) two cases for a mode 4. For each streaming pattern (x), the following information is presented. The bubble dynamics is presented schematically in subfigure (x1), and by one representative snapshot in (x2). A schematic drawing of the streamlines is given in (x3) and is representative of the streak photography in (x4). More information on the modal amplitudes is given in (x5) and (x6). Subfigure (x5) presents the modal amplitudes $\hat{a}_n = \max(|a_n(t)|)$ for the modes $n = 0, \ldots, 8$. Note that for the radial oscillation the value is obtained by first subtracting the mean radius R_0 so that $\hat{a}_0 = \max(|a_0(t) - R_0|)$. Subfigure (x6) presents the temporal evolution of some chosen modal amplitudes, less important modes are left out for more readability. Furthermore the graphs have been normalized so that the normalized temporal amplitude

$$\xi_n(t) = \frac{a_n(t) - R_0\delta_{n0}}{\hat{a}_n} \tag{3.3}$$

lies between -1 and 1. The Kronecker delta δ_{n0} is used here to subtract the radius at rest for the radial mode.

Figure 3.8 shows two characteristic streaming patterns for a bubble that is predominantly oscillating on a mode 2. Case 3.8 (a) shows a cross-like structure with two pairs of recirculation zones close to the bubble surface and symmetric with respect to the axis of symmetry of the shape deformation. This case corresponds to the pattern already presented in figure 3.5 in section 3.3. Case 3.8 (b) also shows a cross-like structure, but no small structures are visible. The main difference in the bubble dynamics between the two cases is that the modal amplitudes a_2 and a_4 are considerably larger for case 3.8 (b) than for case 3.8 (a). Taking into account all experimental results showing a mode 2, we observe that for the cross-like streaming pattern, case 3.8 (a), the modal amplitudes range between $3\,\mu\text{m} < a_2 < 6\,\mu\text{m}$ and $a_4 < 2\,\mu\text{m}$. Opposed to these values, the modal amplitudes for the cross-like streaming patterns without any visible substructures, case 3.8 (b), are larger and range between $10\,\mu\text{m} < a_2 < 13\,\mu\text{m}$ and $3\,\mu\text{m} < a_4 < 4\,\mu\text{m}$.

Figure 3.9 shows four characteristic streaming patterns for a bubble that is predominantly oscillating on a mode 3. Case 3.9 (a) shows a structure with six lobes. A similar pattern has already been presented in section 3.3 in figure 3.6. Case 3.9 (b) shows a structure with eight lobes. This kind of pattern is observed a large number of times. The 8 lobes may be arranged evenly around the circumference or irregularly as can be seen in the example presented here: the two lobes in the perpendicular direction of the axis of symmetry (on its right side) are very close to one another and could be described as one joint structure. Case 3.9 (c) shows a cross-like structure and finally case 3.9 (d) shows a cross-like structure with four round zones of recirculation, each in every corner of the cross and close to the bubble. The here presented cases show larger modal amplitudes for the cross-like structures, cases (c) and (d). This comparison of these four examples is however not representative for all experimental results as will be discussed in section 3.4.2. Besides the modal amplitude a_3 and the radial amplitude a_0, a strong modal

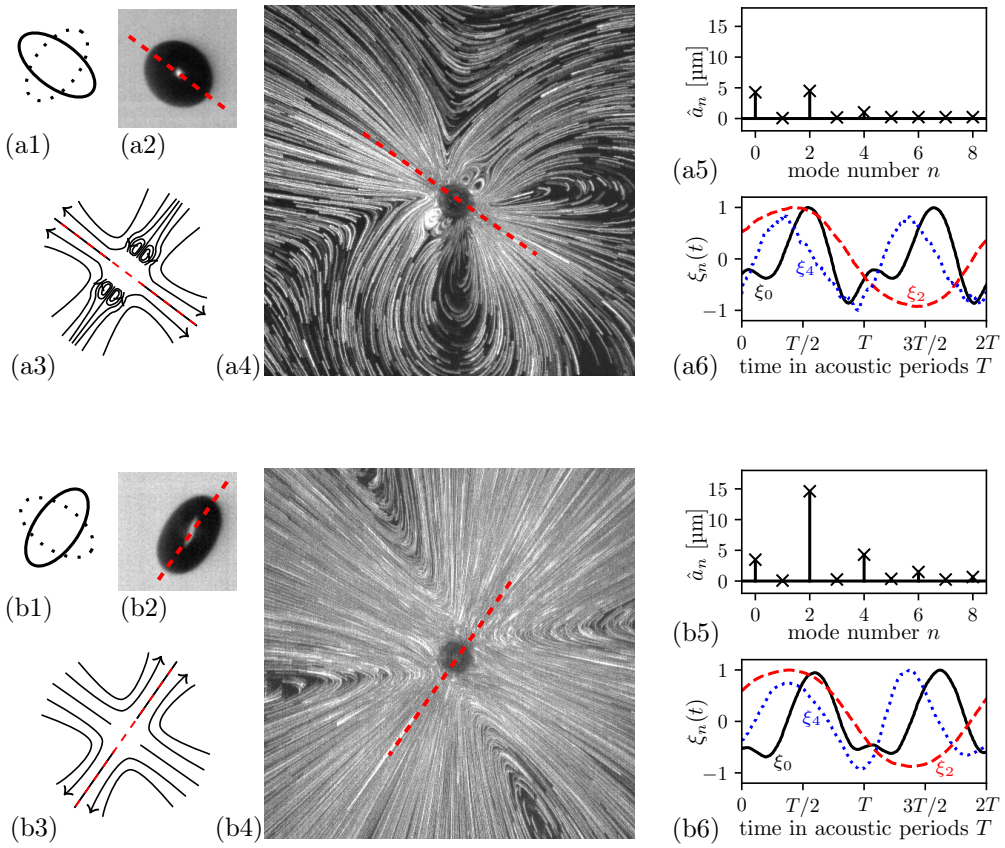

Figure 3.8: Presentation of two different streaming patterns observed for a bubble oscillating in a mode 2: *case (a)* – Cross-shaped pattern with four small lobes close to the bubble ($R_0 = 49.7\,\mu\text{m}$, $p_a = 34.5\,\text{kPa}$); *case (b)* – cross-shaped pattern without any lobes ($R_0 = 44.0\,\mu\text{m}$, $p_a = 23.4\,\text{kPa}$). For each case (x), the information is structured as follows. (x1) schematic drawing of the bubble dynamics, and (x2) representative snapshot of the dynamics (image size $180\,\mu\text{m} \times 180\,\mu\text{m}$); (x3) schematic drawing of the streaming patterns, and (x4) streak photography of the streaming pattern (image size $1\,\text{mm} \times 1\,\text{mm}$, 723 images corresponding to 1.2 ms of signal); (x5) maximum modal amplitudes; (x6) temporal evolution of: black line – ξ_0, red dashed line – ξ_2, and blue dotted line – ξ_4.

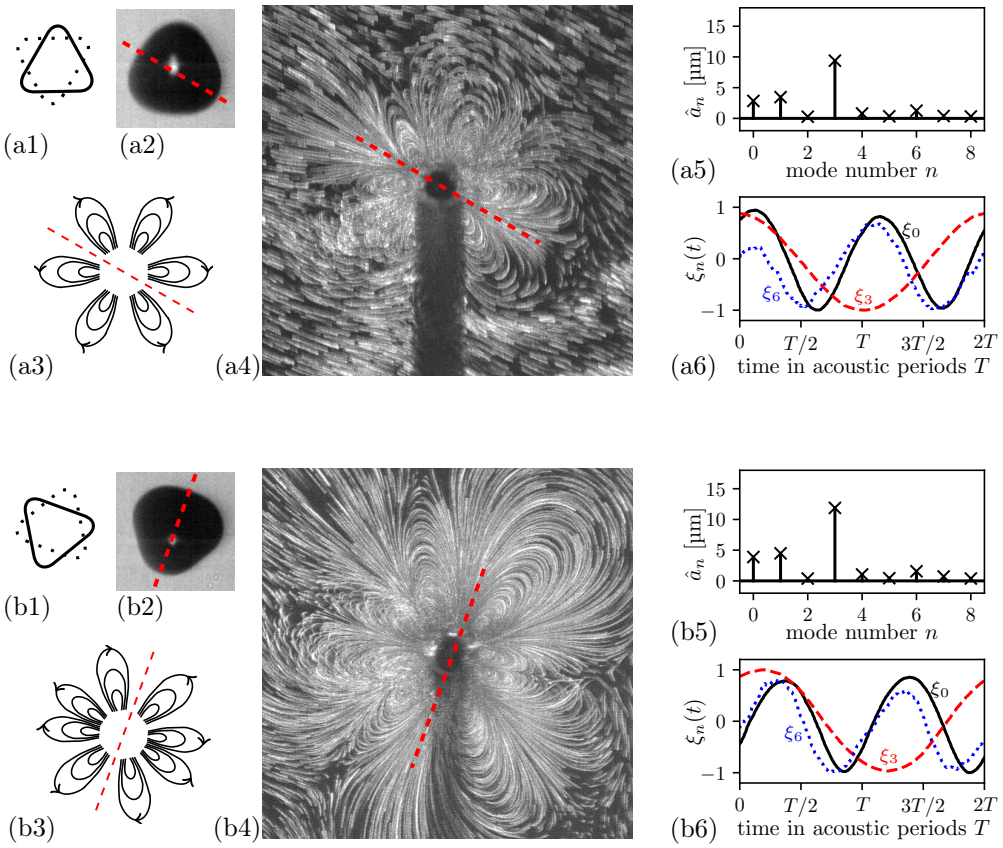

Figure 3.9: Presentation of four different streaming patterns observed for a bubble oscillating in a mode 3: *case (a)* – pattern with six lobes confined around the bubble ($R_0 = 70.8\,\mu m$, $p_a = 9.2\,kPa$); *case (b)* – pattern with eight lobes confined around the bubble ($R_0 = 70.1\,\mu m$, $p_a = 12.4\,kPa$); *case (c)* – cross-shaped pattern without any lobes ($R_0 = 65.7\,\mu m$, $p_a = 15.1\,kPa$); *case (d)* – cross-shaped pattern with four circular zones of recirculation ($R_0 = 68.6\,\mu m$, $p_a = 13.3\,kPa$). For each case (x), the information is structured as follows. (x1) schematic drawing of the bubble dynamics, and (x2) representative snapshot of the dynamics (image size $180\,\mu m \times 180\,\mu m$); (x3) schematic drawing of the streaming patterns, and (x4) streak photography of the streaming pattern (image size $1\,mm \times 1\,mm$, 723 images corresponding to 1.2 ms of signal); (x5) maximum modal amplitudes; (x6) temporal evolution of: black line – ξ_0, red dashed line – ξ_3, and blue dotted line – ξ_6.

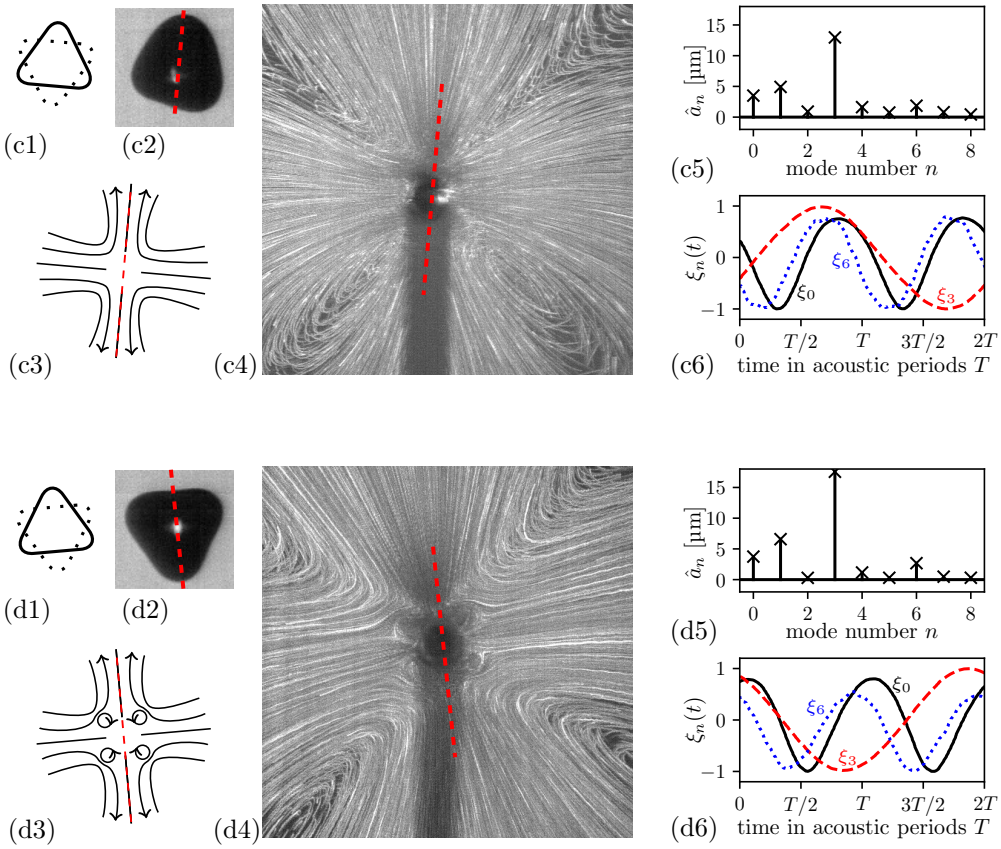

Figure 3.9 (cont.): See first part of figure for caption.

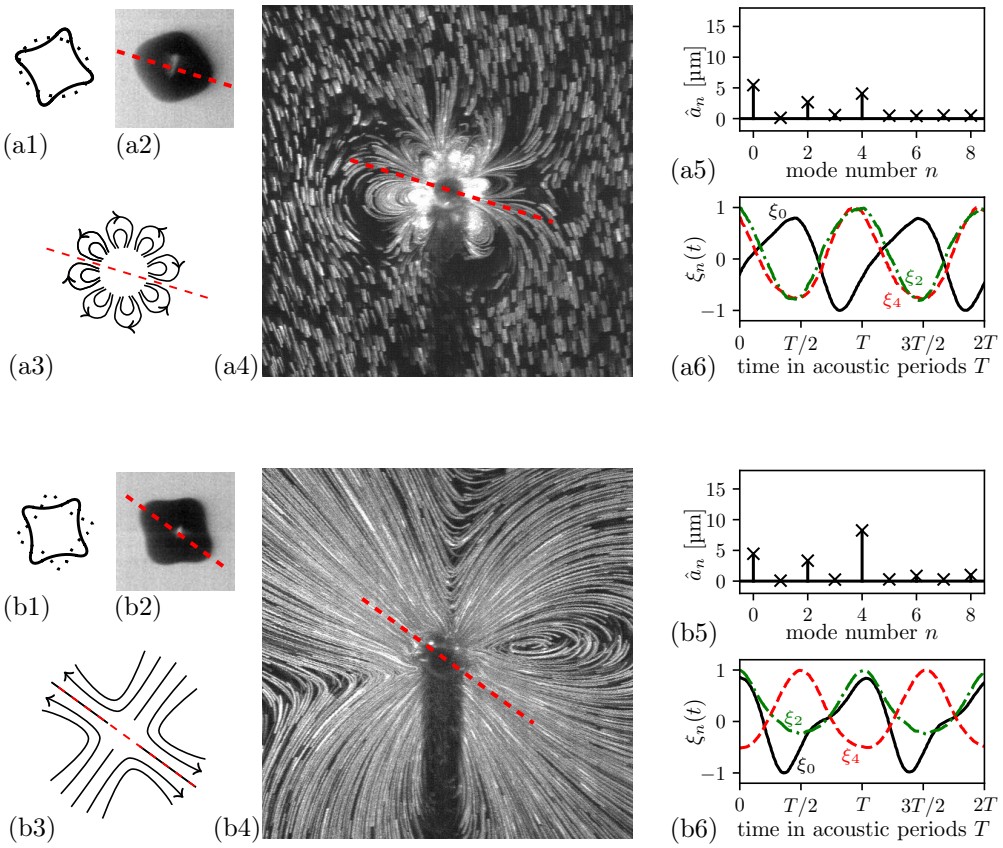

Figure 3.10: Presentation of two different streaming patterns observed for a bubble oscillating in a mode 4: *case (a)* – pattern with eight small lobes confined around the bubble ($R_0 = 56.5\,\mu\text{m}$, $p_a = 17.9\,\text{kPa}$); *case (b)* – cross-shaped pattern ($R_0 = 55.0\,\mu\text{m}$, $p_a = 17.9\,\text{kPa}$,); For each case (x), the information is structured as follows. (x1) schematic drawing of the bubble dynamics, and (x2) representative snapshot of the dynamics (image size $180\,\mu\text{m} \times 180\,\mu\text{m}$); (x3) schematic drawing of the streaming patterns, and (x4) streak photography of the streaming pattern (image size $1\,\text{mm} \times 1\,\text{mm}$, 723 images corresponding to 1.2 ms of signal); (x5) maximum modal amplitudes; (x6) temporal evolution of: black line – ξ_0, green dash-dotted line – ξ_2, and red dashed line – ξ_4.

amplitude a_1 is visible. The corresponding dimensionless variable ξ_1 is not presented in the temporal information in subfigures (x6), as it is always in approximate phase opposition to ξ_3. It has hence been left out for a better readability of (x6). Let us take one last look at the modal amplitude ξ_6 as it is oscillating at the same frequency as the radial mode and hence at the driving frequency. We will discuss the phase difference between these two modes, ξ_0 and ξ_6, in section 3.4.3.

Figure 3.10 shows two characteristic streaming patterns for a bubble that is predominantly oscillating in a mode 4. Case 3.10 (a) shows a structure with eight small lobes close to the bubble. The same case has already been presented in section section 3.3 in figure 3.7. Case 3.10 (b) is a cross-like structure. Generally, patterns with lobes, case (a), show smaller modal amplitudes ($3\,\mu\text{m} < a_4 < 8\,\mu\text{m}$, $a_2 < 4\,\mu\text{m}$) than the cross-like structures ($8\,\mu\text{m} < a_4 < 18\,\mu\text{m}$, $2\,\mu\text{m} < a_2 < 7\,\mu\text{m}$). The modal amplitude a_8 is generally small and is left out in (x6) for more readability. As the mode 4 is a second parametric resonance, it is oscillating at the driving frequency f_{ac}. The dimensionless variables $\xi_0(t)$, $\xi_2(t)$ and $\xi_4(t)$ are oscillating at the same frequency. In all cases, $\xi_0(t)$ and $\xi_4(t)$ are in approximate phase opposition. As $\xi_2(t)$ has been observed to oscillate either in phase with $\xi_0(t)$ or with $\xi_4(t)$ for both cross-like structures and structures with 8 lobes, no certain rule can be deduced for the phase of $\xi_2(t)$.

3.4.2 Classification and bubble size

Studying the patterns from section 3.4.1 one can remark that two classes of patterns appear. The first class gathers patterns that only consist of lobes around the bubble. The streamlines seem to start and end on the bubble surface. The second class gathers patterns that extend much further away from the bubble and have a cross-like structure. Some of these patterns show additional small zones of recirculation with closed streamlines. Table 3.1 gives an overview of this classification. Streaming patterns induced by bubbles with a predominant mode 2 all belong to the second class (large cross-like structure), while patterns induced by modes 3 and 4 can be found in both classes.

When reporting all measurement points into a pressure-radius map, figure 3.11, a clear distinction between the two classes of patterns becomes visible. For $n = 3$ and $n = 4$, the confined lobe patterns are always found for bubbles larger than the n^{th}-mode resonance size $R_{\text{res,n}}$, that is for frequencies below the n^{th}-mode resonance frequency. The large patterns are always found for bubbles smaller than the n^{th}-mode resonance size $R_{\text{res,n}}$, that is for frequencies above the n^{th}-mode resonance frequency. The vertical lines indicated for modes 3 and 4 match well with the respective minima of the pressure threshold deduced from stability analysis by Brenner, Lohse and Dupont [10] within the error margin on the bubble size. Furthermore, the line indicated for the mode 3 corresponds exactly to the third mode resonant radius calculated from first-order approximation analysis by Francescutto and Nabergoj [43]. Note that such a linearized theory is only valid in the vicinity of the first parametric resonance, a similar analysis thus cannot be applied to the mode 4 presented in figure 3.11.

Table 3.1: Definition of *large patterns* and *confined lobe patterns* as well as classification of the cases in figures 3.5 to 3.10.

	confined lobe patterns	**large patterns**
modes 2		figure 3.8 (a), figure 3.5
		figure 3.8 (b)
modes 3	figure 3.9 (a), figure 3.6	figure 3.9 (c)
	figure 3.9 (b)	figure 3.9 (d)
modes 4	figure 3.10 (a), figure 3.7	figure 3.10 (b)

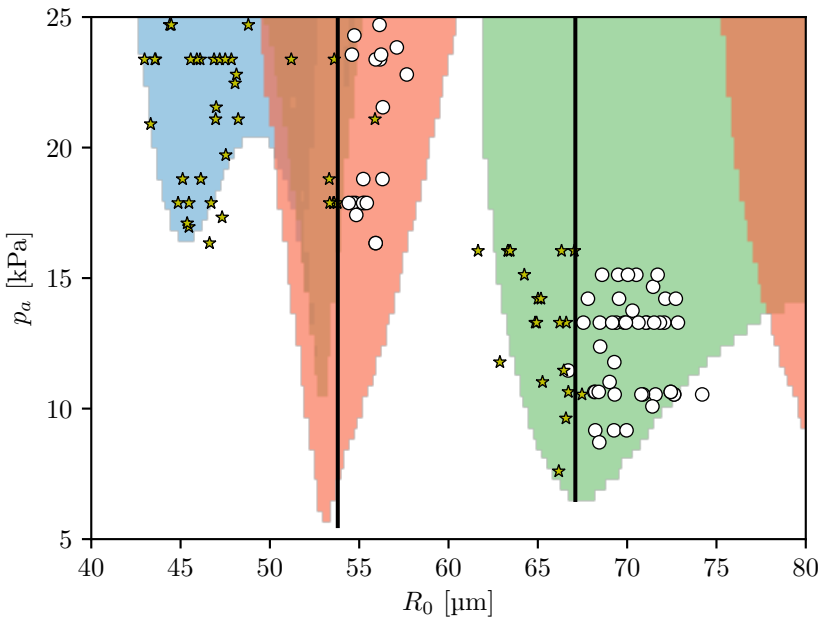

Figure 3.11: Pressure-radius map with all results separated in: ★ – large patterns; ○ – confined lobe patterns, (see table 3.1 for definition).

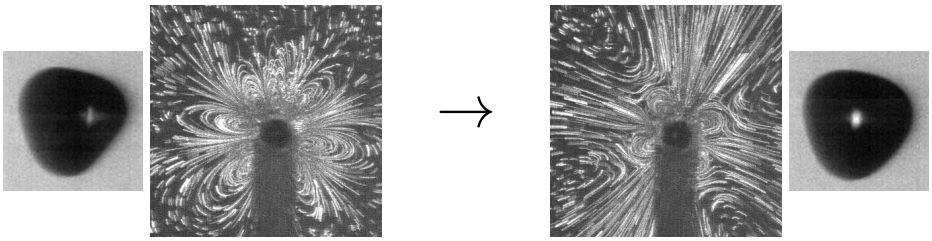

Figure 3.12: Example of one bubble whose pattern changes from a confined lobe pattern to a large pattern while the bubble is diminishing in size. Its radius diminishes from $R_0 = 69.3\,\mu m$ to $68.9\,\mu m$, which despite the larger error margin supports the tendency of a shrinking bubble.

Changing streaming pattern over time

Under some circumstances, it is possible to have a bubble shrinking or growing over time. In this case, it might change from above to below resonant size or inversely. We have observed this several times, when consecutive videos did not show the same streaming pattern. These cases were not included in the above examples, but they support the observation that a simple change in size leads to a variation of pattern. One example is shown in figure 3.12. The particularity here is, that the transition took place during the recording of the streaming. The beginning of the recording shows a lobe-like pattern while the end of the recording shows large pattern.

Transition between different patterns for one and the same bubble have already been observed by Elder [36] and more recently by Tho, Manasseh and Ooi [121] for substrate-attached bubbles. Whereas both studies put mode number variations forward to explain the changing patterns, the example presented by Tho, Manasseh and Ooi [121] also concerns a bubble growing over time.

3.4.3 Modal amplitudes and phase differences for mode 3 bubbles

Let us now focus on bubbles oscillating predominantly on a mode 3, because for these we have the largest number of examples for both lobe-shape and large patterns. As already shown in section 3.4.2, the two classes can be distinguished by the bubble size. In itself this is an interesting observation, but we can try to get more precise information by studying the bubble dynamics in more detail. Let us take a look at the modal amplitudes $\hat{a}_3$, $\hat{a}_0$ and $\hat{a}_6$ as well as the phase difference between modes. As we observe a mode 3, we could suppose that $\hat{a}_3$ plays the most important role in characterizing the bubble dynamics and we can trace the other parameters in relation to it. This is done in figure 3.13, where different markers correspond once again to the two classes, large and lobe-shaped patterns. It becomes obvious that there is a correlation between the different modal amplitudes, the larger $\hat{a}_3$ is, the larger $\hat{a}_0$ and $\hat{a}_6$ are as well. However, the markers for the large patterns and lobe-shaped patterns are confounded so that no distinction between the two classes can be made. On the other hand, when tracing the phase difference between the modal contents a_0 and a_6, a clear division into two parts becomes obvious. While lobe patterns range around zero phase difference, large patterns range around a phase difference

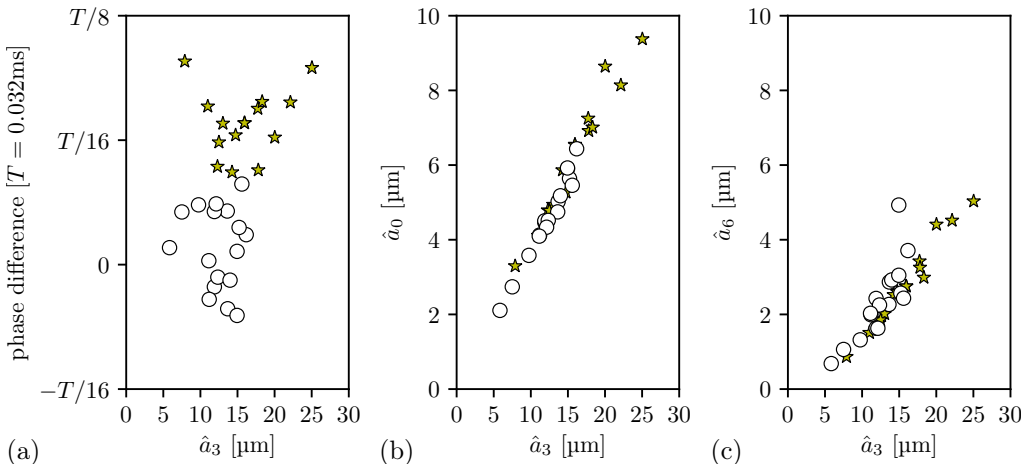

Figure 3.13: Study of amplitude and phasing for bubbles oscillating predominantly on a mode 3 and separated in large patterns – ★ and lobe pattern – ○. The x-axis of all three subplots is the maximum modal amplitude $\hat{a}_3$, the y-axis shows (a) the phase difference between a_0 and a_6, (b) the maximum modal amplitude $\hat{a}_0$ and (c) the maximum modal amplitude $\hat{a}_6$.

of $\pi/8$ or in terms of the acoustic period $T/16$. But why take the phase difference between the mode a_0 and a_6? In fact, the two are oscillating at the same frequency, f_{ac}, while a_3 is oscillating at $f_{\text{ac}}/2$. As we will see when discussing the theoretical model in chapter 4, a time-average between two (perfectly sinusoidal) components oscillating at different frequencies does not contribute to streaming and we have hence no interest to compare the modes a_3 and a_6 for example.

3.5 Interpretation of the experimental results

Before closing this experimental chapter and starting with the theoretical model in chapter 4, let us retake the experimental observations to establish some first conclusions and hypotheses on the physical parameters involved in the definition of the exact microstreaming pattern.

The three patterns presented in figures 3.5 to 3.7 are results that we might expect to observe when considering theoretical models [30, 75] which predict the generation of a $2n$-lobes structure from a shape mode n. Indeed we observe four small zones of recirculation for the mode 2, six lobes for the mode 3, and eight lobes for the mode 4. Even though the models contain simplifying assumptions such as small modal amplitudes, the qualitative agreement between experimental and theoretical observations suggests that the models can at least partly account for the observed patterns. They are however not adapted for an in-depth comparison as none of the models contains the complete set of experimental specifications such as phase shifts and interactions between several modes. A large number of these problems can be overcome with our own model in chapter 4.

For the classifications introduced in section 3.4, we have seen that the bubble size (below/above resonance of the respective shape mode) and phase differences play apparently an im-

portant role. Because the pattern transition occurs at the resonant radius of the shape mode n, intuitive thinking would link this behaviour to a phase shift on the nonspherical oscillation when passing through its modal resonance frequency. A close look at the differential equation ruling the dynamics for shape mode oscillation reveals that such a phase inversion does occur [48]. However, it must be recalled that no microstreaming should be generated from the interaction between two modes oscillating at different frequencies, namely, radial oscillations at the driving frequency and parametrically excited surface oscillations at half the driving frequency. (The calculation of microstreaming always involves time-averaging of the product of two modal components in question, if they oscillate at a different frequency the result is zero as we will see in chapter 4.) Other possible explanations are hence needed. In the following we discuss three of them.

3.5.1 Richer modal content and higher modal amplitudes

At first glance, the classification of the streaming patterns can be linked to the number of excited nonspherical modes and their respective modal amplitudes. Recent theoretical asymptotic developments on nonspherically oscillating bubbles [48] revealed that higher amplitudes and a richer modal content are expected for bubbles smaller than resonant size of a given shape mode. Such richer modal content might lead to a larger number of interactions that could possibly induce streaming. Indeed, this might apply for the examples of mode 4. This can however not be generalized for all studied cases. For bubbles with a predominant mode 3, the modal amplitude alone is not sufficient to explain the different classes of patterns (lobe patterns / large patterns) as can be seen in figure 3.13 (b) and (c).

3.5.2 Translational oscillation

Translational oscillation is known to create large-scale streaming patterns when interacting with radial motion [74]. Experimentally, radial motion is present for all bubbles due to acoustic field excitation. Translational motion a_1 is only observed for bubbles showing a predominant shape mode 3 (figures 3.6 and 3.9). For a mode 3, theoretical studies predict the appearance of all other modes including translational motion due to nonlinear effects [114]. However, the observed translation is not oscillating at the same frequency as the radial mode. It is oscillating at the same frequency as and in phase opposition to the parametically excited mode 3 and its presence is at least partly due to the post-processing, see section 2.5. As it would only be possible to partly correct for this, I prefer to present the unfiltered results here. Yet, large patterns are also observed for a mode 4, for which energy transfer to translational motion is not expected and not observed. Translational motion alone is hence no global explanation for the differentiation of the pattern types.

3.5.3 Phase differences

A good candidate to explain why bubbles larger than resonant size (for the corresponding surface mode) lead to lobe patterns and bubbles smaller than resonant size (for the corresponding surface mode) lead to large patterns is the phase difference between different modal components. The strongest modal components are in general those of modes 0 and n. However, as they do not always oscillate at the same frequency, secondary modes have to be considered as well. As presented in figure 3.13 (a), clear evidence is obtained for the phase difference between mode 0 and mode 6 from the present experimental results of a predominant mode 3. This observation cannot be further backed up by the data for predominant mode 4 bubbles due to difficulties in the correct definition of the phase delay. However, the importance of phase differences is also addressed in some theoretical studies, for instance for the radial mode and translation [74] or for nonspherical modes [117]. Understanding the impact of phase difference on microstreaming characteristics (patterns and velocities) requires to control this phase delay. This has scarcely been done in the past and will be of interest for further experimental investigations. Also, in the development of our numerical model, phase differences were one important factor to take into account.

3.6 Further observations on microstreaming

This section is dedicated to observations which do not yet lead to any coherent hypotheses but that are worth noting nonetheless. Section 3.6.1 reports on some additional streaming patterns but for not well controlled bubble dynamics, section 3.6.2 on patterns obtained in the attempt to create a mode 1 and section 3.6.3 shows some preliminary results obtained for the streaming around a pair of bubbles trapped close to one another.

3.6.1 Other streaming patterns for less well controlled bubbles

While it was mostly possible to keep full control of the bubble, in some cases the bubble would turn, grow or start to move. This manifests through a non-steady-state bubble dynamics and hence not useful streaming patterns in view of the above requirements. However, these cases lead to a couple of interesting patterns, some of which are shown in figure 3.14. The first three subfigures have in common that (nearly) all streamlines seem to leave the bubble surface in a straight line so that a kind of star-like pattern appears. In terms of conservation of mass, this cannot be possible for a bubble with zonal harmonics and an axis of symmetry in the camera plane. I suspect the bubbles therefore being turned so that we can see only the outflowing (e.g. figure 3.14 (a)) or the inflowing (e.g. figure 3.14 (c)) part of the global pattern. We cannot safely associate the streaming pattern to a bubble dynamics because the pattern does not even stay completely stable during one second, mostly due to some rotation of the pattern so that it becomes blurred.

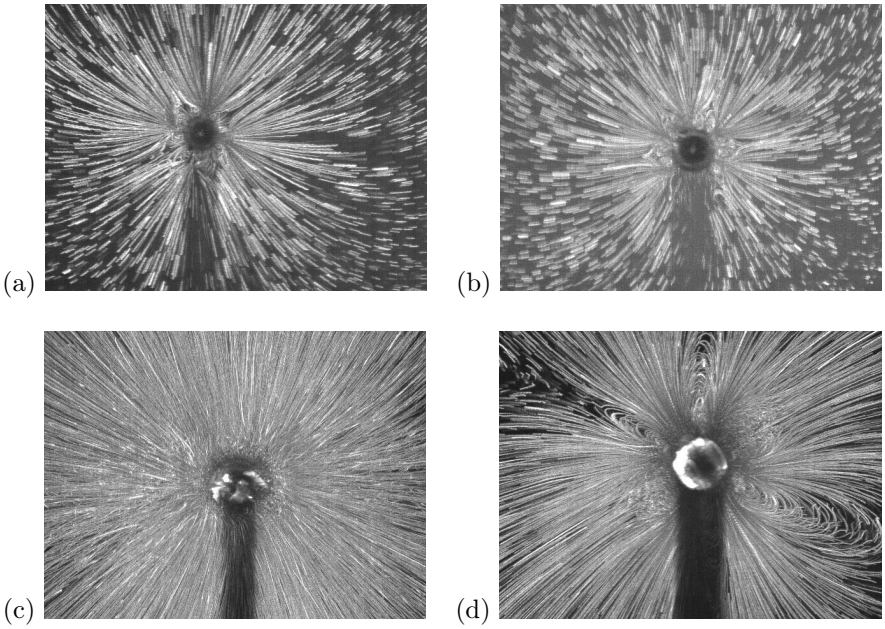

Figure 3.14: Streaming patterns for less well controlled bubbles. The frame size is 1200 µm × 900 µm for all subfigures; (a) approximately 0.2 s of streaming around a bubble oscillating on a mode 4, (b) approximately 0.1 s of streaming around a bubble probably oscillating on a mode 3, (c) approximately 1.2 s of streaming around a bubble oscillating on a mode 3 and (d) approximately 0.6 s of streaming around a bubble probably oscillating on a mode 3

However, for figure 3.14 (a) a mode 4 was observed before and after the streaming and the four times two small zones of recirculation support the fact of a mode 4. Furthermore, this kind of pattern was observed a few times. Figure 3.14 (b) on the other hand is a pure coincidence and only observed one single time. The dynamics just before showed a mode 3 and the number of six (times two?) zones of recirculation can be argued to correspond to this fact. I mainly include this case for the resemblance to figure 3.14 (a) just with another number of small structures. Figure 3.14 (c) was observed for a mode 3 dynamics before and after the streaming. This pattern was observed a couple of times. The last example, figure 3.14 (d) is included as it presents the interesting case of a large cross-like pattern that is superposed with a lobe-shaped pattern. The dynamics recorded before the streaming shows a mode 3, the bubble then became translationally unstable during the streaming recording.

3.6.2 Of the attempt to create mode 1 streaming

As most existing theoretical models include the case of radial plus translational oscillations it would be interesting to study this case experimentally. However, this is not possible with our experimental setup. As a test, I excited the bubble at a modulated frequency, three examples are shown in figure 3.15. The modulated frequency f_m was set so that the standard driving frequency f_{ac} would be a multiple of f_m. The different ratios for the examples shown in figure 3.15 are (a) $f_{ac}/f_m = 40$, (b) $f_{ac}/f_m = 2000$ and (c) $f_{ac}/f_m = 200$. Let me stress, that no surface modes

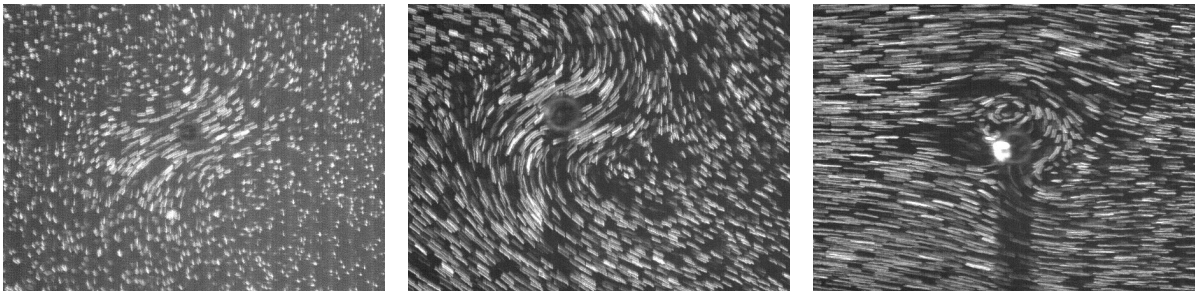

(a) (b) (c)

Figure 3.15: Fluid motion observed due to a bubble oscillating and at the time translating at a modulated frequency of (a) 781.25 Hz, (b) 15.625 Hz and (c) 156.125 Hz. The frame size is 1200 μm $\times$ 900 μm and the recording length 1.2 s for all subfigures.

are excited. As already mentioned earlier and explained in detail in chapter 4 we do not expect to obtain streaming if the radial mode and translational mode oscillate at different frequencies. It is however interesting to note that figure 3.15 (a) is not too different from the streaming pattern obtained by Longuet-Higgins [74] for the case of radial plus translational oscillations. I recall that the images are turned by 90° (see comment on page 67) and that the bubble translation is hence approximately from left to right. Figure 3.15 (b) shows a similar result superposed with some parasite flow. As opposed to the mode 0 alone in figure 3.3 the parasite flow does not just avoid the bubble. For the last example, figure 3.15 (c), no easy explanation is at hand, possibly the relatively strong parasite flow has the same order of magnitude as the bubble induced flow so that a zone of recirculation appears behind the bubble.

3.6.3 Streaming around a pair of bubbles

In real applications, bubbles will oftentimes appear in groups and not only as single bubbles. It is hence desirable to know how bubble dynamics and microstreaming change when bubble-bubble interaction has to be taken into account. As an intermediate step, we hence want to study the case of two bubbles. I supervised the Master project of E. Legrand whose objective was to do a feasibility study for microstreaming around a pair of bubbles.

Experimental setup

The experimental setup is similar to the one introduced in sections 2.3 and 3.1 with only two aspects modified: the creation of the bubbles and the ultrasound field used to trap them. Bubbles were injected through a thin capillary (TSP020375, internal diameter 20 µm) connected to a device allowing to control the air flow through the capillary (Elveflow). In this way, a chain of small bubbles could be created and then trapped by switching the ultrasound field on. A hole was drilled into the lid of the tank in order to partly submerge a second transducer, which was oscillating at 1 MHz. Its role is to trap the bubbles at multiples of half the relatively small wavelength of $\lambda = 1.5$ mm. The radial oscillations induced by the 1 MHz-transducer are so small

that they are not resolved on our recordings. The initial transducer oscillating at 31.25 kHz can be activated separately and is still used to excite bubble oscillations and to trigger surface modes. Note, however, that it is no longer possible to use the method of bubble coalescence to trigger surface modes, but that now the simple increase of the pressure amplitude beyond the pressure threshold is used. Consequently, the axis of symmetry is not defined as before through the impact between two bubbles. In fact, the observations suggest rather that the presence of the second bubble plays a role for the bubble orientation: the axis of symmetry seems to be equal to the connecting line between the two bubbles.

Some chosen results

In short, we managed to trap two bubbles close to each other, excite surface modes and observe streaming patterns. Four examples are gathered in figure 3.16. In all four cases, the bubbles are trapped at a distance of one wavelength of 1.5 mm. It is not possible to visualize the bubble dynamics as nicely as in the rest of this chapter as the main deformation seems to take place in the vertical plane. Deducing from the bubble sizes of the order of 100 µm and the dynamics visible on the videos, a mode 5 is possible. It is interesting to note that in figure 3.16 (a) the two bubbles oscillate in phase and point in the same direction, while in figure 3.16 (b) they point in the opposite direction. In the same way, the streaming pattern is pointing in the same and in opposite direction. Figure 3.16 (c) illustrates the case, where only one of the two bubbles is oscillating on a surface mode. The second bubble is simply an obstacle for the induced flow. An interesting but difficult to analyze case is shown in figure 3.16 (d). Very slight deformations and a motion of the white spot in the bubble center confirm the presence of surface modes. However, the question of which mode is able to induce the circular streaming pattern is still unanswered.

Perspectives

The feasibility study on microstreaming induced by a pair of bubbles was very successful and encourages ongoing experiments. Future work is planned to take place during the PhD-work of G. Regnault. Based on the conducted experiments some parameters are, however, to be optimized. For instance, so far we do not control the bubbles dynamics. It is either necessary to control the bubble oscillations or to understand the naturally induced ones. Other camera view planes and a higher spatial resolution are possible approaches. Furthermore, the method of trapping might be reviewed. So far it was not possible to trap bubbles at a distance of half a wavelength and to excite surface modes at the same time. On the one hand, at a relatively low pressure of the 1 MHz-transducer primary Bjerknes forces were not strong enough to inhibit bubble coalescence. On the other hand, at a relatively high pressure of the 1 MHz-transducer spontaneous acoustic cavitation would create hundreds of supplementary cavitation bubbles. Either an amelioration of the trapping or a completely different method such as optical trapping could be considered.

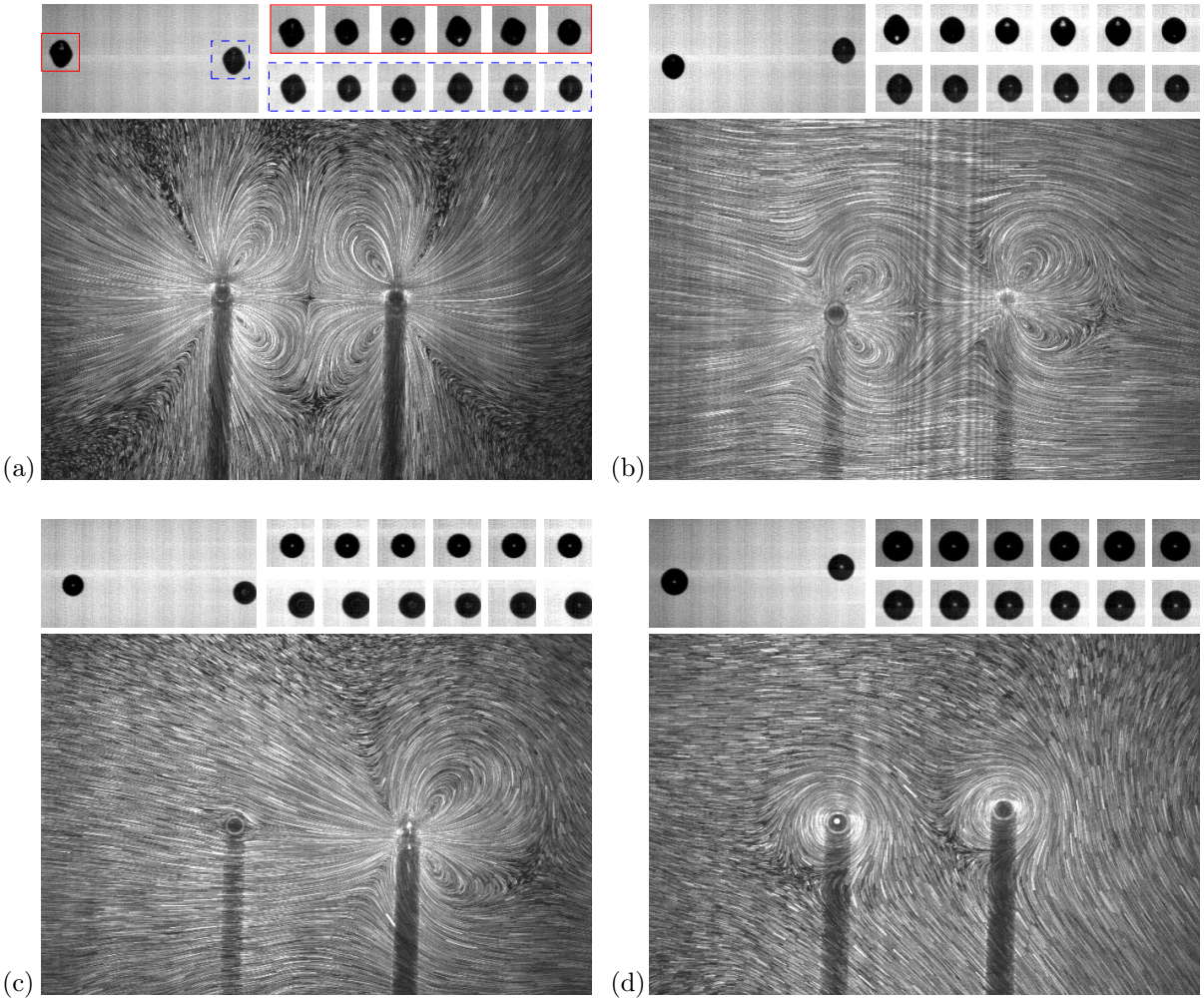

Figure 3.16: Four examples of microstreaming induced by a pair of bubbles. Bubbles are excited by a 31.25 kHz ultrasound field. The upper left frame of every example (1.9 mm × 0.96 mm) shows one snapshot during bubble dynamics, six consecutive zooms on the individual bubbles are added (frame size 0.38 mm × 0.38 mm, sampling frequency 120 kHz). The streak image showing the microstreaming pattern is composed of 700 frames covering about 1 s of signal, the shown frame size is 5 mm × 3.2 mm. Note that the distance between the two bubbles is approximately 1.5 mm corresponding to one wavelength of the 1 MHz transducer. (a) The main surface deformation seems to take place in the vertical plane not correctly resolved on the camera plane, the bubbles seem to oscillate in phase and in the same direction (both point upwards at the same time). (b) As case (a), the bubbles seem to oscillate in phase, but here in opposite direction (left one points upwards while right one points downwards). (c) Only the right bubble is oscillating on a surface mode similarly to the bubbles in cases (a) and (b), the left bubble is only oscillating radially. (d) A surface mode is present, recognizable by the slight shape deformation and the motion of the light dot in the bubble centers.

3.7 Conclusions on the experimental microstreaming results

The present work is the first detailed study on streaming patterns induced by a free, acoustically trapped bubble. We take advantage of the axisymmetry of surface modes to reduce our study to 2D observations. In addition to the pure observation of the streaming, we record the temporal bubble dynamics and are hence able to correlate the two piece of information. A large number of different types of streaming patterns was observed, but in particular a classification into two classes of patterns, lobe patterns and large patterns can be made. Bubbles oscillating predominantly on a mode 2 always lead to large scale patterns. For higher modes, large patterns appear for bubbles smaller than the resonant size of the respective mode, while lobe patterns appear for bubbles larger than resonant size.

The experimental observations allow first interpretations and hypotheses on the physical mechanisms involved in the definition of the different streaming patterns. A good candidate is the observed phase difference between two modes oscillating at the same frequency. Other parameters could be the richness of the modal content and maybe the presence of a translational mode (for a predominant mode 3).

Among the aspects that could be analyzed more closely in the future is notably a detailed experimental campaign on the microstreaming velocities. With the present setup we are able to resolve the streaming sufficiently to get rough ideas about the occurring velocities, the exact resolution of small structures is however difficult. So far we are limited in the zoom due to the photosensitivity of the camera. A stronger laser or an even thinner laser sheet might solve this problem. Furthermore, as already mentioned in the previous section, a complete study on streaming around a pair of bubbles is planned.

Chapter 4

Theoretical model for microstreaming

As written in the introduction, section 1.2, most analytical models for microstreaming include only the case of radial and translational motion. Models including surface modes were derived by Maksimov [75], Doinikov and Bouakaz [31] and Spelman and Lauga [117]. However, all of these models have disadvantages that make them not adapted for profound comparison with experimental data. The model derived by Maksimov [75] is an asymptotic solution generated by the parametrically excited shape mode $n \gg 1$. He further assumes that the amplitude of the shape mode is much larger than the one of the radial mode and hence dominant for the generation of streaming. His model is valid for micrometer sized bubbles at kHz excitation, but not micron-sized bubbles at high kHz or MHz frequencies. Doinikov and Bouakaz [31] and Spelman and Lauga [117] derive models that take into account all modes, but assume that all modes are oscillating at the same frequency. Parametrically excited shape modes are hence not directly accounted for. The model by Doinikov and Bouakaz [31] has the further disadvantage that it does not allow to separate the contributions of different modes and to use experimentally obtained modal amplitudes as input parameters. A further simplification applied by Maksimov [75] and Spelman and Lauga [117] is that they assume a radius much greater than the viscous penetration depth which leads to approximate calculations only valid up to leading order concerning this assumption.

The lack of existing analytical models readily available for direct comparison with our experimental results drove us to develop a new model. Even though I worked on the first, preliminary attempts, the final derivation was mostly done by A. Doinikov and C. Inserra. The implementation of the analytical expressions obtained was done in parallel by G. Regnault, A. Doinikov and myself with different solvers in order to provide redundant results for verification of the correct implementation. The main point of the derivation, its implementation for specific cases as well as some physical conclusions are submitted in [OP6, OP7]. Other specific cases are yet to be published and the last aspect, which is necessary to completely generalize the model, is still under progress.

In the following, I will first explain the general idea of the model in section 4.1 and present the derivation of the general theory in section 4.2, supplementary steps for the calculation are

included in appendix B. The theoretical model is validated through and compared to previous models in section 4.4, and to our experimental results in section 4.5.

4.1 General idea of the theoretical model

The analytical model provides solutions for microstreaming when the complex modal amplitudes of the bubble dynamics are given as input parameters.

No restrictions are imposed on the thickness of the viscous boundary layer with respect to the bubble radius. However, we have to include the simplification that the complex modal amplitude is small compared to the bubble radius at rest, $|s_n|/R_0 \ll 1$. With the present theory, it is possible to calculate the streaming induced by the interaction between two modes oscillating at the same frequency. If more components are present, we can superpose the final pattern from several ones. As it is not obvious to find a general solution, we develop the calculation for several specific cases, starting with the case $0-m$, then $1-1$, $1-m$ and finally $n-n$. The very general case $n-m$ is yet under progress, the main difficulty lies in finding appropriate functions which solve the system.

How does streaming work?

Streaming is due to second (or higher) order effects in the fluid motion. In our case, we limit the model to second-order streaming. Furthermore, streaming is a time-averaged information. In general, authors of streaming models first calculate the first-order time-dependent velocity (or a related quantity) and then, in a second step, the time-averaged second-order streaming velocity. The starting equations are the continuity equations and the Navier-Stokes-equation. Furthermore, boundary conditions have to be taken into account. For our gas bubbles in water these conformity of the normal velocity (that means that the liquid velocity on/very close to the bubble surface is equal to the normal velocity of the bubble surface) and zero tangential stress on the bubble surface for first- and second-order, as well as zero velocity at infinity for second-order calculation. For the here presented model, the somewhat more detailed steps are:

1. First-order solution: time-dependent velocity field.
   (a) Introduce the equation of continuity and the Navier-Stokes equation at first order.
   (b) Define the time-dependent velocity $\boldsymbol{v}$ by its scalar and vector potentials φ and $\boldsymbol{\psi}$.
   (c) Introduce a possible solution for the velocity potential including unknown constants to be found.
   (d) Define the unknown constants by applying the boundary conditions on the bubble surface (conformity of the normal velocity and zero tangential stress).
2. Second-order solution: streaming velocity.

(a) Introduce the time-averaged second-order equation of continuity and Navier-Stokes equation.

(b) Define the (time-averaged) streaming velocity $\boldsymbol{V}$ by its vector potential $\boldsymbol{\Psi}$.

(c) Possibly simplify the resulting equation for specific cases.

(d) Introduce a possible solution for the velocity potential including unknown constants to be found. This leads to one (or more) inhomogeneous differential equation(s) to be solved.

(e) Method of variation of parameters: first solve the homogeneous differential equation and then inject the solution into the inhomogeneous equation, treating all constant parameters of the solution as functions. The resulting system of equations can be solved nearly completely, however four unknown constants per differential equation remain.

(f) Apply the boundary conditions at infinity (zero velocity) to obtain expressions for half of the unknowns.

(g) For the rest of the unknowns, the boundary conditions at the bubble surface (zero normal velocity and zero tangential stress) have to be applied. At second order, this has to be done in Lagrangian reference, as being much easier than in Eularian coordinates. The Lagrangian streaming velocity is defined by $\boldsymbol{V}_L = \boldsymbol{V} + \boldsymbol{V}_S$, where $\boldsymbol{V}$ is the earlier calculated Eularian streaming velocity and $\boldsymbol{V}_S$ the Stokes drift.

The step 1 and the substeps 2 (a) and 2 (b) can be carried out once for all cases. This will be done in section 4.2. The steps 2 (b) to 2 (g) depend on the specific case. Their complexity varies largely with the number of simplifications for the given case. This will be discussed in more detail in section 4.3.

One common point for all specific cases is the general appearance of the analytical solution of the streaming field. As the bubble surface is ruled by Legendre polynomials and as we have a radial problem, the streaming field will be ruled by θ-dependent Legendre polynomials and Associated Legendre polynomials as well as by r-dependent Hankel functions. We will use polar coordinates to handle our problem, a schematic representation is given in figure 4.1. As we will see later, streaming amplitudes depend among others on the modal amplitudes but also on phase differences between the two modes taken into account.

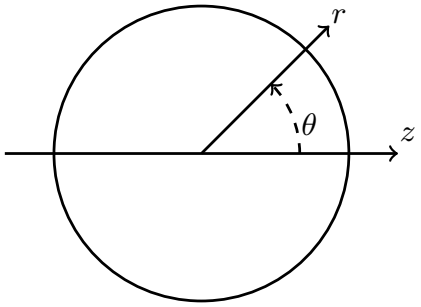

Figure 4.1: Schematic representation of the geometry under study. We use the polar coordinates r and θ. Furthermore, z indicates the axis of symmetry.

4.2 General theory

4.2.1 First-order solution: time dependent velocity field

Our first objective is to find a first-order solution, that means to find the instantaneous first-order velocities induced by the oscillating bubble.

Setting up the problem

To set up the general equations, we need the continuity equation and Navier-Stokes equation. As the bubble radius is small compared to the wavelength, the liquid compressibility can be neglected. Furthermore, convective terms are left out as well. Accordingly, the two equations can be simplified to

$$\nabla \cdot \boldsymbol{v} = 0 \ , \tag{4.1}$$

$$\frac{\partial \boldsymbol{v}}{\partial t} = -\frac{1}{\rho}\nabla p + \nu \Delta \boldsymbol{v} \ . \tag{4.2}$$

A solution for the velocity can be sought as

$$\boldsymbol{v} = \nabla \varphi + \nabla \times \boldsymbol{\psi} \ , \tag{4.3}$$

where $\varphi = \varphi(r, \theta, t)$ is the scalar potential and $\boldsymbol{\psi} = \psi(r, \theta, t)\boldsymbol{e}_\varepsilon$ the velocity potential with the azimuth vector $\boldsymbol{e}_\varepsilon$. In spherical coordinates, their derivatives give the velocity components

$$v_r = \frac{\partial \varphi}{\partial r} + \frac{1}{r \sin\theta}\frac{\partial \psi \sin\theta}{\partial \theta} \ , \tag{4.4a}$$

$$v_\theta = \frac{1}{r}\frac{\partial \varphi}{\partial \theta} - \frac{1}{r}\frac{\partial r\psi}{\partial r} \ . \tag{4.4b}$$

Boundary conditions

To find solutions for the velocity potential we need to know the excitation, in other words the oscillations of the bubble surface. The bubble contour can be expressed as the superposition of

the spherical zonal harmonics

$$r_s = R_0 + \sum_{n=0}^{N} s_n \, \mathrm{e}^{-\mathrm{i}\omega_n t} P_n(\mu) \ . \tag{4.5}$$

We have already seen this expression in equation (1.22). The only differences are that we limit the sum up to the Nth mode, and that we explicitly include the time by $\mathrm{e}^{-\mathrm{i}\omega_n t}$ as well as possible phase delays in the complex amplitude $s_n(t)$ instead of the real value $a_n = \Re(s_n)$. Furthermore, we introduce $\mu = \cos\theta$ for more convenience in writing and omit all explicit time dependencies. As a next step, we need to apply the boundary conditions on the bubble surface $r = R_0$ which are the conformity of the radial velocity

$$v_r = \frac{\mathrm{d}r_s}{\mathrm{d}t} = -\mathrm{i}\sum_{n=0}^{N} \omega_n s_n \, \mathrm{e}^{-\,\mathrm{i}\,\omega_n t} P_n \quad \text{for} \quad r = R_0 \ , \tag{4.6}$$

and the zero shear stress $\sigma_{r\theta}$ on the bubble surface

$$\sigma_{r\theta} = \eta \left(\frac{1}{r}\frac{\partial v_r}{\partial \theta} + \frac{\partial v_\theta}{\partial r} - \frac{v_\theta}{r} \right) = 0 \quad \text{for} \quad r = R_0 \ . \tag{4.7}$$

If the bubble did not have a free surface but a rigid one, the boundary condition of zero velocity would apply instead of equation (4.6).

Solutions for the first-order velocity

Some detailed steps of the derivation are included in appendix B.1.1, so that with the above conditions the calculation finally leads to the velocity components

$$v_r = -\frac{1}{R_0}\sum_{n=0}^{N}(n+1)\,\mathrm{e}^{-\,\mathrm{i}\,\omega_n t}\left[a_n \left(\frac{x_{n0}}{x_n}\right)^{n+2} + n b_n \frac{x_{n0}}{x_n} h_n^{(1)}(x_n) \right] P_n \ , \tag{4.8a}$$

$$v_\theta = \frac{1}{R_0}\sum_{n=1}^{N} \mathrm{e}^{-\,\mathrm{i}\,\omega_n t}\left[a_n \left(\frac{x_{n0}}{x_n}\right)^{n+2} - b_n \frac{x_{n0}}{x_n}\left(h_n^{(1)}(x_n) + x_n h_n^{(1)\prime}(x_n) \right) \right] P_n^1 \ , \tag{4.8b}$$

with the constants

$$a_0 = \mathrm{i} R_0 \omega_0 s_0 \quad \text{for} \quad n = 0 \ , \tag{4.9a}$$

$$a_n = \frac{\mathrm{i} R_0 \omega_n s_n \left[x_{n0}^2 h_n^{(1)\prime\prime}(x_{n0}) - (n^2+n-2) h_n^{(1)}(x_{n0}) \right]}{(n+1)\left[x_{n0}^2 h_n^{(1)\prime\prime}(x_{n0}) + (n^2+3n+2) h_n^{(1)}(x_{n0}) \right]} \quad \text{for} \quad n \geq 1 \ , \tag{4.9b}$$

$$b_n = \frac{2\mathrm{i} R_0 (n+2) \omega_n s_n}{(n+1)\left[x_{n0}^2 h_n^{(1)\prime\prime}(x_{n0}) + (n^2+3n+2) h_n^{(1)}(x_{n0}) \right]} \quad \text{for} \quad n \geq 1 \ . \tag{4.9c}$$

In equations (4.8) and (4.9), $h_n^{(1)}$ is the spherical Hankel function of the first kind and P_n^1 is the associated Legendre polynomial of the first order. Also, we define $h_n^{(1)'}(x_n) = dh_n^{(1)}(x_n)/dx_n$ and so on. Furthermore, $x_{n0} = k_n R_0$ and $x_n = k_n r$ have been defined for easier writing with $k_n = (1+\mathrm{i})/\delta_n$, with $\delta_n = \sqrt{2\nu/\omega_n}$ the viscous penetration depth for the angular frequency ω_n.

In equation (4.8) we can see that for pure radial oscillations, that means $s_n = 0 \quad \forall \quad n > 1$, we only obtain pure radial fluid motion. In fact, $v_\theta = 0$ as P_0^1 is not defined and v_r is decaying with $1/r^2$ in the radial direction. There is no directivity as $P_0(\mu) = 1$. For translational motion and surface modes, directivity is introduced due to the Legendre polynomials, while Hankel functions appear and describe the decay in the radial direction.

4.2.2 Time-averaged second-order equation: microstreaming

Now that we know the time-dependent velocity field, we can go one step further and include second-order components to obtain expressions for the streaming. The equation of continuity and Navier-Stokes equation time-averaged and at second order are

$$\nabla \cdot \boldsymbol{V} = 0 \ , \tag{4.10}$$

$$\rho \Big\langle (\boldsymbol{v} \cdot \nabla)\, \boldsymbol{v} \Big\rangle = \eta \Delta \boldsymbol{V} - \nabla P \ , \tag{4.11}$$

where $\langle\rangle$ denotes time-averaging and $\boldsymbol{V}$ and P are the time-averaged velocity and pressure of the streaming respectively. The corresponding velocity potential is

$$\boldsymbol{V} = \nabla \times \boldsymbol{\Psi} \tag{4.12}$$

with $\boldsymbol{\Psi} = \Psi(r,\theta)\boldsymbol{e}_\varepsilon$ where Ψ is the stream function. Taking the curl of the continuity equation (4.10), and after some mathematical simplifications, see also appendix B.1.2, this leads to

$$\Delta^2 \boldsymbol{\Psi} = -\frac{1}{\nu} \nabla \times \langle \boldsymbol{v} \times \Delta \boldsymbol{\psi} \rangle = \frac{1}{2\nu} \Re\{\nabla \times [(\Delta \boldsymbol{\psi})^* \times \boldsymbol{v}]\} \ , \tag{4.13}$$

where * denotes the complex conjugate and $\Re\{\}$ the real part. Equation (4.13) is a vector equation. By introducing the Laplace operator in spherical coordinates, see appendix B.1.2, it is possible to convert this into the scalar equation

$$\left(\Delta_{r\theta} - \frac{1}{r^2 \sin^2\theta}\right)^2 \Psi = \frac{1}{2\nu r} \Re\left\{ \frac{\partial}{\partial r}\left[r v_r \left(\Delta_{r\theta}\psi^* - \frac{\psi^*}{r^2\sin^2\theta} \right) \right] + \frac{\partial}{\partial \theta}\left[v_\theta \left(\Delta_{r\theta}\psi^* - \frac{\psi^*}{r^2\sin^2\theta} \right) \right] \right\} \ . \tag{4.14}$$

4.2.3 Between which modes does microstreaming occur?

Microstreaming is a slow mean flow in the liquid around the bubble. This is clearly visible by the time average in equation (4.13) and the equivalent expressions of the real part with the complex

conjugates in equations (4.13) and (4.14). More precisely, the time average is taken between the velocity $\boldsymbol{v}$ and the Laplacian of its vector potential $\boldsymbol{\psi}$. As we have seen in equation (4.8), the velocity and hence also its vector potential can be represented by a sum of different terms of the form $\sum_{n=0}^{N} \mathrm{e}^{-\mathrm{i}\omega_n} \ldots$. The modes actually present depend of course on the boundary conditions, in other words the modal content of the bubble dynamics. Through the multiplication $\boldsymbol{v} \times \boldsymbol{\psi}$ we theoretically obtain an interaction between any two modes n and m. However, due to the time averaging any contribution from two modes at different frequencies is zero. In the following we hence require that the frequency of two interacting modes is equal, $\omega_n = \omega_m$. Furthermore, to simplify calculation, we suppose that only two modes are present. Any case with a larger number of modes can later be superposed from these cases. To simplify the writing, we can replace the sum by simply adding the two components of the time dependent quantities $\boldsymbol{\psi}$ and $\boldsymbol{v}$,

$$\boldsymbol{\psi} = \boldsymbol{\psi}_n + \boldsymbol{\psi}_m \quad \text{and} \quad \boldsymbol{v} = \boldsymbol{v}_n + \boldsymbol{v}_m \ . \tag{4.15}$$

The time-averaged potential function can then be written as

$$\Psi = \Psi_{nm} + \Psi_{nn} + \Psi_{mm} \ , \tag{4.16}$$

where Ψ_{nm} is produced by the interaction between the modes n and m and Ψ_{nn} and Ψ_{mm} are produced by the interaction of n and m with themselves respectively. Under the condition that equation (4.15) is valid and that $\omega_n = \omega_m$, this finally leads to the following expressions for the cases Ψ_{nn} (or Ψ_{mm} being equivalent) and Ψ_{nm}:

$$\left(\Delta_{r\theta} - \frac{1}{r^2 \sin^2\theta}\right)^2 \Psi_{nn} = \frac{1}{2\nu r} \Re\left\{k_n^2 \left(\frac{\partial}{\partial r}\left(r v_{r,n} \psi_n^*\right) + \frac{\partial}{\partial \theta}\left(v_{\theta,n} \psi_n^*\right)\right)\right\} \ , \tag{4.17}$$

$$\left(\Delta_{r\theta} - \frac{1}{r^2 \sin^2\theta}\right)^2 \Psi_{nm} = \frac{1}{2\nu r} \Re\left\{k_n^2 \left(\frac{\partial}{\partial r}\left(r v_{r,n} \psi_m^* + r v_{r,m} \psi_n^*\right) + \frac{\partial}{\partial \theta}\left(v_{\theta,n} \psi_m^* + v_{\theta,m} \psi_n^*\right)\right)\right\} \ . \tag{4.18}$$

We can apply explicit expressions for the velocity, equation (4.8), and the vector potential, equation (B.4), into equations (4.17) and (4.18). This is done in appendix B.1.3. But even without executing the whole calculation, it is obvious that the resulting equations are quite cumbersome. It is not obvious to find a general analytical solution.

By the way, equation (4.17) confirms the observation that no streaming is observed for radial pulsations $n = 0$ alone. In this case, no vortical potential, see equation (B.4) is produced so that $\psi_0 = 0$. Consequently the right-hand side of equation (4.17) is zero, which means that there is no generating force for microstreaming.

4.3 Specific analytical cases

Equation (4.17) or respectively equation (4.18) derived in section 4.2 have to be solved in order to calculate the streaming. However due to its complexity this is far from being obvious. In order to simplify, we can consider specific cases.

1. As $n = m = 0$ does not generate any streaming, the easiest case to solve is the interaction between $n = 0$ and an arbitrary m.
2. As an intermediary step, we calculate the case $n = m = 1$.
3. The next case that we consider is $n = 1$ and an arbitrary $m > 1$.
4. Also for the case of an arbitrary $n = m$ there are some simplifications that help solving the equations.
5. The most general case, where both n and m are arbitrary modes but not equal to one another is still under progress. We will see what makes the solution so complex.

4.3.1 Interaction with the radial mode: case 0 – m

Simplifications for the case 0 – m

For the case of interaction between $n = 0$ and an arbitrary m, the explicit form of equation (4.18) can be simplified to

$$\left(\Delta_{r\theta} - \frac{1}{r^2 \sin^2\theta}\right)^2 \Psi_{0m} = D^2 \Psi_{0m} = -\frac{R_0}{2\nu} P_m^1(\mu) \Re\left\{k_0^5 a_0^* b_m \frac{h_m^{(1)}(x) - x h_m^{(1)\prime}(x)}{x^3}\right\} \quad , \tag{4.19}$$

with $x_0 = k_0 r = x$ and the simplified differential operator

$$D = \Delta_{r\theta} - \frac{1}{r^2 \sin^2\theta} = \frac{k_0^2}{x^2}\left[\frac{\partial}{\partial x}\left(x^2 \frac{\partial}{\partial x}\right) + (1-\mu^2)\frac{\partial^2}{\partial \mu^2} - 2\mu \frac{\partial}{\partial \mu} - \frac{1}{1-\mu^2}\right] \quad . \tag{4.20}$$

Ansatz

The right-hand side of equation (4.19) suggests that solutions for the velocity potential should exist in the form

$$\Psi_{0m}(x,\mu) = -\frac{R_0}{2\nu} P_m^1(\mu) \Re\left\{k_0 a_0^* b_m F_m(x)\right\} \quad , \tag{4.21}$$

where $F_m(x)$ is a function to be found. Upon using this approach in equation (4.19) and upon explicit application of the differential operator, this leads to

$$\frac{\mathrm{d}^4 F_m}{\mathrm{d}x^4} + \frac{4}{x}\frac{\mathrm{d}^3 F_m}{\mathrm{d}x^3} - \frac{2m(m+1)}{x^2}\frac{\mathrm{d}^2 F_m}{\mathrm{d}x^2} + \frac{m(m+1)(m^2+m-2)}{x^4} F_m = G_m(x) \tag{4.22a}$$

$$\text{with} \quad G_m(x) = \frac{(m+2)h_m^{(1)}(x) - x h_{m-1}^{(1)}(x)}{x^3} \quad , \tag{4.22b}$$

see appendix B.2.1 for more detailed calculations. Equation (4.22) is a differential equation of fourth order that can be solved by the method of variation of parameters, also known as the Lagrange method. In a first step, we assume solutions of the form x^λ and obtain four values $\lambda = -(m+1)$, $\lambda = -(m-1)$, $\lambda = m$ and $\lambda = m+2$ by solving the homogeneous equivalent form of equation (4.22a), see explicit form in the appendix in equation (B.21). The inhomogeneous equation is then solved by

$$F_m(x) = C_{1m}(x)x^{-(m+1)} + C_{2m}(x)x^{-(m-1)} + C_{3m}(x)x^m + C_{4m}(x)x^{(m+2)} \ . \tag{4.23}$$

Following the method of variation of parameters, it is possible to set up a system of algebraic equations, see once more appendix B.2.1 for further detail, that allows to find solutions for $C_{jm}(x)$. These solutions are

$$C_{1m}(x) = C_{1m0} - \frac{1}{2(2m+1)(2m+3)} \int_{x_{00}}^{x} G_m(s)s^{m+4}\mathrm{d}s \ , \tag{4.24a}$$

$$C_{2m}(x) = C_{2m0} + \frac{1}{2(2m-1)(2m+1)} \int_{x_{00}}^{x} G_m(s)s^{m+2}\mathrm{d}s \ , \tag{4.24b}$$

$$C_{3m}(x) = C_{3m0} - \frac{1}{2(2m-1)(2m+1)} \int_{x_{00}}^{x} G_m(s)s^{3-m}\mathrm{d}s \ , \tag{4.24c}$$

$$C_{4m}(x) = C_{4m0} + \frac{1}{2(2m+1)(2m+3)} \int_{x_{00}}^{x} G_m(s)s^{1-m}\mathrm{d}s \ , \tag{4.24d}$$

where the abbreviation $x_{00} = k_0 R_0$ has been used. We now know the solution, but there are still four constants C_{jm0} to be found.

Applying the boundary conditions

Half of the C_{jm0}-unknowns can be found by applying the boundary condition of zero velocity at $r \to \infty$, which leads to

$$C_{3m0} = \frac{1}{2(2m-1)(2m+1)} \int_{x_{00}}^{\infty} G_m(s)s^{3-m}\mathrm{d}s \ , \tag{4.25a}$$

$$C_{4m0} = -\frac{1}{2(2m+1)(2m+3)} \int_{x_{00}}^{\infty} G_m(s)s^{1-m}\mathrm{d}s \ . \tag{4.25b}$$

To find the constants C_{1m0} and C_{2m0} we must apply the boundary conditions at the bubble surface, but they cannot be considered in a direct way. This is due to the fact that so far we are calculating with the Eularian point of view, where the streaming velocity is denoted as $\boldsymbol{V}$. At second order, we need to take into account that the bubble surface is moving. This is possible in the Lagrangian point of view, where the Lagrangian streaming velocity $\boldsymbol{V}_L$ is obtained by

$$\boldsymbol{V}_L = \boldsymbol{V} + \boldsymbol{V}_S \quad \text{with} \quad \boldsymbol{V}_S = \left\langle \left(\int \boldsymbol{v}\mathrm{d}t \cdot \nabla \right) \boldsymbol{v} \right\rangle \ . \tag{4.26}$$

$\boldsymbol{V}_S$ is the so-called Stokes drift and can be obtained through its given definition. Once an explicit form of the Lagrangian velocity found, equation (B.26), we can then apply the boundary conditions of zero velocity normal to the bubble surface and zero tangential stress,

$$V_{Lr}^{0m} = V_r^{0m} + V_{Sr}^{0m} = 0 \quad \text{for} \quad r = R_0 \ , \tag{4.27}$$

$$\frac{1}{r}\frac{\partial V_{Lr}^{0m}}{\partial \theta} + \frac{\partial V_{L\theta}^{0m}}{\partial r} - \frac{V_{L\theta}^{0m}}{r} = 0 \quad \text{for} \quad r = R_0 \ , \tag{4.28}$$

which leads to

$$C_{1m0} = \frac{B_m - (m^2-1)A_m}{2m+1} \ , \tag{4.29a}$$

$$C_{2m0} = \frac{m(m+2)A_m - B_m}{(2m+1)x_{00}^2} \ , \tag{4.29b}$$

with

$$\begin{aligned} A_m = &-C_{3m0}x_{00}^{2m+1} - C_{4m0}x_{00}^{2m+3} \\ &- \frac{x_{00}^{m-2}}{2}\left[(m+1)h_m^{(1)}(x_{00}) + 2x_{00}h_m^{(1)'}(x_{00}) - \frac{x_{00}^2 h_m^{(1)''}(x_{00})}{m+2}\right] \ , \end{aligned} \tag{4.30a}$$

$$\begin{aligned} B_m = &(1-m^2)C_{3m0}x_{00}^{2m+1} - m(m+2)C_{4m0}x_{00}^{2m+3} \\ &- \frac{x_{00}^{m-2}}{2}\Big[(m+1)(m^2+4m+1)h_m^{(1)}(x_{00}) + (m-1)(m+2)x_{00}h_m^{(1)'}(x_{00}) \\ &\quad - \frac{(m+3)(m+5)x_{00}^2 h_m^{(1)''}(x_{00})}{m+2} + x_{00}^3 h_m^{(1)'''}(x_{00})\Big] \ . \end{aligned} \tag{4.30b}$$

For completion, let me add the final explicit expressions for the Eulerian streaming velocity

$$\begin{aligned} V_r^{0m} &= \frac{1}{r\sin\theta}\frac{\partial}{\partial\theta}(\Psi_{0m}\sin\theta) = -\frac{1}{r}\frac{\partial}{\partial\mu}\left(\Psi_{0m}\sqrt{1-\mu^2}\right) \\ &= \frac{m(m+1)R_0}{2\nu r}P_m(\mu)\Re\left\{k_0 a_0^* b_m F_m(x)\right\} \ , \end{aligned} \tag{4.31a}$$

$$\begin{aligned} V_\theta^{0m} &= -\frac{1}{r}\frac{\partial}{\partial r}(r\Psi_{0m}) = -\frac{1}{r}\frac{\partial}{\partial x}(x\Psi_{0m}) \\ &= \frac{R_0}{2\nu r}P_m^1(\mu)\Re\left\{k_0 a_0^* b_m\left[F_m(x) + xF_m'(x)\right]\right\} \ , \end{aligned} \tag{4.31b}$$

and the Stokes drift

$$\begin{aligned} V_{Sr}^{0m} = \frac{m(m+1)R_0}{2\omega_0 r^4}P_m(\mu)\Re\Bigg\{\mathrm{i}a_0^* b_m\Bigg(&\frac{x_{00}^2 h_m^{(1)''}(x_{00}) - (m-1)(m+2)h_m^{(1)}(x_{00})}{2(m+2)}\left(\frac{x_{00}}{x}\right)^{m+1} \\ &- h_m^{(1)}(x) - xh_m^{(1)'}(x)\Bigg)\Bigg\} \ , \end{aligned} \tag{4.32a}$$

$$V_{S\theta}^{0m} = \frac{R_0}{2\omega_0 r^4} P_m^1(\mu) \Re\Bigg\{ \mathrm{i} a_0^* b_m \Bigg(- \frac{(m+3)[x_{00}^2 h_m^{(1)''}(x_{00}) - (m-1)(m+2) h_m^{(1)}(x_{00})]}{2(m+2)} \left(\frac{x_{00}}{x}\right)^{m+1} + 2h_m^{(1)}(x) - x^2 h_m^{(1)''}(x) \Bigg) \Bigg\} \ . \tag{4.32b}$$

In conclusion, in order to calculate the streaming, we either need the Eulerian formulation from equation (4.32) or the Lagrangian streaming, sum of equations (4.31) and (4.32). The function $F_m(x)$ is defined in equation (4.23) with equation (4.24) and the constants obtained from the boundary conditions in equations (4.25) and (4.29). The constants a_0 and b_m come from the first-order solution, see equation (4.9).

Numerical implementation

In figure 4.2, the above equations are implemented to simulate the streaming induced by the radial mode 0 that interacts with either the translational mode 1 or the mode $m = 2, 3, \ldots, 6$. The parameters for the simulation are $\rho = 1000\,\mathrm{kg\,m^{-3}}$, $\eta = 0.001\,\mathrm{Pa\,s}$, $f_{\mathrm{ac}} = 31.25\,\mathrm{kHz}$ and $R_0 = 55\,\mu\mathrm{m}$. The modal amplitudes are set to $s_0 = 5\,\mu\mathrm{m}$ and $s_m = 10\mathrm{i}\,\mu\mathrm{m}$. As one of the modal amplitudes is a real number and the other one an imaginary number, the phase difference between the modes is $\pi/2$. The plots are made by first calculating the Lagrangian velocity field from the above equations and then letting the Matlab function *streamslice* fit correct streamlines to the velocity field.

In the resulting plots of figure 4.2, we can observe that the pattern consists of $2m$ lobes. It should be noted that the same simulation without a phase difference gives qualitatively a very similar result, the overall velocities are however much smaller, as we will see later in figure 4.7.

The only pattern which has been explicitly presented by other authors is the case $0-1$. And in fact, the general form of our streamlines agrees well with those shown by Longuet-Higgins [74]. Concerning the comparison with our experimental results, we already seem to see some similarities. But we have to be careful with the interpretation, because we have to consider the frequencies of the different modes. So let us reserve this discussion for section 4.5.

4.3.2 Purely translating bubble: case $1-1$

For the calculation of the case $n = m = 1$ equation (4.17) simplifies to

$$\left(\Delta_{r\theta} - \frac{1}{r^2 \sin^2\theta}\right)^2 \Psi_{11} = D^2 \Psi_{11}(x_1, \mu)$$
$$= \mu\sqrt{1-\mu^2}\frac{k_1^4 |b_1|^2}{6\nu x_1^4} \Re\left\{ \bar{x}^4 h_1^{(1)''}(\bar{x})[x_1 h_1^{(1)'}(x_1) - h_1^{(1)}(x_1)]^* - 6x_1^3 h_1^{(1)'}(x_1) h_1^{(1)*}(x_1) \right\} \ , \tag{4.33}$$

where D is once again the simplified differential operator from equation (4.20) and the abbreviation $\bar{x} = k_1 R_0$ has been applied. It is also interesting to note that $k_1^4 = -4/\delta^4$ is a real

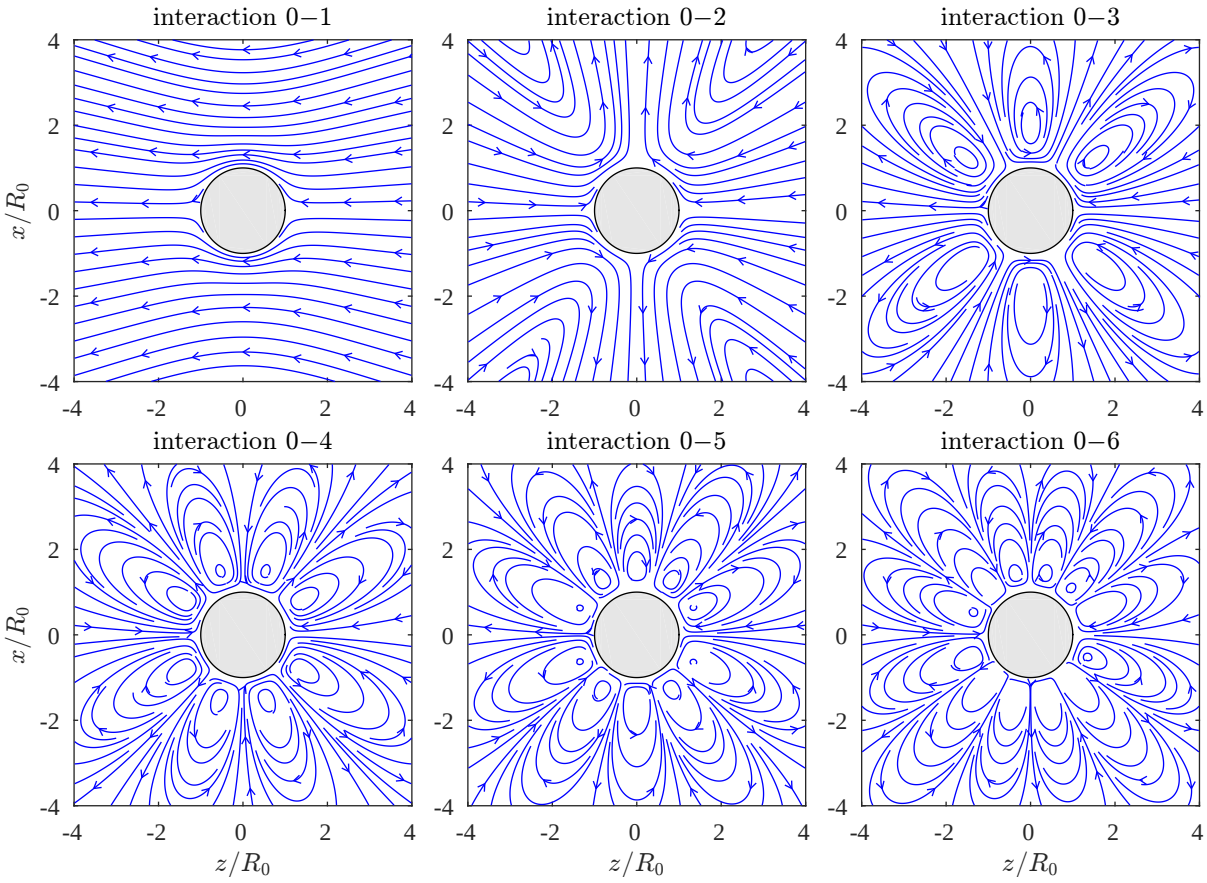

Figure 4.2: Streaming patterns obtained through the interaction of the radial mode 0 and respectively the translational mode 1 and the modes $m = 2, 3, \ldots, 6$.

number. For more simplification let us denote $x = x_1$ in the following. The right-hand side of equation (4.33) suggests solutions of the form

$$\Psi_{11}(x,\mu) = \mu\sqrt{1-\mu^2}\frac{|b_1|^2}{6\nu}\Re\{F(x)\} \ . \tag{4.34}$$

With the method of variation of parameters it is possible to find

$$F(x) = C_1(x)x^{-3} + C_2(x)x^{-1} + C_3(x)x^2 + C_4(x)x^4 \ , \tag{4.35}$$

where the $C_j(x)$ are given in appendix B.2.2. As for the case $0-m$, the constants $C_j(x)$ contain an x-dependent integral plus a constant C_{j0} to be found by the boundary conditions. Once more, the boundary conditions concern matched velocity at infinity and zero normal velocity at the bubble surface as well as zero tangential stress on the bubble surface. All solutions and steps can be found in appendix B.2.2.

4.3.3 Interaction between shape modes and bubble translation: case 1 – m

While the cases $0-m$ and $1-1$ are relatively short, the equations for the case $m-1$ start to become quite cumbersome. As I have already included a rather detailed explanation for the case $0-m$ in section 4.3.1 and also joined most steps for the case $1-1$ in appendix B.2.2, I will shorten the following two sections. Here in the main text, I will mainly include some explanations which allow to follow the broad idea and explain the differences with respect to the previous sections. In appendix B.2.3 I will furthermore include supplementary steps. More details can be found in Doinikov et al. [OP7].

Setting up the problem

For the case $n = 1$ and an arbitrary $m > 1$, the ruling equation takes a lengthy form, see equation (B.40) in appendix B.2.3. It can be transformed into

$$D^2\Psi_{1m}(x,\nu) = \frac{k_1^4}{\nu}\Re\left[b_1^* b_m\left[\mu P_m^1(\mu)G_1(x) + \sqrt{1-\mu^2}P_m(\mu)G_2(x)\right]\right] \ , \tag{4.36a}$$

$$\text{with} \quad G_1(x) = \frac{\bar{x}^4}{6x^4}h_1^{(1)''*}(\bar{x})\left[2h_m^{(1)}(x) - xh_m^{(1)'}(x)\right] + \frac{1}{x}h_1^{(1)*}(x)h_m^{(1)'}(x) - \frac{1}{x^*}h_1^{(1)'*}(x)h_m^{(1)}(x) \ , \tag{4.36b}$$

$$G_2(x) = m(m+1)h_m^{(1)}(x)\left[\frac{\bar{x}^4}{12x^4}h_m^{(1)''}(\bar{x}) - \frac{1}{x}h_1^{(1)'}(x)\right]^* + \frac{(m+1)\bar{x}^{m+1}}{4(m+2)x^{m+5}}\left[\bar{x}^2h_m^{(1)''}(\bar{x}) - (m^2+m-2)h_m^{(1)}(\bar{x})\right] \times \left[x^2h_1^{(1)}(x) - x^3h_1^{(1)'}(x)\right]^* \ , \tag{4.36c}$$

which suggests a solution of the form

$$\Psi_{1m}(x,\mu) = \frac{1}{\nu}\Re\left[b_1^* b_m\left[\mu P_m^1(\mu)F_1(x) + \sqrt{1-\mu^2}P_m(\mu)F_2(x)\right]\right] \ . \tag{4.37}$$

Applying the differential operator and doing some transformation, this leads to one equation containing μP_m^1 and $\sqrt{1-\mu^2}P_m$, both in F_1, F_2, G_1 and G_2. We can separate those two parts:

$$F_1^{IV} + \frac{4}{x}F_1''' - \frac{2m(m+1)}{x^2}F_1'' + \frac{m(m+1)(m^2+m+2)}{x^4}F_1 + \frac{4}{x^2}F_2'' - \frac{4m(m+1)}{x^4}F_2 = G_1 \ , \tag{4.38a}$$

$$F_2^{IV} + \frac{4}{x}F_2''' - \frac{2(m^2+m+2)}{x^2}F_2'' + \frac{m(m+1)(m^2+m+6)}{x^4}F_2 + \frac{4m(m+1)}{x^2}\left[F_1'' - \frac{m(m+1)}{x^2}F_1\right] = G_2 \ . \tag{4.38b}$$

In principle, the problem can be solved in the same way as before for the cases $0-m$ and $1-1$. However, as opposed to before, we now have two coupled equations, hence doubling the number of unknowns and so on. Nonetheless we can start to solve the system by first solving the case of the homogeneous equations $G_1 = G_2 = 0$. Once more, we search for partial solutions of the form $Y_j = \gamma_j x^\lambda$, for $j = 1, 2, \cdots, 8$. We have eight variables γ_j and exponents λ to find instead of the four unknowns before. Solutions for λ are

$$\lambda_1 = -m-2 \ , \ \lambda_2 = m+3 \ , \ \lambda_3 = 2-m \ , \ \lambda_4 = m-1 \ , \quad \lambda_5 = \lambda_6 = -m \ , \ \lambda_7 = \lambda_8 = m+1 \ . \tag{4.39}$$

Then, a system of equations can be set up containing G_1 and G_2 to obtain

$$F_1(x) = \gamma_{11}(x)x^{-m-2} + \gamma_{12}(x)x^{m+3} + \gamma_{13}(x)x^{2-m} + \gamma_{14}(x)x^{m-1} + \gamma_{15}(x)x^{-m} + \gamma_{17}(x)x^{m+1} \ , \tag{4.40a}$$

$$F_2(x) = -(m+1)\gamma_{11}(x)x^{-m-2} - (m+1)\gamma_{12}(x)x^{m+3} + m\gamma_{13}(x)x^{2-m} + m\gamma_{14}(x)x^{m-1} + \gamma_{55}(x)x^{-m} + \gamma_{57}(x)x^{m+1} \ , \tag{4.40b}$$

The values for $\gamma_{11}(x)$, $\gamma_{12}(x)$ and so on are included in the appendix in equation (B.45). The fact that a $\gamma_{55}(x)$ and $\gamma_{57}(x)$ appear is linked to the doubling of $\lambda_5 = \lambda_6$ and $\lambda_7 = \lambda_8$. In equation (B.45), constants $\bar{\gamma}_{11}$, $\bar{\gamma}_{12}$ and so on appear. These eight constants can be obtained by applying the boundary conditions. As before, half of them can be obtained from the boundary condition of zero velocity for $r \to \infty$. The values are given in equation (B.46). For the other four, the Lagrangian streaming has to be formulated, the boundary conditions at the bubble surface (matched normal velocity and zero tangential stress) applied and the whole set of equations solved. The principle stays the same as before, but the involved equations are much more cumbersome.

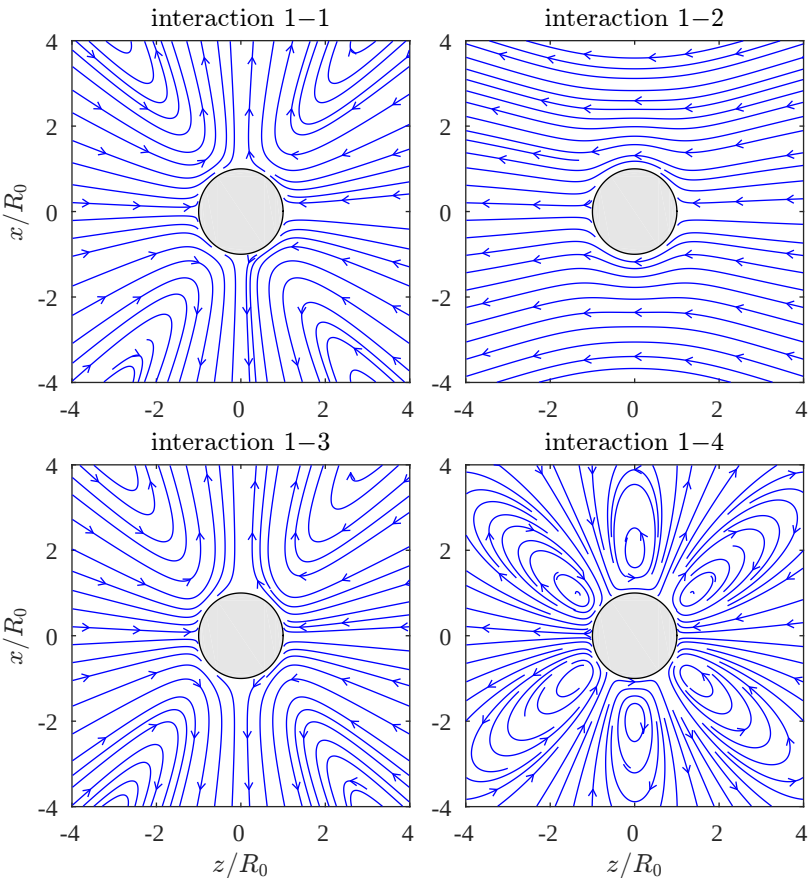

Figure 4.3: Streaming patterns obtained through the interaction of the translational mode 1 with itself and with the shape modes $m = 2$, 3 and 4.

Numerical implementation

The numerical implementation of the self-interacting case $1-1$ from section 4.3.2 and the cases $1-m$ from the present section 4.3.3 for $m = 2$, 3 and 4 is shown in figure 4.3. The same parameters as for figure 4.2 are chosen in the present simulation: $\rho = 1000\,\mathrm{kg\,m^{-3}}$, $\eta = 0.001\,\mathrm{Pa\,s}$, $f_{\mathrm{ac}} = 31.25\,\mathrm{kHz}$ and $R_0 = 55\,\mu\mathrm{m}$. Here, the modal amplitudes are set to $s_1 = 5\,\mu\mathrm{m}$ and $s_m = 10\,\mu\mathrm{m}$. The two modal amplitudes are chosen to be real numbers and the phase shift between the two is consequently equal to zero.

For the pure translation case $1-1$ we observe a cross-like pattern as has been previously shown by Longuet-Higgins [74] and also validated by Spelman and Lauga [117]. For the other cases, where the translational motion is interacting with a surface mode, an interesting arrangement appears: $2(m-1)$ lobes are visible for the case $1-m$. As for the interaction $0-m$ we observe equally spaced lobes around the bubble. Consequently, care has to be taken with their interpretation, for instance both $0-3$ and $1-4$ leading to the same pattern type with six lobes.

4.3.4 Self-interaction of an arbitrary mode: case n – n

Setting up the problem

For the case of a self-interacting mode n, equation (4.17) has to be solved. Let us retake its explicit expression from equation (B.14):

$$\begin{aligned}\left(\Delta_{r\theta} - \frac{1}{r^2\sin^2\theta}\right)^2 \Psi_{nn} \\ = \frac{n+1}{2\nu r^2} P_n P_n^1 \Re\left\{k_n^2 a_n b_n^* \left(\frac{x_{n0}}{x_n}\right)^{n+1} \left[(n+1)h_n^{(1)}(x_n) - x_n h_n^{(1)'}(x_n)\right]^*\right] \\ - \frac{\sqrt{1-\mu^2}}{\nu r^2} P_n^1 P_n^{1'} \Re\left[k_n^2 h_n^{(1)*}(x_n)\left[a_n b_n^* \left(\frac{x_{n0}}{x_n}\right)^{n+1} - b_n b_n^* x_n h_n^{(1)'}(x_n)\right]\right\} \ . \end{aligned} \tag{4.41}$$

We can notice the appearance of two angular functions

$$f_{1,n} = P_n(\mu) P_n^1(\mu) \ , \tag{4.42a}$$

$$f_{2,n} = \sqrt{1-\mu^2} P_n^1(\mu) P_n^{1'}(\mu) \ . \tag{4.42b}$$

In order to obtain linearly independent functions, we transform equation (4.42b) into

$$f_{2,n} = n^2 P_n(\mu) P_n^1(\mu) - \sum_{i=1}^{n-1} (2i+1) P_i(\mu) P_i^1(\mu) \ . \tag{4.43}$$

Accordingly, after some calculation, the solution

$$\psi_{nn}(x,\mu) = \frac{|b_n|^2}{\nu} \Re\left\{\sum_{k=1}^{n} F_k(x) P_k(\mu) P_k^1(\mu)\right\} \tag{4.44}$$

is proposed, where $x = x_n$ for shorter writing.

I will not go into further detail here, but it can be imagined that the appearance of the sum further complicates the solution. In fact, there is a loop which appears and requires the different factors F_n, F_{n-1} etc. to be solved one after another. Apart from that, the logic is similar to the above cases.

Numerical implementation

The numerical implementation of the general self-interacting case is given in figure 4.4. Once again the parameters are: $\rho = 1000\,\mathrm{kg\,m^{-3}}$, $\eta = 0.001\,\mathrm{Pa\,s}$, $f_{\mathrm{ac}} = 31.25\,\mathrm{kHz}$, $R_0 = 55\,\mu\mathrm{m}$ and $s_n = 5\,\mu\mathrm{m}$.

The case $1-1$ is left out in figure 4.4 as it was already presented in figure 4.3. For all shown cases $n-n$ we observe a large cross-like pattern, and for $n \geq 2$ we have $4n$ small supplementary lobes close to the bubble surface. The zoom in the lower row of figure 4.4 aims at highlighting

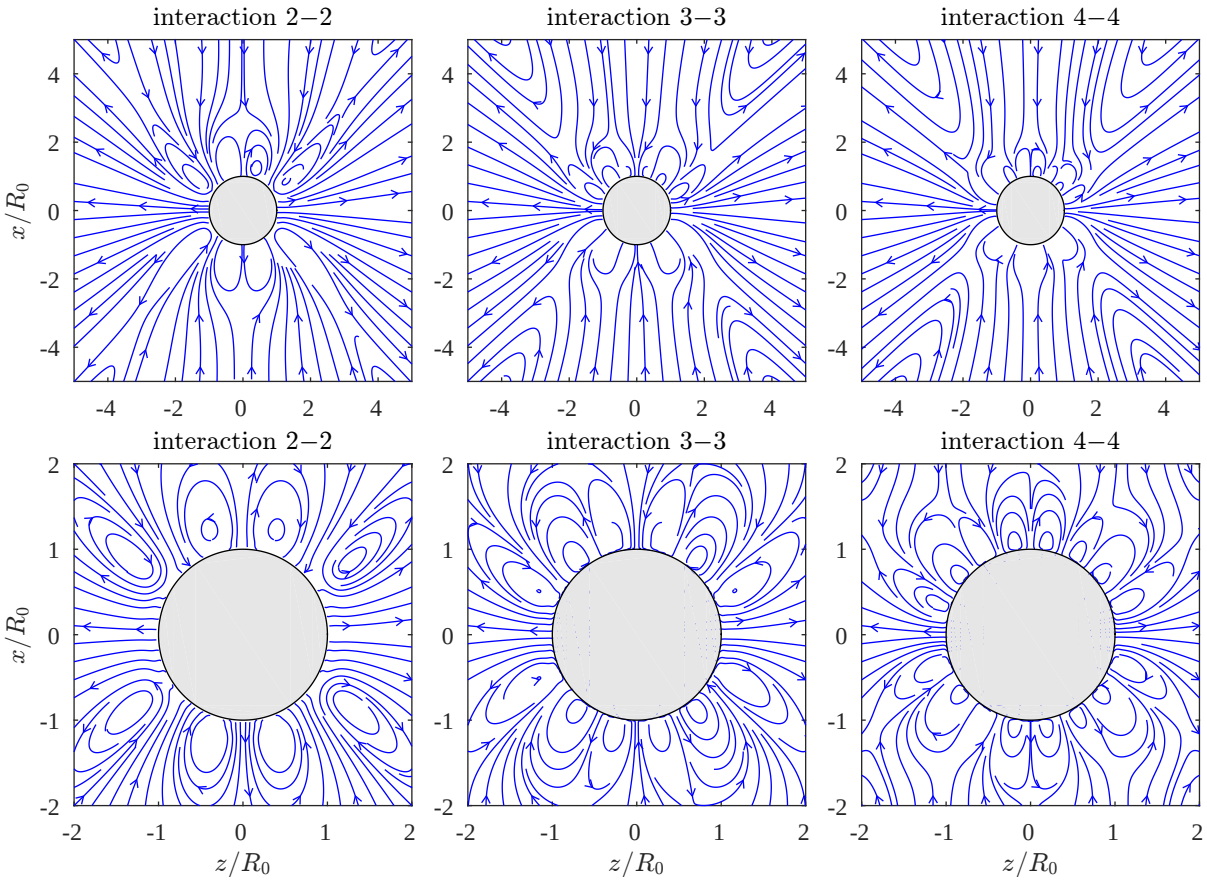

Figure 4.4: Streaming pattern obtained by the self-interacting modes 2, 3 and 4. The upper and lower row show the same patterns, however with a different frame size. While the upper row is zoomed out with respect to the frame sizes in figures 4.2 and 4.3, the lower row is zoomed in to show the small lobes close to the bubble surface.

these zones. We can, however note, that in the zoomed out pattern some of the $4n$ lobes seem to dominate and others are hardly visible in the overall picture. This leads to some resemblance with the experimental results, as we will see in section 4.5.

4.3.5 Interaction between two arbitrary modes: case n – m

As written in the introduction, the general case $n - m$ is still under progress. The general differential equation that has to be solved is given in the appendix in equation (B.15). It can be easily imagined that the solution of this equation becomes even more cumbersome. In fact, we do not only have one or two terms of angular dependence as in the previous cases, but there are three terms to take into account now. So the main difficulty lies in guessing a correct general solution.

4.4 Numerical validation

Before comparing with experimental results let us compare our model with other analytical approaches. The first model that allows to calculate streaming produced by the interaction of modes 0 and 1 was derived by Longuet-Higgins [74]. This case was later included in the arbitrary-mode analysis performed by Spelman and Lauga [117]. However, it is worth noting that in both investigations the physical situation is different from ours. These authors assume a fixed bubble in an oscillating liquid while we assume an oscillating bubble in a liquid which is at rest at infinity. For their case this means that at infinity the first-order liquid velocity tends to a non-zero constant, as expressed by a term with r^2 dependence in Longuet-Higgins' linear stream function

$$\psi_{10,LH}(r,\mu) = \left[\frac{1}{2}\left(r^2 - \frac{1}{2}\right) + \frac{B}{\alpha^2}\frac{1}{r} + \frac{C}{\alpha^2}\left(1 + \frac{1}{\alpha r}\right)e^{-\alpha(r-1)}\right](1-\mu) \ , \tag{4.45}$$

where $\alpha = (1+i)R_0/\delta$ and B and C are coefficients given in [74]. Our physically different approaches are mathematically identical for linear solutions, but not for second-order solutions. Therefore, our results for streaming produced by modes 0 and 1 cannot be transformed into those of Longuet-Higgins. If omitting the r^2 term in the linear solution of Longuet-Higgins, which produces a constant velocity at infinity, and then recalculating the Stokes drift, the second-order boundary conditions and streaming velocities, an adequate comparison with our results could be possible.

As Spelman and Lauga [117] follow the same approach as Longuet-Higgins, their result shows the same feature for the linear streaming velocity. Their corresponding stream function is

$$\psi_{10,SL}(r,\mu) = D_0(1-\mu) - \frac{1}{2}\left[\frac{B_1\sqrt{r}}{\alpha^2}K_{\frac{3}{2}}(\alpha r) + \frac{D_1}{r}\right]\sqrt{1-\mu^2}P_1^1(\mu) \ , \tag{4.46}$$

where $\alpha = (1+i)/\delta$, $K_n(x)$ the modified Bessel function of second kind of order n and B_0, B_1

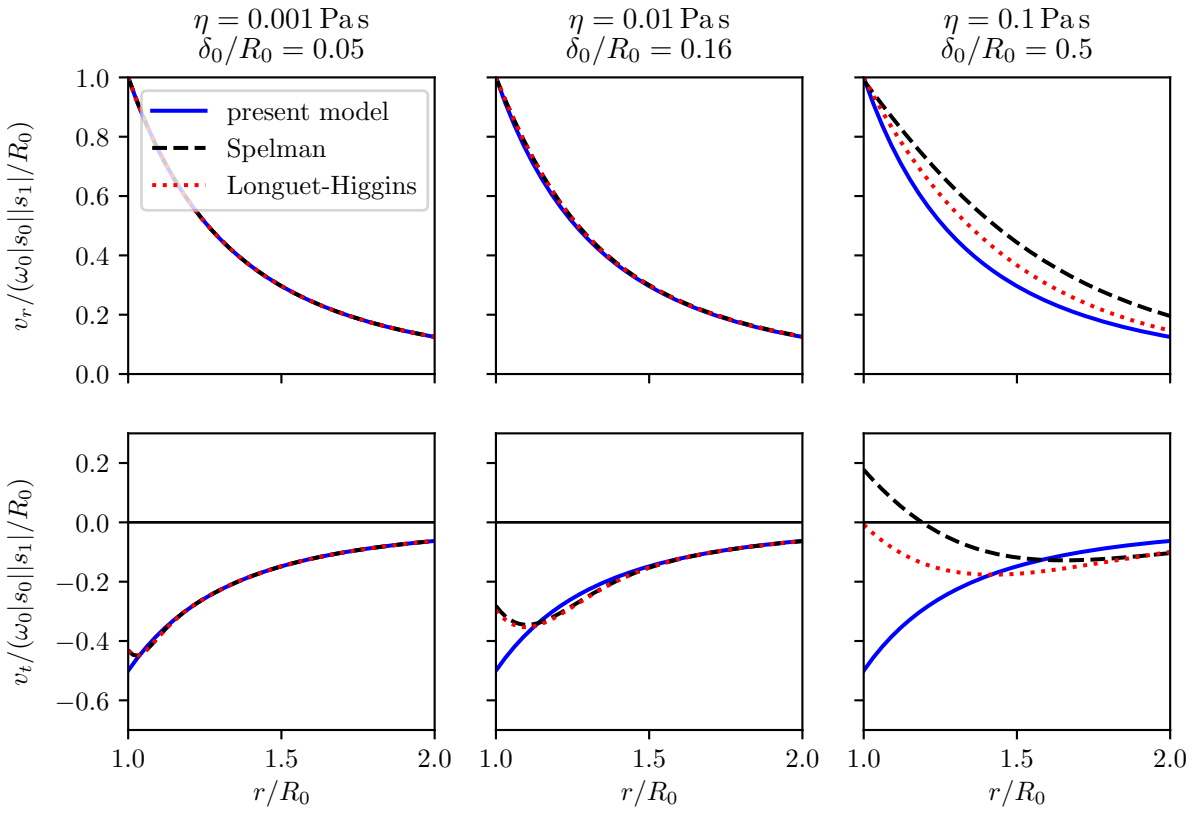

Figure 4.5: Radial dependence of the radial *(upper row)* and tangential linear velocity *(bottom row)* calculated by different models (Longuet-Higgins, Spelman and the present model) and for a varying viscosity η. The here considered interaction is between the modes 0 and 1. Note that the velocity is normalized by the factor $\omega_0|s_0||s_1|/R_0$.

and D_1 constants given in [117]. Similarly to the r^2 term in equation (4.45), we have the term $D_0(1-\mu)$ in equation (4.46), which leads to a constant linear velocity at infinity.

Before discussing the streaming patterns, I will first compare these linear velocities from equations (4.45) and (4.46) to our result from equation (4.31). In order to obtain comparable results, the terms r^2 and $D_0(1-\mu)$ are left out in the respective expressions. Three examples for different values of viscosity are shown in figure 4.5 for the same set of parameters used throughout the whole chapter. For water, $\eta = 0.001\,\mathrm{Pa\,s}$, the results are quasi identical and only a slight difference for the tangential velocity close to the bubble can be observed. However, when increasing the viscosity, a clear distinction between the models becomes visible. In fact, Spelman's and Longuet-Higgins' models are based on the approach of a thin viscous boundary layer, a hypothesis which is no longer valid for large viscosity. The shown results for η up to $0.1\,\mathrm{Pa\,s}$ are physically possible values, the viscosity of pure glycerin is for example $1.48\,\mathrm{Pa\,s}$.

A comparison between the streaming velocities is given in figure 4.6. Here, Spelman's model is left out as it leads to the same results as Longuet-Higgins' for the hypothesis of small viscosity.

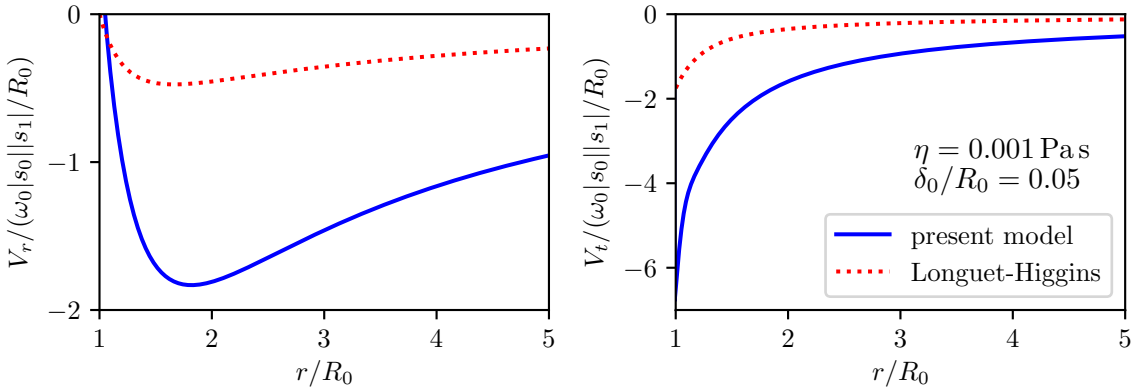

Figure 4.6: Radial dependence of the radial *(left)* and tangential Eulerian streaming velocity *(right)* calculated by Longuet-Higgins' model and the present model for $\eta = 0.001\,\mathrm{Pa\,s}$ and for the interaction between the modes 0 and 1 and a phase difference of $\pi/2$ between them. Note that the velocity is normalized by the factor $\omega_0|s_1||s_0|/R_0$.

As one can see, our theory predicts higher velocity amplitudes. However, it should be emphasized once again that figure 4.6 in fact compares two different physical cases.

Similar simulations can be made for other modal interactions, most of them however excluding Longuet-Higgins' model as it does not consider surface modes. The comparison between Spelman's and our model for the interaction of the radial mode 0 with a surface mode n is still reasonably easy to implement. I omit the figures in the present manuscript as the conclusions are similar to those already obtained with figures 4.5 and 4.6. For small viscosity the linear velocity is very similar, but large discrepancies occur for higher viscosity. Furthermore, our values obtained for streaming velocities are considerably higher than those predicted by Spelman's model. As the experimental streaming velocities have played only a secondary role so far, a comparison of the numerical values to experimental ones has not been done. However, this will surely be an important aspect of future work.

4.5 Comparison with experiments and further interpretation

Let me recall the important experimental results that might benefit from validation through the theoretical model. The first observation was linked to the large variety of patterns and indeed the numerical model confirms this fact. The possible reasons that lead to the distinction were

- dominant mode number,
- richness of modal content,
- appearance of the translational mode and
- phase differences between different appearing modes.

Let me also recall that the theoretical model supposes an interaction between two modes at the same frequency. In order to simulate the experimental cases where more than two modes might

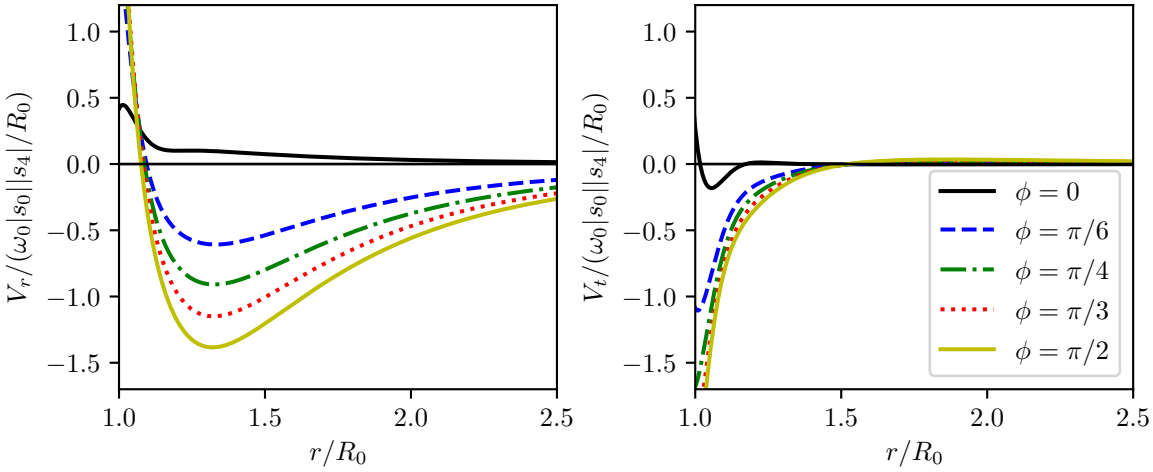

Figure 4.7: Influence of the phase difference ϕ between the two modes generating the streaming, here modes 0 and 4, on the radial Eulerian streaming velocity V_r *(left plot)* and the tangential Eulerian streaming velocity V_t *(right plot)*.

be present, we can simply do a superposition of two or more simulations. Obviously, we do not yet dispose of the full model so the complete simulation is not possible at the current stage. However, oftentimes we can already pick out contributions which seem to be dominant. Note that we have to keep in mind that only modes oscillating at the same frequency can interact to create streaming. In the following, I will discuss the above parameters starting with the phase difference.

4.5.1 Influence of the phase difference on the streaming velocity

The close examination of the experimental case with a predominant mode 3 suggested that the phase difference between two modes, in the experimental case the modes 0 and 6, might play an important role. Even though no predominant interaction $0-6$ (which would lead to 12 lobes around the bubble) is observed, we shall take a look at the influence of phase differences in general.

One example is given in figure 4.7, where the radial and tangential velocity for the interaction $0-4$ are presented for several phase differences between the two modes. The same set of parameters as for the other simulations is used. For this example and the case $0-m$ in general, we observe for the range $0 \leq \phi \leq \pi/2$ that the higher the phase difference, the higher the streaming velocities. Particularly interesting is the case of zero phase difference, where besides very close to the bubble the streaming velocities becomes close to zero. Note that for the here presented figure, the angular dependence has been simply left out. This is possible because the Legendre polynomial or respectively the associated Legendre polynomial appear as simple factors in equation (4.31). It is, however, important to state that the two polynomials are not equal to 1 for the same angle θ. The Legendre polynomial ruling the radial velocity reaches its maximum value for $|P_4(\theta = 0)| = |P_4(\theta = \pi)| = 1$, that means on-axis. The associated Legendre

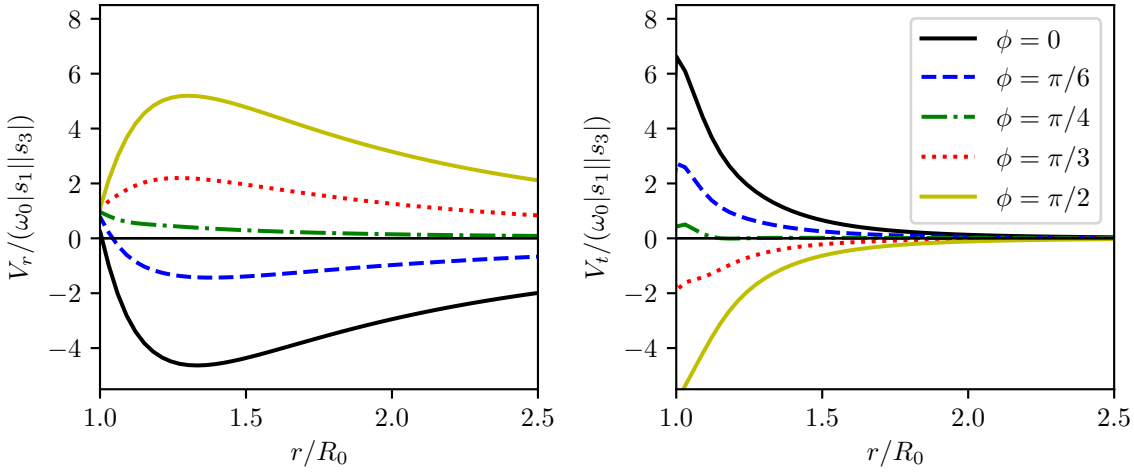

Figure 4.8: Influence of the phase difference ϕ between the two modes generating the streaming, here modes 1 and 3, on the radial streaming velocity v_r *(left plot)* and the tangential streaming velocity v_t *(right plot)*. The calculation has been effected for the angle $\theta = \pi/12 = 15°$ with respect to the axis of symmetry.

Polynomial P_4^1 reaches values larger than 1 but is zero for $\theta = 0$ and $\theta = \pi$. The evolution presented in figure 4.7 has hence the same form everywhere, but with a different factor P_n or P_n^1 for every angle θ.

For the case $1 - m$, the dependence of the streaming velocity on the phase difference ϕ is more complex, because for the respective velocities both, Legendre polynomials and associated Legendre polynomials multiplied with r-dependent functions appear, see equation (B.42a). An example for the interaction between the modes 1 and 3 and a chosen angle $\theta = \pi/12 = 15°$ with respect to the axis of symmetry is given in figure 4.8. We can observe that now minimum streaming velocities are observed for the phase difference $\phi = \pi/4$, while for both $\phi = 0$ and $\phi = \pi/2$ maximum streaming velocities (but with opposite direction) occur.

Without going into further detail here, we can conclude that the phase difference between two modes has an important impact on the streaming velocities. Even though two modes are predominant, their streaming might be negligible if they have the "wrong" phase. On the other hand, seemingly unimportant modes can have a considerable contribution to the overall streaming.

4.5.2 Influence of the modal content on the streaming pattern

As we have seen in chapter 3, the bubble dynamics reveals the presence of not only one single mode, but it is composed of the superposition of several modal amplitudes. Consequently, every combination of two of these modes contributes to the overall streaming pattern. We have to keep in mind that only modes oscillating at the same frequency will lead to streaming. But even if they are oscillating at two different frequencies, some of the extracted curves are far from being purely sinusoidal. The appearance of harmonics or subharmonics might even raise the number of possible interactions. Due to time constraints, I have not yet considered this point any further.

In the same way, I have not yet implemented the superposition of different streaming patterns. This is not a hard task, but it will give much more satisfactory results, once all contributions including the not negligible part for random $n - m$ can be calculated.

But even without those eventually necessary extensions, we can already take a first look at the comparison between experiments and numerical simulations. A graphic summary of the following explanations is given in figure 4.9.

Large, mostly cross-like patterns

For all three predominant modes, we observed large cross-like patterns. And indeed there are different mechanisms that might lead to this kind of pattern.

Mode 2: Experimentally, we observed two different streaming patterns for bubbles oscillating predominantly on a mode 2 (shown here in the first two lines of figure 4.9, complete information in figures 3.5 and 3.8 (a) and (b)). The bubble dynamics consists in particular of modal components of the modes 2, 4 and the radial mode 0. While the parametrically excited mode 2 is oscillating at half the driving frequency, all other modal components oscillate at the driving frequency. However, there are obvious nonlinearities visible in the temporal evolution of the different modal contents. Consequently, interaction could take place even for modes not oscillating at the same frequency.

Theoretically, the result best fitting to the experimentally observed cross-shaped pattern with two pairs of recirculation zones is self-interacting mode 2 (from figure 4.4). The resemblance is in particular visible when a sufficiently large frame size is chosen. A cross-shaped pattern without any zones of recirculation is obtained through the interaction $0 - 2$ (from figure 4.2). In order to understand which of the two patterns dominates, it will be necessary to evaluate the actual streaming velocities, which will not only depend on the modal amplitudes but also on the phase differences. This is not a trivial task in view of the clearly nonlinear bubble dynamics.

Mode 3: Experimentally, we observe two different large patterns for bubbles oscillating on a predominant mode 3 (shown here in the third and fourth line of figure 4.9, complete information in figure 3.9 (c) and (d)). We have cross-like patterns either with or without four zones of recirculation. The bubble dynamics reveals a strong modal amplitude 3 (and possibly a translational motion 1), oscillating at half the driving frequency due to parametric excitation. The also visible radial mode 0 and the slight contributions of the modes 6 and 4 are oscillating at the driving frequency. Nonlinearities are less obvious than for the mode 2 bubbles.

Theoretically, the self-interacting mode 3 (from figure 4.4) seems to be the best guess to explain the cross-like pattern with the four zones of recirculation. When taking a sufficiently large frame size, four of the twelve theoretical, small zones of recirculation seem to dominate. Interactions leading to a purely cross-shaped pattern are the interactions $1 - 3$ and $1 - 1$ (from figure 4.3). This would however suppose that the translational mode 1 is actually present.

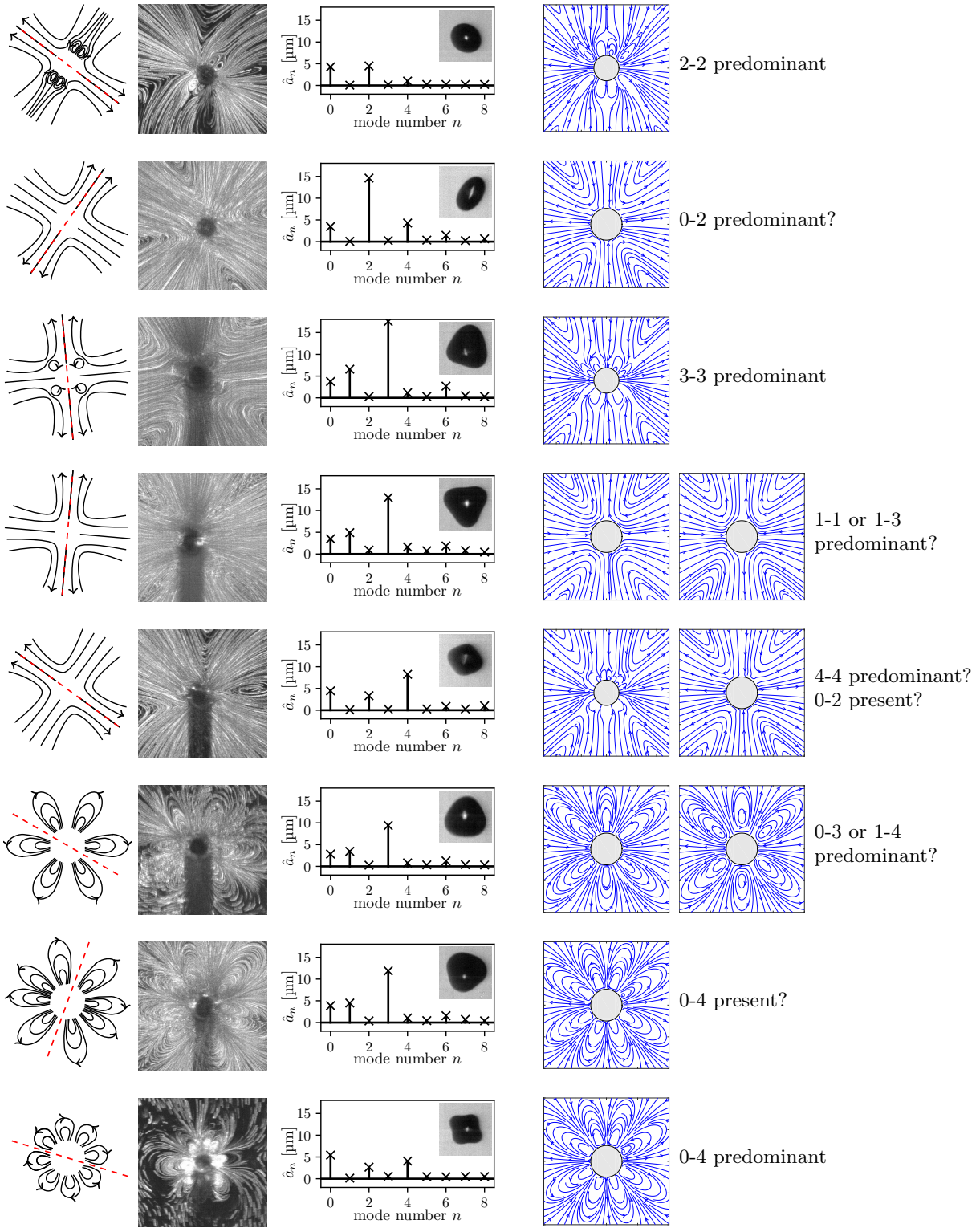

Figure 4.9: Summary of the comparison between experimental results (in black, see figures 3.8 to 3.10 for more details) and numerical solutions (in blue, see figures 4.2 to 4.4 for more details) which lead to a comparable result. Each row contains from left to right: sketch of the experimental pattern, streak image, maximum modal amplitudes $\hat{a}_n$ with one example snapshot, and up to two similar numerical simulations of the analytical model (indicated by text on the right).

Mode 4: We also observe cross-shaped patterns for predominant modes 4 (shown here in the fifth line of figure 4.9, complete information in figure 3.10 (b)). The mode 4 is excited at a second parametric resonance. It is hence oscillating at the driving frequency. Furthermore, rather strong modal components of the radial mode 0 and the mode 2 are visible. Consequently, all modal components are oscillating at the same frequency. Furthermore, nonlinearties are visible on their temporal evolution.

Theoretical patterns which might explain the experimental observation are either the self-interacting mode 4 (from figure 4.4 when assuming that the very small lobes close to the bubble are not large enough to be observed experimentally) or the interaction $0-2$ (from figure 4.2).

Confined lobe patterns

Mode 3: For a mode oscillating predominantly on a mode 3, we observe lobe-shaped patterns that might have either six or eight lobes (shown here in the second to last and third to last line of figure 4.9, complete information in figures 3.6 and 3.9 (a) and (b)). The bubble dynamics reveals a strong modal amplitude 3 (and possibly a translational motion 1), oscillating at half the driving frequency due to parametric excitation. The also visible radial mode 0 and the slight contributions of the modes 6 and 4 are oscillating at the driving frequency. Nonlinearities are not obvious but might still play a role.

Theoretical patterns that might lead to purely lobe-shaped patterns are the interactions $0-m$ (from figure 4.2) and $1-m$ (from figure 4.3). The cases $0-3$ (and possibly $1-4$) are the best explanation for the observed six lobes, even though the respective modes are not oscillating at the same frequency. For the observed eight lobes, the case $0-4$ is so far the only explanation. However, in particular for the very rich modal content of these cases, some still unknown patterns might become important as well. Furthermore, the final pattern will consist of the superposition of all contributions.

Mode 4: The eight lobes observed for a bubbles oscillating on a predominant mode 4 (shown here in the last line of figure 4.9, complete information in figures 3.7 and 3.10 (a)) can be explained very well by the interaction between the mode $0-4$ (from figure 4.2). Both the radial mode and the mode 4 are oscillating at the same frequency.

4.6 Conclusions on the theoretical model

This chapter aimed at giving a good idea of how our theoretical model for microstreaming is derived. As most streaming models, we first derive the linear time-dependent velocity and then the time-averaged second-order streaming velocity. The model supposes the bubbly dynamics as input parameters and does not have any restrictions in bubble size or viscosity. The modal amplitudes are however considered to be small with respect to the bubble size.

As the general solution for the streaming equation is not trivial to find, we have first found specific solutions. As discussed in this chapter, some of them give already promising results as to their accordance to experimental results. Once the general case can be calculated and the superposition of different contributions is taken into account, we expect the model to cover all experimental data in a satisfying way. Moreover, this will then allow to predict streaming patterns and further understand the different mechanisms leading to the different pattern types.

One aspect which is left out in this chapter for more conciseness are the streaming velocities. As they only played a minor role in the experimental part, the additional information here in the theoretical chapter did not seem to add any valuable information. In the long term, however, the streaming velocity plays of course a major role, as it rules shear stresses induced by the flow. A more thorough investigation of this point is hence more than desirable.

Conclusions and prospects

Conclusions

The objective of the present work was the characterization of streaming patterns around acoustically excited, nonspherically oscillating microbubbles. For this, chapter 1 laid the general basis of bubble dynamics, chapter 2 was dedicated to the experimental triggering of nonspherical surface modes and the general understanding of the bubble dynamics and in chapter 3 I presented the experimental results of the microstreaming experiments. To validate these experiments, we developed an analytical model which is presented in chapter 4. With this, the main objective has been achieved and in some aspects I was able to go further than the initially planned purely experimental analysis. In the following, I will summarize some of the most important results from the different chapters in view of the general context.

Before doing so, let me allow one more reference to my supplementary project on jetting of microbubbles, which has been placed in appendix A.

Bubble coalescence and dynamics

In order to trigger surface modes, we have to set the correct parameters, notably bubble size and acoustic pressure. However, in addition to this, we have further requirements: we need a controlled orientation of the excited modes and we need them to oscillate in a steady-state regime. As none of the currently used methods to trigger surface modes fulfills these requirements, we adapted bubble coalescence inside an acoustic field to meet these needs. Indeed, we confirmed that the theoretically predicted modes are obtained via our bubble coalescence experiments. Furthermore, the complete control of the surface oscillations is obtained through the control of their axis of symmetry, which is defined by the direction of impact between the two bubbles. As a supplementary point, the bubble dynamics agrees very well to the numerical implementation of an analytical model.

Experimental microstreaming

With complete control of the bubble dynamics, we were then able to add the observation of microstreaming. During the experiments we aimed for a complete characterization, that means for capturing both streaming and dynamics. First of all, we managed to visualize microstreaming

patterns around nonspherically oscillating and acoustically trapped microbubbles, a work that had not been done in detail before. A large variety of different patterns can be observed. I managed to classify them in two groups, large cross-like patterns and smaller lobe-shaped patterns. For predominant surface modes 3 and 4, the two classes can be distinguished through the bubble size. Based on the bubble dynamics, we were able to form several hypotheses as to the exact physical mechanisms which are involved in the distinction, the most important being the predominant mode, richness of modal content, phase differences between several modes and possibly the occurrence of translational oscillations.

Theoretical streaming model

In order to validate the experimentally obtained streaming and possibly the different hypotheses on the important parameters, we wanted to implement an analytical model. All existing models have however some drawbacks concerning the exact representation of our experimental conditions. For this reason, a new model was developed. It takes the bubble dynamics as input parameters and calculates the streaming as resulting from the interaction between two modes. A richer modal content can hence simply be represented as superposition of several simulations. At this point, a good part of the streaming model has been derived, in particular the general equations have been set up and solutions for all simplified cases have been found. This allows already a first comparison to the experiments and confirms some of the observed patterns. Furthermore, we can qualitatively confirm that the phase difference between two modes plays an important role, in particular for the magnitude of the produced streaming. Also, the richness of the modal content increases the number of possible interactions and hence plays a role for the exact pattern type.

Future work and prospects

In the respective conclusions for the individual chapters I have already mentioned some minor and major aspects that deserve a closer look in future work. I will not repeat every detail here, but rather concentrate on the global picture.

Theoretical streaming model

As written in chapter 4, the theoretical model is yet to be finalized for the general case $n-m$. Once the complete set of interactions available, we will be able to apply it to the experimental data without keeping the present doubt on the possibly missing component. With the superposition of different interactions, a detailed comparison should be possible and I expect it to lead to very satisfying results.

A particularly interesting project would then be the combination of the different theoretical models we use. The input parameters driving frequency, acoustic pressure and bubble radius will provide the bubble dynamics which can then be used for the streaming calculation.

Experimental aspects

On the experimental side, an important aspect is the transition from the perfect case of a single bubble to conditions more likely to be found in real medical applications. Interaction with other bubbles, with cells or different types of boundaries are of interest. Our preliminary tests on a pair of bubbles are currently retaken and extended by G. Regnault and the interaction between a bubble and a cell is investigated by M. Fauconnier.

Boundaries may be introduced in the proximity of the bubble, but bubbles may also be attached to a wall. For this, we first have to understand the bubble dynamics of such a bubble. I have conducted first experiments during my stay in Glasgow and M. Fauconnier is also currently working on this aspect. A next step would then consist in the observation of streaming around such bubbles. This would be particularly interesting as streaming around bubbles attached to a solid boundary has already been investigated by several authors, however usually without surface modes and detailed consideration of the bubble dynamics.

Importance for medical applications

An important point to investigate further is a more quantitative analysis on the streaming velocities and not only on the pattern type. In fact, it is these streaming velocities and the associated shear stresses that are relevant for medical applications such as sonoporation. As an immediate step this means to further improve the experimental setup for streaming visualization in order to allow a better evaluations of the high velocity regions close to the bubble. At the same time a quantitative (and not only qualitative) evaluation of the velocities resulting from the simulations, which has not been done yet due to time constraints, might provide validation of the model and then allow supplementary information difficult to extract from experiments.

I hope that eventually, these rather fundamental physics results will find application in medical applications such as sonoporation. As an example, allowing a safe prediction on the extension of the streaming patterns and magnitude of the induced shear stresses might have beneficial impact to localize the region of impact.

Appendix A

Jetting of contrast agent microbubbles

As emphasized in the introduction, the main body of my work exclusively dealt with air bubbles in water which had radii of some tens of micrometers. However, when discussing the medical context in section 1.1 and the different ways to obtain bubbles in section 1.3, I have already mentioned the possibility to use prefabricated, shelled microbubbles. The present appendix now deals with these bubbles, which are produced for medical applications. Note that a main difference is the bubble size, now only of the order of a few micrometers which leads to relatively high resonance frequencies in the MHz range. The shell itself does not have an important role in our experiments, because we will observe very large expansion ratios, and as Ilovitsh et al. [55] state, in this case the bubble can be modeled in the same way as a non-shelled one. The phenomenon we are interested in is the so-called jetting, a directed and fast deformation of the expanding and imploding microbubble.

Shelled microbubbles were initially used as contrast agents at ultrasound MHz frequencies relatively close to their resonance frequencies and a fairly large number of studies on the microbubble response exists (for example Chomas et al. [17]). However, they also find use in therapeutic applications, and more recently driving frequencies of a few hundred kHz have been studied. For instance for brain-blood-barrier (BBB) opening, relatively low frequencies are necessary for sufficient acoustic transmission through the skull [72]. Ilovitsh et al. [55] recently studied the expansion ratios of contrast agent bubbles at 250 kHz driving and presented their data as streak images. These authors focused on the question of which driving pressure is needed for inertial cavitation to occur. They furthermore argue that inertial cavitation is to be avoided for reparable sonoporation. However, jetting does occur in some applications and its influence on nearby tissue has for instance been studied by Prentice et al. [99] and Chen et al. [15, 14]. We are hence interested in the exact behavior of jetting microbubbles at low driving frequencies, a feature that was not studied before.

I have conducted the here presented experiments during my stay with P. Prentice at the University of Glasgow. The results are published in [OP5].

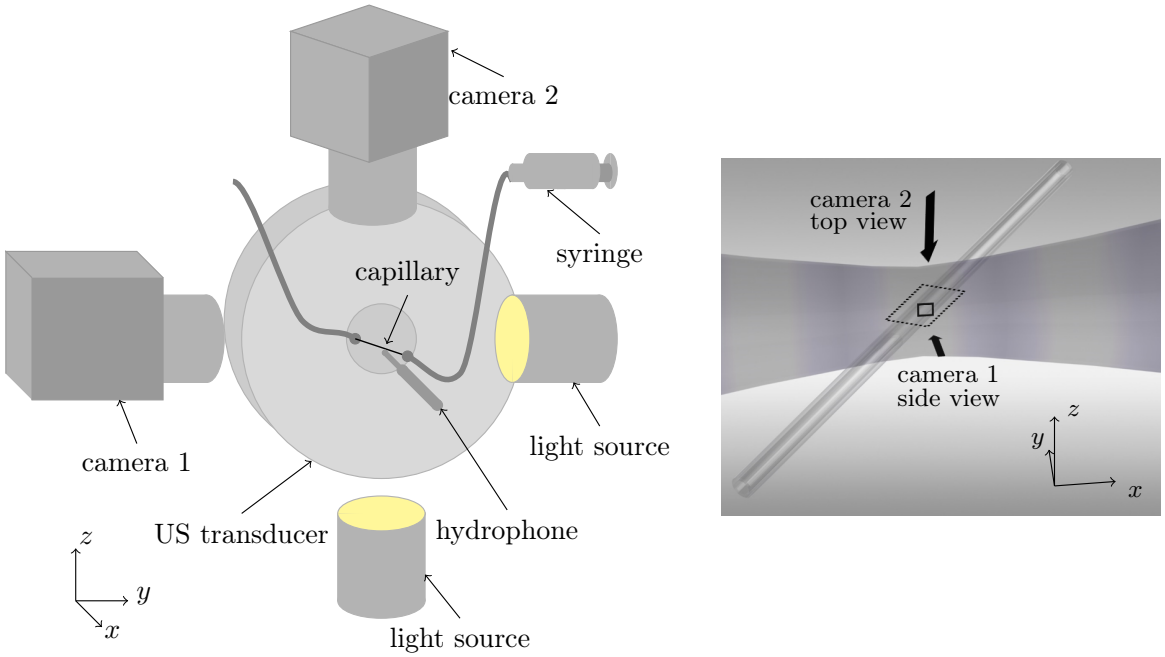

(a) (b)

Figure A.1: Experimental setup for the jetting experiments; (a) schematic representation of the overall setup; (b) zoom on the capillary and ultrasound beam (the wave length is representative with respect to the capillary width), with the camera planes indicated.

A.1 Experimental setup and procedure

A.1.1 Experimental setup

A schematic representation of the experimental setup is shown in figure A.1. Besides the two cameras and the light source for camera 1 all components are submerged inside the tank, which measures 420 mm × 438 mm × 220 mm. The tank was filled with degassed water, which we obtained by filling boiling water into containers, sealing those and letting everything cool down. This leads to less then 4 mg L^{-1} of dissolved oxygen left inside the liquid [116].

Acoustics

A focused ultrasound transducer (H-149, Sonic Concepts) is excited by a waveform generator (DG4102, Rigol Technologies) and a power amplifier (2100L, Electronic and Innovation). The transducer has an outer diameter of 110 mm, and geometrically focuses at 68 mm from the front face. The transducer was mounted vertically so that the generated sound field propagates in the horizontal x-direction. The position of the ultrasound transducer can be adjusted in the vertical z-direction with a millimeter screw. We operated the transducer at its first harmonic of 200 kHz.

A polycarbonate capillary (inner diameter 500 µm, outer diameter 550 µm, Paradigm Optics) was mounted into the chamber via a custom 3-d printed support. The capillary was crossing the

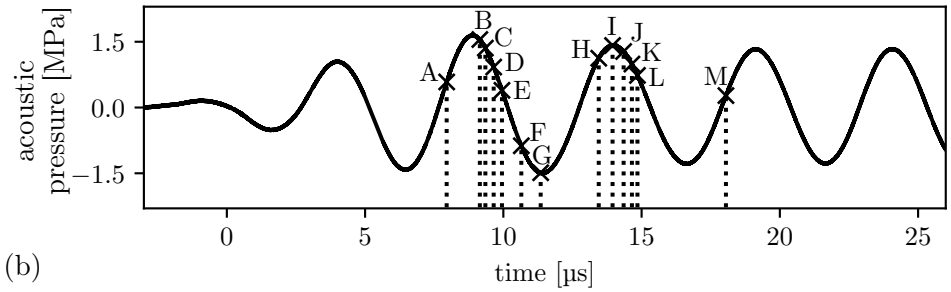

Figure A.2: Hydrophone signal at the focal spot for a transducer voltage set to 1.5 mV peak-peak. The letters indicated here are references for the snapshot series shown in figure A.5.

acoustic focus with an angle of 45° relative to the propagation axis.

The acoustic pressure at the focal spot and behind the capillary was measured with a 0.2 mm polymer Polyvinylidenfluorid needle hydrophone (Precisions Acoustics) aligned to the x-axis, in other words along the axis of ultrasound propagation. The hydrophone position could be adjusted via a xyz micro-manipulator. In previous studies [116], a 5 % attenuation of the ultrasound signal due to the presence of the capillary had been observed. The hydrophone itself has a ±9% magnitude uncertainty associated with the calibration. Voltage data from the needle hydrophone system was amplified by about 25 dB (Hydrophone Amplifier, 7185 Precision Acoustics) and collected to an oscilloscope (MS07104A, Agilent Technologies). For the main part of the work, a 10-cycle acoustic burst was used. The voltage amplitude set for the wave generator was varied between 0.5 V and 1.4 V and led to pressure amplitudes between 0.4 MPa and 1.5 MPa. As for my experimental setup in Lyon, see section 2.3, a linear relation between the applied voltage and the acoustic pressure could be observed. An exemplary hydrophone signals is given in figure A.2. The time $t = 0\,\mu s$ is defined as the beginning of the side view recording. The transducer was triggered at $t = -60\,\mu s$. Note that the propagation time from the transducer to the focal spot explains this delay.

Contrast agent microbubbles

SonoVue TM is a commercial ultrasound contrast agent consisting of phospholipid shelled, sulphur hexafluoride gas-core microbubbles, with a mean diameter between 2 µm and 3 µm (95 % < 10 µm), and associated resonance frequencies larger than 2 MHz. We prepared the SonoVue TM suspensions with non-degassed, de-ionized water and then diluted further to have few enough bubbles to avoid bubble-bubble interaction during the experiments. The suspension was filled in a syringe which was connected to a microlance (internal diameter of about 0.6 mm) which itself was connected to the capillary. A syringe pump (74900, Cole Parmer) allowed to pump a fixed volume of 11 mL h^{-1}. The exhaust end of the capillary vented to a collection reservoir, located outside the water tank.

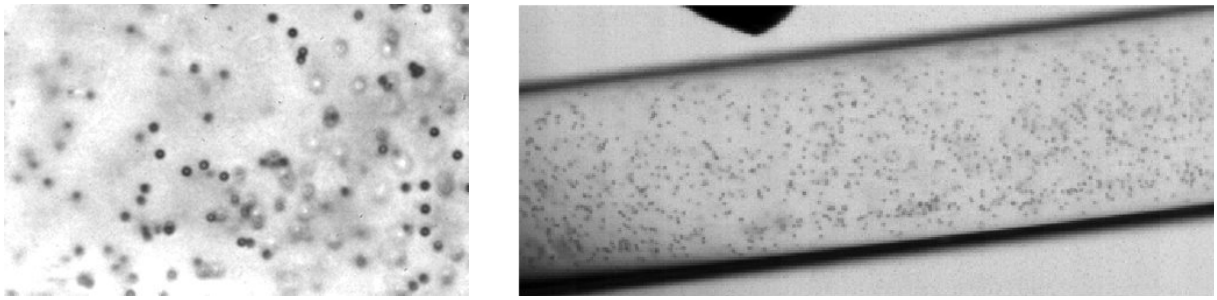

Figure A.3: Snapshots of 7.5 µm diameter beads, *left:* side view (camera 1, frame size 435 µm × 270 µm) and *right:* top view (camera 2, frame size 1670 µm × 700 µm). In the top view image, a part of the hydrophone tip can be seen.

Visualization

We record the bubble jetting with two cameras. The main information is gained from the side view, camera 1 (Shimadzu HPV-X2) equipped with a 20× long working distance objective lens (0.42 NA, Mitutoyo). It is adjusted to film the xz-plane and has a frame size of 400 pixel × 250 pixel leading to a field of view of about 435 µm × 270 µm due to a pixel size of about 1.1 µm. For each experiment 256 images were recorded with a frame rate of 10 Mfps. Illumination was provided by a synchronous (to frame capture) 10 ns laser pulses (CAVILUX Smart, Cavitar), coupled to a liquid light guide and collimating lens. This configuration has been used in previous setups to facilitate the shadowgraphic imaging of the pressure transients due to refractive index variations. This led to the fact that in many cases the shock wave emitted during bubble collapse was slightly visible on our recordings.

The top view imaging, camera 2 (Fastcam SA-Z 2100K, Photron) equipped with a 5×0.14 NA long working distance objective (Mitutoyo, focal length in air 40.0 mm) in a water-tight casing, allowed an overview over the whole cavitation event due to a much larger frame. With a frame size of 384 pixel × 160 pixel and a spatial resolution of about 4.3 µm pixel^{-1} the field of view covers the size of about 1670 µm × 700 µm. Reciprocally, we only dispose of a relatively low sampling rate of 210.000 fps, hence only taking one snapshot per acoustic cycle. The light source necessary for shadowgraphic imaging with camera 1 was provided by a continuous Halogen bulb light source (Thorlabs) coupled to a liquid light guide with the output located at about 10 mm below the capillary.

Figure A.3 shows two sample images, each of them taken with one of the cameras, showing 7.5 ± 0.2 µm diameter polymer microspheres (PS06005, Bangs Laboratories).

A.1.2 Experimental procedures

The different instruments, in particular the two cameras, the ultrasound transducer and oscilloscope were triggered and synchronized with a delay generator (DG535, Stanford Research Systems). Hydrophone measurements were done separately from the jetting and without the presence of microbubbles. The purpose of the present work was not to measure the acoustic

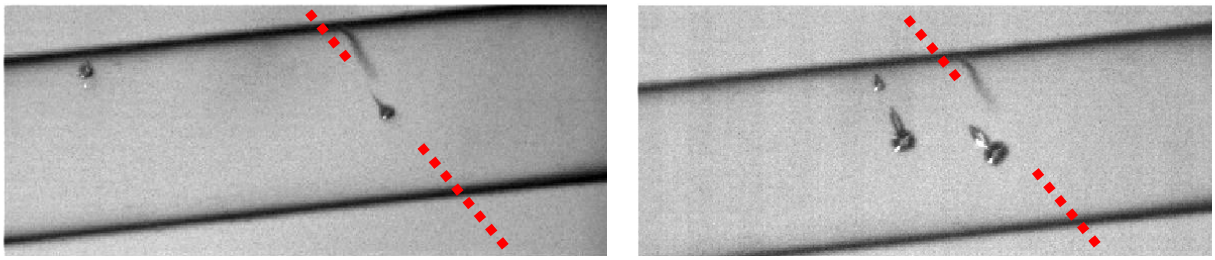

Figure A.4: Two examples of topview images; *left:* bubble is not influenced by other cavitation events and is jetting in the direction of the ultrasound propagation (red dotted line, the gap corresponds approximately to the frame of view of the side view camera); *right:* the jet is deviated due to the presence of other bubbles. Frame size for both is about 1670 µm × 700 µm.

emission of cavitation activity as done in previous work [116], but to visualize the jetting. The information on the hydrophone signal helps to understand the ultrasound field to which the bubbles are exposed.

I conducted a large number of repetitions, each time triggering the ultrasound transducer and recording top and side view images. For further analysis I only kept cases where (1) the bubble was visible in the field of view of camera 1 and (2) no influence of other cavitation events on the bubble could be observed. Two examples, one of a deviated and one of a non-deviated jet are shown in figure figure A.4.

During the experiments, I conducted in particular two measurement series.

1. For the first series, the transducer position was fixed. The pressure amplitude was varied between 0.4 MPa and 1.5 MPa.

2. For the second series, the applied voltage was fixed so that the pressure amplitude was 1.5 MPa in the focal spot. Note that these amplitudes are well above those which are generally applied when ultrasound contrast agents are used. The transducer position was then varied from −1.3 mm to 1.3 mm in 0.1 mm increments in the vertical z-direction. Keeping all other parameters constant, this leads to the observed bubble changing its position relative to the focal spot.

A.2 Major results

The two measurement series had the objective to study the jetting behavior in the dependence on (1) the pressure amplitude and (2) the transducer position. Figure A.5 gathers a large quantity of information, that I will detail step by step in the following. As the question of the directed jetting due to a varying transducer position is faster to discuss, let us start with that point.

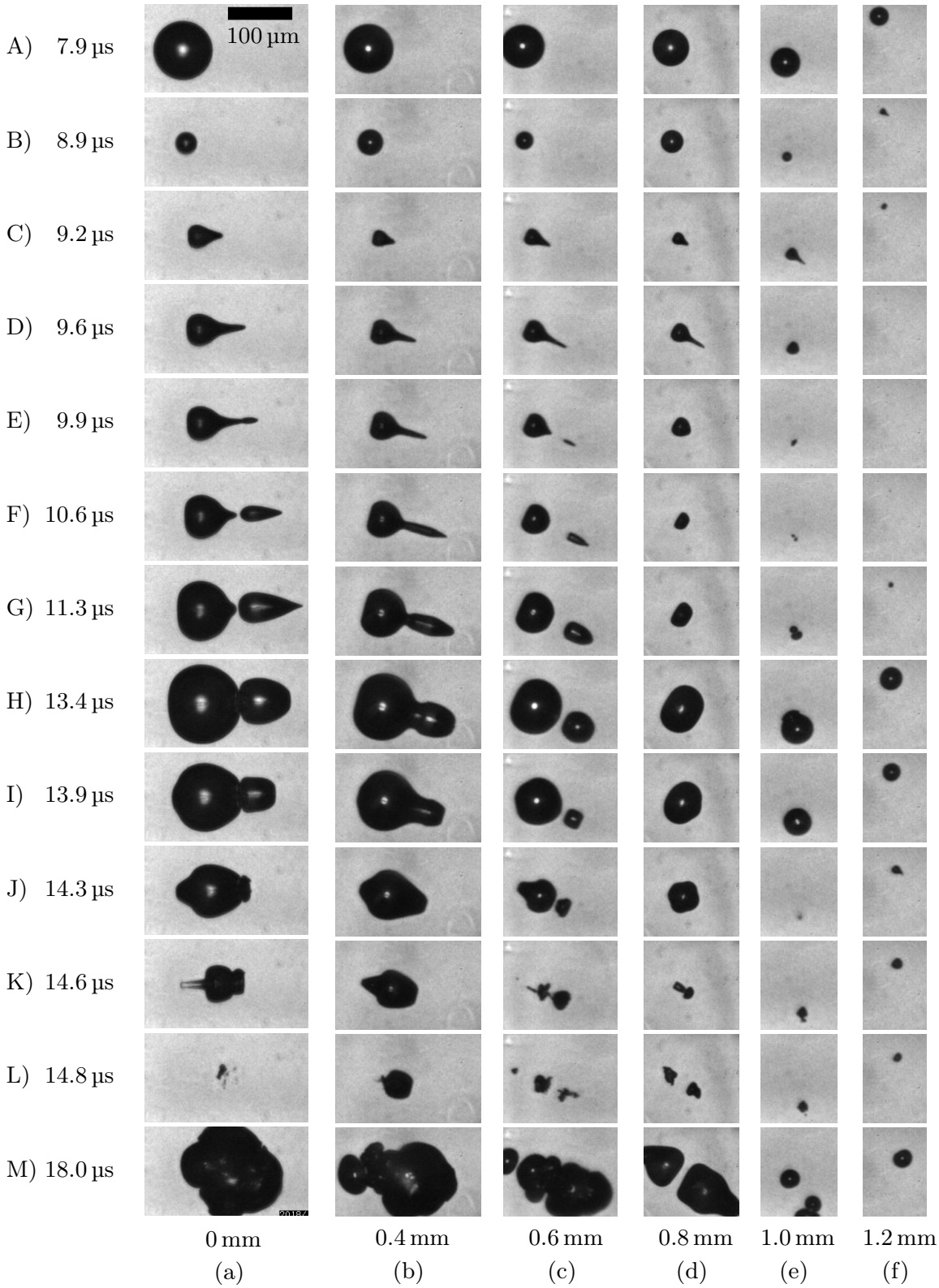

Figure A.5: Representative images of jetting observed with the camera 1 (side view) for different transducer positions (a) 0 mm to (f) 1.2 mm. The peak negative pressure in the focal spot is always 1.5 MPa, see figure A.2, where the characteristic instants A) 7.9 µs to M) 18.0 µs are indicated.

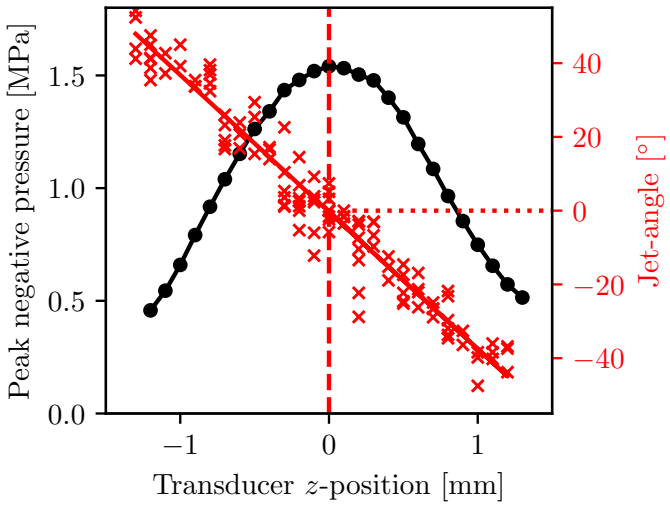

Figure A.6: Jetting angle and peak negative pressure with respect to the transducer position.

A.2.1 Directed jetting

When the transducer is displaced along the z-direction, the position of the focal spot changes with respect to the capillary and the field of view of camera 1. Consequently, a bubble will "feel" a pressure gradient when being exposed to the ultrasound field. As can be seen in the different columns of figure A.5, the jet is deviated from the horizontal direction. This observation is coherent with earlier studies by Gerold et al. [45] and Rosselló et al. [108] who stated for laser induced gas bubbles that the jets are directed along the local pressure gradient. All our experimentally obtained jetting angles with respect to the transducer position are summarized in figure A.6. For the used transducer, a linear dependence can be observed. In figure A.6, we furthermore plot the pressure amplitude in dependence on the transducer position. As can be expected, the pressure is highest on-axis in the focal spot and decreases further away from it. This explains the fact that bubbles in the center of the focal spot have the highest expansion ratios. So, let us discuss the influence of the pressure amplitude in the following in more detail.

A.2.2 Jetting behavior at different pressure amplitudes

As can already be guessed from figure A.5, the jetting behavior depends on the pressure amplitude of the incident acoustic wave. In the following, I will focus on the case of a relatively high pressure field, typically around 1.5 MPa and the case of a relatively low pressure field, typically around 0.5 MPa.

Morphology of a bubble jet at relatively high pressure

The example of figure A.5 column (a) presents the case of a bubble jetting horizontally at 1.5 MPa pressure amplitude, hence a relatively high pressure. When exposed to the pressure wave, a first small expansion to about 5 µm radius can be observed due to the first negative pressure peak

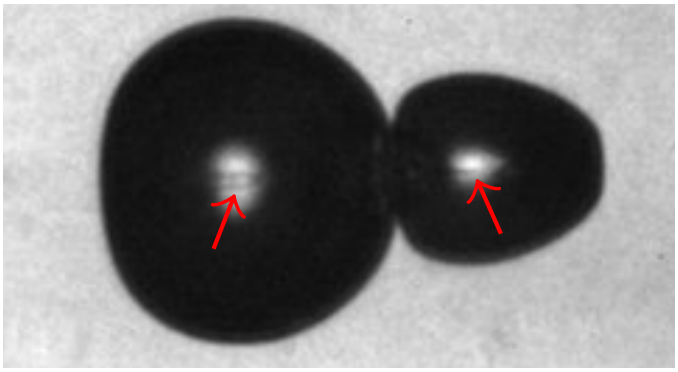

Figure A.7: Zoom onto snapshot (a) H) from figure A.5 to highlight the thin water filament inside the gas bubble.

at about 1.3 µs (visible on the hydrophone data in figure A.2). This small expansion is hardly visible and I have omitted it in figure A.5 for more readability. Furthermore, it has no influence on the following phenomenon. The second negative pressure peak with its minimum at about 6 µs causes a large expansion (here up to roughly 45 µm radius). Due to inertia, the implosion (between 8.9 µs and 9.2 µs) only takes place when there is already a positive pressure applied. Following the implosion, a jet starts to form. In the present example, the jet detaches at 10.6 µs. A very similar morphology can be observed with no splitting, for instance in column (b) of figure A.5. But let us continue to consider column (a), where approximately at the moment when the pressure changes from negative to positive ($\approx$ 12.3 µs), the jetting nose starts to flatten and retract. This initiates a counter-jet, that becomes very prominent at 14.6 µs. The implosion is then followed by a disintegration into a cavitation cloud.

The morphology of the jetting presented here is very similar to the one recently reported by Rosselló et al. [108], who worked with laser induced bubbles, a much lower driving frequency of 26.1 kHz and a higher viscous liquid for an easier visualization of the jetting behavior. Rosselló et al. [108] were the first to report on the rebound-jet. A good explanation is the inverse pressure gradient which occurs while the bubble is expanded and which is acting upon it. In other studies, such as Gerold et al. [45], the acoustic frequency is much higher, so that the very fast change between positive and negative pressure does not interact with the expanded gas cavity.

There is one more well known fact on bubble jetting, which I want to point out. In particular for the large bubbles at high pressure the thin water filament which is formed inside the bubble, and which is the true jet, is well visible on most recordings. One enlarged snapshot with arrows indicating the water filament is shown in figure A.7. Earlier schematic explanations have for instance been given by Ohl and Ikink [88]. It is these water filaments that are being pushed through the bubble and that can have a damaging impact due to their inertia.

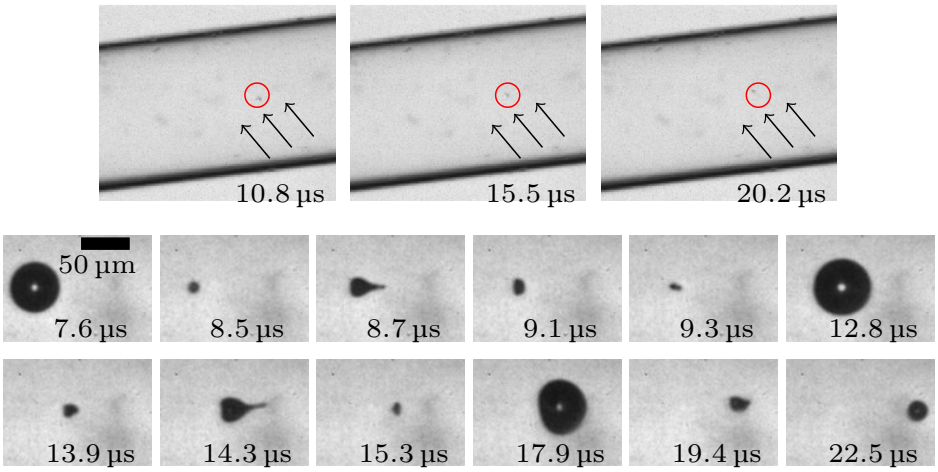

Figure A.8: Repeated on-axis jetting at 0.7 MPa peak negative pressure. The *upper row* shows the top view imaging, where a forward movement becomes visible. The arrows indicate the direction of the ultrasound wave. Note that the moments at which the top view was taken do not correspond to moments of maximum expansion. The two *lower rows* show chosen snapshots of the side view imaging, where repeated jetting becomes obvious.

Repeated jetting at lower pressure

The example of column (f) in figure A.5 corresponds to jetting at relatively low pressure amplitude. Here, the time of expansion is much shorter and the maximum expansion much smaller. As we can see in particular in snapshots B) and J), repeated jetting occurs since the bubble returns to an approximately spherical shape after each implosion. This observation can be confirmed by on-axis jetting at low pressure amplitude. For about 0.5 MPa peak negative pressure, repeated jetting systematically takes place. In figure A.8, I show one example at 0.7 MPa peak negative pressure, as a slightly larger expansion makes the snapshot series easier to read. We can see three expansions followed by an implosion and a jet to the right in the direction of the traveling ultrasound wave. Repeated jetting has been recently reported for bubbles in cavitation clouds formed at a vibrating horn tip [85] and in the context of multibubble sonoluminescence [12, 120]. An interesting aspect but difficult to discern is the last moment of collapse after having formed a jet (9.3 µs and 15.3 µs in figure A.8). In particular in the movie version, a slight movement to the left is discernible. Does this have similar mechanisms to the rebound jet for larger expansions or is it simply explained by the aspherical collapse of a bubble such as described by Ohl et al. [90]?

A.3 Conclusions and perspectives

When micrometer size contrast agent microbubbles are exposed to a few hundred kiloherz ultrasound waves with sufficiently high pressure amplitudes, they show jetting behavior. As reported in the above sections, for 200 kHz driving frequency and peak negative pressures around 0.5 MPa

bubbles usually jet repetitively, whereas at higher pressure amplitudes around 1.5 MPa large expansion ratios and jets including rebound jets with a following disintegration into a cavitation cloud occur.

For medical applications, it is also important to state that the jetting direction depends on the local pressure gradient, hence on the position of the bubble in the acoustic field created by the transducer.

In the same way as my study on microstreaming around one single isolated bubble is an idealized case, the study of jetting of one single bubble is a simplification of real life as well. It is an appropriate way to better understand the underlying physics, but in order to apply them to real medical applications some more aspects have to be taken into account. One of them is the presence of other bubbles, a phenomenon that sometimes occurred during my experiments. As shown in figure A.4, the jet is normally deviated by the presence of other bubbles. Detailed studies on when bubbles jet towards each other or away from each other have been conducted by Fong et al. [42], an important parameter is the phasing at which the bubbles reach maximum size. Under the present conditions bubbles mostly seemed to jet towards each other, which is coherent with the mirror effect of two bubbles growing at the same time. The mirror effect has the same consequence as a solid wall towards which a bubble will jet. In any case, the presence of both an ultrasound wave and other bubbles makes the prediction of the exact behavior more difficult. Further important aspects to study in the future are then the presence of tissue-like boundary conditions, because eventually it is the impact of the jet on tissue that is relevant for medical applications.

Appendix B

Supplementary steps for the theoretical microstreaming model

This appendix contains some supplementary steps for the derivation of the theoretical model in chapter 4 which have been left out for more conciseness of the main document.

B.1 General theory of the analytical model

B.1.1 First-order solution

Solutions for the velocity potentials

In view of the axisymmetry, we have $\varphi = \varphi(r, \theta, t)$ for the scalar velocity potential and $\boldsymbol{\psi} = \psi(r, \theta, t)\boldsymbol{e}_\varepsilon$, where $\boldsymbol{e}_\varepsilon$ is the azimuth vector, and which leads to $\nabla \cdot \boldsymbol{\psi} = 0$. Substituting equation (4.3) into the continuity equation (4.1) gives

$$\Delta\varphi = 0 \ , \tag{B.1}$$

which can be solved in view of the excitation in equation (4.5) by

$$\varphi = \sum_{n=0}^{N} a_n \, \mathrm{e}^{-\mathrm{i}\,\omega_n t} \left(\frac{R_0}{r}\right)^{n+1} P_n \ , \tag{B.2}$$

where a_n are all constants to be found. Substituting equation (4.3) into the Navier-Stokes-equation (4.2), applying the curl $\nabla\times$ on both sides and using the identity $\nabla \times (\nabla \times \boldsymbol{\psi}) = \nabla(\nabla \cdot \boldsymbol{\psi}) - \Delta\boldsymbol{\psi} = -\Delta\boldsymbol{\psi}$ gives

$$\Delta\left(\Delta - \frac{1}{\nu}\frac{\partial}{\partial}\right)\boldsymbol{\psi} = 0 \quad \Rightarrow \quad \left(\Delta - \frac{1}{\nu}\frac{\partial}{\partial}\right)\boldsymbol{\psi} = 0 \quad \text{and} \quad \Delta\boldsymbol{\psi} = 0 \ , \tag{B.3}$$

which, in view of equation (4.5), has the solutions

$$\boldsymbol{\psi} = \boldsymbol{e}_\varepsilon \sum_{n=1}^{N} b_n \, \mathrm{e}^{-\mathrm{i}\omega_n t} h_n^{(1)}(k_n r) P_n^1 + \boldsymbol{e}_\varepsilon \sum_{n=0}^{N} c_n \, \mathrm{e}^{-\mathrm{i}\omega_n t} \left(\frac{R_0}{r}\right)^{n+1} P_n^1 \ , \tag{B.4}$$

where P_n^1 is the associated Legendre polynomial of the first order, $h_n^{(1)}$ is the spherical Hankel function of first kind, $k_n = (1+i)/\delta_n$ and $\delta_n = \sqrt{2\nu/\omega_n}$ is the viscous penetration depth at the frequency ω_n, and b_n and c_n constants to be found. However, taking into account the identity $\nabla \times \left[\boldsymbol{e}_\varepsilon r^{-(n+1)} P_n^1\right] = -n\nabla\left[r^{-(n+1)} P_n\right]$, we find that the solution equation (B.2) and the second part of equation (B.4) are just two version of the same solution. We can hence neglect the part with the c_n factor.

Expressions for the velocity

Once the velocity potentials are known, the components for the velocity itself can be obtained by plugging them into equation (4.4) which then leads to the solution given in the main text, see equation (4.8). To simplify the expression, the following identities (with $P_n' = dP_n/d\mu$ and so on) have been used:

$$\begin{aligned} & P_n^1 = -\sqrt{1-\mu^2} P_n' \quad \text{and} \quad (1-\mu^2)P_n'' = 2\mu P_n' - n(n+1)P_n \\ \Rightarrow \quad & \frac{\mu}{\sqrt{1-\mu^2}} P_n^1 - \sqrt{1-\mu^2} P_n^{1\prime} = -n(n+1)P_n \ . \end{aligned} \tag{B.5}$$

Applying the boundary conditions

In order to determine a_n and b_n in equation (4.8) we can now apply the two boundary conditions equations (4.6) and (4.7) at the bubble surface $r = R_0$. Plugging the condition of conformity in the radial velocity equation (4.6) into equation (4.8a) gives

$$a_0 = \mathrm{i} R_0 \omega_0 s_0 \quad \text{and} \quad a_n + n h_n^{(1)}(x_{n0}) b_n = \frac{\mathrm{i} R_0 \omega_n s_n}{n+1} \quad \text{for} \quad n \geq 1 \ . \tag{B.6}$$

Substituting both parts of equation (4.8) into equation (4.7) leads to

$$2(n+2)a_n + \left[(n^2+n-2)h_n^{(1)}(x_{n0}) - x_{n0}^2 h_n^{(1)\prime\prime}(x_{n0})\right] b_n = 0 \quad \text{for} \quad n \geq 1 \ . \tag{B.7}$$

From equations (B.6) and (B.7) we finally obtain the constants a_0, a_n and b_n given in the main document in equation (4.9).

B.1.2 Time-averaged second-order solution

Due to axial symmetry $\boldsymbol{\Psi} = \Psi(r,\theta)\boldsymbol{e}_\varepsilon$ we consequently have $\nabla \times \boldsymbol{\Psi} = 0$. Similarly to appendix B.1.1, $\nabla \times (\nabla \times \boldsymbol{\Psi}) = -\Delta \boldsymbol{\Psi}$, so that upon applying the curl on the continuity equa-

tion (4.10) we obtain

$$\Delta^2 \boldsymbol{\Psi} = -\frac{1}{\nu} \nabla \times \left\langle (\boldsymbol{v} \cdot \nabla) \boldsymbol{v} \right\rangle \ . \tag{B.8}$$

Applying equation (4.3) in equation (B.8) and doing some mathematical simplifications, one can finally obtain equation (4.13) from the main text. As a next step, we aim to write the vector equation (4.13) as a scalar equation. For this, we need to introduce the Laplace operator in spherical coordinates,

$$\Delta = \Delta_{r\theta} + \frac{1}{r^2 \sin^2\theta} \frac{\partial^2}{\partial \varepsilon^2} \quad \text{with} \quad \Delta_{r\theta} = \frac{1}{r^2} \frac{\partial}{\partial r} \left(r^2 \frac{\partial}{\partial r} \right) + \frac{1}{r^2 \sin\theta} \frac{\partial}{\partial \theta} \left(\sin\theta \frac{\partial}{\partial \theta} \right) \ . \tag{B.9}$$

With the fact $\partial^2 \boldsymbol{e}_\varepsilon / \partial \varepsilon^2 = -\boldsymbol{e}_\varepsilon$ this leads to

$$\Delta^2 \boldsymbol{\Psi} = \boldsymbol{e}_\varepsilon \left(\Delta_{r\theta} - \frac{1}{r^2 \sin^2\theta} \right)^2 \Psi \quad \text{and} \quad \Delta \boldsymbol{\psi} = \boldsymbol{e}_\varepsilon \left(\Delta_{r\theta} - \frac{1}{r^2 \sin^2\theta} \right) \ . \tag{B.10}$$

Applying those expression to equation (4.13), this leads eventually to equation (4.14).

B.1.3 General expression for streaming between the modes n and m

As written in the main text, equation (4.15), we assume that $\boldsymbol{\psi} = \boldsymbol{\psi}_n + \boldsymbol{\psi}_m$ and $\boldsymbol{v} = \boldsymbol{v}_n + \boldsymbol{v}_m$. Furthermore, we suppose $\omega_n = \omega_m$. Under these conditions, the first solution of equation (B.3) becomes

$$\Delta \boldsymbol{\psi} = -k_n^2 \boldsymbol{\psi} \ , \tag{B.11}$$

which, using equation (B.10), gives

$$\Delta_{r\theta} \psi - \frac{\psi}{r^2 \sin^2\theta} = -k_n^2 \psi \ . \tag{B.12}$$

Using this, equation (4.14) can be reduced to

$$\left(\Delta_{r\theta} - \frac{1}{r^2 \sin^2\theta} \right)^2 \Psi = \frac{1}{2\nu r} \Re \left\{ k_n^2 \left(\frac{\partial}{\partial r} (r v_r \psi^*) + \frac{\partial}{\partial \theta} (v_\theta \psi^*) \right) \right\} \ . \tag{B.13}$$

Here, the fact that $k_n^{2*} = -k_n^2$ has been used.

As written in the main text, equation (4.16), we assume that $\Psi = \Psi_{nm} + \Psi_{nn} + \Psi_{mm}$. We hence need solutions for the three terms, and from equation (B.13) we can obtain the two solutions given in the main part of the manuscript in equations (4.17) and (4.18). As a last step, we can apply explicit expressions by using equations (4.8) and (B.4) to obtain

$$\begin{aligned} &\left(\Delta_{r\theta} - \frac{1}{r^2 \sin^2\theta} \right)^2 \Psi_{nn} \\ &\quad = \frac{n+1}{2\nu r^2} P_n P_n^1 \Re \left\{ k_n^2 a_n b_n^* \left(\frac{x_{n0}}{x_n} \right)^{n+1} \left[(n+1) h_n^{(1)}(x_n) - x_n h_n^{(1)\prime}(x_n) \right]^* \right\} \end{aligned}$$

$$- \frac{\sqrt{1-\mu^2}}{\nu r^2} P_n^1 P_n^{1\prime} \Re \left\{ k_n^2 h_n^{(1)*}(x_n) \left[a_n b_n^* \left(\frac{x_{n0}}{x_n} \right)^{n+1} - b_n b_n^* x_n h_n^{(1)\prime}(x_n) \right] \right\} \quad , \tag{B.14}$$

$$\begin{aligned}
&\left(\Delta_{r\theta} - \frac{1}{r^2 \sin^2\theta} \right)^2 \Psi_{nm} \\
&= \frac{n+1}{2\nu r^2} P_n P_m^1 \Re \Bigg\{ k_n^2 a_n b_m^* \left(\frac{x_{n0}}{x_n} \right)^{n+1} \left[(n+1) h_m^{(1)}(x_n) - x_n h_m^{(1)\prime}(x_n) \right]^* \\
&\quad - n k_n^2 b_n b_m^* \left[x_n h_n^{(1)\prime}(x_n) h_m^{(1)*}(x_n) + x_n^* h_n^{(1)}(x_n) h_m^{(1)\prime *}(x_n) \right] \Bigg\} \\
&\quad + \frac{m+1}{2\nu r^2} P_m P_n^1 \Re \Bigg\{ k_n^2 a_m b_n^* \left(\frac{x_{n0}}{x_n} \right)^{m+1} \left[(m+1) h_n^{(1)}(x_n) - x_n h_n^{(1)\prime}(x_n) \right]^* \\
&\quad - m k_n^2 b_m b_n^* \left[x_n h_m^{(1)\prime}(x_n) h_n^{(1)*}(x_n) + x_n^* h_m^{(1)}(x_n) h_n^{(1)\prime *}(x_n) \right] \Bigg\} \\
&\quad - \frac{\sqrt{1-\mu^2}}{\nu r^2} \left[P_n^1 P_m^1 \right]' \Re \Bigg\{ b_m^* k_n^2 h_m^{(1)*}(x_n) \left[a_n \left(\frac{x_{n0}}{x_n} \right)^{n+1} - b_n \left[h_n^{(1)}(x_n) + x_n h_n^{(1)\prime}(x_n) \right] \right] \\
&\quad + b_n^* k_n^2 h_n^{(1)*}(x_n) \left[a_m \left(\frac{x_{n0}}{x_n} \right)^{m+1} - b_m \left[h_m^{(1)}(x_n) + x_n h_m^{(1)\prime}(x_n) \right] \right] \Bigg\} \quad .
\end{aligned} \tag{B.15}$$

B.2 Analytic solutions for specific cases

B.2.1 Case 0 – m

Ansatz

Substituting the approach of equation (4.21) into equation (4.19) we obtain

$$D^2 \left[P_m^1(\mu) F_m(x) \right] = k_0^4 P_m^1 \frac{h_m^{(1)}(x) - x h_m^{(1)\prime}(x)}{x^3} \quad . \tag{B.16}$$

Using the relation

$$(1-\mu^2) P_m^{1\prime\prime}(\mu) - 2\mu P_m^{1\prime} + \left[m(m+1) - \frac{1}{1-\mu^2} \right] P_m^1 = 0 \quad , \tag{B.17}$$

the left-hand side of equation (B.16) can be transformed to

$$D \left[P_m^1(\mu) F_m(x) \right] = k_0^2 P_m^1 \left[\frac{\mathrm{d}^2 F_m}{\mathrm{d}x^2} + \frac{2}{x} \frac{\mathrm{d}F_m}{\mathrm{d}x} - \frac{m(m+1)}{x^2} F_m \right] \tag{B.18}$$

$$\begin{aligned}
\Rightarrow \quad D^2 \left[P_m^1(\mu) F_m(x) \right] = k_0^4 P_m^1 \Bigg[&\frac{\mathrm{d}^4 F_m}{\mathrm{d}x^4} + \frac{4}{x} \frac{\mathrm{d}^3 F_m}{\mathrm{d}x^3} - \frac{2m(m+1)}{x^2} \frac{\mathrm{d}^2 F_m}{\mathrm{d}x^2} \\
&+ \frac{m(m+1)(m^2+m-2)}{x^4} F_m \Bigg] \quad .
\end{aligned} \tag{B.19}$$

The part with the Hankel-function of the right-hand side of equation (B.16) can be transformed in the following way

$$G_m(x) = \frac{h_m^{(1)}(x) - x h_m^{(1)'}(x)}{x^3} = \frac{(m+2)h_m^{(1)}(x) - x h_{m-1}^{(1)}(x)}{x^3} \ . \tag{B.20}$$

Using equations (B.19) and (B.20) in equation (B.17), we obtain a differential equation for F_m, given by equation (4.22) in the main text. The roots $\lambda = -(m+1)$, $\lambda = -(m-1)$, $\lambda = m$ and $\lambda = m+2$ given in the main text are obtained from the equation

$$\lambda(\lambda-1)(\lambda-2)(\lambda+1) - 2m(m+1)\lambda(\lambda-2) + m(m+1)(m^2+m-2) = 0 \tag{B.21}$$

The general solution of the homogeneous differential equation corresponding to equation (4.22a) is hence

$$F_m(x) = C_{1m}x^{-m-1} + C_{2m}x^{-m+1} + C_{3m}x^m + C_{4m}x^{m+2} \ , \tag{B.22}$$

$$F_m(x)' = -(m+1)C_{1m}x^{-m-2} - (m-1)C_{2m}x^{-m} + mC_{3m}x^{m-1} + (m+2)C_{4m}x^{m+1} \ , \tag{B.23}$$

where C_{jm} are constants and the derivative $F_m(x)'$ will be needed later. Now, in order to find the solution of the inhomogeneous differential equation (4.22), we set C_{jm} to be functions of x.

$$F_m(x) = C_{1m}(x)\underbrace{x^{-(m+1)}}_{=y_1} + C_{2m}(x)\underbrace{x^{-(m-1)}}_{=y_2} + C_{3m}(x)\underbrace{x^m}_{=y_3} + C_{4m}(x)\underbrace{x^{(m+2)}}_{=y_4} \ , \tag{B.24}$$

According to the method of variation of parameters, the functions $C_{jm}(x)$ fulfill the following system of algebraic equations:

$$C'_{1m}y_1 + C'_{2m}y_2 + C'_{3m}y_3 + C'_{4m}y_4 = 0 \tag{B.25a}$$

$$C'_{1m}y'_1 + C'_{2m}y'_2 + C'_{3m}y'_3 + C'_{4m}y'_4 = 0 \tag{B.25b}$$

$$C'_{1m}y''_1 + C'_{2m}y''_2 + C'_{3m}y''_3 + C'_{4m}y''_4 = 0 \tag{B.25c}$$

$$C'_{1m}y'''_1 + C'_{2m}y'''_2 + C'_{3m}y'''_3 + C'_{4m}y'''_4 = G_m(x) \ . \tag{B.25d}$$

Solving the algebraic system for each C'_{jm} and then integrating to obtain C_{jm} we obtain the expressions given in equation (4.24).

For the Stokes drift

For modes oscillating at the same frequency $\omega_n = \omega_m$ the Stokes drift becomes

$$\boldsymbol{V}_S^{nm} = \frac{1}{2\omega_n}\Re\{[\mathrm{i}(\boldsymbol{v}_n + \boldsymbol{v}_m)\cdot\nabla](\boldsymbol{v}_n + \boldsymbol{v}_m)^*\} \quad \Rightarrow \tag{B.26a}$$

$$V_{Sr}^{nm} = \frac{1}{2\omega_n}\Re\left\{\mathrm{i}(v_{nr}+v_{mr})\frac{\partial}{\partial r}(v_{nr}+v_{mr})^* - \frac{\mathrm{i}}{r}(v_{n\theta}+v_{m\theta})\left(v_{n\theta}+v_{m\theta}-\frac{\partial}{\partial\theta}(v_{n\theta}+v_{m\theta})\right)^*\right\} \tag{B.26b}$$

$$V_{S\theta}^{nm} = \frac{1}{2\omega_n}\Re\left\{\mathrm{i}(v_{nr}+v_{mr})\frac{\partial}{\partial r}(v_{n\theta}+v_{m\theta})^* - \frac{\mathrm{i}}{r}(v_{n\theta}+v_{m\theta})\left(v_{nr}+v_{mr}-\frac{\partial}{\partial\theta}(v_{n\theta}+v_{m\theta})\right)^*\right\} \tag{B.26c}$$

As for now, we are trying to solve the case $n = 0$ and m, we can further simplify equation (B.26). Furthermore, we know from equation (4.8) that $v_{0\theta} = 0$ and $\partial v_{0r}/\partial\theta = 0$, so that

$$V_{Sr}^{0m} = \frac{1}{2\omega_0}\Re\left\{\mathrm{i}v_{0r}\frac{\partial v_{mr}^*}{\partial r} + \mathrm{i}v_{mr}\frac{\partial v_{0r}^*}{\partial r}\right\} \tag{B.27a}$$

$$V_{S\theta}^{0m} = \frac{1}{2\omega_0}\Re\left\{\mathrm{i}v_{0r}\frac{\partial v_{m\theta}^*}{\partial r} - \frac{\mathrm{i}v_{0r}v_{m\theta}^*}{r}\right\} \tag{B.27b}$$

Plugging in equation (4.8) and using equation (4.9) in order to express a_m as a function of b_m, we finally obtain equation (4.32).

B.2.2 Case 1 – 1

Setting up the problem

For the calculation of the case $n = m = 1$ equation (B.14) simplifies to

$$\left(\Delta_{r\theta} - \frac{1}{r^2\sin^2\theta}\right)^2\Psi_{11} = -\frac{\mu\sqrt{1-\mu^2}}{\nu r^2}\Re\left\{-k_1^2a_1b_1^*\left(\frac{R_0}{r}\right)^2[h_1^{(1)}(x_1) - x_1h_1^{(1)'}(x_1)]^* - k_1b_1b_1^*x_1h_1^{(1)'}(x_1)h_1^{(1)*}(x_1)\right\} . \tag{B.28}$$

When introducing the simplified differential operator D from equation (4.20) and replacing a_1 by b_1, see equation (4.9), this gives

$$D^2\Psi_{11}(x_1,\mu) = \mu\sqrt{1-\mu^2}\frac{k_1^4|b_1|^2}{6\nu x_1^4}\Re\left\{\bar{x}^4h_1^{(1)''}(\bar{x})[x_1h_1^{(1)'}(x_1) - h_1^{(1)}(x_1)]^* - 6x_1^3h_1^{(1)'}(x_1)h_1^{(1)*}(x_1)\right\} . \tag{B.29}$$

Here, the abbreviation $\bar{x} = k_1R_0$ has been applied. Let us in the following introduce the further simplification $x = x_1$ for more convenience. From equation (B.29), we suppose analytical solutions to have the form

$$\Psi_{11}(x,\mu) = \mu\sqrt{1-\mu^2}\frac{|b_1|^2}{6\nu}\Re\{F(x)\} . \tag{B.30}$$

Substituting this approach into equation (B.28) we obtain

$$\frac{\mathrm{d}^4 F_m}{\mathrm{d}x^4} + \frac{4}{x}\frac{\mathrm{d}^3 F_m}{\mathrm{d}x^3} - \frac{12}{x^2}\frac{\mathrm{d}^2 F_m}{\mathrm{d}x^2} + \frac{24}{x^4}F_m = G_m(x) \tag{B.31a}$$

$$\text{with} \quad G_m(x) = \frac{1}{x^4}\left[\bar{x}h_1^{(1)''}(\bar{x})\left[xh_1^{(1)'}(x) - h_1^{(1)}(x)\right]^* - 6x^3 h_1^{(1)'}(x)h_1^{(1)*}(x)\right] \ . \tag{B.31b}$$

As before, we can use the method of variation of parameters to solve equation (B.31a). From the homogeneous form we obtain $\lambda = -3$, $\lambda = -1$, $\lambda = 2$ and $\lambda = 4$. The corresponding inhomogeneous equation then has the solution

$$F(x) = C_1(x)\underbrace{x^{-3}}_{y_1} + C_2(x)\underbrace{x^{-1}}_{y_2} + C_3(x)\underbrace{x^{2}}_{y_3} + C_4(x)\underbrace{x^{4}}_{y_4} \ , \tag{B.32}$$

The same system as in equation (B.25) with the here noted y can be set up. Solving the system for C_j' and then integrating to obtain C_j gives

$$C_1(x) = C_{10} - \frac{1}{70}\int_{\bar{x}}^{x} s^6 G(s)\mathrm{d}s \ , \tag{B.33a}$$

$$C_2(x) = C_{20} + \frac{1}{30}\int_{\bar{x}}^{x} s^4 G(s)\mathrm{d}s \ , \tag{B.33b}$$

$$C_3(x) = C_{30} - \frac{1}{30}\int_{\bar{x}}^{x} s G(s)\mathrm{d}s \ , \tag{B.33c}$$

$$C_4(x) = C_{40} + \frac{1}{70}\int_{\bar{x}}^{x} s^{-1} G(s)\mathrm{d}s \ . \tag{B.33d}$$

Once again, C_{j0} are constants to be determined by the boundary conditions.

Boundary conditions

Applying the equation (B.30) and plugging it into the definition for the radial and tangential velocity as done in equation (4.31), we obtain

$$V_r^{11} = -\frac{|b_1|^2}{6\nu r}(1-3\mu^2)\Re\left\{F(x)\right\} \tag{B.34a}$$

$$V_\theta^{11} = -\frac{|b_1|^2}{6\nu r}\mu\sqrt{1-\mu^2}\Re\left\{F(x) + xF'(x)\right\} \ . \tag{B.34b}$$

From the boundary condition of zero velocity at infinity follows

$$C_{30} = \frac{1}{30}\int_{\bar{x}}^{\infty} s G(s)\mathrm{d}s \ , \tag{B.35a}$$

$$C_{40} = -\frac{1}{70}\int_{\bar{x}}^{\infty} s^{-1} G(s)\mathrm{d}s \ . \tag{B.35b}$$

For the boundary conditions on the bubble surface we need again the Lagrangian streaming and hence the Stokes drift. From the general expression for radial and tangential velocity from

equation (4.8) and by applying $n = 1$ follows for the time-dependent velocity

$$v_{1r} = -\,\mathrm{e}^{-\mathrm{i}\,\omega_1 t}\frac{k_1 b_1}{3}\frac{\mu}{x^3}\left[\bar{x}^4 h_1^{(1)''}(\bar{x}) + 6x^2 h_1^{(1)}(x)\right] \ , \tag{B.36a}$$

$$v_{1\theta} = -\,\mathrm{e}^{-\mathrm{i}\,\omega_1 t}\frac{k_1 b_1}{6}\frac{\sqrt{1-\mu^2}}{x^3}\left[\bar{x}^4 h_1^{(1)''}(\bar{x}) - 6x^3 h_1^{(1)'}(x) + 6x^2 h_1^{(1)}(x)\right] \ . \tag{B.36b}$$

Substituting equation (B.36) into equation (4.26), we obtain

$$\begin{aligned} V_{Sr}^{11} &= \frac{1}{2\omega_1}\Re\left\{\mathrm{i}v_{r1}\frac{\partial v_{1r}^*}{\partial r} + \frac{\mathrm{i}v_{1\theta}}{r}\frac{\partial v_{1r}^*}{\partial \theta}\right\} \\ &= \frac{|b_1|^2}{6\omega_1 r^3}(1-3\mu^2)\Re\left\{6\mathrm{i}x h_1^{(1)*}(x) h_1^{(1)'}(x) - \mathrm{i}\frac{\bar{x}^4 h_1^{(1)''}(\bar{x})}{x^2}\left[2h_1^{(1)}(x) - x h_1^{(1)'}(x)\right]^*\right\} \ , \end{aligned} \tag{B.37a}$$

$$\begin{aligned} V_{S\theta}^{11} &= \frac{1}{2\omega_1}\Re\left\{\mathrm{i}v_{r1}\frac{\partial v_{1r}^*}{\partial r} + \frac{\mathrm{i}v_{1\theta}}{r}\frac{\partial v_{1r}^*}{\partial \theta}\right\} \\ &= \frac{|b_1|^2}{6\omega_1 r^3}\mu\sqrt{1-\mu^2}\Re\left\{6\mathrm{i}x h_1^{(1)}(x) h_1^{(1)''*}(x) + \mathrm{i}\frac{\bar{x}^4 h_1^{(1)''}(\bar{x})}{x^2}\left[6h_1^{(1)}(x) - x^2 h_1^{(1)''}(x)\right]^*\right\} \ . \end{aligned} \tag{B.37b}$$

With the same type of boundary condition as in equation (4.27), matched normal velocity and zero tangential stress on the bubble surface, the last two unknowns can be calculated to

$$C_{10} = \frac{B - 6A}{10} \ , \tag{B.38a}$$

$$C_{20} = \frac{16A - B}{10\bar{x}^2} \ , \tag{B.38b}$$

with

$$A = -C_{30}\bar{x}^5 - C_{40}\bar{x}^7 + \bar{x}^3 h_1^{(1)''*}(\bar{x})\left[2h_1^{(1)}(\bar{x}) + \bar{x}h_1^{(1)'}(\bar{x})\right] - 6\bar{x}^2 h_1^{(1)'}(\bar{x}) h_1^{(1)*}(\bar{x}) \ , \tag{B.39a}$$

$$\begin{aligned} B = &-6C_{30}\bar{x}^5 - 16C_{40}\bar{x}^7 + \bar{x}^4 h_1^{(1)'''}(\bar{x})\left[\bar{x}^2 h_1^{(1)''*}(\bar{x}) - 6h_1^{(1)*}(\bar{x})\right] \\ &- 2\bar{x}^3 h_1^{(1)''}(\bar{x})\left[2\bar{x}^2 h_1^{(1)''*}(\bar{x}) + 3\bar{x}^* h_1^{(1)'*}(\bar{x}) - 6h_1^{(1)*}(\bar{x})\right] \\ &+ 48\bar{x}^3 h_1^{(1)''*}(\bar{x}) h_1^{(1)}(\bar{x}) - 36\bar{x}^2 h_1^{(1)*}(\bar{x}) h_1^{(1)'}(\bar{x}) \ . \end{aligned} \tag{B.39b}$$

B.2.3 Case 1 – m

Equation to solve

For the case $1 - m$ with $m > 1$ the general equation (B.15) becomes

$$\begin{aligned} &\left(\Delta_{r\theta} - \frac{1}{r^2\sin^2\theta}\right)^2 \Psi_{1m} \\ &\quad = \frac{1}{\nu r^2} P_m^1 \Re\left\{k_1^2 a_1 b_m^* \left(\frac{x_{10}}{x_1}\right)^2 \left[2h_m^{(1)}(x_1) - x_1 h_m^{(1)'}(x_1)\right]^*\right. \end{aligned}$$

$$
\begin{aligned}
&- k_1^2 b_1 b_m^* \left[x_1 h_1^{(1)'}(x_1) h_m^{(1)*}(x_1) + x_1^* h_1^{(1)}(x_1) h_m^{(1)'*}(x_1) \right] \Bigg\} \\
&- \frac{m+1}{2\nu r^2} \sqrt{1-\mu^2} P_m \Re \Bigg\{ k_1^2 a_m b_1^* \left(\frac{x_{10}}{x_1} \right)^{m+1} \left[(m+1) h_1^{(1)}(x_n) - x_1 h_1^{(1)'}(x_1) \right]^* \\
&\quad - m k_1^2 b_m b_1^* \left[x_1 h_m^{(1)'}(x_1) h_1^{(1)*}(x_1) + x_1^* h_m^{(1)}(x_1) h_1^{(1)'*}(x_1) \right] \Bigg\} \\
&+ \frac{\sqrt{1-\mu^2}}{\nu r^2} \left[\sqrt{1-\mu^2} P_m^1 \right]' \Re \Bigg\{ b_m^* k_1^2 h_m^{(1)*}(x_1) \left[a_1 \left(\frac{x_{10}}{x_1} \right)^2 - b_1 \left[h_1^{(1)}(x_1) + x_1 h_1^{(1)'}(x_1) \right] \right] \\
&\quad + b_1^* k_1^2 h_1^{(1)*}(x_1) \left[a_m \left(\frac{x_{10}}{x_1} \right)^{m+1} - b_m \left[h_m^{(1)}(x_1) + x_1 h_m^{(1)'}(x_1) \right] \right] \Bigg\} \ . \qquad \text{(B.40)}
\end{aligned}
$$

The x-values used here for more clearness will be replaced in the following for more convenience, so that $x_1 = rk_1 = x$ and $x_{01} = R_0 k_1 = \bar{x}$. This can be transformed into equation (4.36) given in the main text.

Ansatz

Substitution of equation (4.37) into equation (4.36) gives

$$
\begin{aligned}
&D^2 \left[\mu P_m^1(\mu) F_1(x) \right] + D^2 \left[\sqrt{1-\mu^2} P_m(\mu) F_2(x) \right] \\
&\qquad = k_1^2 \mu P_m^1(\mu) G_1(x) + k_1^2 \sqrt{1-\mu^2} P_m(\mu) G_2(x) \ . \qquad \text{(B.41)}
\end{aligned}
$$

The left-hand side of equation (B.41) can be transformed and then split into two equations, separating into contributions with μP_m^1 (equation (4.38a)) and with $\sqrt{1-\mu^2} P_m$ (equation (4.38b)).

Results

The Eulerian velocity is

$$
\begin{aligned}
V_r^{1m} &= -\frac{1}{\nu r} \Re \left\{ b_1 b_m^* \left[\mu P_m(\mu) [m(m+1) F_1(x) - 2F_2(x)] \right. \right. \\
&\qquad \left. \left. + \sqrt{1-\mu^2} P_m^1(\mu) [F_1(x) - F_2(x)] \right] \right\} \ , \qquad \text{(B.42a)} \\
V_r^{1m} &= -\frac{1}{\nu r} \Re \left\{ b_1 b_m^* \left[\mu P_m^1(\mu) [F_1(x) + x F_2'(x)] + \sqrt{1-\mu^2} P_m(\mu) [F_2(x) - x F_2'(x)] \right] \right\} \ , \qquad \text{(B.42b)}
\end{aligned}
$$

with

$$
\begin{aligned}
F_1(x) &= \gamma_{11}(x) x^{-m-2} + \gamma_{12}(x) x^{m+3} + \gamma_{13}(x) x^{2-m} \\
&\quad + \gamma_{14}(x) x^{m-1} + \gamma_{15}(x) x^{-m} + \gamma_{17}(x) x^{m+1} \ , \qquad \text{(B.43)} \\
F_1(x) &= -(m+1)\gamma_{11}(x) x^{-m-2} - (m+1)\gamma_{12}(x) x^{m+3} + m\gamma_{13}(x) x^{2-m} \\
&\quad + m\gamma_{14}(x) x^{m-1} + \gamma_{55}(x) x^{-m} + \gamma_{57}(x) x^{m+1} \ , \qquad \text{(B.44)}
\end{aligned}
$$

and their respective derivatives. The expressions for $G_1(x)$ and $G_2(x)$ were given in equation (4.36). The variables γ_{jl} can be obtained by

$$\gamma_{11}(x) = \bar{\gamma}_{11} + \frac{1}{2(2m+1)(2m+3)(2m+5)} \int_{\bar{x}}^{x} [-mG_1(s) + G_2(s)] s^{m+5} \mathrm{d}s \ , \tag{B.45a}$$

$$\gamma_{12}(x) = \bar{\gamma}_{12} + \frac{1}{2(2m+1)(2m+3)(2m+5)} \int_{\bar{x}}^{x} [mG_1(s) - G_2(s)] s^{-m} \mathrm{d}s \ , \tag{B.45b}$$

$$\gamma_{13}(x) = \bar{\gamma}_{13} + \frac{1}{2(2m+1)(2m-1)(2m-3)} \int_{\bar{x}}^{x} [(m+1)G_1(s) + G_2(s)] s^{m+1} \mathrm{d}s \ , \tag{B.45c}$$

$$\gamma_{14}(x) = \bar{\gamma}_{14} - \frac{1}{2(2m+1)(2m-1)(2m-3)} \int_{\bar{x}}^{x} [(m+1)G_1(s) + G_2(s)] s^{4-m} \mathrm{d}s \ , \tag{B.45d}$$

$$\gamma_{15}(x) = \bar{\gamma}_{15} - \frac{1}{2(2m-1)(2m+1)(2m+3)} \int_{\bar{x}}^{x} [3G_1(s) + 2G_2(s)] s^{m+3} \mathrm{d}s \ , \tag{B.45e}$$

$$\gamma_{17}(x) = \bar{\gamma}_{17} + \frac{1}{2(2m-1)(2m+1)(2m+3)} \int_{\bar{x}}^{x} [3G_1(s) + 2G_2(s)] s^{2-m} \mathrm{d}s \ , \tag{B.45f}$$

$$\gamma_{55}(x) = \bar{\gamma}_{55} - \frac{1}{2(2m-1)(2m+1)(2m+3)} \int_{\bar{x}}^{x} [2m(m+1)G_1(s) + G_2(s)] s^{m+3} \mathrm{d}s \ , \tag{B.45g}$$

$$\gamma_{57}(x) = \bar{\gamma}_{57} + \frac{1}{2(2m-1)(2m+1)(2m+3)} \int_{\bar{x}}^{x} [2m(m+1)G_1(s) + G_2(s)] s^{2-m} \mathrm{d}s \ , \tag{B.45h}$$

and the missing constants $\bar{\gamma}_{jl}$ are found by applying the boundary conditions. The half of the constants is obtained from the boundary conditions of zero velocity at infinity,

$$\bar{\gamma}_{12} = -\frac{1}{2(2m+1)(2m+3)(2m+5)} \int_{\bar{x}}^{\infty} [mG_1(s) - G_2(s)] s^{-m} \mathrm{d}s \ , \tag{B.46a}$$

$$\bar{\gamma}_{14} = \frac{1}{2(2m+1)(2m-1)(2m-3)} \int_{\bar{x}}^{\infty} [(m+1)G_1(s) + G_2(s)] s^{4-m} \mathrm{d}s \ , \tag{B.46b}$$

$$\bar{\gamma}_{17} = -\frac{1}{2(2m-1)(2m+1)(2m+3)} \int_{\bar{x}}^{\infty} [3G_1(s) + 2G_2(s)] s^{2-m} \mathrm{d}s \ , \tag{B.46c}$$

$$\bar{\gamma}_{57} = -\frac{1}{2(2m-1)(2m+1)(2m+3)} \int_{\bar{x}}^{\infty} [2m(m+1)G_1(s) + G_2(s)] s^{2-m} \mathrm{d}s \ . \tag{B.46d}$$

(B.46e)

The other half demands a more complex calculation including the Lagrangian expression for the boundary conditions at the bubble surface and involves lengthy expressions, which can be found in [OP7].

Appendix C

Diverse

C.1 Coefficients for Shaw's model

This section contains the coefficients necessary to calculate the bubble dynamics with coupling between different modes according to Shaw's model. They are directly taken from Shaw [114], and mainly added here for completeness of the manuscript.

$$M_{a_{nij}} = G_{d_{ijn}} - G_{c_{nij}} - G_{c_{inj}} - G_{c_{ijn}} \tag{C.1a}$$

$$M_{b_{nij}} = G_{d_{jin}} + G_{d_{ijn}} + 2(G_{e_{nij}} + G_{e_{jin}}) - G_{d_{nij}} - G_{d_{inj}} \tag{C.1b}$$

$$M_{c_{nij}} = G_{e_{nij}} + G_{e_{jin}} \tag{C.1c}$$

$$M_{d_{nij}} = G_{e_{nij}} + G_{e_{jin}} - G_{e_{inj}} \tag{C.1d}$$

$$G_{c_{nij}} = \frac{2n^2 - n + 1}{n+1} I_{a_{nij}} - \frac{2}{n+1}\left[\Lambda_{b_{nij}} - \frac{2\Lambda_{a_{nij}}}{i+1}\right] \tag{C.1e}$$

$$G_{d_{nij}} = \frac{\Lambda_{c_{nij}}}{(n+1)(j+1)} - \frac{\Lambda_{b_{jin}} - j(j-1)I_{a_{nij}}}{j+1} - \frac{4(n-1)}{n+1} I_{a_{nij}} \tag{C.1f}$$

$$G_{d_{nij}} = \frac{(n^2 - jn + 3j + 3)I_{a_{nij}} + I_{c_{nij}}}{(n+1)(j+1)} \tag{C.1g}$$

$$\Lambda_{a_{nij}} = (n+1)(n+i+1)I_{a_{nij}} + I_{c_{nij}} \tag{C.1h}$$

$$\Lambda_{b_{nij}} = \frac{1}{2}(n+1)(n^2+4n+4)I_{a_{nij}} + (n+2)I_{c_{inj}} \tag{C.1i}$$

$$\Lambda_{c_{nij}} = (n+i+1)(n+i+2)I_{a_{nij}} + I_{c_{nij}} + +I_{c_{inj}} \tag{C.1j}$$

$$I_{a_{nij}} = \int_{-1}^{1} P_n P_i P_j \mathrm{d}\mu \tag{C.1k}$$

$$I_{c_{nij}} = -\int_{-1}^{1} (1-\mu^2) P_n \frac{\mathrm{d}P_i}{\mathrm{d}\mu}\frac{\mathrm{d}P_j}{\mathrm{d}\mu}\mathrm{d}\mu \tag{C.1l}$$

Here, P_n denote the Legendre polynomials and $\mu = \cos\theta$.

Bibliography

[1] D. Ahmed, A. Ozcelik, N. Bojanala, N. Nama, A. Upadhyay, Y. Chen, W. Hanna-Rose and T. J. Huang. "Rotational manipulation of single cells and organisms using acoustic waves". In: *Nature communications* 7 (2016).

[2] A. V. Alexandrov, C. A. Molina, J. C. Grotta, Z. Garami, S. R. Ford, J. Alvarez-Sabin, J. Montaner, M. Saqqur, A. M. Demchuk, L. A. Moyé et al. "Ultrasound-enhanced systemic thrombolysis for acute ischemic stroke". In: *New England Journal of Medicine* 351.21 (2004), pp. 2170–2178.

[3] R. E. Apfel. "Sonic effervescence: A tutorial on acoustic cavitation". In: *The Journal of the Acoustical Society of America* 101.3 (1997), pp. 1227–1237.

[4] T. Barbat, N. Ashgriz and C.-S. Liu. "Dynamics of two interacting bubbles in an acoustic field". In: *Journal of Fluid Mechanics* 389 (1999), pp. 137–168.

[5] R. Ben Haj Slama, B. Gilles, M. B. Chiekh and J. C. Béra. "PIV for the characterization of focused field induced acoustic streaming: seeding particle choice evaluation". In: *Ultrasonics* 76 (2017), pp. 217–226.

[6] T. B. Benjamin and A. T. Ellis. "Self-propulsion of asymmetrically vibrating bubbles". In: *Journal of Fluid Mechanics* 212 (1990), pp. 65–80.

[7] N. Bertin, T. A. Spelman, O. Stephan, L. Gredy, M. Bouriau, E. Lauga and P. Marmottant. "Propulsion of bubble-based acoustic microswimmers". In: *Physical Review Applied* 4.6 (2015), p. 064012.

[8] V. Bjerknes. *Fields of force.* (New York: Columbia University Press), 1906.

[9] F. G. Blake. "Bjerknes forces in stationary sound fields". In: *The Journal of the Acoustical Society of America* 21.5 (1949), pp. 551–551.

[10] M. P. Brenner, D. Lohse and T. F. Dupont. "Bubble shape oscillations and the onset of sonoluminescence". In: *Physical Review Letters* 75.5 (1995), p. 954.

[11] K.-T. Byun and H.-Y. Kwak. "A model of laser-induced cavitation". In: *Japanese journal of applied physics* 43.2R (2004), p. 621.

[12] C. Cairós and R. Mettin. "Simultaneous high-speed recording of sonoluminescence and bubble dynamics in multibubble fields". In: *Physical review letters* 118.6 (2017), p. 064301.

[13] R. V. Chaudhari and H. Hofmann. "Coalescence of gas bubbles in liquids". In: *Reviews in Chemical Engineering* 10.2 (1994), pp. 131–190.

[14] H. Chen, A. A. Brayman, W. Kreider, M. R. Bailey and T. J. Matula. "Observations of translation and jetting of ultrasound-activated microbubbles in mesenteric microvessels". In: *Ultrasound in medicine & biology* 37.12 (2011), pp. 2139–2148.

[15] H. Chen, W. Kreider, A. A. Brayman, M. R. Bailey and T. J. Matula. "Blood vessel deformations on microsecond time scales by ultrasonic cavitation". In: *Physical review letters* 106.3 (2011), p. 034301.

[16] A. K. Chesters and G. Hofman. "Bubble coalescence in pure liquids". In: *Mechanics and Physics of Bubbles in Liquids*. Springer, 1982, pp. 353–361.

[17] J. Chomas, P. Dayton, D. May and K. Ferrara. "Nondestructive subharmonic imaging". In: *IEEE transactions on ultrasonics, ferroelectrics, and frequency control* 49.7 (2002), pp. 883–892.

[18] A. J. Coleman, J. E. Saunders, L. A. Crum and M. Dyson. "Acoustic cavitation generated by an extracorporeal shockwave lithotripter". In: *Ultrasound in Medicine & Biology* 13.2 (1987), pp. 69–76.

[19] J. Collis, R. Manasseh, P. Liovic, P. Tho, A. Ooi, K. Petkovic-Duran and Y. Zhu. "Cavitation microstreaming and stress fields created by microbubbles". In: *Ultrasonics* 50.2 (2010), pp. 273–279.

[20] C. C. Coussios and R. A. Roy. "Applications of acoustics and cavitation to noninvasive therapy and drug delivery". In: *Annual Review of Fluid Mechanics* 40 (2008), pp. 395–420.

[21] O. Couture, J.-F. Aubry, M. Tanter and M. Fink. "Time-reversal focusing of therapeutic ultrasound on targeted microbubbles". In: *Applied Physics Letters* 94.17 (2009), p. 173901.

[22] L. A. Crum. "Bjerknes forces on bubbles in a stationary sound field". In: *The Journal of the Acoustical Society of America* 57.6 (1975), pp. 1363–1370.

[23] L. A. Crum. "Acoustic cavitation series: part five rectified diffusion". In: *Ultrasonics* 22.5 (1984), pp. 215–223.

[24] D. Cunningham, W. H. Allum, S. P. Stenning, J. N. Thompson, C. J. Van de Velde, M. Nicolson, J. H. Scarffe, F. J. Lofts, S. J. Falk, T. J. Iveson et al. "Perioperative chemotherapy versus surgery alone for resectable gastroesophageal cancer". In: *New England Journal of Medicine* 355.1 (2006), pp. 11–20.

[25] B. J. Davidson and N. Riley. "Cavitation microstreaming". In: *Journal of Sound and Vibration* 15.2 (1971), pp. 217–233.

[26] A. Delalande, S. Kotopoulis, M. Postema, P. Midoux and C. Pichon. "Sonoporation: mechanistic insights and ongoing challenges for gene transfer". In: *Gene* 525.2 (2013), pp. 191–199.

[27] A. A. Doinikov. "Translational motion of two interacting bubbles in a strong acoustic field". In: *Physical Review E* 64.2 (2001), p. 026301.

[28] A. A. Doinikov. "Translational motion of a spherical bubble in an acoustic standing wave of high intensity". In: *Physics of Fluids (1994-present)* 14.4 (2002), pp. 1420–1425.

[29] A. A. Doinikov. "Translational motion of a bubble undergoing shape oscillations". In: *Journal of Fluid Mechanics* 501 (2004), pp. 1–24.

[30] A. A. Doinikov and A. Bouakaz. "Acoustic microstreaming around a gas bubble". In: *The Journal of the Acoustical Society of America* 127.2 (2010), pp. 703–709.

[31] A. A. Doinikov and A. Bouakaz. "Acoustic microstreaming around an encapsulated particle". In: *The Journal of the Acoustical Society of America* 127.3 (2010), pp. 1218–1227.

[32] A. A. Doinikov and A. Bouakaz. "Effect of a distant rigid wall on microstreaming generated by an acoustically driven gas bubble". In: *Journal of Fluid Mechanics* 742 (2014), pp. 425–445.

[33] P. C. Duineveld. "Bouncing and coalescence of two bubbles in pure water". In: *IUTAM Symposium on Waves in Liquid/Gas and Liquid/Vapour Two-Phase Systems*. Springer. 1995, pp. 151–160.

[34] P. C. Duineveld. "The influence of an applied sound field on bubble coalescence". In: *The Journal of the Acoustical Society of America* 99.1 (1996), pp. 622–624.

[35] C. Eckart. "Vortices and streams caused by sound waves". In: *Physical review* 73.1 (1948), p. 68.

[36] S. A. Elder. "Cavitation microstreaming". In: *The Journal of the Acoustical Society of America* 31.1 (1959), pp. 54–64.

[37] A. I. Eller. "Force on a bubble in a standing acoustic wave". In: *The Journal of the Acoustical Society of America* 43.1 (1968), pp. 170–171.

[38] A. I. Eller and L. A. Crum. "Instability of the motion of a pulsating bubble in a sound field". In: *The Journal of the Acoustical Society of America* 47.3B (1970), pp. 762–767.

[39] A. I. Eller and H. Flynn. "Rectified diffusion during nonlinear pulsations of cavitation bubbles". In: *The Journal of the Acoustical Society of America* 37.3 (1965), pp. 493–503.

[40] Z. C. Feng and L. G. Leal. "Translational instability of a bubble undergoing shape oscillations". In: *Physics of Fluids* 7.6 (1995), pp. 1325–1336.

[41] K. Ferrara, R. Pollard and M. Borden. "Ultrasound microbubble contrast agents: fundamentals and application to gene and drug delivery". In: *Annu. Rev. Biomed. Eng.* 9 (2007), pp. 415–447.

[42] S. W. Fong, D. Adhikari, E. Klaseboer and B. C. Khoo. "Interactions of multiple spark-generated bubbles with phase differences". In: *Experiments in fluids* 46.4 (2009), pp. 705–724.

[43] A. Francescutto and R. Nabergoj. "Pulsation amplitude threshold for surface waves on oscillating bubbles". In: *Acta Acustica united with Acustica* 41.3 (1978), pp. 215–220.

[44] M. M. Fyrillas and A. J. Szeri. "Dissolution or growth of soluble spherical oscillating bubbles". In: *Journal of Fluid Mechanics* 277 (1994), pp. 381–407.

[45] B. Gerold, P. Glynne-Jones, C. McDougall, D. McGloin, S. Cochran, A. Melzer and P. Prentice. "Directed jetting from collapsing cavities exposed to focused ultrasound". In: *Applied Physics Letters* 100.2 (2012), p. 024104.

[46] G. Gormley and J. Wu. "Observation of acoustic streaming near Albunex® spheres". In: *The Journal of the Acoustical Society of America* 104.5 (1998), pp. 3115–3118.

[47] R. K. Gould. "Rectified diffusion in the presence of, and absence of, acoustic streaming". In: *The Journal of the Acoustical Society of America* 56.6 (1974), pp. 1740–1746.

[48] M. Guédra and C. Inserra. "Bubble shape oscillations of finite amplitude". In: *Journal of Fluid Mechanics* 857 (2018), pp. 681–703.

[49] M. Guédra, C. Inserra, C. Mauger and B. Gilles. "Experimental evidence of nonlinear mode coupling between spherical and nonspherical oscillations of microbubbles". In: *Physical Review E* 94.5 (2016), p. 053115.

[50] D. Hanahan and R. A. Weinberg. "The hallmarks of cancer". In: *cell* 100.1 (2000), pp. 57–70.

[51] D. Hanahan and R. A. Weinberg. "Hallmarks of cancer: the next generation". In: *cell* 144.5 (2011), pp. 646–674.

[52] D.-Y. Hsieh and M. S. Plesset. "Theory of rectified diffusion of mass into gas bubbles". In: *The Journal of the Acoustical Society of America* 33.2 (1961), pp. 206–215.

[53] C. Hullin. "The stability of pulsating air-bubbles in water". In: *Acta Acustica united with Acustica* 37.2 (1977), pp. 64–73.

[54] K. Hynynen, N. McDannold, N. Vykhodtseva and F. A. Jolesz. "Noninvasive MR imaging–guided focal opening of the blood-brain barrier in rabbits". In: *Radiology* 220.3 (2001), pp. 640–646.

[55] T. Ilovitsh, A. Ilovitsh, J. Foiret, C. F. Caskey, J. Kusunose, B. Z. Fite, H. Zhang, L. M. Mahakian, S. Tam, K. Butts-Pauly et al. "Enhanced microbubble contrast agent oscillation following 250 kHz insonation". In: *Scientific reports* 8.1 (2018), p. 16347.

[56] J. Jiao, Y. He, T. Leong, S. E. Kentish, M. Ashokkumar, R. Manasseh and J. Lee. "Experimental and theoretical studies on the movements of two bubbles in an acoustic standing wave field". In: *The Journal of Physical Chemistry B* 117.41 (2013), pp. 12549–12555.

[57] J. Jiao, Y. He, K. Yasui, S. E. Kentish, M. Ashokkumar, R. Manasseh and J. Lee. "Influence of acoustic pressure and bubble sizes on the coalescence of two contacting bubbles in an acoustic field". In: *Ultrasonics Sonochemistry* 22 (2015), pp. 70–77.

[58] J. B. Keller and M. Miksis. "Bubble oscillations of large amplitude". In: *The Journal of the Acoustical Society of America* 68.2 (1980), pp. 628–633.

[59] V. A. Khokhlova, J. B. Fowlkes, W. W. Roberts, G. R. Schade, Z. Xu, T. D. Khokhlova, T. L. Hall, A. D. Maxwell, Y.-N. Wang and C. A. Cain. "Histotripsy methods in mechanical disintegration of tissue: towards clinical applications". In: *International Journal of Hyperthermia* 31.2 (2015), pp. 145–162.

[60] J. Kolb and W. L. Nyborg. "Small-Scale Acoustic Streaming Effects in Liquids". In: *The Journal of the Acoustical Society of America* 26.5 (1956), pp. 1237–1242.

[61] M. Kornfeld and L. Suvorov. "On the destructive action of cavitation". In: *Journal of Applied Physics* 15.6 (1944), pp. 495–506.

[62] H. Lamb. "Hydrodynamics". In: *Aufl., Cambridge: Univ. Press* 427 (1932).

[63] M. Lanoy, C. Derec, A. Tourin and V. Leroy. "Manipulating bubbles with secondary Bjerknes forces". In: *Applied Physics Letters* 107.21 (2015), p. 214101.

[64] W. Lauterborn. "Numerical investigation of nonlinear oscillations of gas bubbles in liquids". In: *The Journal of the Acoustical Society of America* 59.2 (1976), pp. 283–293.

[65] W. Lauterborn and T. Kurz. "Physics of bubble oscillations". In: *Reports On Progress in Physics* 73.10 (2010), p. 106501.

[66] C. P. Lee and T. G. Wang. "Outer acoustic streaming". In: *The Journal of the Acoustical Society of America* 88.5 (1990), pp. 2367–2375.

[67] T. G. Leighton. "Derivation of the Rayleigh-Plesset equation in terms of volume". In: *ISVR Technical Report No. 308* (2007).

[68] T. G. Leighton, A. J. Walton and M. J. W. Pickworth. "Primary bjerknes forces". In: *European Journal of Physics* 11.1 (1990), p. 47.

[69] I. Lentacker, I. De Cock, R. Deckers, S. De Smedt and C. Moonen. "Understanding ultrasound induced sonoporation: definitions and underlying mechanisms". In: *Advanced drug delivery reviews* 72 (2014), pp. 49–64.

[70] J. Lighthill. "Acoustic streaming". In: *Journal of sound and vibration* 61.3 (1978), pp. 391–418.

[71] J. R. Lindner. "Microbubbles in medical imaging: current applications and future directions". In: *Nature Reviews Drug Discovery* 3.6 (2004), pp. 527–533.

[72] N. Lipsman, Y. Meng, A. J. Bethune, Y. Huang, B. Lam, M. Masellis, N. Herrmann, C. Heyn, I. Aubert, A. Boutet et al. "Blood–brain barrier opening in Alzheimer's disease using MR-guided focused ultrasound". In: *Nature communications* 9.1 (2018), p. 2336.

[73] R. H. Liu, J. Yang, M. Z. Pindera, M. Athavale and P. Grodzinski. "Bubble-induced acoustic micromixing". In: *Lab on a Chip* 2.3 (2002), pp. 151–157.

[74] M. S. Longuet-Higgins. "Viscous streaming from an oscillating spherical bubble". In: *Proceedings of the Royal Society of London A: Mathematical, Physical and Engineering Sciences*. Vol. 454. 1970. The Royal Society. 1998, pp. 725–742.

[75] A. Maksimov. "Viscous streaming from surface waves on the wall of acoustically-driven gas bubbles". In: *European Journal of Mechanics-B/Fluids* 26.1 (2007), pp. 28–42.

[76] A. Maksimov and T. Leighton. "Pattern formation on the surface of a bubble driven by an acoustic field". In: *Proceedings of the Royal Society A: Mathematical, Physical and Engineering Sciences* 468.2137 (2011), pp. 57–75.

[77] P. Marmottant and S. Hilgenfeldt. "Controlled vesicle deformation and lysis by single oscillating bubbles". In: *Nature* 423.6936 (2003), pp. 153–156.

[78] P. Marmottant, J. Raven, H. Gardeniers, J. Bomer and S. Hilgenfeldt. "Microfluidics with ultrasound-driven bubbles". In: *Journal of Fluid Mechanics* 568 (2006), pp. 109–118.

[79] R. Mettin and A. A. Doinikov. "Translational instability of a spherical bubble in a standing ultrasound wave". In: *Applied Acoustics* 70.10 (2009), pp. 1330–1339.

[80] M. Minnaert. "XVI. On musical air-bubbles and the sounds of running water". In: *The London, Edinburgh, and Dublin Philosophical Magazine and Journal of Science* 16.104 (1933), pp. 235–248.

[81] C. A. Molina, M. Ribo, M. Rubiera, J. Montaner, E. Santamarina, R. Delgado-Mederos, J. F. Arenillas, R. Huertas, F. Purroy, P. Delgado et al. "Microbubble administration accelerates clot lysis during continuous 2-MHz ultrasound monitoring in stroke patients treated with intravenous tissue plasminogen activator". In: *Stroke* 37.2 (2006), pp. 425–429.

[82] G. Mychaskiw, A. E. Badr, R. Tibbs, B. R. Clower and J. H. Zhang. "Optison (FS069) disrupts the blood-brain barrier in rats". In: *Anesthesia & Analgesia* 91.4 (2000), pp. 798–803.

[83] E. A. Neppiras and B. E. Noltingk. "Cavitation produced by ultrasonics: theoretical conditions for the onset of cavitation". In: *Proceedings of the Physical Society. Section B* 64.12 (1951), p. 1032.

[84] B. E. Noltingk and E. A. Neppiras. “Cavitation produced by ultrasonics”. In: *Proceedings of the Physical Society. Section B* 63.9 (1950), p. 674.

[85] T. Nowak and R. Mettin. “Unsteady translation and repetitive jetting of acoustic cavitation bubbles”. In: *Physical Review E* 90.3 (2014), p. 033016.

[86] W. L. Nyborg. “Acoustic streaming near a boundary”. In: *The Journal of the Acoustical Society of America* 30.4 (1958), pp. 329–339.

[87] D. Obreschkow, M. Tinguely, N. Dorsaz, P. Kobel, A. De Bosset and M. Farhat. “The quest for the most spherical bubble: experimental setup and data overview”. In: *Experiments in Fluids* 54.4 (2013), p. 1503.

[88] C.-D. Ohl and R. Ikink. “Shock-wave-induced jetting of micron-size bubbles”. In: *Physical review letters* 90.21 (2003), p. 214502.

[89] C.-D. Ohl, M. Arora, R. Ikink, N. De Jong, M. Versluis, M. Delius and D. Lohse. “Sonoporation from jetting cavitation bubbles”. In: *Biophysical journal* 91.11 (2006), pp. 4285–4295.

[90] C.-D. Ohl, T. Kurz, R. Geisler, O. Lindau and W. Lauterborn. “Bubble dynamics, shock waves and sonoluminescence”. In: *Philosophical Transactions of the Royal Society of London. Series A: Mathematical, Physical and Engineering Sciences* 357.1751 (1999), pp. 269–294.

[91] C.-D. Ohl and B. Wolfrum. “Detachment and sonoporation of adherent HeLa-cells by shock wave-induced cavitation”. In: *Biochimica et Biophysica Acta (BBA)-General Subjects* 1624.1-3 (2003), pp. 131–138.

[92] M. Pernot, G. Montaldo, M. Tanter and M. Fink. ““Ultrasonic stars” for time-reversal focusing using induced cavitation bubbles”. In: *Applied Physics Letters* 88.3 (2006), p. 034102.

[93] Y. A. Pishchalnikov, O. A. Sapozhnikov, M. R. Bailey, J. C. Williams Jr, R. O. Cleveland, T. Colonius, L. A. Crum, A. P. Evan and J. A. McAteer. “Cavitation bubble cluster activity in the breakage of kidney stones by lithotripter shockwaves”. In: *Journal of endourology* 17.7 (2003), pp. 435–446.

[94] M. S. Plesset. “The dynamics of cavitation bubbles”. In: *Journal of applied mechanics* 16 (1949), pp. 277–282.

[95] M. S. Plesset. “On the stability of fluid flows with spherical symmetry”. In: *Journal of Applied Physics* 25.1 (1954), pp. 96–98.

[96] H. Poritsky. “Proceedings of the First US National Congress on Applied Mechanics”. In: Am. Soc. Mech. Eng. 1952.

[97] M. Postema, P. Marmottant, C. T. Lancée, S. Hilgenfeldt and N. de Jong. "Ultrasound-induced microbubble coalescence". In: *Ultrasound in Medicine & Biology* 30.10 (2004), pp. 1337–1344.

[98] F. Prabowo and C.-D. Ohl. "Surface oscillation and jetting from surface attached acoustic driven bubbles". In: *Ultrasonics sonochemistry* 18.1 (2011), pp. 431–435.

[99] P. Prentice, A. Cuschieri, K. Dholakia, M. Prausnitz and P. Campbell. "Membrane disruption by optically controlled microbubble cavitation". In: *Nature physics* 1.2 (2005), p. 107.

[100] A. Prosperetti. "Bubble phenomena in sould fields: part two". In: *Ultrasonics* 22.3 (1984), pp. 115–124.

[101] A. Prosperetti. "Viscous effects on perturbed spherical flows". In: *Quarterly of Applied Mathematics* 34.4 (1977), pp. 339–352.

[102] A. Prosperetti and Y. Hao. "Modelling of spherical gas bubble oscillations and sonoluminescence". In: *Philosophical Transactions of the Royal Society of London A: Mathematical, Physical and Engineering Sciences* 357.1751 (1999), pp. 203–223.

[103] S. Qin, C. F. Caskey and K. W. Ferrara. "Ultrasound contrast microbubbles in imaging and therapy: physical principles and engineering". In: *Physics in medicine and biology* 54.6 (2009), R27.

[104] L. Rayleigh. "On the circulation of air observed in Kundt's tubes, and on some allied acoustical problems". In: *Philosophical Transactions of the Royal Society of London* 175 (1884), pp. 1–21.

[105] L. Rayleigh. "VIII. On the pressure developed in a liquid during the collapse of a spherical cavity". In: *The London, Edinburgh, and Dublin Philosophical Magazine and Journal of Science* 34.200 (1917), pp. 94–98.

[106] A. J. Reddy and A. J. Szeri. "Coupled dynamics of translation and collapse of acoustically driven microbubbles". In: *The Journal of the Acoustical Society of America* 112.4 (2002), pp. 1346–1352.

[107] N. Riley. "On a sphere oscillating in a viscous fluid". In: *The Quarterly Journal of Mechanics and Applied Mathematics* 19.4 (1966), pp. 461–472.

[108] J. Rosselló, W. Lauterborn, M. Koch, T. Wilken, T. Kurz and R. Mettin. "Acoustically induced bubble jets". In: *Physics of Fluids* 30.12 (2018), p. 122004.

[109] T. Sanada, A. Sato, M. Shirota and M. Watanabe. "Motion and coalescence of a pair of bubbles rising side by side". In: *Chemical Engineering Science* 64.11 (2009), pp. 2659–2671.

[110] T. Sato, M. Tinguely, M. Oizumi and M. Farhat. "Evidence for hydrogen generation in laser-or spark-induced cavitation bubbles". In: *Applied Physics Letters* 102.7 (2013), p. 074105.

[111] H. Schlichting. "Berechnung ebener periodischer Grenzschichtstromungen". In: *Phys. Z.* 33 (1932), pp. 327–335.

[112] S. J. Shaw. "The stability of a bubble in a weakly viscous liquid subject to an acoustic traveling wave". In: *Physics of Fluids* 21.2 (2009), p. 022104.

[113] S. J. Shaw and P. D. M. Spelt. "Critical strength of an electric field whereby a bubble can adopt a steady shape". In: *Proceedings of the Royal Society A: Mathematical, Physical and Engineering Sciences* 465.2110 (2009), pp. 3127–3143.

[114] S. J. Shaw. "Translation and oscillation of a bubble under axisymmetric deformation". In: *Physics of Fluids (1994-present)* 18.7 (2006), p. 072104.

[115] S. Shklyaev and A. Straube. "Linear oscillations of a compressible hemispherical bubble on a solid substrate". In: *Physics of Fluids* 20 (2008), p. 052102.

[116] J. H. Song, A. Moldovan and P. Prentice. "Non-linear acoustic emissions from therapeutically driven contrast agent microbubbles". In: *Ultrasound in medicine & biology* (2019).

[117] T. A. Spelman and E. Lauga. "Arbitrary axisymmetric steady streaming: flow, force and propulsion". In: *Journal of Engineering Mathematics* 105.1 (2017), pp. 31–65.

[118] R. L. Stover, C. W. Tobias and M. M. Denn. "Bubble coalescence dynamics". In: *AIChE journal* 43.10 (1997), pp. 2385–2392.

[119] H. Strube. "Numerische Untersuchungen zur Stabilitat nichtapharisch schwingender Blasen". In: *Acustica* 25 (1971), pp. 289–303.

[120] A. Thiemann, F. Holsteyns, C. Cairós and R. Mettin. "Sonoluminescence and dynamics of cavitation bubble populations in sulfuric acid". In: *Ultrasonics sonochemistry* 34 (2017), pp. 663–676.

[121] P. Tho, R. Manasseh and A. Ooi. "Cavitation microstreaming patterns in single and multiple bubble systems". In: *Journal of Fluid Mechanics* 576 (2007), pp. 191–233.

[122] T. Verraes, F. Lepoint-Mullie, T. Lepoint and M. S. Longuet-Higgins. "Experimental study of the liquid flow near a single sonoluminescent bubble". In: *The Journal of the Acoustical Society of America* 108.1 (2000), pp. 117–125.

[123] M. Versluis, D. E. Goertz, P. Palanchon, I. L. Heitman, S. M. van der Meer, B. Dollet, N. de Jong and D. Lohse. "Microbubble shape oscillations excited through ultrasonic parametric driving". In: *Physical Review E* 82.2 (2010), p. 026321.

[124] A. Vogel, J. Noack, K. Nahen, D. Theisen, S. Busch, U. Parlitz, D. Hammer, G. Noojin, B. Rockwell and R. Birngruber. "Energy balance of optical breakdown in water at nanosecond to femtosecond time scales". In: *Applied Physics B: Lasers and Optics* 68.2 (1999), pp. 271–280.

[125] A. van Wamel, K. Kooiman, M. Harteveld, M. Emmer, J. Folkert, M. Versluis and N. De Jong. "Vibrating microbubbles poking individual cells: drug transfer into cells via sonoporation". In: *Journal of controlled release* 112.2 (2006), pp. 149–155.

[126] C. Wang, S. V. Jalikop and S. Hilgenfeldt. "Size-sensitive sorting of microparticles through control of flow geometry". In: *Applied Physics Letters* 99.3 (2011), p. 034101.

[127] M. Ward, J. Wu and J.-F. Chiu. "Experimental study of the effects of Optison® concentration on sonoporation in vitro". In: *Ultrasound in Medicine & Biology* 26.7 (2000), pp. 1169–1175.

[128] J. Wu and G. Du. "Streaming generated by a bubble in an ultrasound field". In: *The Journal of the Acoustical Society of America* 101.4 (1997), pp. 1899–1907.

[129] J. Wu, J. P. Ross and J.-F. Chiu. "Reparable sonoporation generated by microstreaming". In: *The Journal of the Acoustical Society of America* 111.3 (2002), pp. 1460–1464.

[130] X. Xi, F. Cegla, R. Mettin, F. Holsteyns and A. Lippert. "Study of non-spherical bubble oscillations near a surface in a weak acoustic standing wave field". In: *The Journal of the Acoustical Society of America* 135.4 (2014), pp. 1731–1741.

[131] L. Zarembo. "Acoustic streaming". In: *High-intensity ultrasonic fields*. Springer, 1971, pp. 135–199.

[132] Y. Zhang and S. Li. "A general approach for rectified mass diffusion of gas bubbles in liquids under acoustic excitation". In: *Journal of Heat Transfer* 136.4 (2014), p. 042001.

[133] Y. Zhou, K. Yang, J. Cui, J. Ye and C. Deng. "Controlled permeation of cell membrane by single bubble acoustic cavitation". In: *Journal of controlled release* 157.1 (2012), pp. 103–111.

Own publications

[OP1] S. Cleve, M. Guédra, C. Inserra, C. Mauger and P. Blanc-Benon. "Surface modes with controlled axisymmetry triggered by bubble coalescence in a high-amplitude acoustic field". In: *Physical Review E* 98 (2018), p. 033115.

[OP2] S. Cleve, M. Guédra, C. Mauger, C. Inserra and P. Blanc-Benon. "Microstreaming induced by acoustically trapped, non-spherically oscillating microbubbles". In: *Journal of Fluid Mechanics* 875 (2019), pp. 597–621.

[OP3] S. Cleve, M. Guédra, M. Cyril, C. Inserra and P. Blanc-Benon. "Experimental investigation of microstreaming induced by free nonspherically oscillating microbubbles". In: *Proceedings of Meetings on Acoustics 21ISNA*. Vol. 34. 1. ASA. 2018, p. 045030.

[OP4] S. Cleve, M. Guédra, C. Mauger, C. Inserra and P. Blanc-Benon. "A method for triggering surface modes by bubble coalescence". In: *Proceedings of the 10th International Symposium on Cavitation (CAV2018)*. ASME Press. 2018.

[OP5] S. Cleve, C. Inserra and P. Prentice. "Contrast Agent Microbubble Jetting during Initial Interaction with 200-kHz Focused Ultrasound". In: *Ultrasound in medicine & biology* 45.11 (2019), pp. 3075–3080.

[OP6] A. A. Doinikov, S. Cleve, G. Regnault, C. Mauger and C. Inserra. "Acoustic microstreaming produced by nonspherical oscillations of a gas bubble. I. Case of modes 0 and m". In: *Physical Review E* 100.3 (2019), p. 033104.

[OP7] A. A. Doinikov, S. Cleve, G. Regnault, C. Mauger and C. Inserra. "Acoustic microstreaming produced by nonspherical oscillations of a gas bubble. II. Case of modes 1 and m". In: *Physical Review E* 100.3 (2019), p. 033105.

[OP8] M. Guédra, S. Cleve, C. Mauger, P. Blanc-Benon and C. Inserra. "Dynamics of nonspherical microbubble oscillations above instability threshold". In: *Physical Review E* 96.6 (2017), p. 063104.

dernière page de la thèse

AUTORISATION DE SOUTENANCE

Vu les dispositions de l'arrêté du 25 mai 2016,

Vu la demande du directeur de thèse

Monsieur P. BLANC-BENON

et les rapports de

M. R. METTIN
Professeur - III. Physikalisches Institut - Friedrich-Hund-Platz 1 - 37077 Göttingen - Allemagne

et de

M. P. MARMOTTANT
Directeur de Recherche CNRS - Laboratoire Interdisciplinaire de Physique - Université Grenoble Alpes - Service Courrier UGA - Pôle Phitem - Laboratoire LIPhy - CS 40 700
38058 Grenoble cedex 9

Madame CLEVE Sarah

est autorisée à soutenir une thèse pour l'obtention du grade de **DOCTEUR**

Ecole doctorale MECANIQUE, ENERGETIQUE, GENIE CIVIL ET ACOUSTIQUE

Fait à Ecully, le 25 septembre 2019

P/Le directeur de l'E.C.L.
Le directeur des Etudes

Grégory VIAL